Technische Universität München
Fakultät für Chemie
Lehrstuhl für Theoretische Chemie

Ab Initio simulation of core-level spectroscopies and correlated materials

Georg S. Michelitsch

Dissertation

Technische Universität München
Fakultät für Chemie
Lehrstuhl für Theoretische Chemie

Ab Initio simulation of core-level spectroscopies and correlated materials

---

Georg Siegmund Michelitsch

Vollständiger Abdruck der von der Fakultät für Chemie der Technischen Universität München zur Erlangung des akademischen Grades eines

Doktors der Naturwissenschaften (Dr. rer. nat.)

genehmigten Dissertation.

Vorsitzender: Priv.-Doz. Dr. Harald Oberhofer

Prüfer der Dissertation:

1. Prof. Dr. Karsten Reuter
2. Prof. Dr. Johannes Barth

Die Dissertation wurde am 06.02.2019 bei der Technischen Universität München eingereicht und durch die Fakultät für Chemie am 12.03.2019 angenommen.

Gewidmet meiner Großmutter.

Abstract

Modern material science is a flourishing field comparable to traditional engineering but at a much smaller length scale. It is concerned not only with solid state materials of specific targeted properties at the macroscale but also, and more importantly, functionalized (coated) surfaces, nano-machinery, catalysis, and atomic-scale self-assembled structures. The targeted properties are often materials, which could serve to further miniaturize the length scales of complex logical building blocks, data storage mechanisms, or overcoming the limitations in the catalysis of chemical reactions in solution by bringing them to the surface. The traditional semiconductor-based silicon technology based on chemical etching and lithographic processes is currently at the pinnacle of development. Further improvements are hampered on purely physical grounds, where the operation on a few nanometers already hits the limits where quantum mechanical effects lead to unpredictable and unstable side-effects. On-surface assembly of substances of intrinsic magnetism and 3-dimensional molecular structures allows these unprecedented materials on a surface to replicate silicon technology at a smaller scale with much higher flexibility with respect to the employed materials. Alongside this development the traditionally chemical discipline of organic or metal-organic reaction schemes is re-discovered, catalyzing chemical conversion not by solvated ions in solution but realizing it on a solid catalyst surface. However, the outcome of a reaction on a surface is not as straightforwardly characterized at the submolecular level. One of the most established methodologies to analyze a long-range ordered material are X-ray spectroscopic methods in the ionization or absorptive regime, allowing to indirectly probe the occupied and unoccupied states of the material under study. Alongside spectroscopy, scanning tunneling microscopy is often used to obtain a visual image of materials, hidden from the bare eye. However, the information obtained from either of aforementioned methods does not have a direct, analytic, bijective mapping to a molecular arrangement. It is only by the ab-initio simulation of these materials and their accompanying analytical techniques, that experimental signatures can be properly assigned to a molecular structure and mere educated guesses can be backed by a solid theoretical model. This work lays the foundation for a theoretical description of x-ray studies of core electrons at experimental length scales of not only light elements and organic molecules but also heavy metals and strongly correlated materials, such as transition metal and rare earth compounds. It presents an overview and critical evaluation of the currently established approximate methodologies and extends them in a systematic manner. Examples are given for a library of gas-phase compounds containing nitrogen and carbon atoms, a transition metal cluster, surface assemblies of single atoms and self-assembled metal-organic frameworks of transition and rare earth metals on coinage surfaces and a thorough theoretical treatment of their bonding environment, spectroscopic and microscopic signatures.

Zusammenfassung

Die Disziplin der modernen Materialwissenschaften ist im Grunde genommen eine Ingenieurswissenschaft abgebildet auf viel kleinere Größenskalen. Dieses Fachgebiet beschäftigt sich mit dem Design und der Entwicklung von Materialien, die nicht nur aufgrund ihrer makroskopischen Eigenschaften von Interesse sind, sondern dient in einem noch viel wichtigeren Kontext dazu neuartige Materialen zu entwickeln, welche sich in funktionalisierten Oberflächen, Nanomaschinen, Katalyse, und Selbstassemblierung auf atomaren Level wiederspiegeln. Die Zielgrößen dieser Forschung sind oftmals Materialien, welche zur weiteren Miniaturisierung von komplexen logischen Grundbausteinen, Datenspeicherung, oder zur Verbesserung der katalytischen Umsetzung von chemischen Stoffen abseits der traditionellen nasschemischen Methoden, an Oberflächen, beitragen. Die etablierte Halbleiter-basierte Silizium-Technologie, welche vorwiegend auf nasschemische Ätzprozesse und Lithographie aufbaut ist momentan auf dem Gipfel der technologischen Entwicklung. Weitere Verbesserungen werden dadurch blockiert, dass die Größenskalen an physikalische Grenzen stoßen, an welchen quantenmechanische Effekte zu unvorhersagbaren Effekten und instabilen Verhalten führen. Assemblierung von Materialien mit intrinsischen magnetischen Eigenschaften in dreidimensionalen Strukturen erlaubt es bisher unerreichte molekulare Strukturen zu erzeugen, welche die etablierten Silizium-basierten Technologie mit wesentlich höherer Flexibilität an zugrundeliegenden Materialien und erzielbarer Funktionalität replizieren. Ganz nebenbei führt die Forschung an diesen Materialien dazu, dass die ehemals klassisch chemische Disziplin der organischen oder metallorganischen Synthese an Oberflächen wiederentdeckt wird, wobei die Katalyse nicht durch Ionen in Lösung, sondern an Oberflächen stattfindet. Eines der größen Probleme stellt jedoch die Charakterisierung der Reaktionsprodukte dar. Wohingegen in moderner organischer Synthese mit vielfältigen Methoden die exakte atomare Zusammensetzung einer Verbindung mit Leichtigkeit aufklärt werden kann, ist dies für Festkörper kein triviales Unterfangen. Eine der weit verbreitetsten Analysemethoden ist Röntenspektroskopie, welche in ionisierender oder absorptiver Variante Auskunft über die besetzten und unbesetzten Zustände des zugrundeliegenden Materials gibt. Daneben bietet auch Rastertunnelmikroskopie die Möglichkeit Strukturen sichtbar zu machen, welche mit dem freien Auge nicht auszumachen sind. Obwohl diese Methoden wichtige Informationen liefern gibt es leider keine direkte, analytische, bijektive Abbildung von dieser Information zu einer molekularen Struktur. Nur unter Zuhilfenahme von ab-initio Simulationen der Materialien und der zugehörigen analytischen Signaturen ist es möglich diese Zuordnung einer molekularen Struktur zu erzielen und auf Erfahrung basierende Vermutungen durch solide theoretische Modelle zu untermauern. Diese Arbeit legt den Grundstein für eine theoretische Beschreibung von Röntgenspektroskopie von kernnahen Elektronen in Systemen von experimenteller Größenordnung, und dies überdies nicht nur für leichte Elemente und organische Moleküle, sondern auch für schwere Elemente und stark korrelierte Materialen, wie Übergangsmetalle und Verbindungen mit seltenen Erden. Die Arbeit liefert einen Überblick und eine kritische Betrachtung der momentan etablierten Methoden und erweitert diese in systematischer Manier. Als konkrete Beispiele werden eine kleine Bibliothek an Verbindungen bestehend aus Stickstoff und Kohlenstoff in der Gasphase, ein Übergangsmetallcluster, Oberflächenstrukturen von einzelnen Atomen, selbstassemblierten metallorganischen Netzwerken mit Übergangsmetallen und seltenen Erden auf Münzmetallen und eine tiefgehende theoretische Betrachtung der chemischen Bindung und der spektroskopischen und mikroskopischen Signaturen im Detail behandelt.

Contents

1 Introduction **1**

2 Density functional theory **5**
2.1 The Hohenberg-Kohn theorems 5
2.2 The Kohn-Sham approach to DFT 6

3 Approximate methodologies in the simulation of core-level spectroscopies **9**
3.1 The core-hole relaxation 10
3.2 Spectroscopy with approximate core-level constraining approaches 13
3.3 The core-hole localization 17
3.4 $L_{2,3}$-edge spectra in the approximate formalism 19

4 Simulation of magnetic materials and localized magnetic properties **21**
4.1 The self-interaction error and possible remedies 23
4.2 Case study: Dy on graphene/Ir(111) 28

5 Publications **33**
5.1 Assembly of Robust Holmium-Directed 2D Metal-Organic Coordination Complexes and Networks on the Ag (100) Surface 34
5.2 Remote functionalization in surface-assisted dehalogenation by conformational mechanics: organometallic self-assembly of 3,3′,5,5′-tetrabromo-2,2′,4,4′,6,6′-hexafluorobiphenyl on Ag(111) 36
5.3 Efficient Simulation of Near-Edge X-ray Absorption Fine Structure (NEXAFS) in Density-Functional Theory: Comparison of Core-Level Constraining Approaches 37

6 Summary, Conclusions and Outlook **39**

Acknowledgments / Danksagung **41**

Bibliography **43**

Appendices **51**

List of Illustrations

Figures

1.1 Schematic comparison of core-level ionization and absorption spectroscopy. 2

3.1 Eigenstate alignment as a function of the core-hole occupation for a carbon atom and the benzene molecule. 11
3.2 Typical deviations from a linear behavior of the eigenvalues of the system as a function of fractional occupation. 12
3.3 Overview of numerical core-hole constraining approaches used in the simulation X-ray spectroscopic experiments. 14
3.4 Pyrazine Kohn-Sham states of 1s character before and after the Boys-localization procedure. 18
3.5 Pyrazine Kohn-Sham states of a core-ionized system based on orbitals of a Boys-localized and a non-localized ground state. 19
3.6 Geometry and NEXAFS $L_{2,3}$-edge spectrum for the $MnSi_{11}$ compound 20

4.1 Commensurate structure of corrugated (10×10) graphene on (9×9) Ir(111) 29
4.2 Adsorption energy and spin magnetic moment vs. adsorption height for dysprosium on flat graphene ((4×4) surface unit cell). 30
4.3 Adsorption energy and spin magnetic moment vs. adsorption height for dysprosium on corrugated graphene ((10×10) surface unit cell). 31

Tables

3.1 Experimental and simulated ionization potentials of the pyrazine molecule based on delocalized and localized core states. 19

4.1 Comparison of adsorption height and corrugation of graphene on the Ir(111) facet. 29

List of Abbreviations

AMF	around mean field
CEBE	core-electron binding energy
DFA	density functional approximation
DFT	density functional theory
DFT+U	Hubbard-corrected density functional theory
DOS	density of states
ΔSCF	delta self-consistent field
fcc	face-centered cubic
FCH	full core hole
FLL	fully localized limit
GGA	generalized gradient approximation
GS	ground state
GTP	generalized transition potential
GTS	generalized transition state
hcp	hexagonal closed packed
HEG	homogeneous electron gas
HK	Hohenberg-Kohn
KS	Kohn-Sham
LDA	local density approximation
MOF	metal-organic framework
NEXAFS	near-edge X-ray absorption fine structure
PAW	projector augmented wave
PZ-SIC	Perdew-Zunger self-interaction correction
SOC	spin-orbit coupling
STM	scanning tunneling microscope
TP	transition potential
TS	transition state
XCH	excited core hole
XGTP	excited generalized transition potential
XPS	X-ray photoelectron spectroscopy
XTP	excited transition potential

1 Introduction

This work is a publication-based dissertation, and should therefore stand as a supplement of the articles already published in international scientific journals. In this thesis, the background on all theoretical models is provided in a swift manner, relating to the original publications of myself or other researchers if necessary, therefore setting my work in context with current and previous research on the same matter. The ultimate goal is to give the reader an insight into the reasons behind the work on many different projects and how they were all in line with the original aims of my dissertation.

X-ray based photoelectric experiments have become one of the leading characterization tools when it comes to questions concerning the chemical composition of a material, the orientation of adsorbates, and its magnetic properties. The basic functional principle is that the energy of an impacting photon is transferred to an electron of the system under study. Of course this simple one-electron picture is much more complicated in a real situation where many electrons of an extended system, equivalent by translational symmetry, are excited. The observed experimental signature is thus a superposition of many similar events, which can be detected by measurement of either electrons emitted from the material or via secondary processes, such as fluorescence or Auger decay. The nature of the detection and secondary processes are also the reason for broadened peaks in the experimental spectrum. In theory, the measurement is expected to deliver a line spectrum because of the quantized nature of matter at the length scales relevant to electrons and photons. However, noise and aforementioned reasons lead to absorption spectra with broad resonances overlapping and thus hiding the actual positions and making the interpretation difficult. Already before the discovery of quantum mechanics, a lot was learned about the behavior of matter with respect to radiation, and this theoretical development helped in understanding the first basic atomic absorption spectra of hydrogen or alkali metals via Balmer's formula or the even more well-known Rydberg formula for the line spectra of atoms. At that time there was still no knowledge about quantum mechanics and the different effects which lead to the more complicated absorption spectra of heavier elements or even compound materials. However, the theoretical development continued at a remarkable pace following the discovery of quantum mechanics and eventually also succeeded to provide interpretations and rationalization for more complicated materials, and the fine structure of the experimental measurements. The photoelectric effect[1] laid the foundation for the theoretical understanding of the interaction of radiation with matter. The first experiments of this kind in the X-ray regime became what we know today as X-ray photo-electron spectroscopy (XPS) and probe the ionization energy of a material by transferring enough energy to a core-electron to move it above the vacuum level and thus ionize the system[2, 3]. Chemical speciation was discovered shortly later, meaning that the same atomic species has different excitation energies depending on their chemical environment[4, 5]. Near-edge X-ray absorption fine structure (NEXAFS) is a related spectroscopic technique, where the absorbed energy from the incoming photon excites a photo-electron in previously unoccupied states of the probe material, thus forming a bound state[6]. Whereas XPS only allows to probe the occupied states of a specific system, the NEXAFS method allows to probe all unoccupied states of the system, which are, of course, heavily influenced by chemical bonding in the valence region. The significance of this method was discovered but in the second half of the past century, when the resolution of spectrometers was improved and what was previously interpreted as one big absorption edge (peak), split into many signals[7–9]. The previous models employed mainly a scattering formulism (which is still the method of choice to evaluate the EXAFS - extended x-ray absorption fine structure) to resolve oscillating signals further away from the absorption edge. Since there is no strict distinction what is to be considered "near edge", this sometimes leads to misunderstandings. The topic of this work are the electronic transitions, which occur intra-atomic, inside the same atom, whereas sometimes inter-atomic scattering effects are also referred to as NEXAFS. A schematic comparison between XPS and NEXAFS is given in Figure 1.1.

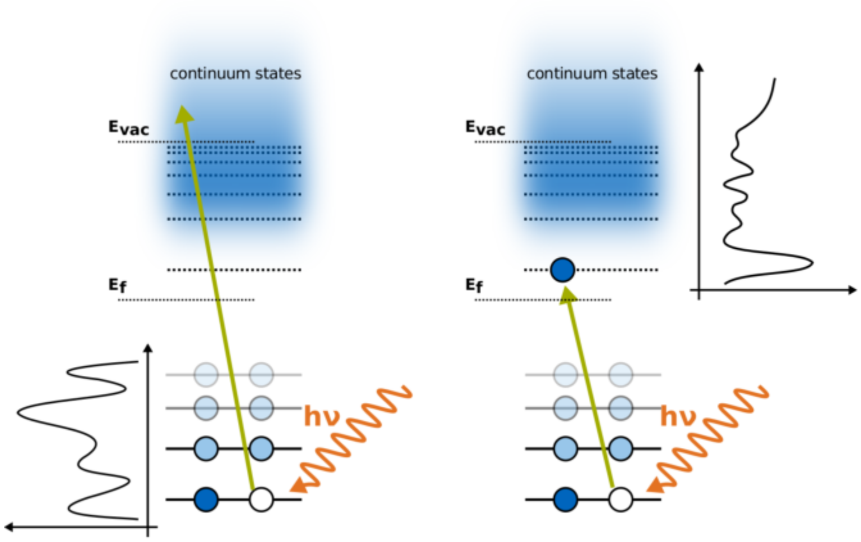

Fig. 1.1: *Schematic comparison of the ionization (XPS, on the left) and absorption (NEXAFS, on the right) regime of core-level spectroscopies. As explained in the main text, the XPS spectroscopy probes the occupied state of a system by ionizing the electrons into the continuum, whereas in the absorptive regime one core electron is ionized in different unoccupied states. A typical shape of both spectra is shown to the left of the ionization scheme and to the right of the absorption scheme. Whereas in XPS typically close-lying peaks of a similar broadening are observed in a narrow energetic region (where they overlap), in NEXAFS a sharp, isolated peak of high intensity is followed by fewer smaller peaks with an increasing broadening until by excitation into high-lying Rydberg states, or, finally into the continuum, the large broadening does not allow to observe single peaks anymore.*

In this work I will be approaching two - at the first glance entirely set apart - topics, where computational modeling is required to understand experimental measurement. In the first chapter I will be introducing the concept of a core-hole and its effect on the electronic structure of the remaining (non-ionized) electronic structure of the molecular ion, followed then by recapitulating the main approaches towards the simulation of spectroscopic properties in a one-particle picture. Although approximate, these methods are the workhorse of modern electronic structure theory when it comes to the simulation of spectroscopic properties of experimentally accessible length scales. I will conclude this chapter with a glance at a crucial ingredient in the simulation of core-hole spectra, namely the localization requirement of a hole state on a targeted atom. In the second chapter I will be approaching the simulation of materials characterized by localized d and f-electrons, also known as *correlated materials*. Their outstanding property is, that unlike simple metals or organic molecules, they can not be described sufficiently well anymore by prevalent semi-local density-functional theory (DFT) methods. This is mainly due to the partially filled d- and f-shells in the transition metal or lanthanide/actinide series exhibiting a large local electronic interaction[10–13]. The main shortcoming in the simulation is attributed to the self-interaction error in semi-local DFT, which leads to an overestimated Coulomb-repulsion, which in turn gives a bad description of the localized states[14–19]. This shortcoming can be cured through the application of hybrid DFT functionals, which unfortunately incur a large computational cost. Model Hamiltonians such as DFT+U, a locally interacting potential based on the Hubbard model, constitute an efficient way to recover the same physics and are thus the second topic of this work. The second chapter will thus introduce in more detail the shortcomings of common DFT-based approaches in the simulation of strongly correlated materials and a recapitulation of the DFT+U theory. This is followed by a case study of a lanthanide element - Dysprosium, where we were interested in the nature of the chemical bond to corrugated graphene on top of Ir(111). X-ray spectroscopy, as mentioned in the beginning, is a very established technique in the routine analysis of material science. As such, it is of use aswell in the analysis of strongly correlated materials. My work should lay the foundation of a sound description of the electronic structure to be paired with a sound description of spectroscopic properties, both on an equally economic footing with respect to the computational workload. The final chapter collects a short summary of the publications authored during the course of this thesis.

2 Density functional theory

This entire thesis makes heavy usage of terminology associated with a theoretical concept of ubiquitous use in the field of condensed matter physics and also extensive use in the theoretical modeling of isolated molecules, namely Density-Functional Theory (DFT). This chapter will thus recapitulate in a brief manner the most important ideas, methodologies, and their associated terminology needed to follow not only the theoretical concept but also their implementation in software. The content of this chapter is based on introductory textbooks on the matter such as the ones from Koch and Holthausen[20] or Parr and Yang[21] and substantiated (where needed) by original citations.

2.1 The Hohenberg-Kohn theorems

The central problem in the application of wave-function based simulations is the sheer number of variables which has to be taken into account. In other words, the (electronic) wave-function $\Psi(\mathbf{r_i})$ of a system as the quantity to represent all information about the system carries $3N$ coordinates $(\mathbf{r_i})$ for a N-particle system. Although accessible for small molecules, wave-function based methods are therefore severly restricted in their application with increasing system size, since solving the Schrödinger equation $\hat{H}\Psi = E\Psi$ for the correct wave-function Ψ and total energy E of the system requires to operate on that many-dimensional object. The landmark publication of Hohenberg and Kohn (HK)[22] put forward two theorems which abandoned the need for the full many-particle wave function in place of a much easier accessible quantity - the electron density $\rho(\mathbf{r})$, a function of only 3 coordinates. The first Hohenberg-Kohn theorem states, that there is a direct mapping in the form of a functional (meaning a function of a function, i.e. a mapping from a space of functions to e.g. the real numbers) between the electronic density $\rho(\mathbf{r})$ (resulting from an external potential) and the total energy E. The exact form of this functional is elusive up until today, but the idea by itself provides the opportunity to find what became known as Density-Functional approximations (DFAs). Following the first theorem, all parts which constitute the total energy are also functionals of the density, as such we can write:

$$E_{\mathrm{HK}}[\rho(\mathbf{r})] = V_{\mathrm{ne}}[\rho(\mathbf{r})] + T[\rho(\mathbf{r})] + V_{\mathrm{ee}}[\rho(\mathbf{r})] = F_{\mathrm{HK}}[\rho(\mathbf{r})] + \int \rho(\mathbf{r}) v_{\mathrm{ne}}(\mathbf{r}) d\mathbf{r} \tag{2.1}$$

The terms in the above equation are the potential between nuclei and electrons V_{ne}, the kinetic energy functional $T[\rho(\mathbf{r})]$, and the electron-electron interaction potential $V_{\mathrm{ee}}[\rho(\mathbf{r})]$. The latter two terms constitute what is often referred to as the Hohenberg-Kohn functional F_{HK}, since it is system-independent (has no dependence on the number of electrons N or their respective position to the nuclei, as well as the charge of these). Since there is no prior knowledge of the exact form of the HK-functional, the common approximation consists in supplementing the classical Coulomb-interaction between two particles J, as it is readily formulated as a functional of the electron density $J[\rho(\mathbf{r})]$. Assuming that the unknown F_{HK} would be expanded in powers of the electronic charge e^2, this would correspond to the first-order term, while the kinetic energy would cover the zeroth order. Higher-order terms do not have a classically known corresponding kernel, therefore they are collected in a separate term together with all errors we incur by introducing the classical Coulomb kernel, we can call it the non-classical (ncl) energy term $E_{\mathrm{ncl}}[\rho(\mathbf{r})]$. At this point, having introduced all the approximations mentioned so far, we can write down the total energy as a functional of the density:

$$E[\rho(\mathbf{r})] = \int \rho(\mathbf{r}) v_{\mathrm{ne}}(\mathbf{r}) d\mathbf{r} + T[\rho(\mathbf{r})] + J[\rho(\mathbf{r})] + E_{\mathrm{ncl}}[\rho(\mathbf{r})] \tag{2.2}$$

In the next section we will see how this term E_{ncl} is approximated in practical calculations. Before, we should mention the second HK theorem, which states, that the HK functional F_{HK} will deliver the ground state energy if, and only if, the input is the ground state density ρ_0.

$$E_0 = E[\rho_0(\mathbf{r})] < E[\rho(\mathbf{r})] \tag{2.3}$$

This sounds very familiar, as the *variational principle* in wave-function theories states exactly the same in terms of the wave function. It therefore does not come as a surprise that the variational principle is the origin of this theorem. The remaining ingredients to actually be able to perform a DFT calculation are now 1) a way as of how to obtain this ground state density and 2) finding approximations to best describe the non-classical energy term. DFT, by itself, is an exact theory, the degree as to which exact results of a pratical calculation are obtained depends on how well the exact functional is approximated.

2.2 The Kohn-Sham approach to DFT

In the previous section we have concluded that there needs to be some kind of functional which connects the ground state electron density with the total energy or other kind of observables of a system. We separated out certain contributions of this functional by physical intuition without giving a functional form. Of course we would know a functional form of the Coulomb potential since it operates on charges and that is what the electron density is made of. But a more difficult part is the kinetic energy operator $\hat{T}$. How can we calculate the contribution to the kinetic energy if the information about single electrons as a separable quantity is lost? Early approaches tried to use the homogeneous electron gas as the basis for finding an energy functional but failed due to the overall potential being repulsive, failing even to predict molecules to be stable. The big breakthrough was the idea of Kohn and Sham (KS)[23], to model the kinetic energy in the same way as it is done in wave-function theory, but using an auxiliary system of non-interacting particles, defined such as that the density which would result by summing up all these occupied orbitals corresponds to the ground state density.

$$\rho(\mathbf{r}) = \sum_{\mathrm{i}=1}^{\mathrm{N}} f_{\mathrm{i}} |\psi_{\mathrm{i}}(\mathbf{r})|^2 \tag{2.4}$$

This is not in contradiction with the Hohenberg-Kohn theorems, since the same density can be connected via two different mappings to a given external potential. As such, the Kohn-Sham approach is a valid approach and we introduce a new quantity, the KS-orbital $\psi_i(\mathbf{r})$, which is occupied by a (non-necessarily integer) number of electrons f_{i}. These will become important in the later chapter on spectroscopic methodologies, where the eigenvalues ϵ_{i} associated with the KS-orbitals form the basis of the calculation of the transition energy. However, the initial reason to introduce this system of non-interacting single-particle functions was to evaluate the kinetic energy operator. The associated error connected with this approximation is added to the non-classical part of the Hohenberg-Kohn functional to yield what is nowadays famously known as the *exchange-correlation functional* E_{xc}. Therefore, in the general form the working equation of the Kohn-Sham approach to DFT is written as:

$$E[\rho(\mathbf{r})] = \sum_{\mathrm{i}=1}^{\mathrm{N}} \langle \psi_i(\mathbf{r})| -\frac{1}{2}\nabla^2 + v_{\mathrm{ne}}(\mathbf{r})|\psi_{\mathrm{i}}(\mathbf{r})\rangle + \frac{1}{2}\int\int \frac{\rho(\mathbf{r})\rho(\mathbf{r}')}{|\mathbf{r}-\mathbf{r}'|} d\mathbf{r}d\mathbf{r}' + E_{\mathrm{xc}}[\rho(\mathbf{r})] \tag{2.5}$$

The KS-orbitals are in a practical calculation expanded in a linear combination of basis functions. A basis function is an arbitrary analytic (or numerically stored on a grid, such as it is in our case of the FHI-aims code[24]) function, which represents an as-good-as-possible model of the actual single particle wave-function. A linear combination of basis functions yields an orbital $\psi_i = \sum_{\mathrm{k}} c_{\mathrm{k}}\phi_{\mathrm{k}}$. The coefficients c_{k} are optimized such as that the density resulting from a sum over all KS-orbitals (cf. eq. 2.4) minimizes the total energy. When these coefficients for each orbital are stored in a computer, these are commonly referred to as the *Kohn-Sham eigenvector*. This is the quantity which will be transformed (rotated) for the formation of maximally localized states, as introduced in the later section 3.3. The intrinsic property of electron spin is introduced in DFT typically via an assumption of *collinear* spin orientation, which means that we assume that the electron spins are aligned with a magnetic field oriented in one direction (typically chosen along the z-axis of the system). Under this assumption the Kohn-Sham problem is solved for *spin-orbitals* of the spin-up ψ_{i}^{+} and spin-down ψ_{i}^{-} components. This means the working equation of DFT (eqn. 2.5) is solved twice at the same time for both spin channels, while only the electronic potential connects both spin channels due to the total density being formed as a sum over all states. Furthermore, the maximum occupation of a single spin state is 1.0 electrons. It is this occupation of a single particle state, which will be modified in the approximative approaches to electronic spectroscopies as introduced in the section 3.2. Since both spin channels are optimized separately from each other, depending on the energetic ordering of the spin orbitals with respect to each other, a different number of electrons can occupy either one channel. This is the signature of a magnetic systems, where the difference of the spin-up density ρ^{+} and the spin-down density ρ^{-} is not equal to 0, the actual value is called the *spin magnetic moment* of the system under study and makes up the largest part of the total magnetization of a system, with the minor components being related to spin-orbit coupling. More on the particularities of the simulation of magnetic systems with DFT is given in chapter 4 and section 3.4.

In KS-DFT, the only term without an explicit functional form in eq. 2.5 is the exchange-correlation functional. This is at the same time the most problematic part, since these are all effects and errors together introduced by the previous approximations. As such, there are currently many different approaches on how to approach the functional form, some rely on physical intuition, some corresponding to a mere parametrized form compared to experimental or wave-function based data. However, many of these DFAs share common ideas and as such they were categorized in a hirarchical fashion, named *Jacob's ladder*[25]. At the lowest rung of this ladder one finds the local density approximation (LDA), which treats the exchange-correlation kernel based on the solution of the homogeneous electron gas (HEG) and was already suggested by Hohenberg and Kohn in their initial publication on DFT[22]. As the HEG was already well-described at this time by Monte-Carlo methods[26], these results served as a sound input and the LDA method performs well for materials of slowly varying electron density, such as true metals. However, the description worsens for semiconductors, ionic systems, and molecules. The next step is the generalized gradient approximation (GGA), which takes the variations in the electronic density into account by introducing the gradient of the density. A very popular example is the functional by Perdew, Becke, and Ernzerhof (PBE)[27], which up until today enjoys great popularity in the solid state community. The GGA functionals were very successful for a large variety of materials, even for organic molecules and has become the de-facto standard for condensed matter physics[28–31]. On the third rung, the logical improvement is to include the Laplacian of the electronic density (or the kinetic energy density in the orbital expansion). Approaches such as these became known as meta-GGA. Finally, on account of the self-interaction error present in DFT, the fourth rung introduces the exact exchange interaction, known form Hartree-Fock theory, in an ad-hoc fashion into the exchange-correlation functional. The basis for the exchange interaction is conveniently given by the single-particle orbitals of the Kohn-Sham approach to DFT. More details on hybrid functionals and associated methods on how to overcome the self-interaction error in DFT will be given in the theory section 4.1 as a prelude to this simulation of magnetic materials in DFT.

3 Approximate methodologies in the simulation of core-level spectroscopies

The interpretation of many kinds of spectroscopies, including those resulting from irradiation in the X-ray regime, has benefited a lot from the insight given by theoretical modeling, which can happen at different levels of accuracy. Frequently employed at the time of measurement or by the group of experimentalists themselves are methods based on model Hamiltonians, which assign parameters to an interacting model of the system and optimize these parameters until the final spectrum matches to the simulation[32, 33]. Although these tools are a great help in disentangling overlapping resonances, there are limits as to their applicability when the model is not apt for the system under study or the result is tainted by fitting artifacts. On the other hand, the development done in the simulation of quasi-particle physics permits to correctly describe the self-energy (the response of a system to the presence of a (quasi-)particle) and in the following their dielectric function to great accuracy. This includes methods such as time-dependent DFT (TD-DFT) [34, 35], the Bethe-Salpeter equation (BSE)[36, 37], coupled-cluster approaches (CC)[38–40], or a multi-reference calculation[41–43]. However, these kind of methods are limited in their applicability in system size and computational effort. To strike a balance between the accuracy given by an ab-initio description of the system at hand (and thus having exact control up to which level the predicted physics are expected to be correct) and the applicability in a sense of whether or not these calculations can be performed with relatively low computational effort, approximate methodologies based on occupational constraints of the electronic structure in a DFT calculation were developed and successfully applied[44–49].

This chapter is separated in four sections. Section 3.1 introduces the effects, which a core hole has on all other occupied and unoccupied states of the system, and outlines an important physical background for section 3.2, where the mathematical background for approximate methodologies in the simulation of core-hole spectroscopies within the realm of ground-state DFT and the methods themselves are explained. The chapter 3.3 highlights the importance of the localization of core-ionized states on the example of the pyrazine molecule. Finally, in a very brief showcase on a transition metal compound, the applicability of the approximate methodologies to higher-lying core states (at the $L_{2,3}$-edge) is demonstrated in chapter 3.4.

3.1 The core-hole relaxation

The ionization of an electron is a localized process (as we will see in the later chapter 3.3) which introduces a hole state in the system under study. This ionization (or excitation) process leads to changes in the potential acting at a very specific point of the material and changes the effective charge Z_{eff} of the atom, which is ionized. Which atom in a molecule is affected by the ionization is determined by the energy of the incident radiation $E = h\nu$ which is transferred to the system under study and, if large enough, overcomes what has been termed the core-electron binding energy (CEBE). The magnitude of CEBEs is determined by a multitude of factors, first of all it depends on the element, but then experiences changes due to the chemical environment, the presence of magnetic fields (or interaction with other charged particles in the system). As such, CEBEs are used experimentally to characterize a material by what is called their spectrum. Depending on which experimental method is chosen, either absorption spectroscopy (excited electrons are transferred to previously unoccupied states above the Fermi level) or ionization spectroscopy (excited electrons are entirely removed from the system), the resulting spectral signatures are different. Even more so are the methods to predict them in simulations. In Figure 3.1, we present results of a computer experiment about the changes effectuated due to a change in the occupation of certain molecular orbitals of a carbon atom and the benzene molecule and the accompanying effect of the change in Z_{eff} on all the molecular orbitals. In the top row of Figure 3.1 the occupation of one 1s core state of a carbon atom (left) and the benzene molecule (right) were modified. The immediate effect of the increased (less shielded) effective charge is a decrease in the eigenvalue of not only the state affected by the change but also all other states. This is especially pronounced for the occupied states (all states up to the LUMO state, also highlighted in orange). When the core state is entirely empty, the change in eigenvalues in the valence region is about 50 eV, whereas the change in the core region is on the order of 100 eV. This gives us an idea of the order of magnitude by which electronic eigenstates are influenced due an ionization event, as we would observe in XPS, an actual ionization of the system leaving behind a positive background charge. In the right column, the same process is repeated for a Kohn-Sham state of the benzene molecule. The most drastic observation here is that the energetic change in the eigenstates due to the many more electrons present in the benzene molecule is reduced, since electrons from neighboring atoms allow for a more effective screening of the positive point charge, which are not available for a single atom. Correspondingly, the valence orbitals are shifted by approximately 10 eV and the core states by about 50 eV. The message learned from this computer experiment is first, the order of magnitude effectuated by a core-ionization process and second, how electrons in a bonded system can help in effectively screening the hole state and as such decrease the core-level shift.

Next in Figure 3.1 is the same computer experiment, except that instead of ionizing the system, the electron removed from the core state is placed in the LUMO orbital. We thus simulate a neutral excitation, as it would be observed in absorption spectroscopy experiments. For the carbon atom we see a very similar behavior of the eigenstate alignment as compared with the ionization process above, although lessened in magnitude. For the benzene molecule, however, we observe that the valence states of the system are barely shifted as compared with the already only little shifted states of the ionization process above. Nevertheless, one important effect is seen for both the carbon atom and the benzene molecule: a state rearrangement and state splitting. This is especially pronounced for the case where the core orbitals have been entirely depleted and the valence states respond not only with a shift towards lower energies but also an orbital-dependent shift and thus a splitting of states. It is this splitting which is important in the simulation of

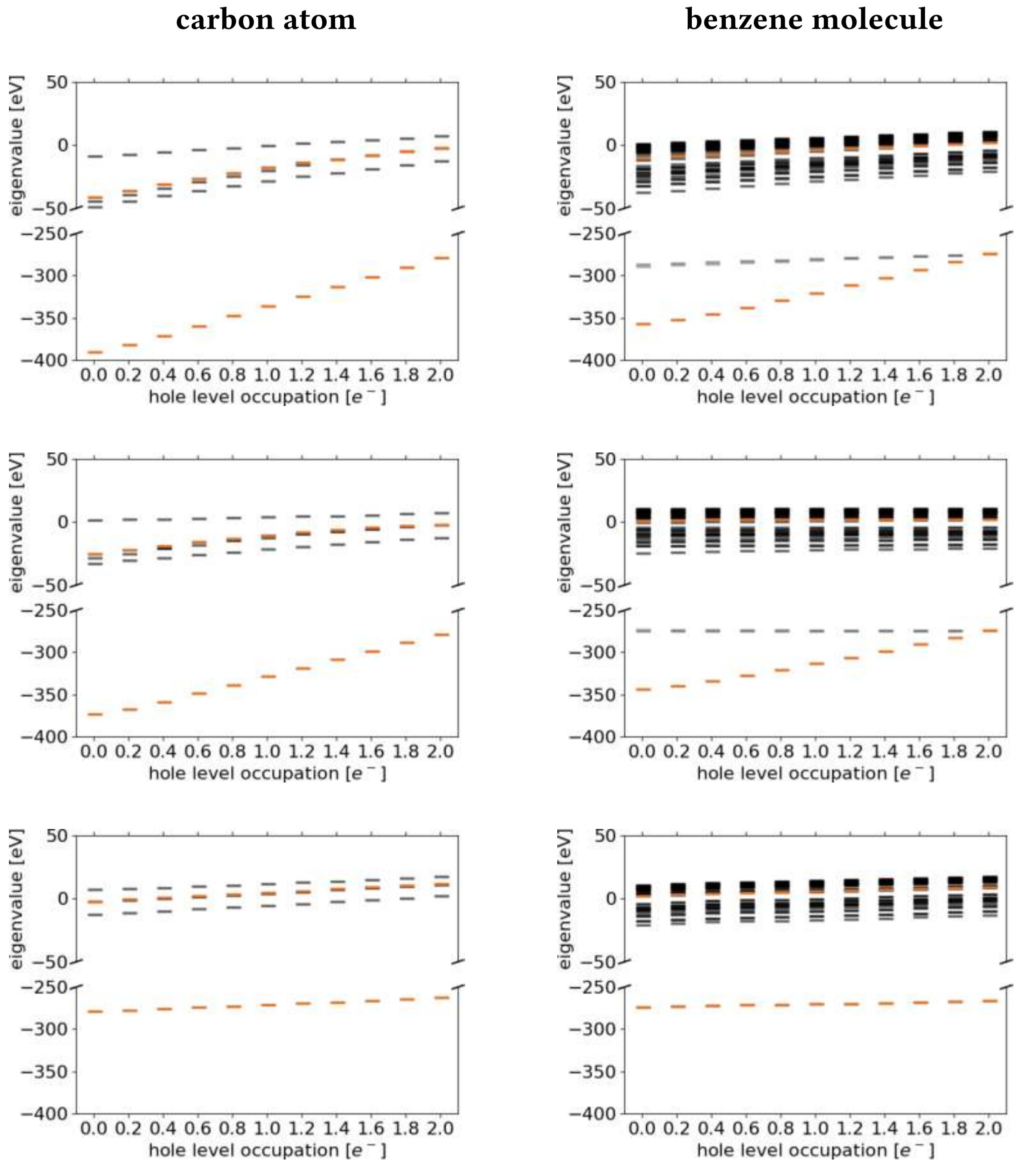

Fig. 3.1: *Eigenstate alignment for an atom of carbon (left column) and the benzene molecule (right column) when the occupation of the 1s core state (lower state highlighted in orange) and/or the LUMO state (upper state highlighted in orange) is modified between 0 and 2 electrons. Results based on a DFT-HSE06[50] calculation using the FHI-aims default 'tight' basis set settings. In the first row only the core occupation is modified, the center row is a neutral excitation where electrons are transferred to the LUMO and in the third row only the valence orbital state is modified.*

core-level absorption spectra, because the energy required to reach an unoccupied state is equal to the difference in energy between the core and excited state orbital. More on that statement will be detailed later in chapter 3.2.

Finally, the lowermost row of diagrams simulates the effect of modifying the occupation of the LUMO state, while leaving the core states untouched. This would be an ionization of the system by forming an anion. The valence orbital eigenvalues change only very little in the atomic calculation (by less than 5 eV) and about or even less for the benzene molecule. Furthermore, we do not see a splitting of degenerate valence states due to the ionization process. A curious detail which is very obvious especially from the diagrams concerning single carbon atoms is the approximately linear change of the energy eigenvalues with respect to the occupation. This, and an accompanying derivative discontinuity[51] have been the subject of many studies and also became a measure for the quality of a density-functional approximation as compared to the unknown exact functional[15, 52, 53]. Whereas the exact functional will have an exactly linear change of the eigenvalue, LDA and GGA-type functionals do show a convex behavior and those including exact exchange typically a concave behavior[15, 17]. A close to perfect linear behavior will greatly increase numerical integral equations w.r.t. the occupation number of an electronic structure, which will be needed in a later chapter. Figure 3.2 schematically shows the

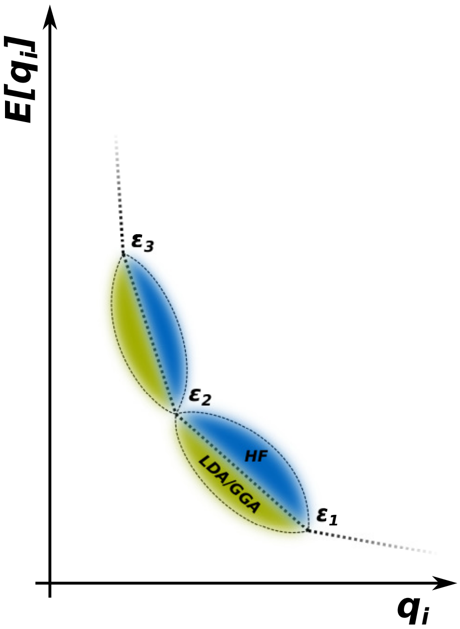

Fig. 3.2: *Typical deviations from a linear behavior of the eigenvalues of the system* (ϵ_i) *as a function of fractional occupation* q_i. *The dashed line marks the value which the exact functional would give. Functionals without explicit self-interaction correction show a negative deviation and delocalization which manifests itself in the figure as a convex deviation (LDA/GGA, green area). On the contrary, Hartree-Fock or inclusion of exact exchange leads to an overestimation of the eigenvalues and a concave deviation from the optimal function (HF, blue area).*

deviations from this optimal behavior for common density functional approximations such as the LDA and GGA or the Hartree-Fock (HF) theory. It is also a quite straightforward assumption, that a (weighted) sum of both approaches should cancel the erroneous convex and concave deviations to a great extent. This approach is known as a hybrid functional and is addressed further in section 4.1, which discusses possible remedies to the shortcomings in common density functionals.

3.2 Spectroscopy with approximate core-level constraining approaches

The first major subject of the work presented in this thesis is the simulation of core-level excitations using different approximative methodologies within the framework of DFT. All the following approaches are based on time-dependent perturbation theory, which leads to the following expression for the transition probability of an electron into another state:

$$P_{\mathrm{i}\rightarrow\mathrm{f}}(\omega) \;=\; \frac{2\pi}{\hbar}\mu_{\mathrm{i}f}^{2}\delta(E_{\mathrm{f}} - E_{\mathrm{i}} - \hbar\omega) \quad . \tag{3.1}$$

The transition dipole moments $\mu_{\mathrm{i}f}^{2}$, together with the transition energy ($\mathrm{E_f}$-$\mathrm{E_i}$ = $\hbar\omega$) are all ingredients needed to assemble a simulated absorption spectrum within the framework of time-dependent perturbation theory, which, when applied to spectroscopy, is commonly referred to as Fermi's golden rule. As such, a simulation can only access a line-spectrum of sharp delta-peak like structures. In the experiment, these delta-peaks are broadened for a multitude of reasons, among which thermal broadening and electronic decay processes are probably the most important. Nevertheless, a simulated line spectrum in most cases already corresponds nicely to the experimental signature. It has, however, become common practice[54, 55] to introduce an empirical broadening by replacing the delta peaks with gaussians and adding them up numerically. The broadening parameters are element-specific and usually increase linearly starting from an initial value. In the following we will discuss briefly how to calculate both the transition energy and the transition intensity. The more difficult quantity to evaluate is the transition energy. Subsumed in Figure 3.3 are approximate methodologies in the simulation of core-hole spectra which are all based on different approximations to the electronic transition energy given by the so-called ΔSCF (sometimes, when used in the context of DFT, also referred to as ΔKS) energy. In a ΔSCF calculation, the total energy of a system including a core-hole-state is subtracted from the total energy of the ground state calculation[56]. In a one-electron picture this approach recovers the true excitation energy to a great extent. This methodology is used widely and successfully in the simulation of the ionization energy of a system where the final state energy $\mathrm{E_f}$ is the total energy of the N-1 ion (with N being the number of electrons in the neutral system). The ionization energy is then given by

$$E_{\mathrm{XPS}} = E_{\mathrm{f}} - E_{\mathrm{i}} = E(q_{\mathrm{c}} = 0) - E(q_{\mathrm{c}} = 1) \quad . \tag{3.2}$$

Here, $\mathrm{q_c}$ is the occupation number of the core state probed. However, the ΔSCF approach is less satisfactory for X-ray absorption simulation where the unoccupied state is probed because it in principle incurs the simulation of all possible excitons on every symmetry-inequivalent atom of the underlying geometry. In other words, rather than simulating a core-hole state with the electron removed from the system, the electron is placed once in every unoccupied state. Remedies to this limitation were proposed by an integral approximation to this total energy difference, reformulated as an eigenvalue difference of an auxiliary electronic structure[57–59]. While more details on the mathematical derivation of these core-hole constraining approaches are given in the publication on the subject[57], I shall give here a short qualitative description. The ΔSCF approach is a difference of two ground state total energies of the system.

$$\Delta E_{\Delta\mathrm{SCF}} = E_{\mathrm{f}} - E_{\mathrm{i}} = E(q_{\mathrm{c}} = 0, q_{\mathrm{u}} = 1) - E(q_{\mathrm{c}} = 1, q_{\mathrm{u}} = 0) \quad . \tag{3.3}$$

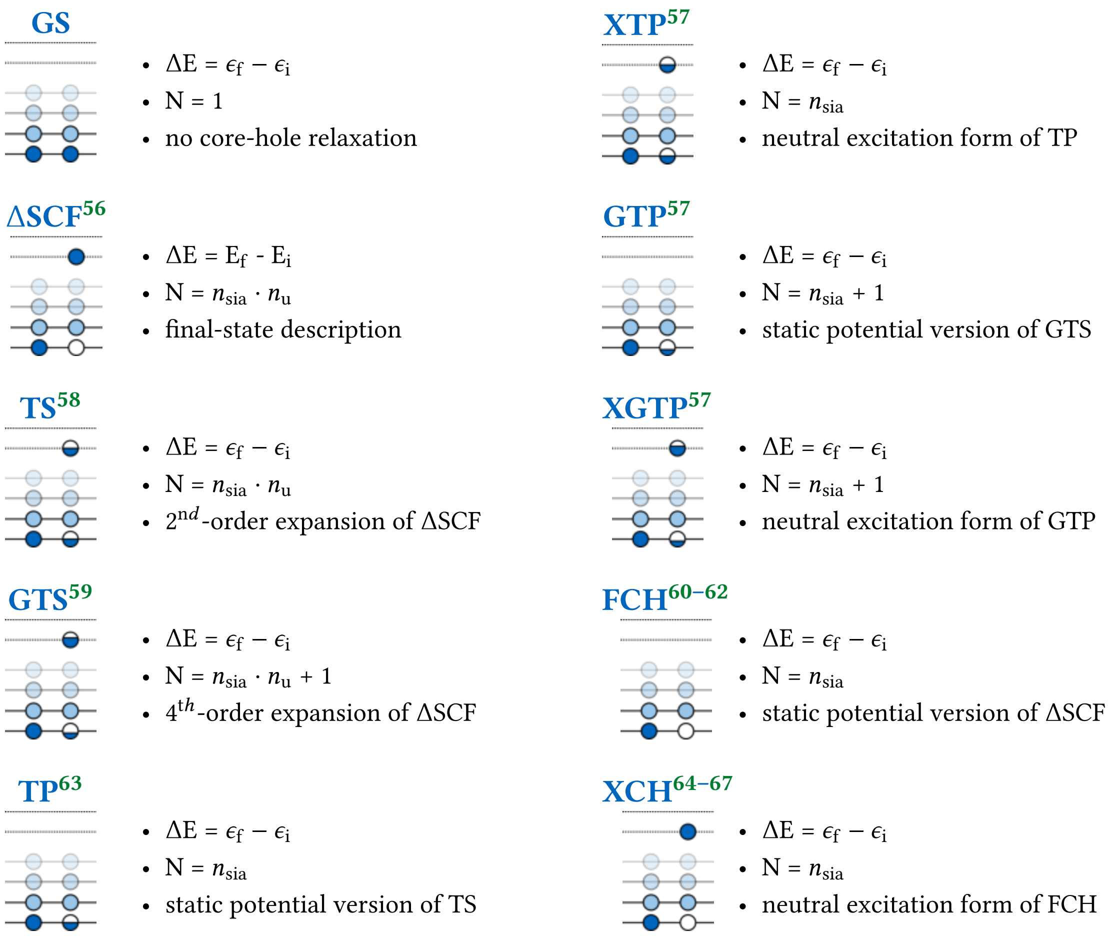

GS
- $\Delta E = \epsilon_f - \epsilon_i$
- N = 1
- no core-hole relaxation

ΔSCF[56]
- $\Delta E = E_f - E_i$
- $N = n_{sia} \cdot n_u$
- final-state description

TS[58]
- $\Delta E = \epsilon_f - \epsilon_i$
- $N = n_{sia} \cdot n_u$
- 2^{nd}-order expansion of ΔSCF

GTS[59]
- $\Delta E = \epsilon_f - \epsilon_i$
- $N = n_{sia} \cdot n_u + 1$
- 4^{th}-order expansion of ΔSCF

TP[63]
- $\Delta E = \epsilon_f - \epsilon_i$
- $N = n_{sia}$
- static potential version of TS

XTP[57]
- $\Delta E = \epsilon_f - \epsilon_i$
- $N = n_{sia}$
- neutral excitation form of TP

GTP[57]
- $\Delta E = \epsilon_f - \epsilon_i$
- $N = n_{sia} + 1$
- static potential version of GTS

XGTP[57]
- $\Delta E = \epsilon_f - \epsilon_i$
- $N = n_{sia} + 1$
- neutral excitation form of GTP

FCH[60–62]
- $\Delta E = \epsilon_f - \epsilon_i$
- $N = n_{sia}$
- static potential version of ΔSCF

XCH[64–67]
- $\Delta E = \epsilon_f - \epsilon_i$
- $N = n_{sia}$
- neutral excitation form of FCH

Fig. 3.3: *Overview of the core-hole constraining approaches being used in the simulation of X-ray spectroscopic experiments. N is the total number of calculations required to simulate a NEXAFS spectrum.* n_{sia} *is the number of symmetry-inequivalent atoms of the same species,* n_u *is the number of unoccupied states considered.*

Here, q_c is the occupation of the core-state KS orbital and q_u is the occupation of the (formerly) unoccupied KS state above the Fermi level. E_f and E_i are the total energies of the final (core-ionized) and initial (ground) state electronic structure. The energy given by ΔSCF as the starting point, can be rewritten as an integral over the varying occupations during the electronic transition.

$$\begin{aligned}\Delta E_{\Delta SCF} &= \\ &= \int_{x=1}^{0} \frac{dE(q_c = x, q_u = 1 - x)}{dx} dx \\ &= \int_{x=1}^{0} \left\{ \frac{\partial E(q_c = x, q_u = 1 - x)}{\partial q_c} - \frac{\partial E(q_c = x, q_u = 1 - x)}{\partial q_u} \right\} dx \qquad (3.4)\end{aligned}$$

Furthermore, in employing the Slater-Janak theorem[68] $\frac{\partial E}{\partial q_\mathrm{i}} = \epsilon_\mathrm{i}$ it is possible to arrive at eq. (3.3) in terms of KS eigenvalues ϵ_i:

$$\Delta E_{\Delta\mathrm{SCF}} = \int_{x=1}^{0} \left\{\epsilon_\mathrm{c}(q_\mathrm{c} = x, q_\mathrm{u} = 1 - x) - \epsilon_\mathrm{u}(q_\mathrm{c} = x, q_\mathrm{u} = 1 - x)\right\} dx \quad . \tag{3.5}$$

To arrive at an eigenvalue difference the integral first had to be split in two parts (due to the core- and valence-state contribution) and then substituted for $\frac{\partial q_c}{\partial x} = 1$ and $\frac{\partial q_u}{\partial x} = -1$. This, however, still leaves us with an integral equation of sorts which we avoid to evaluate exactly by numerically approximating it. A popular choice (and a perfectly valid one, when thinking of the linear relationship between the total energy of a system and the electronic occupation, cf. chapter 3.1) would be the midpoint integration rule $\int_a^b f(x)dx \simeq (b - a)f((a + b)/2)$. This results in

$$\Delta E_\mathrm{TS} = \epsilon_\mathrm{u}(q_\mathrm{c} = 0.5, q_\mathrm{u} = 0.5) - \epsilon_\mathrm{c}(q_\mathrm{c} = 0.5, q_\mathrm{u} = 0.5) \quad . \tag{3.6}$$

This is also termed Slater's Transition State (TS) approach [58]. Slater showed this initially by subtracting a series expansion of a state with 0.5 electrons occupation from the difference of two series expansions of the ground state and a state with an electron transferred to a previously unoccupied state[58]. It became widely known and employed as such but was only at a later point reformulated via the more accessible integral approximation[59]. Based on numerical integral evaluations, the ΔSCF energy from equation 3.3 can in principle be approximated to arbitrary accuracy, while it was shown that the midpoint rule recovers already the better part of it[58]. Furthermore, if using more than one point to approximate the integral numerically, one DFT calculation for each auxiliary structure of fractional occupation needs to be performed. Since in every simulation first a ground state calculation needs to be performed, a weighted sum of the ground state and one partially occupied state thus represents the most economic solution with increased accuracy and was termed the generalized transition state concept[59]. Most of the methods listed in Figure 3.3 are derived via mathematical approximations to the ΔSCF energy, with the *excited* variants (those methods with an acronym starting with the letter X) constituting non-mathematically motivated approaches, which were sought for ease of computation because of the problems inherent to the simulation of charged periodic surfaces, in particular the divergence of the electrostatic energy[69, 70]. It is important to note here, that the mathematical accuracy is higher in the *generalized* formulisms (GTS, GTP) as compared to their regular counterparts (TS, TP), because less integrals are neglected. The ten approaches shown in Figure 3.3 can be classified in two major categories: First, those which require the explicit modeling of each possible transition from an initial (core) state to an unoccupied (empty valence) state. These methods are ΔSCF, TS, and GTS. The only actual advantage in doing the TS and GTS methods in place of the ΔSCF approach is the ease of evaluation of the dipole transition moments $\mu_{\mathrm{i}f}^2$ which are given by exactly the same KS-eigenstates, which give also rise to the eigenvalue difference and have a direct correspondence to the transition intensity in experiment.

$$\mu_{\mathrm{i}f} = \langle\psi_\mathrm{i}|\hat{x}|\psi_\mathrm{f}\rangle \quad . \tag{3.7}$$

ψ_i and ψ_f are here the KS eigenvectors of states i and f, respectively. The second category contains all remaining methods (GS, TP, GTP, XTP, XGTP, XCH, FCH), which either neglect the (part of an) excited electron entirely in the calculation or only include it in an average way. This means, that they are either a truncated mathematical approximation or a non-deterministic approximation to the transition energy. It should be noted here, that the names "transition state", "transition potential" and "(part of an) excited electron" are misleading and prompt the association with a chemical reaction pathway. However, the "transition state" as Slater designated his approach, is merely a mathematically clever chosen auxiliary electron structure with the peculiar property, that the eigenvalue differences are an approximation to the ΔSCF method. This also without a doubt guarantees, that the best approximative method in Figure 3.3 can, in the ideal case, only deliver the accuracy of ΔSCF, assuming the ΔSCF approach could technically be realized without problems. How this is not the case and how some explicit methods actually outperform ΔSCF for technical reasons is the subject of a publication[57], where all these methods are critically reviewed.

3.3 The core-hole localization

In the procedures lined out in the previous chapter the occupations of certain orbitals belonging to atoms inside a chemically bound structure, such as a molecule or a solid state material, need to be modified in order to approximate the excitation energy of the X-ray experiment. The computational ansatz used in the Kohn-Sham variant of DFT employs the linear combination of atomic orbitals (LCAO) in order to form a molecular orbital. These molecular orbitals are the states/orbitals previously mentioned, of which the occupation needs to be modified to meet the respective requirements of partial occupation, given by the derivations in the previous chapter. By the nature of forming a linear combination of atomic orbitals of the entire system and the tendency of common approximations to the exchange and correlation potentials to delocalize the electrons initially belonging to one atom onto others, the molecular states often become delocalized among many, if not even all atoms in the system[15–19]. This problem in delocalization is accentuated stronger if the systems under study contains many instances of the same atom and even more in the case of a symmetric arrangement of these. However, if the spectroscopic excitation of an electron is modeled with the methods mentioned before, we require a hole of the character of a certain angular momentum channel to be introduced locally on a specific atom, therefore giving rise to two possible channels on how to construct this: First, when using a localized basis set, a projection of the hole state on the Kohn-Sham basis. Second, the Kohn-Sham states of the ground state density can aswell serve to this extent, if they are maximally localized via a unitary transformation[71, 72], keeping the ground state density invariant but changing the spatial localization of each Kohn-Sham state. In the course of this thesis I followed the latter approach, using the Foster-Boys localization procedure[71] to achieve named transformation of Kohn-Sham states. Depicted in Figure 3.4 are the KS-spin states of the pyrazine molecule prior and after successful localization following the Boys-algorithm. The Boys algorithm requires either a maximization of

$$\xi_{\mathrm{Boys}} = \sum_{\mathrm{i}} \sum_{\mathrm{x}} \langle \psi_{\mathrm{i}} | \hat{x} | \psi_{\mathrm{i}} \rangle \quad , \tag{3.8}$$

or a minimization of

$$\xi = \sum_{\mathrm{i}} \sum_{\mathrm{x}} (\langle \psi_{\mathrm{i}} | \hat{x}^2 | \psi_{\mathrm{i}} \rangle - \langle \psi_{\mathrm{i}} | \hat{x} | \psi_{\mathrm{i}} \rangle^2) \quad . \tag{3.9}$$

Here, the index i extends over all KS-states considered in the transformation (only the occupied realm to keep the total density invariant with the transformation) and the index x extends over all spatial coordinates. The avid reader will quickly make out the large resemblance of the equations given above with the transition dipole moment operator in equation 3.7. Thus, in order to perform a Boys localization procedure according to equations 3.8 and 3.9, the dipole transition matrix has to be formed and properly preconditioned. This means that all elements belonging to unoccupied states are set to zero in order to avoid linear combinations of occupied and unoccupied states. Optionally, in order to avoid an nonphysical linear combination of states of different angular momentum channels, the Boys-procedure could be applied to only a subset of the states. As already pointed out for very early investigations of optical spectra for small molecules[76–78], the localization of the core-hole is a crucial ingredient in the construction of the proper potential of the Hartree-Fock Hamiltonian, which can be straightforwardly transferred to the Kohn-Sham formulism, where the (missing) density of a localized electron (hole) leads to a different shape

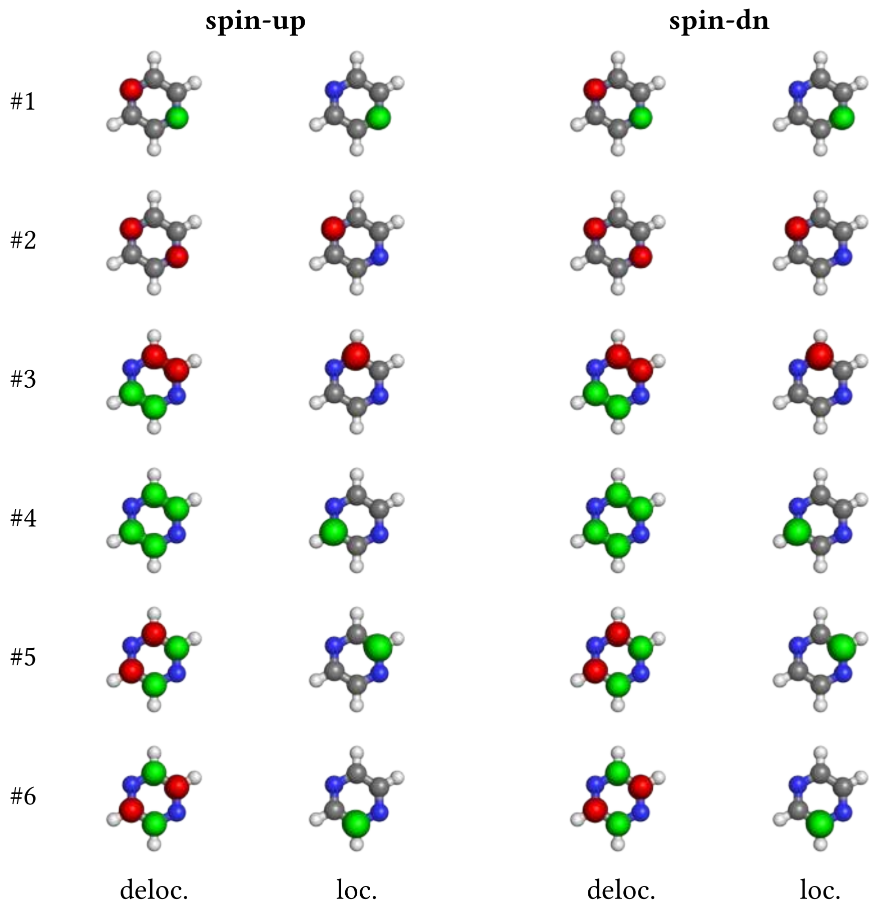

Fig. 3.4: *Kohn-Sham states of 1s character for both spin channels of the carbon and nitrogen atoms in the pyrazine molecule before (deloc.) and after (loc.) the Boys-localization procedure applied to them. Easily discernible, the molecular orbital states have non-vanishing contributions from all atoms of the same species (N atoms for KS-states #1 and #2, and C atoms from #3 to #6). Simulation with FHI-aims[24, 73] and the PBE0[74] functional using the def2-QZVP[75] basis set.*

of the potential as a delocalized description. In essence, an initially delocalized hole state will in most cases remain delocalized throughout the entire calculation, whereas an initially localized core hole will remain localized to the atom it belongs to. This can be seen in Figure 3.5, where the final KS-states for DFT calculations based on a delocalized and localized core-state are shown. To showcase the effect of the (de-)localization of a core hole on the ionization energy for the example given above, the ionization potential is calculated by a ΔSCF approach, where the total energy of the system with a core-hole (the pyrazinium ion) is subtracted from the total energy of the ground state pyrazine molecule. The resulting energies are then compared to experimental results for the ionization potential[79] and reproduced in Table 3.1. Although no perfect agreement with the experimental data is achieved, the results based on a localized core hole description are in much better agreement than those based on a delocalized hole, validating the approach taken in this work.

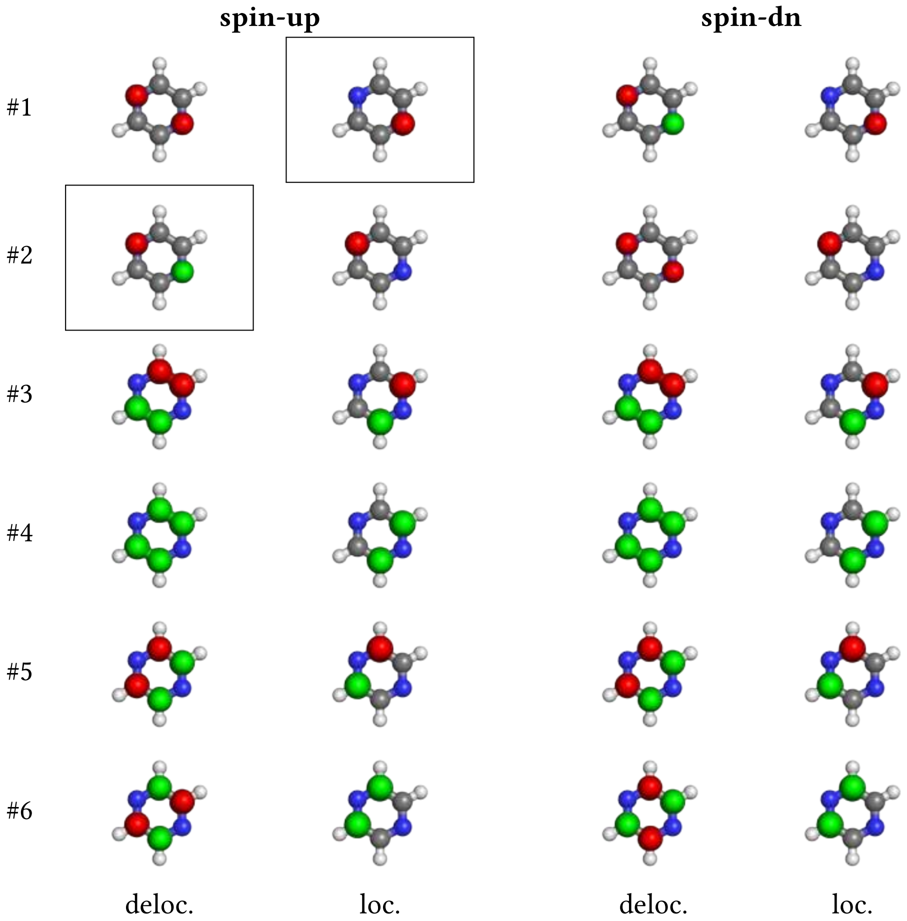

Fig. 3.5: *The eigenstates of the N1s core-hole calculation with a hole state based on a regular ground state DFT calculation and a Boys-localized core state. The state carrying the hole is highlighted with a box. By comparison with Figure 3.4 the carbon 1s states (#3 to #6) tend to again delocalize in both spin channels, while the N1s states stay localized as it is required. Computational details are the same as in Figure 3.4*

Tab. 3.1: *Experimental and simulated ionization potentials of the pyrazine molecule based on delocalized and localized core states. Computational details are the same as in Figure 3.4*

	$\mathrm{IP}_{\mathrm{exp.}}$[79]	$\mathrm{IP}_{\mathrm{deloc.}}$	$\mathrm{IP}_{\mathrm{loc.}}$
N1s	405.6	400.8	404.7
C1s	291.7	285.1	291.2

3.4 $L_{2,3}$-edge spectra in the approximate formalism

All previous investigations related only to the K-edge spectroscopic signatures of materials, which requires to ionize an electron from a 1s core-state into previously unoccupied states. Although these edges are still probed and measured on a daily basis, much more information can be gained in approaching the higher edges, such as the $L_{2,3}$ and $M_{4,5}$-edges. The spectroscopic notation here relates to transitions from an initial spin-orbit split ground state, in other terms the $2p^{\frac{1}{2}}$

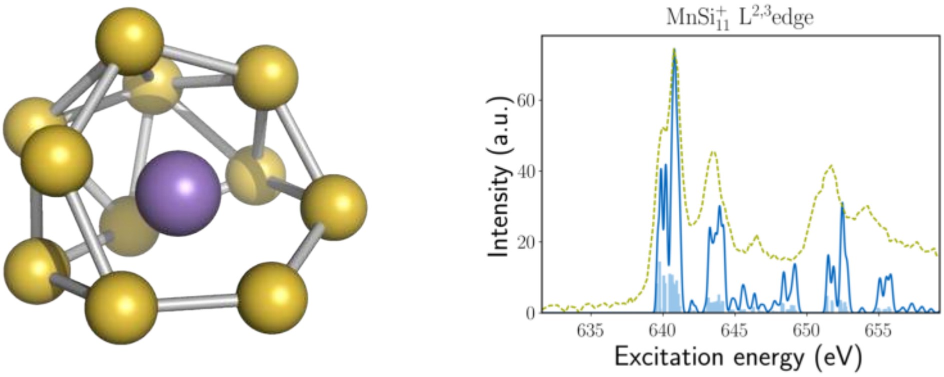

Fig. 3.6: *Geometry and NEXAFS $L_{2,3}$-edge spectrum for the $MnSi_{11}$ compound using the HSE06 functional, the TP approximation, and non self-consistent SOC.*

and $2p^{\frac{3}{2}}$ states for the $L_{2,3}$-edge and the $3d^{\frac{3}{2}}$ and $3d^{\frac{5}{2}}$ states at the $M_{4,5}$-edge, respectively. The reason for the splitting of the non-relativistically degenerate eigenstates is the interaction of an electrons intrinsic magnetic moment with the magnetic field induced by its own motion around the nucleus. To recapitulate the entire theory of relativistic density-functional theory and the approximations leading to the second variational approach applied in the spin-orbit coupling (SOC), as employed in the preliminary study described here, would be beyond the scope of this thesis. However, the interested reader is referred to the publication on the implementation in the FHI-aims code[80]. The author simply wishes to showcase in this short section that the approximate computational formalisms as introduced in the previous chapter also readily apply to a spin-orbit-split ground state and the agreement of a simulation of the Mn-$L_{2,3}$-edge NEXAFS spectrum of a molecular compound is staggering when compared to the experiment. Shown in Figure 3.6 is a silicon-caged manganese compound, which is part of a larger family of similar compounds for which experimental spectroscopic data is available[81]. Clearly visible from the comparison of the experimental and theoretical curves as shown in Figure 3.6, the energetic splitting between the L_2 and L_3 edge is well-reproduced at this level of theory, same as the transition energy and relative intensities. In the simulation, account of the strongly correlated d electrons was taken by employing the hybrid functional HSE06[50] and the relativistic spin-orbit coupling was modeled using a non-self consistent approach. The simulation of strongly correlated materials will be discussed in greater detail in section 4.1 of the following chapter.

4 Simulation of magnetic materials and localized magnetic properties

Lanthanides, their name being derived from the greek λανϑάνω, literally translated as *to escape notice*, constitute the first class of elements with a (partially) filled subshell of the high angular momentum number l=3. Including the elements Scandium (Sc) and Yttrium (Y), these elements are called *rare earth elements*. As the etymology and naming scheme already suggests, these elements are found only in small quantities on earth, their abundance in the earths crust being mostly only a few ppm, with the notable exception of Promethium (Pm), which does not seem to be naturally occurring on earth at all [82]. Owing to their late discovery, scarce availability, and high price, they were long not studied in chemistry and physics. It was only by the end of the 20th century that noteworthy applications surged the interest in these materials, which, living up to their initial naming, escaped notice for so long. Chemically speaking, lanthanides offer a partially occupied *4f* shell, deeply penetrating in the Xe-shell, shielded below the *5s*, *5p*, and *6s* states and thus effectively appearing as if the electronic anisotropy of the atoms was quenched, as shown experimentally[83, 84] and explained by theory[85, 86]. Due to this unique attribute, the magnetic and spectroscopic properties of atoms bound chemically do not change much due to the ligating surroundings but remain rather atomic in nature. Furthermore, owing to the so-called *lanthanide contraction*, the atomic radii of the elements decrease with increasing atomic number slowly, making the elements interchangeable in any kind of matrix (either organometallic compounds or solid state material), yet changing the magnetic properties. In organometallic complexation, the bonds formed are mainly characterized by a strong ionic character, with strong Lewis Base ligands being preferred counterparts to Ln-ions, such as carboxylates[87, 88]. The overall preferred oxidation state of lanthanides is +III and due to their huge surface area coordination numbers between 3 and 12 were observed[88, 89], with 8-9 being the most common[90–94]. Their initial organometallic chemistry was dominated by typical small coordination complexes including solvents (water, ammonia) as ligands, but soon moved to porphine and porphyrine ligands[95], which sometimes even coordinate the metal atom in a double-decker fashion[96]. Their high coordination numbers and similar coordination chemistry made them especially interesting in the application in metal organic frameworks (MOFs)[97–101]. More recently, their catalytic behavior has been studied aswell[102, 103]. These materials are of special interest due to their intrinsic magnetic properties, determined through the partially unoccupied, yet protected, *4f* subshell[88]. Early accounts of single molecule magnets[104, 105] were quickly accompanied by surface-assemblies of single atoms with intriguing magnetic properties[88, 106–108]. These basically constitute the smallest magnets we currently have at our disposal and it has been demonstrated that single atoms can be modified with the help of an STM tip to switch their magnetization, showing long-time stability at low temperatures[106–108]. These measurements were done at very low temperatures of a few tens of Kelvin, since otherwise the thermal motion would grant too much kinetic energy to the atoms and no regular spaced arrays were available. In order to be able to study single atom magnets at higher temperatures, these need to be immobilized by some kind of support. Thin films of 2-dimensional MOFs would alleviate that shortcoming and, as previously mentioned, are not expected to change the magnetic properties of the enclosed atoms due to the outer-lying 6s states. Part of my research focused on understanding of the atomic adsorption sites of single atom magnets with and without a stabilizing support such as linker molecules. However, common Density-Functional Theory approaches fail at the description of exactly those properties of lanthanide atoms, which make them special: their strongly localized *4f* subspace. To this extent, we first need to understand the problem of common density-functional approximations with respect to electron interaction and (de)localization. The chapter 4.1 addresses this issue, followed by a report on our findings for Dysprosium atoms adsorbed on graphene, grown on Ir(111) in chapter 4.2, which laid the foundation to a project where I, in collaboration with experimental colleagues, worked with Holmium atoms as the coordinated species in different 2d-metal organic networks on Ag(100), culminating in my publication on the subject as shortly introduced in chapter 5.1.

4.1 The self-interaction error and possible remedies

One unfortunate shortcoming of common DFAs is the incorrect description of localized states, such as the d and f states found in transition metals and lanthanides[109–112]. Probably the dominant part of this erroneous description is rooted in what became known as the self-interaction error in DFT, which is a direct consequence of the Coulomb operator in KS-DFT (J^{DFT}) being a functional of the density and not of single orbital contributions, as in wave-function theories such as Hartree-Fock (J^{HF})[113–115]. The latter brings along the advantage, that the exchange-integrals (K^{HF}) exactly cancel the self-interaction contributions. The exchange term arises from the two-electron operator $O_2 = r_{12}^{-1}$ acting on a determinental wave-function in Hartree-Fock as a second term next to the classical Coulomb term. As such it is the mathematical consequence of introducing the antisymmetry property for the wave-function via a *Slater*-determinental[116] ansatz for the wave-function, required by the fermionic nature of electrons. The cancellation of self-interaction is given in the equations below for the case of i=j as: $J_{ii}^{\mathrm{HF}} = K_{ii}^{\mathrm{HF}}$. KS-DFT does work with the density formed from a non-interacting system of auxiliary particles and not separately optimized orbitals. Therefore, in DFT, it is not possible to exactly cancel the self-interaction same as in HF. In principle though, DFT is an exact theory and the exact DFT functional does achieve this, thus the shortcoming is rooted in the density functional approximations used, where it is not possible to correct for the interaction of the density at point $\mathbf{r}_1$ with the density at point $\mathbf{r}_2$ as given in the equation for $J^{\mathrm{DFT}}[\rho]$ below.

$$J^{\mathrm{DFT}}[\rho] = \iint \frac{\rho(\mathbf{r}_1)\rho(\mathbf{r}_2)}{|\mathbf{r}_1 - \mathbf{r}_2|} d\mathbf{r}_1 d\mathbf{r}_2 \tag{4.1}$$

$$J_{ij}^{\mathrm{HF}}(r_1) = \iint \psi_i^*(\mathbf{r}_1)\psi_j^*(\mathbf{r}_2)\frac{1}{|\mathbf{r}_1 - \mathbf{r}_2|}\psi_i(\mathbf{r}_1)\psi_j(\mathbf{r}_2) d\mathbf{r}_1 d\mathbf{r}_2 = \langle ij|O_2|ij\rangle \tag{4.2}$$

$$K_{ij}^{\mathrm{HF}}(r_1) = \iint \psi_i^*(\mathbf{r}_1)\psi_j^*(\mathbf{r}_2)\frac{1}{|\mathbf{r}_1 - \mathbf{r}_2|}\psi_i(\mathbf{r}_2)\psi_j(\mathbf{r}_1) d\mathbf{r}_1 d\mathbf{r}_2 = \langle ij|O_2|ji\rangle \tag{4.3}$$

The spatial coordinates of interacting charges (electrons in case of HF and the local density (ρ) in case of DFT) are summarized in $\mathbf{r}_1$ and $\mathbf{r}_2$, ψ_i and ψ_j denominate single-particle wave-functions. Remedies were already proposed early on by Perdew and Zunger [117], in the form of corrective orbital-dependent potentials based on transformed Kohn-Sham states. The approach became widely known as the Perdew-Zunger Self-Interaction-Correction (PZ-SIC).

$$E_{\mathrm{xc}}^{\mathrm{PZ-SIC}} = E_{\mathrm{xc}}[\rho] - \sum_{i}^{N} E_{\mathrm{SI}}[\rho_i] \qquad \text{with:} \quad E_{\mathrm{SI}}[\rho_i] = E_{\mathrm{xc}}[\rho_i] + J[\rho_i] \tag{4.4}$$

Here, the energy correction to the exchange-correlation energy E_{xc} consists of a sum of single-particle self-interaction correction terms $E_{\mathrm{SI}}[\rho_i]$, formed from the single-particle densities of the non-interacting Kohn-Sham system $\rho_i = \phi_i^2$ with ϕ_i designating the single-particle wave-functions. N is the total number of single particles. Since in the exact functional for a single particle, the correction should vanish, the E_{xc} should equal the Coulomb energy and cancel exactly. The correlation energy for a single electron is $E_{\mathrm{c}} = 0$. However, the PZ-SIC was blessed but with limited success, as the corrections to atomic and molecular properties are non-systematic, functional-dependent (although the formulism itself should be independent of the underlying

functional) and could not always actually improve the result[118–120].
Another systematic improvement along the same line of thought of introducing the missing exchange interaction in the DFT formulism was introduced by the application of Hybrid-DFT functional approximations. There, a weighted amount (typically between 10 and 50%) of the Hartree-Fock exchange (K^{HF} in equation 4.3) is introduced in the DFT functional. A general hybrid functional thus treats the exchange-correlation energy as follows:

$$E_{\mathrm{xc}}^{\mathrm{hyb}} = E_{\mathrm{xc}}^{\mathrm{DFT}} + \alpha(E_{\mathrm{x}}^{\mathrm{HF}} - E_{\mathrm{xc}}^{\mathrm{DFT}}) \tag{4.5}$$

Where $E_{\mathrm{x}}^{\mathrm{HF}}$ is the energy contribution resulting from the matrix elements $K_{ij}^{\mathrm{HF}}(r_1)$ in equation 4.3 and the parameter α governs the amount of exact exchange included. The largest difference to the PZ-SIC is that the exact exchange is calculated for all orbitals, rather than only accounting for the terms where i=j and variable amounts of exchange (α) are included. Different kinds of functionals, created by following this line of thought became very established in molecular systems and following their success, were also applied in solid-state simulations. However, the computational cost is much higher than a treatment with a semi-local functional[121, 122] and the applicability is not as universal since the ad-hoc added exchange-contribution introduces problems in the simulation of metallic materials, where the unbalanced sum of exchange and correlation terms leads to errors in the description of the band structure at the Fermi level[122–126]. These are mainly attributed to the long-ranged decay of the Hartree-Fock exchange which leads to an overestimation of the band gap, a crucial ingredient to keep metals behave as metals in the simulation.
Another route to model the strong local correlation correctly and at the same time alleviate the problems introduced via the self-interaction is the introduction of an orbital-dependent tuned local potential. The potential can be tuned such that the wrong description of a subspace is cured, while treating the remaining system by the underlying DFT functional. Although such a semi-empirical model introduces a new parameter and thus takes a step away from a true *ab-initio* description, it permits an economic and straightforward approach in the simulation of a specific class of materials - transition and rare earth metal systems. Probably the most popular methodology to introduce such an orbital dependent potential is termed DFT+U[127] and based upon ideas from the ubiquitous Hubbard-model[128–133], which was very successful in describing general trends in the study of aforementioned materials. The classical Hubbard model assumes a lattice of electrons with one state on each site. The Hamiltonian is written as a sum of the on-site energy ϵ_0, the on-site repulsive interaction U, and a hopping term t_{ij}, as also known from the tight binding model, permitting electrons to move from one site to the adjacent (nearest neighbor):

$$\hat{H}_{\mathrm{Hub}} = \sum_{a\sigma} \left[\epsilon_0 \hat{n}_{a\sigma} + \frac{U}{2} \hat{n}_{a\sigma} \hat{n}_{a-\sigma} - t_{ab} c_{a\sigma}^{\dagger} c_{b\sigma} \right] \quad . \tag{4.6}$$

Here, the sum runs over all sites a of the lattice. $\hat{n}_a = c_{a\sigma}^{\dagger} c_{a\sigma}$ is the number operator of the state a and spin channel σ. $c_{a\sigma}^{\dagger}$ and $c_{a\sigma}$ are the ubiquitous annihilation and creation operators in second quantization. The DFT+U method relies on the on-site potential U from the Hubbard model acting on a chosen subset of states in the DFT description. The idea is that one can use the Hubbard model (which is self-interaction free by design) to describe the strongly correlated electrons in the d and f shells and treat the rest with a regular DFT functional. In the most general form the DFT+U energy can be written as follows (suppressing spin degree of freedom for clarity):

$$E^{\mathrm{DFT+U}}[\rho, n_{\mathrm{Im}}] = E^{\mathrm{DFT}}[\rho] + E^{\mathrm{U}}[n_{\mathrm{Im}}] - E^{\mathrm{dc}}[n_{\mathrm{Im}}] \tag{4.7}$$

Here, the energy contribution of the subspace treated by the Hubbard on-site potential (E^{U}) is added to the energy of the regular DFT-functional (E^{DFT}) in an ad-hoc fashion. However, since E^{DFT} also covers this portion of the electronic structure a double-counting correction (E^{dc}) has to be applied. The avid reader will immediately recognize, that the total energy of the DFT+U functional is now a functional of two quantities, namely the density ρ and the on-site occupation n_{Im} of orbital m at atomic site I. It remains the problem of defining such occupation numbers for the Hubbard correction. Usually these occupation numbers enter the description via a so called DFT+U occupation matrix which is obtained via a local projection on a projector function representing the correlated subspace in question (typically d- or f-shells of a transition of rare earth metal). There are currently four different projectors in use in common implementations of DFT+U. They all agree on the following common form to form the occupation matrix:

$$n_{\mathrm{Imm}'\sigma} = \sum_{\gamma} f_\gamma \left\langle \Psi_{\gamma\sigma} \middle| P_{\mathrm{Imm}'} \middle| \Psi_{\gamma\sigma} \right\rangle \tag{4.8}$$

Here, the sum runs over the KS-states Ψ_γ each occupied by f_γ electrons. $P_{\mathrm{Imm}'}$ is a local projection operator, which defines how to assemble the occupation matrix $n_{\mathrm{Imm}'\sigma}$ of the correlated subspace. A common choice to define the subspace occupation matrix is a projection on the basis functions, but in the case of a non-orthogonal basis (as most implementations are using nowadays), the definition is thus not entirely unambiguous. The aim is to have a local basis on which the Hubbard Hamiltonian can be applied to act locally. The most straightforward projector would thus be the so-called *full* projector $P^{\mathrm{full}}_{\mathrm{Imm}'\sigma}$, projecting on chosen basis functions directly. The big disadvantage, when using a non-orthogonal basis, consists of non-vanishing overlap to other (arbitrary) basis functions. To account for this, the *on-site*[134, 135] projection $P^{\mathrm{site}}_{\mathrm{Imm}'\sigma}$ is based on the dual basis functions $\tilde{\varphi}_{Im'\sigma}$:

$$\tilde{\varphi}_{Im'\sigma} = \sum_{\mathrm{Im}\sigma} \left| \varphi_{\mathrm{Im}\sigma} \right\rangle S^{-1}_{\mathrm{mm}'\sigma} \tag{4.9}$$

fulfilling the biorthogonal relations $\langle \tilde{\varphi}_{Im\sigma} | \varphi_{\mathrm{Im}'\sigma} \rangle = \delta_{\mathrm{mm}'}$. Due to exactly these biorthogonal relations, the projector formed by dual functions by definition does not overlap with any other basis function except for m = m′, also note that in case of an orthogonal basis set, the *on-site* projector would be exactly the same as the *full* projector. However, both of these projectors still do not fulfill the sum rule $\mathrm{Tr}(n_{\mathrm{Imm}'\sigma}) = N$[136], which was first addressed by introducing the *dual*[135] $P^{\mathrm{dual}}_{\mathrm{Imm}'\sigma}$ projector. The *dual* projector takes an intermediate form between the *full* and *on-site*, mathematically equal to the well-known Mulliken population analysis[137]. Finally, when a dual basis is used to generate the occupation matrix, care needs to be taken that all observables obtained by operations on it, such as occupancies, local moments or energy, are defined in a way so as to be tensorially invariant with the basis transformation. This property is not ensured in the case of the previously discussed projectors, since they produce non-traceable matrices or in other words involve sums of products of different character. The *tensorial*[138] $P^{\mathrm{tens}}_{\mathrm{Imm}'\sigma}$ projection ensures that property by forming a local inverse overlap matrix $O^{-1}_{\mathrm{Imm}'\sigma}$ for each site of projection independently by inversion of a subset of the overlap matrix of the entire Hilbert space spanned by the non-orthogonal basis functions. These operators are then used to construct the dual basis similar as shown in equation 4.9, but by replacing the inverse overlap matrix $S^{-1}_{\mathrm{mm}'\sigma}$ by the local overlap matrix $O^{-1}_{\mathrm{Imm'}\sigma}$. The four projectors are termed on-site, full, dual, and tensorial:

$$P^{\mathrm{full}}_{Imm'\sigma} = |\varphi_{\mathrm{m}\sigma}\rangle\langle\varphi_{\mathrm{m'}\sigma}| \qquad n^{\mathrm{full}}_{\mathrm{Imm'}\sigma} = \sum_{\alpha\beta} S_{\alpha\mathrm{m}} D_{\alpha\beta\sigma} S_{\beta\mathrm{m'}} \tag{4.10}$$

$$P^{\mathrm{site}}_{Imm'\sigma} = |\tilde{\varphi}_{\mathrm{m}\sigma}\rangle\langle\tilde{\varphi}_{\mathrm{m'}\sigma}| \qquad n^{\mathrm{site}}_{\mathrm{Imm'}\sigma} = D_{\mathrm{mm'}\sigma} \tag{4.11}$$

$$P^{\mathrm{dual}}_{Imm'\sigma} = \frac{1}{2}\left[|\tilde{\varphi}_{\mathrm{m}\sigma}\rangle\langle\varphi_{\mathrm{m'}\sigma}| + |\varphi_{\mathrm{m}\sigma}\rangle\langle\tilde{\varphi}_{\mathrm{m'}\sigma}|\right] \qquad n^{\mathrm{dual}}_{\mathrm{Imm'}\sigma} = \frac{1}{2}\sum_{\alpha}\left[D_{\alpha\mathrm{m}\sigma} S_{\alpha\mathrm{m'}} + S_{\alpha\mathrm{m}} D_{\alpha\mathrm{m'}\sigma}\right] \tag{4.12}$$

$$P^{\mathrm{tens}}_{Imm'\sigma} = |\varphi_{\mathrm{m}\sigma}\rangle O^{-1}_{\mathrm{Imm'}\sigma}\langle\varphi_{\mathrm{m'}\sigma}| \qquad n^{\mathrm{tens}}_{\mathrm{Imm'}\sigma} = \sum_{\alpha\beta} S_{\alpha\mathrm{m}} D_{\alpha\beta\sigma} S_{\beta\mathrm{m'}} O^{-1}_{\mathrm{mm'}} \tag{4.13}$$

In the above equations the projector functions as well as the resulting occupation matrices are given as a function of either the density kernel $D_{\alpha\beta\sigma}$ (the density matrix in terms of the dual basis) or the density matrix $D_{\mathrm{mm'}\sigma}$ and, if the overlap due to a non-orthogonal basis set is accounted for, the overlap matrices $S_{\alpha\mathrm{m}}$. In the case of the *dual* projector the density matrices carry indices of both the dual ($\alpha\beta$) and primal (mm′) space by construction. Most popularly a projection on the basis functions is performed, but more recently an approach to project on KS-states, in essence a linear combination of basis functions as a new basis for the occupation matrix, was chosen. These could be either the canonical Kohn-Sham states or maximally-localized variants such as maximally localized Wannier functions (MLWFs)[138, 139], or Boys-localized Kohn-Sham states[140]. The former approaches favor a rather atomic description of the strongly correlated subspace and thus prevail in systems of a pronounced ionic bonding character, whereas the latter approach is suitable for systems characterized by a stronger hybridization of the correlated subspace with the surrounding atoms due to chemical bonding. Independent of the choice of projector, the DFT+U Hamiltonian takes the form of a HF-like interactive potential which is restricted on a subspace of states. In shorthand notation, the DFT+U functional for a single site I can be written as follows:

$$\begin{aligned} E^{\mathrm{U}}_{\mathrm{I}}[n_{\mathrm{m}\sigma}] &= \frac{1}{2}\sum_{\mathrm{m}\sigma} \langle mm''|\hat{V}_{\mathrm{ee}}|m'm'''\rangle\, n_{\mathrm{mm'}\sigma} n_{\mathrm{m''m'''}-\sigma} \\ &+(\langle mm''|\hat{V}_{\mathrm{ee}}|m'm'''\rangle - \langle mm''|\hat{V}_{\mathrm{ee}}|m'''m'\rangle) n_{\mathrm{mm'}\sigma} n_{\mathrm{m''m'''}\sigma} \end{aligned} \tag{4.14}$$

Here, the set of {m} values represents the basis of the local subspace on which the DFT+U Hamiltonian acts. On each center of the system such a potential is applied, thus E^{U} from equation 4.7 comprises a triple sum $\sum_{\mathrm{Im}\sigma}$. $\hat{V}_{\mathrm{ee}}$ represents the screened Coulomb operator in the given subspace, σ the spin. The functional form is reminiscent of the already previously mentioned Coulomb and exchange integrals in equation 4.2 and 4.3 and thus recovers an exact self-interaction correction for the given subspace (second term in equation 4.14, cf. equation 4.2f) in addition to the tuned orbital-dependent potential. However, the explicit calculation of the Fock-integrals is avoided in the DFT+U functional and instead parameterized. The value of the parameter U is chosen to represent a *screened* Coulomb and exchange interaction, rather than including the exact exchange integrals, which would decompose into a sum of Fock-integrals (as it is done in hybrid functionals). This applies to both the full version of DFT+U by Liechtenstein [141] and the simplified version by Dudarev[142], which neglects higher-order Fock-integrals altogether. Finally, the strongly correlated electrons are now treated twice in the DFT description, since the underlying DFT functional treats the subsystem aswell. Therefore, the double-counting term as introduced in equation 4.7 needs to be addressed. Again, different choices on how to recover the specific part of the mean-field treatment need to be devised since the original DFT functional is not cast in terms of localized states but rather the total density. The initial idea consisted in expressing the corrective potential in fluctuations around the mean field occupation, which became termed the around mean-field (AMF) approach[127, 143]:

$$E_{\mathrm{dc}}^{\mathrm{AMF}} = \frac{1}{2} \sum_{\mathrm{m}\sigma \neq \mathrm{m}'-\sigma} U(n_{\mathrm{m}\sigma} - \bar{n}_{\sigma})(n_{\mathrm{m}'-\sigma} - \bar{n}_{-\sigma}) \tag{4.15}$$

Here, $\bar{n}$ is the average occupation of a state expressed by the number of available electrons in the respective subspace (and thus element-specific), divided by the maximum size of the subspace (for example 10 in the case of d-electrons). Another idea was to assume all occupied states as degenerate in energy within the subspace, thus each of the states contributing exactly the same energy to the total energy term[143, 144]. By following the combinatorics of two interacting states at a time (cf. equation 4.14), a sum over two states out of the total number of states in the correlated subspace (for example 10 in the case of d-orbitals) is formed. Each of these states contributes exactly an energy equal to the U-value. It can therefore be approximated in the fully localized limit (FLL) (FLL) as:

$$E_{\mathrm{dc}}^{\mathrm{FLL}} = \frac{1}{2} U N(N-1) \tag{4.16}$$

Here, the number of correlated, fully occupied states is $N = Tr(n_{\mathrm{I}\sigma})$ (incorporating, of course, all issues which arise due to non-conserving sum rules of the occupation matrix as mentioned above). Concluding, the $N(N-1)/2 = \sum_{\mathrm{x}=0}^{\mathrm{N}-1} x$ factor equals to the number of possible choices of two out of the number of correlated states. As usual, the truth lies somewhere in between the two extreme cases depicted by the AMF and FLL formalism. In an attempt to find the correct "break-even" point between a very localized and very delocalized description, a self-consistent intermediate description was introduced by Ylvisaker[143].

Concluding, there are four possible choices of occupation matrices, three choices of double-counting corrections and a free parameter (the value of U), which itself is not only element-specific, but also depends on the functional in use, the choice of occupation matrix/projector, double-counting correction, the size of the basis set, etc. Although this methodology might seem volatile due to the abundance of different approximations, it has nevertheless been applied very successfully towards the simulation of strongly correlated materials and became an essential addition to the already established DFT functionals. Depending on the specific use case, one of the introduced models performs better or worse. It has to be stressed here, that this method relies more than many other simulation techniques on a close collaboration with experiment, but as soon as a suitable description via a DFT+U Hamiltonian has been formulated, that electronic structure can be used to study further details of the system out of experimental reach at negligible computational overhead compared to a regular LDA or GGA calculation.

4.2 Case study: Dy on graphene/Ir(111)

As previously shown by Baltic et al. [106], Dysprosium atoms do show a long-range regular surface adsorption pattern on graphene / Ir(111) when heated from low temperature (10K) to a little higher temperatures (40K). The long-range order exhibited by the rare earth metal is surprising, as one would expect a rather statistical atomic adsorption pattern, as seen at 10K, to persist, or the formation of randomly sized clusters to arise. In order to understand the nature of the adsorption site, the very same system was studied and the results are presented in this chapter.

Computational Details Spin-collinear density-functional theory (DFT) calculations were performed for periodic supercells with the Quantum ESPRESSO [145] and FHI-aims [24] computing packages. Geometry optimizations for a (10×10) surface unit-cell graphene sheet on a three layer Ir(111) slab with a (9×9) surface unit-cell were performed with FHI-aims at "tight" computational settings, Γ-point sampling and using a 60 Å vacuum region. In these calculations electronic exchange and correlation (xc) was treated on the generalized-gradient approximation level with the PBE [27] functional, augmented by dispersive interactions through the Tkatchenko-Scheffler $\mathrm{TS}^{\mathrm{surf}}$ method [146]. The graphene sheet and the topmost two layers of Ir were fully relaxed until residual forces were below 10^{-3} eV/Å. The resulting corrugated graphene sheet was frozen and employed in subsequent Dy adsorption calculations. These adsorption calculations were done with the Quantum ESPRESSO package for a free-standing flat graphene sheet with one Dy atom adsorbing in a (4×4) surface unit-cell and for the corrugated graphene sheet as determined before with one Dy atom adsorbing in the (9×9) surface unit-cell. In both cases adsorption energy curves as a function of the vertical adsorption height of the Dy atom were computed at different high-symmetry sites of the graphene lattice. The adsorption energy obtained at 10 Å height is used as zero reference, and negative adsorption energies indicate exothermicity. In order to improve the description of the *4f* electrons of the Dy adsorbate, the PBE+$\mathrm{TS}^{\mathrm{surf}}$ treatment was extended by the DFT+U formalism. We employed a value of U=5.0 to reproduce the *4f*-eigenvalue alignment for the interacting system as obtained by hybrid-level HSE06 [50] calculations with FHI-aims for the smaller flat graphene system. A plane wave cutoff of 30 Ry, projector augmented wave (PAW) (PAW) pseudopotentials for Dy [147] and C [148], Γ-point sampling, and a Gaussian smearing of the orbital occupations by 0.2 Ry were employed.

Results The first thing to be understood before any more assumptions can be made about adsorption positions is the nature of the immobilized support. In order to superimpose graphene (lattice constant of 2.45 Å) on top of an iridium metal slab (lattice constant of 3.87 Å), a common repetition unit is needed. The present system is special in that sense, because the superimposed unit cells are large and graphene on Ir(111) forms a so-called Moiré pattern which can be mimicked in the simulation by a (10×10) graphene surface-unit cell on top of a (9×9) Iridium bulk metal, as shown on the left of Figure 4.1. In our simulation (computational settings mentioned above) we obtained a corrugated graphene sheet on top of the Ir(111) facet, highlighting three high-symmetry sites, which we further considered as possible adsorption sites in our study and are henceforth referred to as *hcp*, *fcc* and *ontop* positions. Two of these sites are situated in a concave pocket of the corrugated sheet, one at a convex protrusion. There is an additional highly symmetric adsorption site available compared to a flat sheet of graphene (as shown on the right side of Figure 4.2), which only offers two possible adsorption sites, namely a sixfold *hollow* site and a *ontop* site. The obtained corrugated geometry of the graphene sheet above Ir(111) is in good agreement

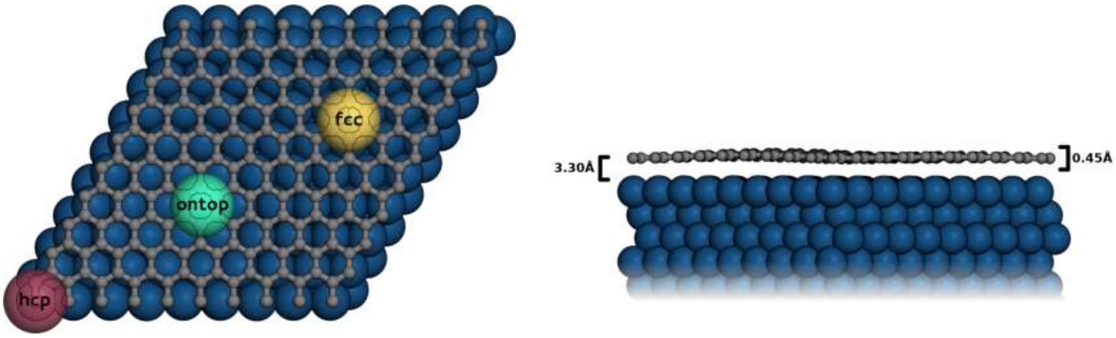

Fig. 4.1: *Commensurate structure of corrugated* (10×10) *graphene on* (9×9) *Ir(111), highlighting the three high-symmetry sites considered in our study (left). Side-view of the commensurate structure, highlighting the corrugation and adsorption height (right).*

Tab. 4.1: *Comparison of adsorption height (h) and corrugation (d) of graphene on the Ir(111) facet. Theoretical [149], experimental[150, 151] and combined theoretical and experimental studies[152] on the graphene/Ir(111) Moiré pattern.*

this study	[149]		[152]		[150]	[151]	
PBE+TS^{surf}	M06-L	optB88-vdW	XSW	VASP PBE+D3	SXRD, EXXR	LEED, AFM	
3.30	3.52	3.53	3.38	3.41	3.38±0.04	3.39±0.03	h [Å]
0.45	0.22	0.34	<1	0.35	0.38±0.04	0.47±0.05	d [Å]

with previous studies as compiled in Table 4.1. The sheet is at an average height of 3.3 Å above the Ir surface and exhibits a corrugation of 0.45 Å. The surprisingly high corrugation already permits some speculation about the reason for site-specific adsorption on the surface. If some of the previously conjugated π-bonds in graphene are broken due to the corrugation, the result would be a locally varying chemical reactivity on the moiré patterned surface. To follow up further on this assumption, binding energy curves for a single atom of Dysprosium were recorded for pristine graphene and graphene on Ir(111). As mentioned above in section 4.1, the description of the *4f* subspace using a GGA functional such as the employed PBE-functional, is not sufficient to correctly account for the strongly localized *4f* electrons. Therefore, we employed the DFT+U approach, as introduced in chapter 4.1, to alleviate this shortcoming. The U value of 5.0 was chosen such as to match the eigenstate alignment of a HSE06 calculation of the free atom above graphene. This goes alongside with the main assumption, that with respect to the *4f* states, there is little change between the adsorbed atom and the free atom and that they furthermore do not participate in the bonds formed to the substrate and thus apply the same corrective potential valid for the free atom case to the adsorbed atom. One of the effects of this corrective DFT+U potential is, that the *4f* eigenstates are not located at the Fermi-level (where instead only the *6s* states are found). The results for the adsorption of a Dysprosium atom on a flat sheet of graphene shown in Figure 4.2 suggest, that on both adsorption positions, only physisorption occurs, and that there is no significant preference of one adsorption site over another. In the top diagram the adsorption energy curves are shown as a total energy difference between the fixed geometry

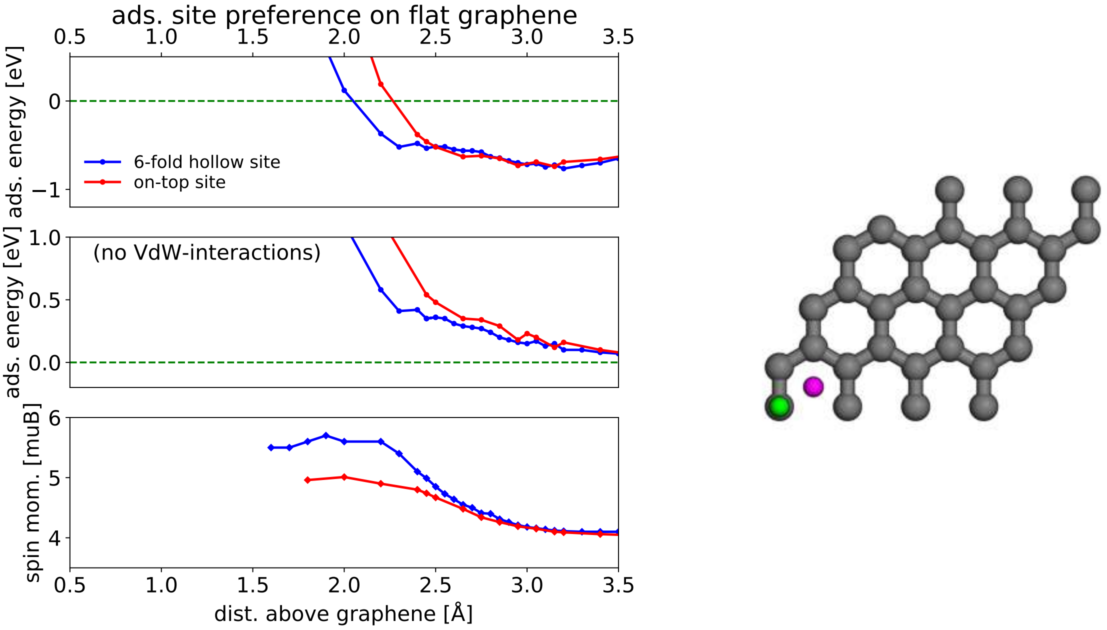

Fig. 4.2: Adsorption energy and spin magnetic moment vs. adsorption height for dysprosium on flat graphene ((4×4) surface unit cell, left). (4×4) surface unit cell of flat ideal graphene, highlighting the two high-symmetry sites considered in our study (right).

and the respective components, in the center diagram, the same adsorption curves are shown but with the dispersive (van-der-Waals) contribution subtracted. Additionally, we see at the lower diagram, that as soon as the Dysprosium-atom is pushed deep into the surface, the spin magnetic moment increases gradually, but at the equilibrium adsorption distance, the atomic magnetic moment of 4 μB is recovered. Therefore, we would expect no site-specificity if the system under study were flat as a layer of free-standing graphene. However, in the case of Dysprosium adsorbed on corrugated graphene, the picture changes. In our simulation, for ease of computation, we relied on the adsorption on top of the previously obtained corrugated graphene rather than the entire slab-system, because the interaction between Ir(111) at 3.3 Å from the surface is assumed to be negligible and the main chemical interaction to be recovered from the different chemical environment due to the corrugation. We find this assumption to be true by recording adsorption energy curves as shown at the left in Figure 4.3. By subtracting the van-der-Waals contribution to the adsorption energy, we can exclude the *hcp* site, since there is no chemical interaction. Between the two remaining adsorption sites, the *fcc* and *ontop* position are mostly degenerate in energy, yet the *ontop* adsorption energy curve has a steeper slope and a slight energetic preference as compared to the *fcc* site. We can thus rationalize, that there is not a chemical interaction with the surface possible due to the corrugation of the surface and that the *ontop* position is energetically slightly more favorable. The spin magnetic moment as shown in the lowermost diagram of Figure 4.3 shows the same behavior as already encountered for the adsorption on pristine, flat graphene, where the number of unpaired electrons increases upon pushing the Dysprosium atom into the surface, yet at the equilibrium distance a predominantly atomic occupation is observed. At the right side in Figure 4.3 the different (up- and down-) density of states (DOS) of the system with

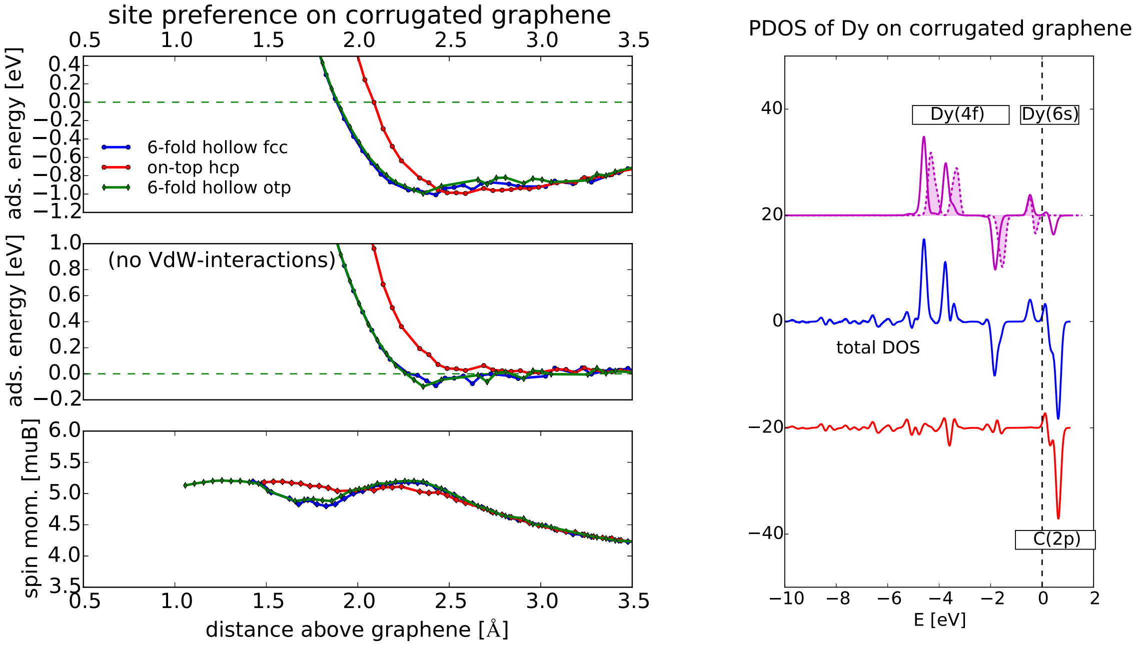

Fig. 4.3: *Adsorption energy and spin magnetic moment vs. adsorption height for dysprosium on corrugated graphene (*(10×10) *surface unit cell, left). Projected density of states of the adsorbed (solid line) and separated (dashed line) system (right).*

Dysprosium adsorbed on corrugated graphene is shown. Highlighted in color are the total DOS (blue line), the projection onto Dy states (purple lines) and the projection on C states (red line). For the Dy projection, results are shown for Dy at the optimized height in the *fcc* hollow site (solid line) and at 10 Å height as representation for the free Dy atom (dashed line). Note the shift of the spin down 6*s* state above the Fermi level in case of the adsorbed Dy atom (solid vs. dashed purple line). This explains, that the chemical interaction of the Dysprosium atom with the graphene substrate happens via the *6s* states of Dysprosium and *2p* states of the graphene sheet. The *4f* subspace is not affected by the bonding to the surface and the Dysprosium atoms retain their atomic magnetic properties, as also evidenced from experimental measurements [106] and our simulation of the spin magnetic moment, which increases only by pushing the atom even further into the surface, and thus away from the equilibrium distance.

Although this system is of large academic interest, the equilibrium distance adsorption energies from Figure 4.3 are on the order of about 1 eV. Therefore, by increasing the temperature of the system even further, we expect that the corrugation does not offer enough support to stabilize the Dysprosium atoms to specific positions. Room-temperature applications would therefore require to immobilize Lanthanide atoms by some kind of more rigid support. A combined experimental/computational study of a system along this lines is the topic of publication further detailed in chapter 5.1.

5 Publications

This chapter presents a short summary of the main publications which resulted from my research during my PhD studies. A short motivation and summary of each publication is given, followed by a paragraph on my individual contribution to the work.

5.1 Assembly of Robust Holmium-Directed 2D Metal-Organic Coordination Complexes and Networks on the Ag (100) Surface

M. Uphoff[1], G.S. Michelitsch[1], R. Hellwig, K. Reuter, H. Brune, F. Klappenberger, and J.V. Barth
ACS Nano **12**, 11552-11560, (2018)
DOI: 10.1021/acsnano.8b06704

Content This publication was a direct follow-up of my work outlined in chapter 4.2, where I established protocols towards the simulation of lanthanide materials adsorbed on large surface materials. The project combined together the skillsets of the three participating working groups along the common idea of immobilizing magnetic materials on a surface. Our collaborators around H. Brune from the EPFL in Switzerland had previously gained much experience with single atom magnets at surfaces, the colleagues around J.V. Barth from the TUM's Physics department contributed their knowledge on the formation and self-assembly of 2d-metal organic networks on a surface, which should provide the additional rigidity not present in the system previously discussed (cf. chapter 4.2). I contributed with our experience in large-scale DFT simulations with the added complexity of locally strongly correlated electrons embedded in a non-magnetic, metal support. The main focus of the simulation was to explain and reproduce the experimental STM signatures, elucidate the underlying structural parameters, investigate the influence of the lanthanide presence on aforementioned observables, and, finally, explain the unbalanced formation of two different networks, with a clear preference of one over the other. The subject of study was the element Holmium in conjunction with organic linker molecules featuring carboxylate functional groups (terephthalic acid) to form a metal-organic assembly. Holmium is the next element in line right after Dysprosium, which had been extensively studied in the group in Switzerland before, thus chosen for this study. The main message of the publication is that Holmium does form organometallic frameworks on the metal surface, where the Holmium atoms retain most of their intrinsic magnetic moment. Furthermore, an interconnected thin film of this network is hampered in formation due to a lattice mismatch between the substrate and adsorbate, which can not be compensated by a rotation.

Individual contributions I developed and simulated adsorption models for both observed surface-assemblies based on the information given from the experiment (STM signatures and cell dimensions). The initial models relied on free-standing layers of surface assemblies, which were unable to explain the instability of the checkerboard structure as compared with the cloverleaf structure. By including the substrate, the effect of the Ag(100) surface unit cell and the induced strain became apparent. To that extent, I also had to develop new protocols in how to run DFT+U calculations on a large scale, which reliably give a converged ground state solution of the system. I had to make heavy use of a technique termed *matrix control*[13, 153–155], which allows to fix the occupational constraints of the correlated subspace and keeping them static during the entire calculation and only after having converged the system under that given boundary condition I allowed for a self-consistent solution. Since the DFT+U potential is a rather harsh correction imposed on top of the underlying electronic structure, a direct simulation is hardly reliably accessible, especially when doing a geometry optimization. A typical calculation involves the simulation of all possible ways of how to place 11 electrons in 14 orbitals and keeping the occupation matrix fixed, then perform a self-consistent DFT+U calculation with that boundary condition and use the lowest-energy solution wave-function coefficients to restart a fully self-consistent run using a linear mixer, very low values of gaussian smearing for the occupations and a very small mixing value. Only then can a self-consistent DFT+U calculation using a Pulay-mixing scheme with a small mixing value be converged. Based on the geometries and electronic structure obtained for the models, I simulated Tersoff-Hamann STM signatures and analyzed charge rearrangement and relative stability of the two surface-assemblies to substantiate and further explain experimental findings. I wrote all parts of the manuscript with respect to the simulation, providing some of the key messages of the publications. I helped Martin in rewriting the entire manuscript so as to reflect best the findings of our combined experimental/theoretical study.

---

[1] These authors contributed equally to the work.

5.2 Remote functionalization in surface-assisted dehalogenation by conformational mechanics: organometallic self-assembly of 3,3′,5,5′-tetrabromo-2,2′,4,4′,6,6′-hexafluorobiphenyl on Ag(111)

M. Lischka, G. S. Michelitsch, N. Martsinovich, J. Eichhorn, A. Rastgoo-Lahrood, T. Strunskus, R. Breuer, K. Reuter, M. Schmittel, and M. Lackinger
Nanoscale **10**, 12035-12044 (2018)
DOI: 10.1039/C8NR01987H

Content This work was initiated by the colleagues around M. Lackinger at the TUM to study the influence of fluorination of reaction educts in surface-supported Ullmann couplings on the outcome of the reaction. Due to the mixture of reaction products observed, experimental techniques such as core-level spectroscopies (XPS, NEXAFS) as well as surface-sensitive electron microscopies (STM) were recorded alongside theoretical modeling of the material. Owing to our expertise with core-level calculations and structural studies of surface-adsorbates, we could assist with DFT simulations of the surface adsorbate geometries and the resulting STM images. As a result of the variety of different reaction outcomes it was only by the theory support that all different reaction products could be quantified and some structural motives resolved in the first place. The main findings reported in our article were that fluorination leads to some unprecedented new chemistry characterized by sterically controlled debromination of the educt species leading to formation of different kinds of 1d chains rather than 2d materials.

Individual contributions My contribution to this work consisted in assigning structural motives to the STM images provided by our colleagues, thus identifying similar, yet distinctively different adsorption patterns (some only differing in molecule-molecule distances but sharing the same backbone). I also performed XPS simulations of partially debrominated compounds to help assign the core-level shifts from experiment and thus allow a rough quantification of the relative abundance of different surface assemblies. I furthermore wrote the parts in the article relating to the simulation, critically compared the experimental and theoretical results to confirm and/or rectify initial models and took part in writing and proofreading of the entire manuscript.

5.3 Efficient Simulation of Near-Edge X-ray Absorption Fine Structure (NEXAFS) in Density-Functional Theory: Comparison of Core-Level Constraining Approaches

G. S. Michelitsch and K. Reuter
J. Chem. Phys., accepted (2019)

Content This work started when I realized that there are many different approximate methodologies currently in use to simulate core-level absorption spectra, but few available publications employed more than one of these and even fewer motivated the choice of an approximation. It seemed to me that more recently there was a preference for the TP method for surface adsorbate simulations of light elements, while for water and ice spectra XCH and FCH are used (cf. chapter 3.2 for more details on these). To my knowledge, nobody ever collected all these auxiliary electronic structures and compared them for one class of materials in order to see whether systematic trends arise. Furthermore, we were very much interested in how well our numerical atomic orbital basis functions perform for spectroscopic properties since similar studies usually require a purpose-tailored basis set. Owing to close ties with experimental colleagues in surface science interested in organic surface adsorbates, I chose a small library of nitrogen and carbon containing heterocyclic molecules as a test set. Since the different auxiliary electronic structures inherent to the approximations derive from each other in a systematic way, we realized quickly, that certain methods (such as the GTP, XTP, and XGTP) were so far missing in the literature and very little use is made of explicit approaches (which model every possible transition) in absorption spectroscopy. To this extent, the given article compares ten different auxiliary electronic structures, based on two DFT functionals (PBE and PBE0), as well as the dependency on our two different numerical atomic orbital basis sets and benchmarks them against experimental data for the NEXAFS absorption spectra of five different molecules. We find that already at an average basis set size and the GGA level of approximation most methods reach the limit of their accuracy and that while the transition energies seem to follow an initial state rule, the transition intensities follow a final state rule. We furthermore give a mathematical derivation and formulation of all approaches and recommendations on the usage of these approximate methodologies used in conjunction with DFT.

Individual contributions I had the idea to collect, derive and benchmark all approaches in one publication and decided on the compound library and general scope. In order to localize KS-states for spectroscopic simulation, I implemented the Boys-localization based on an existing routine (which calculated the Boys centers) and developed and implemented a subspace-restricted version of it. Together we worked out the details of the work, especially with respect to the different basis sets, different functionals and, finally, the new approaches. I performed the calculations and drafted the manuscript, which we then revised together.

6 Summary, Conclusions and Outlook

The topics addressed throughout this work were very diverse yet all involve a proper understanding and description of the electronic structure of molecules and metal-organic compounds. In the early chapters, the influence of a core-hole on the energy eigenvalue of a Kohn-Sham state was studied as a function of not only the fractional occupation, but also the system size and thus the number of screening electrons. The findings are in line with what was previously known, that there is a close to linear behavior of the eigenvalue w.r.t. the occupation. Following these preliminary studies is a mathematical derivation of numerical approximations to the ΔSCF scheme to the calculation of excitation energies, where all currently employed and a few additional approaches are discussed. A thorough investigation of their performance for the light elements carbon and nitrogen is given in the publication on the subject, highlighting that already when using semi-local functionals and an average-sized basis set accurate predictions can be made when using a one-point integral approximation, such as TP or XTP. It is furthermore shown, that the transition dipole moments are a robust approximation to the intensity of a particular transition. This all holds under the important boundary condition of a proper hole-state localization, which is stressed in section 3.3, where the methodology implemented over the course of this thesis, the Boys localization procedure, is briefly introduced. In conclusion, given a proper localization of the core-hole state and a proper approximative scheme towards the simulation of XPS or NEXAFS spectra, a reliable assignment of peak positions is possible. This is of great interest to a large class of materials, known as *strongly correlated materials*, which feature partially occupied *d*- and *f*-shells, which are characterized by a strong local coulomb interaction. As this is not correctly described in the typical mean-field, non-interacting particle picture of DFT at the local or semi-local level, in the second chapter an economic approach, the DFT+U method is introduced. DFT+U is a model Hamiltonian approach which, unlike regular DFT functionals, is not sharply defined but offers a large variety of customization not only by parameters but also in the way it is implemented. A brief recourse of the most prominent approaches taken to date is given in section 4.1, followed by a case study of adsorption of Dysprosium atoms on graphene on Ir(111), which was only possible in using the DFT+U approach. The knowledge from this study was carried over to another project involving the simulation of metal-organic frameworks incorporating Holmium, highlighting peculiar intricacies in the electronic structure of the *4f* electrons as outlined in the accompanying publication.

To sum up, in the course of this thesis robust protocols towards the simulation of X-ray spectroscopy and strongly correlated materials were developed, both relying on the same foundation in terms of computational efficiency, density functional choice, and basis set. What remains to be done is to evaluate how well these methods perform in the periodic limit and apply them to the simulation of core-level spectroscopies of magnetic materials on a surface support at experimental length scales.

Acknowledgments / Danksagung

First and foremost I wish to thank my direct supervisor Karsten Reuter for his continuous trust and support throughout my entire time as his student in Munich. Whenever we had a meeting I had the feeling before that I did not achieve what I should have, but left the meeting with an entirely different impression - motivated and full of new ideas. Thank you for giving me the liberty to do my research as I saw fit, make the important experiences and mistakes myself and teach myself a great thing about organized thinking and especially the management of myself, the people around me, and events which involve many other people. Also a big thank you to Reinhard Maurer for being my mentor in scientific and less scientific matters.

Second, I need to give my thank to the people who were constantly working so that I could work as efficiently as possible, this is Ruth who managed all my contracts and doings with the bureaucracy and Christoph Scheurer who taught me a lot about IT infrastructure and teaching. Thank you Harald for your open ears with all problems related to physics and austrian politics. Thank you to my roomies Matthias Kick and David Egger, without whom the insanity of IT administration would've been a hopeless endeavor as well as our first-level supportive Xristoph Muschielok and Christian Kunkel. Special thanks to Matthias for teaching me the dark arts of DFT+U while not having me turned to the dark side and proofreading my interpretation of his mystical doings.

A big thank goes to my numerous students, although I might have been a little over-enthusiastic and under-available at times I had a great time with all of you and it was great to guide you through your projects and discover new and exciting things together. I name here Sina Stegmaier, Martin Stöhr, Hanna Türk, Markus Pielmeier, David Bodesheim, and Carsten Staacke.

Of course I also wish to thank the entire group, who I've known for such a long time now and have seen change and develop over the years. Thanks for the morning coffee and tea discussions and the Kaffekombinat and TeaKartel of which I had the honor to be one of the first members. Thanks for a great time at the movie nights, enjoying to boycott the mensa with me, and joining in when we were having a great time at karaoke or our numerous international food evenings.

Thank you to all my collaborators in the groups of J.V. Barth, H. Brune, M. Lackinger, and P. Rinke.

Also a big thank goes to Moritz Lipp, who tirelessly listened to my stories and still kept me on the right track to graduation. I hope that you will be in the same situation quite soon!

Last but not least a big thanks to my family and relatives, who supported the crazy idea of mine to do a PhD and didn't doubt that I will succeed. Thank you, Chen Si for putting up with my moods and supporting me through the final stages of my work.

I also acknowledge support of the Technische Universität München - Institute of Advanced Study, funded by the German Excellence Initiative for financially supporting my PhD research.

Munich, January 2019

Bibliography

[1] A. Einstein, Ann. Phys. **322**, 132 (1905) (cit. on p. 1).

[2] C. Nordling, E. Sokolowski, and K. Siegbahn, Phys. Rev. **105**, 1676 (1957) (cit. on p. 1).

[3] E. Sokolowski, C. Nordling, and K. Siegbahn, Ark. Fys. **12**, 301 (1957) (cit. on p. 1).

[4] S. Hagström, C. Nordling, and K. Siegbahn, Phys. Lett. **9**, 235 (1964) (cit. on p. 1).

[5] K. Siegbahn, Rev. Mod. Phys. **54**, 709 (1982) (cit. on p. 1).

[6] J. Stöhr, *NEXAFS spectroscopy*, Vol. 25, Springer Series in Surface Sciences (Springer Berlin Heidelberg, Berlin, Heidelberg, 1992) (cit. on p. 1).

[7] K. C. Rule, Phys. Rev. **68**, 246 (1945) (cit. on p. 2).

[8] K. C. Williams, Proc. Phys. Soc. **87**, 983 (1966) (cit. on p. 2).

[9] F. M. F. de Groot, "X-ray absorption of transition metal oxides," PhD thesis (Radboud University, 1991) (cit. on p. 2).

[10] G. Pacchioni, J. Chem. Phys. **128**, 182505 (2008) (cit. on p. 3).

[11] J. T. Pegg, X. Aparicio-Anglès, M. Storr, and N. H. de Leeuw, J. Nucl. Mater. **492**, 269 (2017) (cit. on p. 3).

[12] E. Finazzi, C. Di Valentin, G. Pacchioni, and A. Selloni, J. Chem. Phys. **129**, 154113 (2008) (cit. on p. 3).

[13] B. Dorado, G. Jomard, M. Freyss, and M. Bertolus, Phys. Rev. B **82**, 1 (2010) (cit. on pp. 3, 34).

[14] A. J. Cohen, P. Mori-Sanchez, and W. Yang, Science **321**, 792 (2011) (cit. on p. 3).

[15] P. Mori-Sánchez, A. J. Cohen, and W. Yang, Phys. Rev. Lett. **100**, 146401 (2008) (cit. on pp. 3, 12, 17).

[16] M. Lundberg and P. E. M. Siegbahn, J. Chem. Phys. **122**, 224103 (2005) (cit. on pp. 3, 17).

[17] J. Autschbach and M. Srebro, Acc. Chem. Res. **47**, 2592 (2014) (cit. on pp. 3, 12, 17).

[18] J. P. Perdew, A. Ruzsinszky, L. A. Constantin, J. Sun, and G. I. Csonka, J. Chem. Theory Comput. **5**, 902 (2009) (cit. on pp. 3, 17).

[19] A. J. Cohen, P. Mori-Sánchez, and W. Yang, Chem. Rev. **112**, 289 (2012) (cit. on pp. 3, 17).

[20] W. Koch and M. C. Holthausen, *A chemist's guide to density functional theory* (Wiley-VCH Verlag GmbH, Weinheim, Germany, July 2001) (cit. on p. 5).

[21] R. G. Parr and W. Yang, *Density-functional theory of atoms and molecules* (Oxford University Press, Oxford, July 1989), p. 333 (cit. on p. 5).

[22] P. Hohenberg and W. Kohn, Phys. Rev. **136**, B864 (1964) (cit. on pp. 5, 7).

[23] W. Kohn and L. J. Sham, Phys. Rev. **140**, A1133 (1965) (cit. on p. 6).

[24] V. Blum, R. Gehrke, F. Hanke, P. Havu, V. Havu, X. Ren, K. Reuter, and M. Scheffler, Comput. Phys. Commun. **180**, 2175 (2009) (cit. on pp. 7, 18, 28).

[25] J. P. Perdew, in Aip conference proceedings, Vol. 577, August 2001 (2001), pp. 1–20 (cit. on p. 7).

[26] D. M. Ceperley and B. J. Alder, Phys. Rev. Lett. **45**, 566 (1980) (cit. on p. 7).

[27] J. P. Perdew, K. Burke, and M. Ernzerhof, Phys. Rev. Lett. **77**, 3865 (1996) (cit. on pp. 8, 28).

[28] S. F. Sousa, P. A. Fernandes, and M. J. Ramos, J. Phys. Chem. A **111**, 10439 (2007) (cit. on p. 8).

[29] H. S. Yu, S. L. Li, and D. G. Truhlar, J. Chem. Phys. **145**, 130901 (2016) (cit. on p. 8).

[30] A. D. Becke, J. Chem. Phys. **140**, 18A301 (2014) (cit. on p. 8).

[31] J. P. Perdew, J. A. Chevary, S. H. Vosko, K. A. Jackson, M. R. Pederson, D. J. Singh, and C. Fiolhais, Phys. Rev. B **46**, 6671 (1992) (cit. on p. 8).

[32] A. Uldry, F. Vernay, and B. Delley, Phys. Rev. B **85**, 1 (2012) (cit. on p. 9).

[33] E. Stavitski and F. M. de Groot, Micron **41**, 687 (2010) (cit. on p. 9).

[34] M. Stener, G. Fronzoni, and M. de Simone, Chem. Phys. Lett. **373**, 115 (2003) (cit. on p. 9).

[35] N. A. Besley and F. A. Asmuruf, Phys. Chem. Chem. Phys. **12**, 12024 (2010) (cit. on p. 9).

[36] J. Vinson and J. J. Rehr, Phys. Rev. B **86**, 1 (2012) (cit. on p. 9).

[37] J. Vinson, J. J. Rehr, J. J. Kas, and E. L. Shirley, Phys. Rev. B **83**, 115106 (2011) (cit. on p. 9).

[38] M. Nooijen and R. J. Bartlett, J. Chem. Phys. **102**, 6735 (1995) (cit. on p. 9).

[39] S. Coriani, O. Christiansen, T. Fransson, and P. Norman, Phys. Rev. A **85**, 1 (2012) (cit. on p. 9).

[40] B. Peng, P. J. Lestrange, J. J. Goings, M. Caricato, and X. Li, J. Chem. Theory Comput. **11**, 4146 (2015) (cit. on p. 9).

[41] J. P. Coe and M. J. Paterson, Theor. Chem. Acc. **134**, 3 (2015) (cit. on p. 9).

[42] S. I. Bokarev, M. Dantz, E. Suljoti, O. Kühn, and E. F. Aziz, Phys. Rev. Lett. **111**, 1 (2013) (cit. on p. 9).

[43] G. Grell, S. I. Bokarev, B. Winter, R. Seidel, E. F. Aziz, S. G. Aziz, and O. Kühn, J. Chem. Phys. **143**, 074104 (2015) (cit. on p. 9).

[44] W. Egelhoff, Surf. Sci. Rep. **6**, 253 (1987) (cit. on p. 9).

[45] L. Triguero, O. Plashkevych, L. Pettersson, and H. Ågren, J. Electron Spectrosc. Relat. Phenom. **104**, 195 (1999) (cit. on p. 9).

[46] Y. Takahata and D. P. Chong, J. Electron Spectrosc. Relat. Phenom. **133**, 69 (2003) (cit. on p. 9).

[47] M. Cavalleri, M. Odelius, D. Nordlund, A. Nilsson, and L. G. M. Pettersson, Phys. Chem. Chem. Phys. **7**, 2854 (2005) (cit. on p. 9).

[48] Z. Zeng, X. Ma, W. Ding, and W. Li, Sci. China Chem. **53**, 402 (2010) (cit. on p. 9).

[49] S. García-Gil, A. García, and P. Ordejón, Eur. Phys. J. B **85**, 239 (2012) (cit. on p. 9).

[50] A. V. Krukau, O. A. Vydrov, A. F. Izmaylov, and G. E. Scuseria, J. Chem. Phys. **125**, 224106 (2006) (cit. on pp. 11, 20, 28).

[51] J. P. Perdew, R. G. Parr, M. Levy, and J. L. Balduz, Phys. Rev. Lett. **49**, 1691 (1982) (cit. on p. 12).

[52] P. Mori-Sánchez, A. J. Cohen, and W. Yang, J. Chem. Phys. **125**, 201102 (2006) (cit. on p. 12).

[53] A. J. Cohen, P. Mori-Sánchez, and W. Yang, Phys. Rev. B **77**, 115123 (2008) (cit. on p. 12).

[54] C. Kolczewski, R. Püttner, O. Plashkevych, H. Ågren, V. Staemmler, M. Martins, G. Snell, A. S. Schlachter, M. Sant'Anna, G. Kaindl, and L. G. M. Pettersson, J. Chem. Phys. **115**, 6426 (2001) (cit. on p. 13).

[55] C. Kolczewski and K. Hermann, J. Chem. Phys. **118**, 7599 (2003) (cit. on p. 13).

[56] P. S. Bagus, Phys. Rev. **139**, A619 (1965) (cit. on pp. 13, 14).

[57] G. S. Michelitsch and K. Reuter, J. Chem. Phys. **accepted** (2019) (cit. on pp. 13, 14, 16).

[58] J. C. Slater, **6**, 1 (1972) (cit. on pp. 13–15).

[59] A. R. Williams, R. A. deGroot, and C. B. Sommers, J. Chem. Phys. **63**, 628 (1975) (cit. on pp. 13–15).

[60] I. Tanaka, H. Araki, M. Yoshiya, T. Mizoguchi, K. Ogasawara, and H. Adachi, Phys. Rev. B **60**, 4944 (1999) (cit. on p. 14).

[61] C. Elsässer and S. Köstlmeier, Ultramicroscopy **86**, 325 (2001) (cit. on p. 14).

[62] B. Hetényi, F. De Angelis, P. Giannozzi, and R. Car, J. Chem. Phys. **120**, 8632 (2004) (cit. on p. 14).

[63] L. Triguero, L. G. M. Pettersson, and H. Ågren, Phys. Rev. B **58**, 8097 (1998) (cit. on p. 14).

[64] D. Prendergast and G. Galli, Phys. Rev. Lett. **96**, 215502 (2006) (cit. on p. 14).

[65] K. Lie, R. Høier, and R. Brydson, Phys. Rev. B **61**, 1786 (2000) (cit. on p. 14).

[66] R. Buczko, G. Duscher, S. J. Pennycook, and S. T. Pantelides, Phys. Rev. Lett. **85**, 2168 (2000) (cit. on p. 14).

[67] R. Ahuja, P. A. Brühwiler, J. M. Wills, B. Johansson, N. Mårtensson, and O. Eriksson, Phys. Rev. B **54**, 14396 (1996) (cit. on p. 14).

[68] J. F. Janak, Phys. Rev. B **18**, 7165 (1978) (cit. on p. 15).

[69] S. W. de Leeuw, J. W. Perram, and E. R. Smith, Proc. R. Soc. Lond. A **373**, 27 (1980) (cit. on p. 15).

[70] J. Neugebauer and M. Scheffler, Phys. Rev. B **46**, 16067 (1992) (cit. on p. 15).

[71] J. M. Foster and S. F. Boys, Rev. Mod. Phys. **32**, 300 (1960) (cit. on p. 17).

[72] M. Rossi, M. Ceriotti, and D. E. Manolopoulos, J. Phys. Chem. Lett. **7**, 3001 (2016) (cit. on p. 17).

[73] X. Ren, P. Rinke, V. Blum, J. Wieferink, A. Tkatchenko, A. Sanfilippo, K. Reuter, and M. Scheffler, New J. Phys. **14**, 053020 (2012) (cit. on p. 18).

[74] C. Adamo and V. Barone, J. Chem. Phys. **110**, 6158 (1999) (cit. on p. 18).

[75] F. Weigend, F. Furche, and R. Ahlrichs, J. Chem. Phys. **119**, 12753 (2003) (cit. on p. 18).

[76] P. S. Bagus and H. F. Schaefer, J. Chem. Phys. **56**, 224 (1972) (cit. on p. 17).

[77] H. Jonkmann, G. van der Velde, and W. Nieuwpoort, Proceedings of the 4th SRC Atlas Symposium, edited by J. Brown and V. Saunders, 243 (1975) (cit. on p. 17).

[78] R. Broer and W. Nieuwpoort, Chem. Phys. **54**, 291 (1981) (cit. on p. 17).

[79] G. Vall-llosera, B. Gao, A. Kivimäki, M. Coreno, J. Álvarez Ruiz, M. de Simone, H. Ågren, and E. Rachlew, J. Chem. Phys. **128**, 044316 (2008) (cit. on pp. 18, 19).

[80] W. P. Huhn and V. Blum, Phys. Rev. Mater. **1**, 033803 (2017) (cit. on p. 20).

[81] V. Zamudio-Bayer, L. Leppert, K. Hirsch, A. Langenberg, J. Rittmann, M. Kossick, M. Vogel, R. Richter, A. Terasaki, T. Möller, B. v. Issendorff, S. Kümmel, and J. T. Lau, Phys. Rev. B **88**, 115425 (2013) (cit. on p. 20).

[82] W. Haynes, *CRC Handbook of Chemistry and Physics* (CRC Press, 2016) (cit. on p. 21).

[83] C. I. Hancox, S. C. Doret, M. T. Hummon, L. Luo, and J. M. Doyle, Nature **431**, 281 (2004) (cit. on p. 21).

[84] B. K. Newman, N. Brahms, Y. S. Au, C. Johnson, C. B. Connolly, J. M. Doyle, D. Kleppner, and T. J. Greytak, Phys. Rev. A **83**, 012713 (2011) (cit. on p. 21).

[85] R. V. Krems, J. Kłos, M. F. Rode, M. M. Szcześniak, G. Chałasiński, and A. Dalgarno, Phys. Rev. Lett. **94**, 013202 (2005) (cit. on p. 21).

[86] R. V. Krems and A. A. Buchachenko, J. Chem. Phys. **123**, 101101 (2005) (cit. on p. 21).

[87] J. I. Urgel, B. Cirera, Y. Wang, W. Auwärter, R. Otero, J. M. Gallego, M. Alcamí, S. Klyatskaya, M. Ruben, F. Martín, R. Miranda, D. Ecija, and J. V. Barth, Small **11**, 6358 (2015) (cit. on p. 21).

[88] D. Écija, J. I. Urgel, A. P. Seitsonen, W. Auwärter, and J. V. Barth, Acc. Chem. Res. **51**, 365 (2018) (cit. on p. 21).

[89] J.-C. G. Bünzli, J. Coord. Chem. **67**, 3706 (2014) (cit. on p. 21).

[90] D.-L. Long, A. J. Blake, N. R. Champness, and M. Schröder, Chem. Commun., 1369 (2000) (cit. on p. 21).

[91] D.-L. Long, A. J. Blake, N. R. Champness, C. Wilson, and M. Schröder, J. Am. Chem. Soc. **123**, 3401 (2001) (cit. on p. 21).

[92] D.-L. Long, R. J. Hill, A. J. Blake, N. R. Champness, P. Hubberstey, D. M. Proserpio, C. Wilson, and M. Schröder, Angew. Chem. Int. Ed. **43**, 1851 (2004) (cit. on p. 21).

[93] D.-l. Long, A. J. Blake, N. R. Champness, C. Wilson, and M. Schröder, Angew. Chem. **113**, 2509 (2001) (cit. on p. 21).

[94] J. I. Urgel, D. Ecija, W. Auwärter, and J. V. Barth, Nano Lett. **14**, 1369 (2014) (cit. on p. 21).

[95] F. Bischoff, K. Seufert, W. Auwärter, A. P. Seitsonen, D. Heim, and J. V. Barth, J. Phys. Chem. C **122**, 5083 (2018) (cit. on p. 21).

[96] D. Écija, W. Auwärter, S. Vijayaraghavan, K. Seufert, F. Bischoff, K. Tashiro, and J. V. Barth, Angew. Chem. Int. Ed. **50**, 3872 (2011) (cit. on p. 21).

[97] T. M. Reineke, M. Eddaoudi, M. Fehr, D. Kelley, and O. M. Yaghi, J. Am. Chem. Soc. **121**, 1651 (1999) (cit. on p. 21).

[98] L. Pan, K. M. Adams, H. E. Hernandez, X. Wang, C. Zheng, Y. Hattori, and K. Kaneko, J. Am. Chem. Soc. **125**, 3062 (2003) (cit. on p. 21).

[99] C. Qin, X.-L. Wang, E.-B. Wang, and Z.-M. Su, Inorg. Chem. **44**, 7122 (2005) (cit. on p. 21).

[100] D. Ecija, J. I. Urgel, A. C. Papageorgiou, S. Joshi, W. Auwarter, A. P. Seitsonen, S. Klyatskaya, M. Ruben, S. Fischer, S. Vijayaraghavan, J. Reichert, and J. V. Barth, Proc. Natl. Acad. Sci. U.S.A. **110**, 6678 (2013) (cit. on p. 21).

[101] J. I. Urgel, D. Ecija, W. Auwärter, A. C. Papageorgiou, A. P. Seitsonen, S. Vijayaraghavan, S. Joshi, S. Fischer, J. Reichert, and J. V. Barth, J. Phys. Chem. C **118**, 12908 (2014) (cit. on p. 21).

[102] B. Cirera, J. Björk, R. Otero, J. M. Gallego, R. Miranda, and D. Ecija, J. Phys. Chem. C **121**, 8033 (2017) (cit. on p. 21).

[103] R. Hellwig, M. Uphoff, T. Paintner, J. Björk, M. Ruben, F. Klappenberger, and J. V. Barth, Chem. Eur. J. **24**, 16126 (2018) (cit. on p. 21).

[104] R. Sessoli and A. K. Powell, Coord. Chem. Rev. **253**, 2328 (2009) (cit. on p. 21).

[105] D. N. Woodruff, R. E. P. Winpenny, and R. A. Layfield, Chem. Rev. **113**, 5110 (2013) (cit. on p. 21).

[106] R. Baltic, M. Pivetta, F. Donati, C. Wäckerlin, A. Singha, J. Dreiser, S. Rusponi, and H. Brune, Nano Lett. **16**, 7610 (2016) (cit. on pp. 21, 28, 31).

[107] F. Donati, S. Rusponi, S. Stepanow, C. Wackerlin, A. Singha, L. Persichetti, R. Baltic, K. Diller, F. Patthey, E. Fernandes, J. Dreiser, A. ljivan, K. Kummer, C. Nistor, P. Gambardella, and H. Brune, Science **352**, 318 (2016) (cit. on p. 21).

[108] F. D. Natterer, K. Yang, W. Paul, P. Willke, T. Choi, T. Greber, A. J. Heinrich, and C. P. Lutz, Nature **543**, 226 (2017) (cit. on p. 21).

[109] P. Rinke, A. Qteish, J. Neugebauer, C. Freysoldt, and M. Scheffler, New J. Phys. **7**, 126 (2005) (cit. on p. 23).

[110] D. Vogel, P. Krüger, and J. Pollmann, Phys. Rev. B **52**, R14316 (1995) (cit. on p. 23).

[111] D. Vogel, P. Krüger, and J. Pollmann, Phys. Rev. B **54**, 5495 (1996) (cit. on p. 23).

[112] D. Vogel, P. Krüger, and J. Pollmann, Phys. Rev. B **55**, 12836 (1997) (cit. on p. 23).

[113] V. Fock, Z. Physik **61**, 126 (1930) (cit. on p. 23).

[114] J. C. Slater, Phys. Rev. **35**, 210 (1930) (cit. on p. 23).

[115] D. R. Hartree and W. Hartree, Proc. R. Soc. Lond. A **150**, 9 (1935) (cit. on p. 23).

[116] J. C. Slater, Phys. Rev. **34**, 1293 (1929) (cit. on p. 23).

[117] J. P. Perdew and A. Zunger, Phys. Rev. B **23**, 5048 (1981) (cit. on p. 23).

[118] S. Klüpfel, P. Klüpfel, and H. Jónsson, Phys. Rev. A **84**, 1 (2011) (cit. on p. 24).

[119] S. Klüpfel, P. Klüpfel, and H. Jónsson, J. Chem. Phys. **137**, 124102 (2012) (cit. on p. 24).

[120] P. Klüpfel, S. Klüpfel, K. Tsemekhman, and H. Jónsson, in *Applied parallel and scientific computing* (Springer Berlin Heidelberg, 2012), pp. 23–33 (cit. on p. 24).

[121] T. Todorova, A. P. Seitsonen, J. Hutter, I.-F. W. Kuo, and C. J. Mundy, J. Phys. Chem. B **110**, 3685 (2006) (cit. on p. 24).

[122] I. C. Gerber, J. G. Ángyán, M. Marsman, and G. Kresse, J. Chem. Phys. **127**, 054101 (2007) (cit. on p. 24).

[123] J. Paier, M. Marsman, and G. Kresse, J. Chem. Phys. **127**, 024103 (2007) (cit. on p. 24).

[124] F. Tran, D. Koller, and P. Blaha, Phys. Rev. B **86**, 1 (2012) (cit. on p. 24).

[125] Y.-R. Jang and B. Deok Yu, J. Phys. Soc. Jpn. **81**, 114715 (2012) (cit. on p. 24).

[126] W. Gao, T. A. Abtew, T. Cai, Y.-Y. Sun, S. Zhang, and P. Zhang, Solid State Commun. **234-235**, 10 (2016) (cit. on p. 24).

[127] V. I. Anisimov, J. Zaanen, and O. K. Andersen, Phys. Rev. B **44**, 943 (1991) (cit. on pp. 24, 27).

[128] J. Hubbard, Proc. R. Soc. Lond. A **276**, 238 (1963) (cit. on p. 24).

[129] J. Hubbard, Proc. R. Soc. Lond. A **277**, 237 (1964) (cit. on p. 24).

[130] J. Hubbard, Proc. R. Soc. Lond. A **281**, 401 (1964) (cit. on p. 24).

[131] J. Hubbard, Proc. R. Soc. Lond. A **296**, 100 (1967) (cit. on p. 24).

[132] J. Hubbard, Proc. R. Soc. Lond. A **296**, 82 (1967) (cit. on p. 24).

[133] J. Hubbard, Proc. R. Soc. Lond. A **296**, 100 (1967) (cit. on p. 24).

[134] H. Eschrig, K. Koepernik, and I. Chaplygin, J. Solid State Chem. **176**, 482 (2003) (cit. on p. 25).

[135] M. J. Han, T. Ozaki, and J. Yu, Phys. Rev. B **73**, 1 (2006) (cit. on p. 25).

[136] W. E. Pickett, S. C. Erwin, and E. C. Ethridge, Phys. Rev. B **58**, 1201 (1998) (cit. on p. 25).

[137] R. S. Mulliken, J. Chem. Phys. **23**, 1833 (1955) (cit. on p. 25).

[138] D. D. O'Regan, M. C. Payne, and A. A. Mostofi, Phys. Rev. B **83**, 1 (2011) (cit. on pp. 25, 26).

[139] D. D. O'Regan, N. D. M. Hine, M. C. Payne, and A. A. Mostofi, Phys. Rev. B **82**, 2 (2010) (cit. on p. 26).

[140] H. C. Türk, "Defining the Correlated Subspace in Hubbard Corrected DFT using Boys Projector Functions," MSc Thesis (Technische Universität München, 2018) (cit. on p. 26).

[141] A. I. Liechtenstein, V. I. Anisimov, and J. Zaanen, Phys. Rev. B **52**, R5467 (1995) (cit. on p. 26).

[142] S. L. Dudarev, G. A. Botton, S. Y. Savrasov, C. J. Humphreys, and A. P. Sutton, Phys. Rev. B **57**, 1505 (1998) (cit. on p. 26).

[143] E. R. Ylvisaker, W. E. Pickett, and K. Koepernik, Phys. Rev. B **79**, 1 (2009) (cit. on p. 27).

[144] M. T. Czyżyk and G. A. Sawatzky, **49**, 14211 (1994) (cit. on p. 27).

[145] P. Giannozzi, S. Baroni, N. Bonini, M. Calandra, R. Car, C. Cavazzoni, D. Ceresoli, G. L. Chiarotti, M. Cococcioni, I. Dabo, A. Dal Corso, S. de Gironcoli, S. Fabris, G. Fratesi, R. Gebauer, U. Gerstmann, C. Gougoussis, A. Kokalj, M. Lazzeri, L. Martin-Samos, N. Marzari, F. Mauri, R. Mazzarello, S. Paolini, A. Pasquarello, L. Paulatto, C. Sbraccia, S. Scandolo, G. Sclauzero, A. P. Seitsonen, A. Smogunov, P. Umari, and R. M. Wentzcovitch, J. Phys.: Condens. Matter **21**, 395502 (2009) (cit. on p. 28).

[146] V. G. Ruiz, W. Liu, E. Zojer, M. Scheffler, and A. Tkatchenko, Phys. Rev. Lett. **108**, 146103 (2012) (cit. on p. 28).

[147] M. Topsakal and R. Wentzcovitch, Comp. Mat. Sci. **95**, 263 (2014) (cit. on p. 28).

[148] A. Dal Corso, Comp. Mat. Sci. **95**, 337 (2014) (cit. on p. 28).

[149] M. Andersen, "Graphene and polycyclic aromatic hydrocarbons modeled with density functional theory," PhD thesis (2014) (cit. on p. 29).

[150] F. Jean, T. Zhou, N. Blanc, R. Felici, J. Coraux, and G. Renaud, Phys. Rev. B **91**, 245424 (2015) (cit. on p. 29).

[151] S. K. Hämäläinen, M. P. Boneschanscher, P. H. Jacobse, I. Swart, K. Pussi, W. Moritz, J. Lahtinen, P. Liljeroth, and J. Sainio, Phys. Rev. B **88**, 201406 (2013) (cit. on p. 29).

[152] C. Busse, P. Lazić, R. Djemour, J. Coraux, T. Gerber, N. Atodiresei, V. Caciuc, R. Brako, A. T. N'Diaye, S. Blügel, J. Zegenhagen, and T. Michely, Phys. Rev. Lett. **107**, 036101 (2011) (cit. on p. 29).

[153] B. Dorado, B. Amadon, M. Freyss, and M. Bertolus, Phys. Rev. B **79**, 1 (2009) (cit. on p. 34).

[154] J. P. Allen and G. W. Watson, Phys. Chem. Chem. Phys. **16**, 21016 (2014) (cit. on p. 34).

[155] M. Kick, K. Reuter, and H. Oberhofer, J. Chem. Theor. Comput. (2019) (cit. on p. 34).

Appendices

.1 Paper #1 52
.2 Paper #2 71
.3 Paper #3 101

.1 Paper #1

Assembly of Robust Holmium-Directed 2D Metal-Organic Coordination Complexes and Networks on the Ag (100) Surface

M. Uphoff[1], G.S. Michelitsch[1], R. Hellwig, K. Reuter, H. Brune, F. Klappenberger, and J.V. Barth
ACS Nano **12**, 11552-11560, (2018)
DOI: 10.1021/acsnano.8b06704

Reprinted under the terms of the ACS Copyright Agreement.
©2018 American Chemical Society.

---

[1] These authors contributed equally to the work.

ACS NANO
Cite This: *ACS Nano* 2018, 12, 11552−11560
www.acsnano.org

Downloaded via TU MUENCHEN on December 21, 2018 at 08:21:17 (UTC).
See https://pubs.acs.org/sharingguidelines for options on how to legitimately share published articles.

Assembly of Robust Holmium-Directed 2D Metal−Organic Coordination Complexes and Networks on the Ag(100) Surface

Martin Uphoff,[†,§] Georg S. Michelitsch,[‡,§] Raphael Hellwig,[†] Karsten Reuter,[‡] Harald Brune,[¶] Florian Klappenberger,*[,†] and Johannes V. Barth*[,†]

[†]Department of Physics (E20), Technische Universität München, James-Franck-Straße 1, 85748 Garching, Germany

[‡]Department of Chemistry, Chair of Theoretical Chemistry, Technische Universität München, Lichtenbergstraße 4, 85748 Garching, Germany

[¶]Institute of Physics, Ecole Polytechnique Fédérale de Lausanne (EPFL), Station 3, 1015 Lausanne, Switzerland

Supporting Information

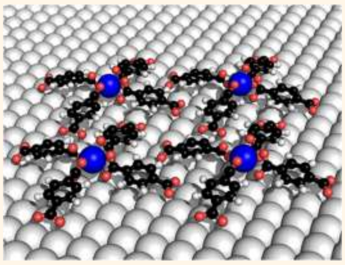

ABSTRACT: **We describe the formation of lanthanide−organic coordination networks and complexes under ultra-high-vacuum conditions on a clean Ag(100) surface. The structures comprise single Ho atoms as coordination centers and 1,4-benzenedicarboxylate (from terephtalic acid, TPA) as molecular linkers. Using low-temperature scanning tunneling microscopy, we find two different chiral phases of surface-supported metal−organic structures incorporating Ho atoms. Density functional theory calculations can explain the structure of both binding motifs and give possible reasons for their varying formation under the respective Ho/TPA ratios, as well as deposition and annealing temperatures. Metal−ligand interactions drive the formation of cloverleaf-shaped mononuclear Ho−TPA$_4$ complexes establishing supramolecular arrays stabilized through hydrogen bonding. A 2D lanthanide−organic reticulation is observed when changing the stoichiometry between the two building blocks. The combined insights from scanning tunneling microscopy and density functional theory reveal the relative stability, charge transfer, and bonding environment of both motifs.**

KEYWORDS: *metal−organic coordination, self-assembly, lanthanides, holmium, carboxylates, terephthalic acid, scanning tunneling microscopy, density functional theory*

In recent years the use of lanthanides in molecular architectures has been a burgeoning field of research, exploiting the high coordination numbers lanthanides offer in comparison to other metals. Inspired by the potential revealed in three-dimensional compounds and networks,[1−7] recent studies focus on the development and control of interfacial nanosystems[8−11] and architectures.[12−16] Additionally, their magnetic properties are of high interest to the scientific community, and major steps were done in the fabrication of lanthanide-based magnetic devices including single-molecule magnetic complexes.[17−23] Recent experiments reveal prospects toward single-atom memory for single Ho atoms on a surface.[24,25] They offer the ultimate smallest memory unit of magnetic storage devices, but are so far unstable in their confinement on the surface and exhibit loss of their magnetic hysteresis above 50 K.[26]

In order to stabilize single Ho atoms against diffusion on the surface, we utilize on-surface metal−organic self-assembly. As previously shown, the formation of coordination superlattices and networks permits creating and preserving stable magnetic quantum states, whereby the embedding of metal atoms in specific coordination configurations with organic ligands can greatly influence the electronic structure of the metal centers and hence their spin states.[20,21,23,27] Moreover, through changing the environment by such measures, the lifetime of the spin states can be greatly increased.[28]

In this work, we explore the potential of organic linker molecules combined with Ho atoms at a well-defined metal surface toward the formation of robust metal−organic nanostructures. We employ a simple, prototypical linker species, namely, 1,4-benzenedicarboxylic acid (terephtalic acid - TPA). It is a versatile building block for the creation of supramolecular architectures on noble metal surfaces and semiconductors[29−31] and has also been employed for lanthanide-based metal−organic coordination.[32] On reactive surfaces, thermal excitation can transform the functional groups into carboxylate species whereby the deprotonation can drive phase transformations[33] and enable the formation of metal−organic coordination motifs.[28] Utilizing scanning

Received: September 2, 2018
Accepted: October 8, 2018
Published: October 8, 2018

© 2018 American Chemical Society

DOI: 10.1021/acsnano.8b06704
ACS Nano 2018, 12, 11552−11560

tunneling microscopy (STM), we investigate the self-assembly behavior on Ag(100), *i.e.*, a weakly reactive surface with square symmetry. Although there is a relatively high activation barrier for deprotonation on this substrate, it was chosen because it provides the possibility to afford magnesium oxide layers, thus creating interfaces with exceptional properties regarding lanthanide-based nanomagnetism.[24,34]

Through first characterizing purely organic adlayers we show that heating-induced deprotonation generates a carboxylate precursor phase before significant loss of molecules through desorption sets in. This enables the subsequent creation of Ho-directed nanostructures. *Via* controlling the preparation conditions (*i.e.*, Ho-molecule ratio, deposition, and annealing temperatures), we can steer the formation of two distinct Ho−TPA phases consisting of metal−organic complexes and coordination networks, respectively. By means of density functional theory (DFT) calculations we develop structural models for the supramolecular assemblies explaining the experimental findings in great detail. Furthermore, through the DFT analysis we gain insight into the Ho coordination chemistry including the charge redistribution of the coordination nodes and the influence of the surface. We give an explanation for the chirality of the structures and a detailed analysis of strain effects, which are of general relevance in the field of surface-confined metallosupramolecular engineering. Our work highlights the potential of Ho for the construction of surface-supported large-scale nanoarchitectures that bear prospects for nanomagnetism. Simultaneously, we lay a foundation to further exploit the exceptional magnetic properties of Ho on surfaces that arise from the occurrence as single confined entities.

RESULTS AND DISCUSSION

Before we investigated Ho-directed structure formation we characterized samples with purely organic adlayers aiming at the preparation of a reactive precursor layer featuring functional groups in the carboxylate state, thus ready to coordinate to lanthanide atoms. In a first attempt, TPA molecules were deposited onto a freshly cleaned Ag(100) surface held at room temperature *via* organic molecular beam epitaxy (OMBE, T_{OMBE} = 160 °C).

The preparation resulted in long-range ordered domains where all molecules exhibited the same apparent height (Figure 1a, inset, note that all presented STM images were recorded at 4.5 K). The intermolecular distance along the molecular chains, d_0 = 9.7 Å, is consistent with previous reports on hydrogen-bonded assemblies of intact TPA, as suggested by the superimposed molecular models. Subsequent annealing of the sample resulted in strong desorption losses, disqualifying this approach as a starting point for Ho-carboxylate architectures. The comparison to previous results on Cu(100)[28,35−37] and Ag(111)[38] indicates that the adhesion of TPA to the Ag(100) surface is quite limited and more similar to the close-packed Ag(111) than to the Cu(100).

Then, we developed a so-called hot deposition approach, where TPA is deposited onto a hot substrate; that is, the sample is held at 450 K during the 10 min deposition time. STM data obtained on that sample reveal that this preparation protocol results in a purely organic phase with a coverage near to one monolayer (ML). The molecules form a regular adsorption pattern (Figure 1a), in which they appear as oval protrusions exhibiting either one of two relative brightness levels. A brighter species is surrounded by six darker ones, while each darker species is surrounded by three brighter and three darker ones. Thus, the unit cell outlined in the figure now contains six molecules. The prominent differences regarding relative brightness, unit cell size, and orientation of the molecules in comparison to the previous phase of intact TPA (Figure 1a, inset) indicate that the adsorbates should now exhibit a different substrate registry and chemical nature.

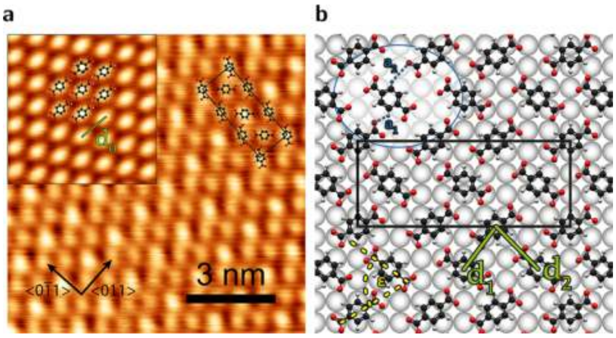

Figure 1. Precursor phase (a) STM image of an organic layer consisting of TPA molecules with deprotonated end groups on the Ag(100) surface obtained upon adsorption at 450 K. A regular pattern of molecules appearing to be higher in topography is visible, Inset: TPA deposited at RT on Ag(100). Tunneling current I_{T} = 1.1 nA, bias voltage V_{B} = 3 mV. (b) Tentative model of the organic precursor layer. The heterogeneous topography distribution of the molecules is due to higher lying TPA molecules on the bridge sites of the silver substrate. The unit cell of the organic network is marked as a black rectangle, identifying it as a $p(10 \times 4)$ structure with respect to the underlying lattice.

The small overlay in the top right corner of Figure 1a depicts the orientation of the molecules, and a tentative adsorption model is presented in Figure 1b. Following previous NEXAFS studies of TPA on Cu(100),[33] we assume a flat adsorption geometry of the phenyl ring on the surface. The model describes the adlayer as a $p(10 \times 4)$ superstructure with a density of 0.15 molecule per Ag atom and consists of doubly deprotonated TPA, *i.e.*, where both functional groups are in the carboxylate state and the phenyl ring still contains its four H atoms. It rationalizes the relative brightness pattern through associating the dimmer and brighter species with molecules adsorbed with their phenyl ring centered on hollow and bridge sites of the Ag lattice, respectively. Additionally, the model shows a slight rotation of the hollow site molecules around the normal vector of the phenyl ring plane. This results in a distorted T-shaped binding motif, where the carboxylates do not face the hydrogen atoms of the phenyl rings in an exactly perpendicular fashion, but rather at an angle of ε = 73°, as depicted in Figure 1b. We suggest that the center positions of the molecules are determined by molecule−substrate interaction, whereas weak, noncovalent lateral interactions between the molecules, presumably dominated by proton acceptor ring interaction,[39] induce the rotation of the molecules. The occurring intermolecular distances of nearby atoms are situated between a minimum of a_1 = 2.1 Å and a maximum of a_2 = 3.5 Å (blue circle in Figure 1b), thus exhibiting typical values for noncovalent interaction.[40]

By a detailed analysis of the distances between molecules, we obtain indirect evidence on their chemical state. The two nearest neighbor distances of the precursor phase are labeled as d_1 and d_2 in Figure 1b. Considering the substrate registry, the distances between bridge and hollow site molecules (d_1) are

7.2 Å and between two hollow site molecules (d_2) 8.2 Å, respectively. The layer is denser than the previous assembly of intact TPA (*cf.* Figure 1a inset), where the corresponding distances amount to 7.2 and 9.7 Å (d_0). Previous studies revealed consistent values. Assemblies of doubly deprotonated TPA on Cu(100) exhibited $d_1 = d_2 = 7.65$ Å.[36] Similar distances ($d_1 = d_2 = 7.4$ Å) were also found on Pd(111).[41] By contrast, packing schemes of intact TPA on Au(111)[42] showed $d_1 = 8.5$ Å and $d_2 = 9.9$ Å, consistent with our values for the intact phase and with the case of intact TPA on Cu(100), where $d_1 = 8.1$ Å and $d_2 = 12.8$ Å.[33] This comparison strongly indicates that the precursor phase on Ag(100) contains predominantly doubly deprotonated TPA.

We thus conclude that the described hot deposition method enables us to obtain a full ML of ditopic carboxylate linkers with very few impurities and defects. This is a favorable outcome, since later annealing steps for the preparation of metal−organic coordination networks (MOCNs) always result in a slight loss of molecules due to thermal desorption.

For coverages below a full ML (again obtained by hot deposition) two organic phases are present. Besides the precursor phase discussed above, small islands of a less dense phase form between the big islands of the precursor phase. Details on this "transition phase" are given in the Supporting Information (*cf.* S1(a)).

Ho-Directed Assembly. For investigating the potential of surface-supported Ho as coordination centers we prepared a series of samples systematically varying the preparation parameters. We obtained the best results for dosing Ho at room temperature onto a full monolayer of the precursor phase followed by annealing the sample at 450 K for 10 min. Depending on the Ho dosage, two different types of metal−organic structures were observed. Ho dosages refer to fractions of monolayers of the close-packed Ho(0001) surface (hcp crystal lattice, see Supporting Information).

Cloverleaf Phase. An STM image of a TPA/Ag(100)-$p(10 \times 4)$ precursor sample exposed to a low dosage of Ho (~0.015 ML) is depicted in Figure 2a.

The essential binding motif is composed of four bright features pointing toward a medium bright center interpreted as a cloverleaf shape (red outline). Similar cloverleaf phases have been reported on Cu(100), involving iron or gadolinium[15] as coordination centers and multitopic carboxylate linkers[43,44] including TPA.[36] Analogously, we suggest that here four linker species coordinate to one Ho atom, as depicted by the model overlay, making it an 8-fold coordination to the surrounding oxygens. According to STM data, the unit cell vectors of this metal−organic superstructure enclose an angle of 22.2 ± 1.8° with respect to the primitive lattice vectors of the Ag(100) surface (shown in the bottom left corner of Figure 2a). This corresponds to a quadratic unit cell of 15.6 ± 0.08 Å.

With our DFT-based geometry optimization we obtained the adsorption model shown in Figure 2b, where the unit cell is highlighted by a black rectangle. It confirms that four carboxyl groups are coordinated to one Ho atom. More specifically, the involved carboxylates are concertedly rotated by an angle of 53° around the C−C axis connecting them to the phenyl rings, thus rendering a chiral coordination scheme. This behavior of the linker groups was weakly implied in a previous study[15] and can now be confirmed by our calculations. The chirality is better visualized in Figure 4a and b, depicting the two enantiomers side-by-side. It has been shown that the adsorption of achiral molecules can entail surface-induced chirality along with chiral recognition on the formation of extended islands, greatly influencing the electronic structure.[45] This could be utilized to steer the systems nanomagnetic properties. The arrangement of the metal−organic complexes is forming a fully commensurate pattern. The top-left part of Figure 2a depicts an overlay of a simulated STM image calculated from the model and demonstrates the excellent agreement with the observed features in the STM data.

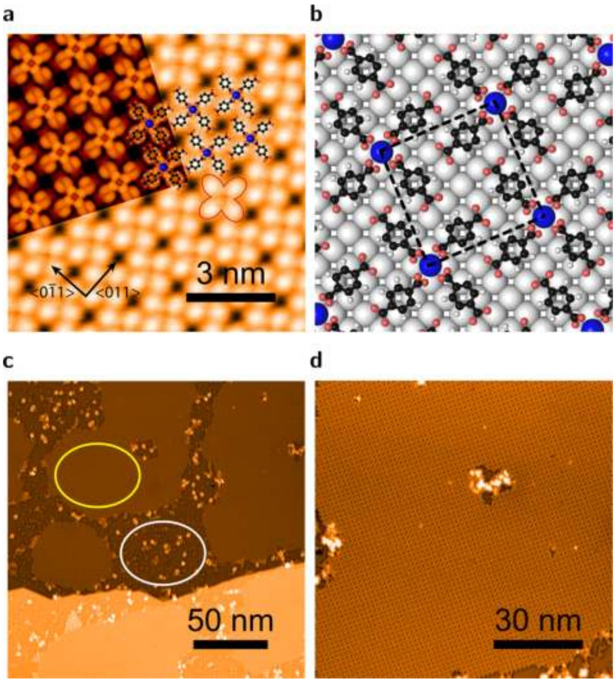

Figure 2. (a) High-resolution constant-current STM image of the $Ho(TPA)_4/Ag(100)$-$p(\sqrt{29} \times \sqrt{29})R21.8°$ cloverleaf phase, superimposed by a simulated STM image rendered from the DFT model. Molecules and Ho atoms are superimposed to mark their positions ($I_T = 500$ pA, $V_B = -2$ mV). (b) DFT model for the cloverleaf phase. The unit cell is marked by the dashed square. (c) 200 nm × 200 nm STM image showing the extent of islands on the silver surface. There are some clusters and molecules in the organic transition phase present, partly decorated by Ho adatoms (example area indicated by white ellipsoid). (d) 100 nm × 100 nm excerpt from (c) showing the quality of the islands.

In our DFT calculations Ho atoms preferentially reside at the energetically favorable[46] hollow positions of the silver lattice and the lower O atoms of the carboxylates assume positions close to the Ag top sites. With respect to the primitive crystal directions the unit cell constitutes a square $p(\sqrt{29} \times \sqrt{29})R21.8°$ superstructure with a size of 15.56 Å × 15.56 Å, agreeing nicely with the experimental value of 15.6 Å for the side length. The molecule density is 0.14 molecule per silver atom. Moreover, the cloverleaf phase exhibits organizational chirality, and both enantiomorphic arrangements have been observed on the same sample (see Supporting Information Figure S2).

The TPA molecules appear as bright oval protrusions in the STM image, whereas the Ho atoms appear transparent. The fact that the metal centers are not producing visible features in STM data is commonly observed for metal−organic coordination motifs.[15,47,48] Through translating the theoretical model with respect to the STM data, it can be inferred that the

DOI: 10.1021/acsnano.8b06704
ACS Nano 2018, 12, 11552−11560

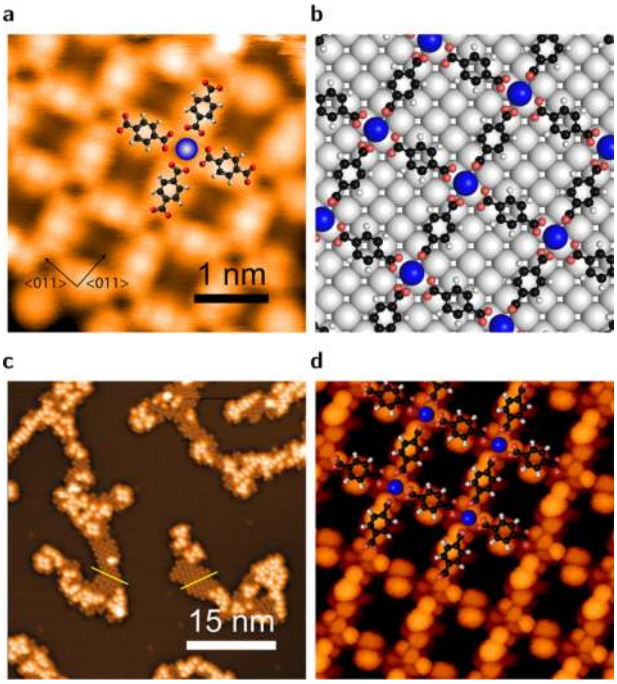

Figure 3. (a) High-resolution constant-current STM image of the Ho(TPA)$_2$/Ag(100)-$p(\sqrt{17} \times \sqrt{17})R14.04°$ checkerboard phase. Molecules and Ho atoms are superimposed to mark their positions. (b) DFT model for the checkerboard phase. (c) 200 nm × 200 nm STM image showing the extent of islands on the silver surface. The islands are rather small and decorated on the edges by excess Ho atoms. The yellow lines indicate the two domain orientations. (d) Simulated STM signature of the checkerboard structure.

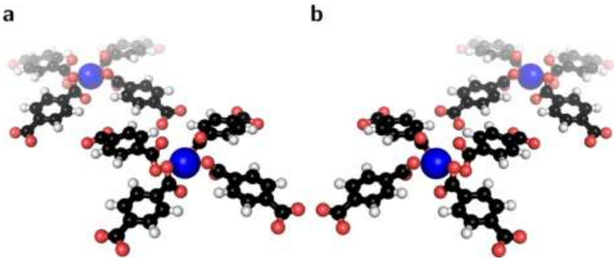

Figure 4. (a, b) Bonding environment in the mononuclear cloverleaf structure with the carboxylate linkers tilted by approximately 53° with respect to the molecular plane. As can be seen, the complex is chiral due to the concerted rotation of the carboxyl groups.

linkers reside with their phenyl rings on the hollow site of the Ag(100) surface and their long axis parallel to the ⟨011⟩ directions. This positioning is equivalent to that of TPA coordinated by Fe on Cu(100).[28] Assuming the hollow site for the phenyl ring is in accordance with previous findings of aromatic molecules on metal surfaces.[49−52] We substantiate this with our DFT calculations, as shown in Figure 2b.

The Ho atoms in the cloverleaf phase are 8-fold coordinated to the carboxylate ligands. This is a key difference with respect to the cloverleaf phase of TPA-Fe on Cu(100), where the iron is 4-fold coordinated. We assign this behavior to the rather ionic character of lanthanide−organic compounds featuring higher coordination numbers[53] and the increased surface area available for coordination in the case of Ho with significantly larger atomic diameter as compared to iron. A similar 8-fold coordination motif was reported for Gd atoms and TPA on Cu(111).[15] The rare earth atoms do not differ significantly in their chemical properties since the 4f-shell is located below the 6s^2 orbitals. The TPA molecules face the Ho atoms with one of their carboxylate groups, which must rotate out of the substrate plane for steric reasons. Studies of Dy-TPA architectures not involving DFT calculations were presented in terms of a coplanar orientation of the carboxylates.[32] However, our DFT calculations clearly reveal a concerted rotation of the functional groups in those structures, in agreement with Urgel *et al.*[15] DFT simulations of the proposed bonding model (more details for DFT calculations given below) yield a Ho−O distance of 2.3−2.4 Å and a Ho−C distance of 2.7 Å. These distances are in accordance with previous findings for gadolinium−carboxylate molecular assemblies, where the Gd−O distance was found to be 2.6 and 2.4−2.7 Å, as deduced from the experimental analysis and DFT calculations, respectively.[15]

As mentioned above, we propose an adsorption of the molecules at the hollow positions of the silver lattice and along the ⟨011⟩ directions. This results in a distance of 3.0−3.2 Å between the oxygen atoms of the uncoordinated carboxylate group and the hydrogen atoms of the molecule facing each other in a T-shape fashion. This distance suggests comparably weak lateral bonding. Thus, molecule−substrate interaction should dominate the forces on the uncoordinated functional group. Consistently, our DFT calculations demonstrate that the uncoordinated carboxylate groups act as anchors to the surface, as evident from the charge transfer analysis below.

More interesting are the possibilities for binding between neighboring molecules arranged next to each other in the same orientation and slightly shifted along their axis. Here, two hydrogen atoms are very close to each other (2.1 Å) and cause a repulsive force between the molecules. On the other hand, one of the free carboxylate oxygen atoms is close to one of the ortho-hydrogen atoms, and their distance of 3.0 Å would result in an attractive force caused by hydrogen bonding. These effects seem to balance each other out, leading to a configuration of the molecules as described above. Nonetheless, a slight shift and turn of the molecules would be compatible with our STM observations and would increase the H−H distance. In fact, the DFT calculations show a slight shift of the phenyl ring away from the hollow position, and thereby the H−H distance is increased to 2.2 Å.

When examining islands on a larger scale, we observed that the cloverleaf phase forms extended regular domains up to 200 nm in diameter. The limitation is presumably imposed by the size of the substrate terraces. Figure 2c depicts an overview image of a typical sample with an island of the cloverleaf phase highlighted by the yellow ellipsoid. We were able to get up to ~70% of the silver surface covered with the cloverleaf phase. This filling factor refers to the area fraction of the substrate covered with the cloverleaf phase, determined by STM topography images and averaged over several frames. Although the molecule density is lower than in the precursor phase, it was not possible to obtain a saturated monolayer. We associate this behavior with the desorption of molecules during the annealing step. The islands show a high regularity and nearly no defects. This indicates an effective self-correcting mechanism during the assembly of the metal−organic structure. Also after annealing the sample again to 450 K the islands persist and no significant desorption took place.

DOI: 10.1021/acsnano.8b06704
ACS Nano 2018, 12, 11552−11560

However, since all measurements were done at low temperatures, it is not possible to determine whether the islands are stable up to that temperature or whether they dissolve and re-form upon cooldown. The rest of the surface is bare silver or covered by a small amount of molecules (~2.5% of the entire surface), partly decorated by Ho clusters. In Figure 2c, the white ellipsoid indicates an area of the surface where these molecules can be seen. The molecules not participating in the cloverleaf phase are arranged in the purely organic transition phase described in the Supporting Information (darker protrusions in the white ellipsoid in Figure 2c). Some of these molecules have a Ho adatom adsorbed on their center (bright protrusions), presumably on the phenyl ring. Upon higher Ho dosage all additional molecules can be incoporated in Ho−adatom complexes, mostly consisting of four TPA molecules in a quadratic arrangement with four Ho atoms on top.

Checkerboard Phase. Increasing the Ho dosage applied to a precursor sample by a factor of 10 (~0.15 ML) leads to the formation of a different metal−organic phase. An exemplary STM image is shown in Figure 3a. The TPA molecules now interlink Ho centers, making the phase a MOCN, which we henceforth call checkerboard phase. Opposing molecules adsorb collinearly and exhibit uniform contrast, so an 8-fold coordination is present, with all oxygen atoms orientated toward the Ho atoms. This results in a stoichiometry of 1:2 of Ho:TPA. The close-up STM topography in Figure 3a clearly resolves the orientation of the molecules, as indicated by the overlaid TPA models. The phenyl ring appears as a round protrusion in the middle of two oval protrusions marking the positions of the carboxylate groups. Again, the Ho atoms do not produce visible features in STM, for the same reasons as discussed above for the cloverleaf phase. However, the positioning of the molecules can only be reconciled by the presence of Ho coordination centers.

A model of the checkerboard phase is reproduced in Figure 3b. Similar to the cloverleaf phase, the vectors of the unit cell are rotated with respect to those of the substrate. An analysis of the model reveals a $p(\sqrt{17} \times \sqrt{17})R14.04^\circ$ superstructure with a local molecule density of 0.12 molecule per silver atom. Its domains can be rotated both clockwise and counterclockwise with respect to the silver substrate. The end groups of the carboxylates are concertedly rotated in both network directions, similar to the cloverleaf phase, as evident from the DFT calculations. The latter also reveal that for Ho at hollow positions appreciable strain exists, which is understood as the reason that the Ho atoms are now moved to bridge sites. Also, the phenyl rings of the TPA molecules reside on the bridge positions of the Ag(100) surface. Figure 3c shows the expected two enantiomorphic structures in the bottom part of the image, where the two domain orientations are indicated by yellow lines.

It can also be seen in the figure that the island size is very small (strips of ~5 nm width) compared to the cloverleaf phase. A possible explanation is that due to the larger unit cell the silver substrate enforces upon the MOCN, the bond formation capability with the interconnecting nodes is impaired. This hypothesis is strongly corroborated by the DFT simulation as discussed later. We were not able to obtain coverages beyond approximately 15% of the surface with this phase, although we started off with a full monolayer of the precursor phase. The small islands always come with additional Ho atoms adsorbed on some of the molecules and show an anisotropic, ribbon-like growth. Again, the networks remain after reheating the sample to 450 K and subsequent cooldown.

A simulated STM image is shown in Figure 3d. The anisotropic differences in contrast could not be resolved *via* STM, probably due to unknown tip effects at such low bias voltages.

It has to be noted here that although the Ho dosage on the surface is 10 times higher than with the cloverleaf phase, the amount of anticipated Ho on the surface inferred from STM data (*cf.* Figure 3c) does not match the preparation stoichiometry. We propose a higher desorption of Ho−carboxylate complexes and clusters with Ho acting as an enhancing agent in the mechanism, although this is just a hypothesis and we cannot support this by other experiments or calculations. Decoration of step edges could also interfere.

DFT Analysis of Ho−TPA Networks. Dispersion-corrected DFT calculations were performed for periodic supercells of both structures. A free-standing overlayer of the checkerboard phase was allowed to freely adsorb on the metal slab to find the equilibrium adsorption geometry. This approach is similar to previous calculations on metal−carboxylate architectures on metal surfaces.[47,54] The calculations reveal a severe strain of the checkerboard structure, when stacked commensurably onto the Ag(100) surface. The silver lattice then imposes a Ho−Ho distance of 11.9 Å on the entire structure, while a free-standing layer of the structure would have a lattice periodicity of 11.4 Å. If the initial C_4-symmetric geometry with the Ho atom centered on the Ag(100)-hollow site is optimized toward an equilibrium structure, the geometry relaxation will always break the linker−Ho bond on one end of the TPA molecule (*cf.* Figures 4 and S4 in the Supporting Information). Figure 5 shows an intermediate 8-fold-coordinated MOCN structure with the Ho atom adsorbed on the hollow site and the directions of the forces acting on the respective atoms. The structure does not represent a global minimum of the potential energy surface, and the forces acting on the molecule would require to break open one or both carboxyl−Ho bonds to relieve the strain.

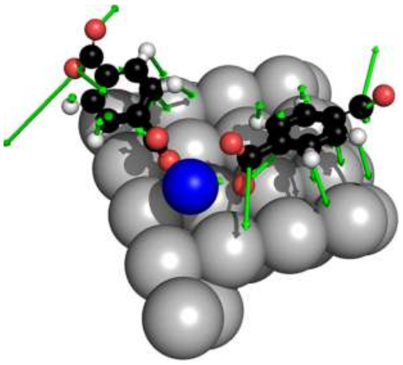

Figure 5. Forces (green vectors) acting on the linker molecules in the unrelaxed checkerboard structure where the Ho is still positioned in the hollow place (*cf.* Figure S4, H2). Magnitude of vectors not to scale.

A fully reticulated two-dimensional metal−organic framework could only be stabilized by allowing this symmetry breaking from the initially assumed C_4 to a C_2 symmetry axis centered on the Ho atom. The reduction in symmetry is

Table 1. Mulliken Charges of the Cloverleaf and Checkerboard Structures per Atom and per Unit Cell[a]

	cloverleaf				checkerboard		
charge	O^{surf}	O^{Ho}	Ho	Ag	O	Ho	Ag
e/atom	−0.32	−0.37	+1.17	+0.05	−0.36	+1.12	+0.01
e/cell	−2.54	−2.95	+1.17	+1.47	−2.90	+1.12	+0.46

[a] In the cloverleaf structure, two distinct species of oxygen atoms are present, the Ho-bonded O^{Ho} and the surface-anchored O^{surf}.

accompanied by the Ho atom leaving the Ag(100) hollow sites. This removes part of the strain in the structure, since the TPA molecule does not need to bend from one hollow site toward the next one. We assign this observed strain as the primary reason that the checkerboard pattern could only be observed in small band-shaped islands of less than 10 observable subunits in the shorter dimension, as opposed to MOCNs with commensurable registry.[12,36,48] A symmetry reduction is also discernible in the STM data, in the shape of the framework hollow sites, where either cushion-shaped C_4-, C_2-, or C_1-symmetric squares with concave arched edges are observed. This symmetry breaking due to substrate-induced stress is also reflected in the simulation. A Mulliken population analysis (as listed in Table 1 for Ho, Ag, and O) suggests charge transfer from the Ho atom toward the carboxylate linker atoms. Further electron density is depleted from the surface in the vicinity of the bonding node (*cf.* Figure 6).

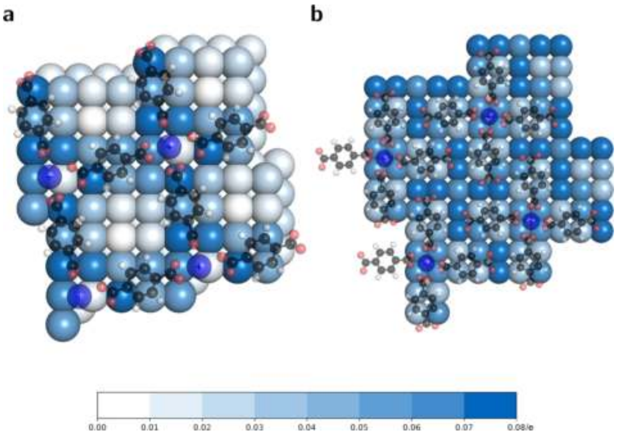

Figure 6. Hotspots of the charge transfer between the substrate and the adsorbate. Highlighted in blue are the areas of high electron depletion compared to white (no electron charge depletion) in fractions of *e*. Adsorbate shown without color coding for reference purposes.

The C_4-symmetric arrangement of the cloverleaf deduced from the experimental data is fully consistent with our calculations. The optimized geometries obtained for both the high-symmetry cloverleaf and the broken-symmetry checkerboard phase are stable minima of the potential energy surface with relaxed bond distances fully consistent with those derived from the STM measurements, thereby strongly supporting the structural models derived from the experimental data. The simulated STM images in Figures 2a and 3d indicate that the Ho site is transparent at the employed tunneling conditions, since the 4f eigenstates in both bonding environments lie at far too high and low energies with respect to E_F. Indeed, there is a local minimum seen at the interconnecting Ho nodes in the experimental data. Similar observations for different lanthanide atoms have already been reported elsewhere.[15] The smaller, yet bright protrusions around the central depression (Ho center) are clearly unoccupied states of the neighboring carboxylic oxygens, in our simulations presumably overdelocalized by the employed semilocal DFT functional.[55] To a much smaller extent the same signatures are also visible in some of the experimentally recorded images as shown in Figures 2a and 3a. The Mulliken population analysis shown in Table 1 for Ho, Ag, and two species of nonequivalent oxygen atoms suggests very similar values for the charge transfer from both the Ho and the substrate toward the carboxylate linkers. The charge transfer from the substrate occurs primarily at two points: the anchor points of the dangling carboxylate linkers and at the Ho node (*cf.* Figure 6). In contrast to the cloverleaf structure, all carboxylate groups in the checkerboard pattern are rotated out of plane to accommodate the bonding environment and effectively reduce the charge transfer. The charges do not add up to zero, because only atoms with charge transfer to the surface are listed here.

CONCLUSIONS

In conclusion, two different types of thermally robust molecular architectures of TPA and Ho on the Ag(100) surface were fabricated by finely tuning the deposition parameters. We were able to build up enantiomorphic islands of mononuclear lanthanide−carboxylate compounds with $Ho(TPA)_4/Ag(100)\text{-}p(\sqrt{29} \times \sqrt{29})R21.8°$ structure, high lateral extent, surface coverage, and low defect density. Reticulated MOCNs have a $Ho(TPA)_2/Ag(100)\text{-}p(\sqrt{17} \times \sqrt{17})R14.04°$ structure and feature reduced island sizes due to interfacial strain effects. The two observed metal−organic architectures are both chiral, due to a rotation of the superstructure with respect to the silver lattice and a concerted rotation of the carboxylates. In the case of the cloverleaf phase conformational chirality is also present. These structural models receive further support by DFT calculations, which identified high strain as a potential reason for the limited extent to which the checkerboard phase could be grown experimentally. The chiral signature of the Ho coordination sphere could afford intriguing new magnetic features. Additionally, our DFT calculations give insight into the charge redistribution within the molecular architectures. Stabilization of single Ho atoms with 8-fold coordination in the cloverleaf structure is a particularly promising approach to exploit the recently found magnetic properties of Ho atoms on surfaces without being hampered by the onset of Ho diffusion at low temperatures. This work shows that Ho can be stably deployed as single atoms on surfaces, which opens up the possibility to investigate the nanomagnetic properties of Ho in a well-defined molecular environment, *e.g.*, by means of X-ray magnetic circular dichroism. The possibility to grow insulating decoupling layers such as NaCl or MgO on Ag(100) provides prospects to tune their magnetic properties *via* supramolecular on-surface engineering, and a comparison of Ho−carboxylates on both MgO and Ag will give further insight into this intriguing field of research.

METHODS

Experimental Details. Measurements were performed under ultra-high-vacuum conditions (base pressure below 2.0×10^{-11} mbar) with a commercial Joule-Thomson-STM from SPECS. For this work experiments were carried out at 4.5 K. All shown images were taken in constant current mode using electrochemically etched tungsten tips that were cleaned by Ar-ion sputtering and field emission on a clean silver surface. The bias voltage was applied to the sample.

Samples were prepared by repeated cycles of Ar-ion ($U = 0.9$ kV) sputtering and annealing at 500 °C. We used a Ag(100) crystal from Surface Preparation Laboratory. The TPA molecules were purchased from Fluka (purity ≥99%) and evaporated from a home-built quartz crucible Knudsen cell at a temperature of 160 °C. Prior to preparation the molecules were degassed for purification extensively. The Ho atoms were evaporated *via* a home-built foil evaporator (see Supporting Information). The sample temperatures were measured *via* a thermocouple directly on the crystal.

Computational Details. Dispersion-corrected DFT calculations were performed for periodic supercells with the FHI-aims[56] computing package. Geometry optimizations for the smallest possible surface unit cell comprising two (four for cloverleaf) TPA molecules and one atom of Ho were performed with FHI-aims at "tight" computational settings ("light" for Ag), 3 × 3 × 1 k-point sampling, and using a 30 Å vacuum region. In these calculations electronic exchange and correlation was treated on the generalized-gradient approximation level with the PBE[55] functional, augmented by dispersive interactions through the Tkatchenko−Scheffler $\mathrm{TS}^{\mathrm{surf}}$ method.[57] In order to improve the description of the strong local coulomb interaction of the 4f electrons, a Hubbard-type correction (DFT+U) was employed. The value of $U = 5.8$ eV for the Ho 4f states was chosen to reproduce the energetic splitting of occupied and unoccupied states of a model $\mathrm{Ho[OAc]_3}$ complex treated on the HSE06[58] level (details given in the Supporting Information). The metal−organic compound was fully relaxed until residual forces were below 2.5×10^{-3} eV/Å. The cell size was chosen to match integer multiples of the optimal lattice constant for bulk silver as obtained by a fit to the Birch−Murnaghan equation of state. The experimental results suggest a $\sqrt{17} \times \sqrt{17}R14.0°$ conformation for the checkerboard pattern and a $\sqrt{29} \times \sqrt{29}R21.8°$ conformation for the cloverleaf pattern. The Ho−Ho distance thus determines the repetition unit, and the required metal surface unit cell was adapted to form a closed surface (4 × 4 for checkerboard and 5 × 5 for cloverleaf, respectively). In the geometry optimizations of the checkerboard structure the first metal slab layer was allowed to relax. For the larger cloverleaf pattern only one fixed layer of Ag was used to mimic a metal support. For the optimized geometries, the Tersoff−Hamann approach[59] was employed to simulate STM images, providing a means of directly comparing the electronic structure of the obtained geometry to the experimental signature. Integration over all electronic density of states within 20 meV around the metallic Fermi level produced the final image. The obtained images were smoothened using the rolling ball algorithm[60] with a ball radius of 0.5 Å.

ASSOCIATED CONTENT

Supporting Information

The Supporting Information is available free of charge on the ACS Publications website at DOI: 10.1021/acsnano.8b06704.

> Organic transition phase, chirality of Ho−$\mathrm{TPA_4}$ complexes, determination of the U-value, structural relaxation details, node bonding environment, experimental details (PDF)

AUTHOR INFORMATION

Corresponding Authors

*E-mail: florian.klappenberger@tum.de.
*E-mail: jvb@tum.de.

ORCID

Martin Uphoff: 0000-0003-3480-4632
Georg S. Michelitsch: 0000-0003-2392-9413
Karsten Reuter: 0000-0001-8473-8659
Harald Brune: 0000-0003-4459-3111
Florian Klappenberger: 0000-0002-2877-6105
Johannes V. Barth: 0000-0002-6270-2150

Author Contributions

§M. Uphoff and G. S. Michelitsch contributed equally to this work.

Notes

The authors declare no competing financial interest.

ACKNOWLEDGMENTS

This work has been funded by the German Excellence Initiative and the European Union Seventh Framework Programme, under support of the Technische Universität München and its Institute for Advanced Study under grant agreement no. 291763. Funding was also provided by the ERC Advanced Grant MolArt (grant no. 247299) and the German Research Foundation via KL 2294/6-1 and is gratefully acknowledged. G.S.M. and K.R. gratefully acknowledge the Gauss Centre for Supercomputing e.V. (www.gauss-centre.eu) for funding this project by providing computing time on the GCS Supercomputer SuperMUC at Leibniz Supercomputing Centre (www.lrz.de) under grant no. PR92ME.

REFERENCES

(1) Bünzli, J.-C. G. Review: Lanthanide Coordination Chemistry: From Old Concepts to Coordination Polymers. *J. Coord. Chem.* **2014**, *67*, 3706−3733.

(2) Reineke, T. M.; Eddaoudi, M.; Fehr, M.; Kelley, D.; Yaghi, O. M. From Condensed Lanthanide Coordination Solids to Microporous Frameworks Having Accessible Metal Sites. *J. Am. Chem. Soc.* **1999**, *121*, 1651−1657.

(3) Pan, L.; Adams, K. M.; Hernandez, H. E.; Wang, X.; Zheng, C.; Hattori, Y.; Kaneko, K. Porous Lanthanide-Organic Frameworks: Synthesis, Characterization, and Unprecedented Gas Adsorption Properties. *J. Am. Chem. Soc.* **2003**, *125*, 3062−3067.

(4) Qin, C.; Wang, X.-L.; Wang, E.-B.; Su, Z.-M. A Series of Three-Dimensional Lanthanide Coordination Polymers with Rutile and Unprecedented Rutile-Related Topologies. *Inorg. Chem.* **2005**, *44*, 7122−7129.

(5) Long, D.-L.; Blake, A. J.; Champness, N. R.; Wilson, C.; Schröder, M. Lanthanum Coordination Networks Based on Unusual Five-Connected Topologies. *J. Am. Chem. Soc.* **2001**, *123*, 3401−3402.

(6) Long, D.-L.; Hill, R. J.; Blake, A. J.; Champness, N. R.; Hubberstey, P.; Proserpio, D. M.; Wilson, C.; Schröder, M. Non-Natural Eight-Connected Solid-State Materials: A New Coordination Chemistry. *Angew. Chem., Int. Ed.* **2004**, *43*, 1851−1854.

(7) Long, D.-L.; Blake, A. J.; Champness, N. R.; Wilson, C.; Schröder, M. Unprecedented Seven- and Eight-Connected Lanthanide Coordination Networks. *Angew. Chem., Int. Ed.* **2001**, *40*, 2443−2447.

(8) Écija, D.; Auwärter, W.; Vijayaraghavan, S.; Seufert, K.; Bischoff, F.; Tashiro, K.; Barth, J. V. Assembly and Manipulation of Rotatable Cerium Porphyrinato Sandwich Complexes on a Surface. *Angew. Chem., Int. Ed.* **2011**, *50*, 3872−3877.

(9) Cirera, B.; Björk, J.; Otero, R.; Gallego, J. M.; Miranda, R.; Ecija, D. Efficient Lanthanide Catalyzed Debromination and Oligomeric Length-Controlled Ullmann Coupling of Aryl Halides. *J. Phys. Chem. C* **2017**, *121*, 8033−8041.

(10) Bischoff, F.; Seufert, K.; Auwärter, W.; Seitsonen, A. P.; Heim, D.; Barth, J. V. Metalation of Porphyrins by Lanthanide Atoms at Interfaces: Direct Observation and Stimulation of Cerium Coordination to 2H-TPP/Ag(111). *J. Phys. Chem. C* **2018**, *122*, 5083−5092.

(11) Hellwig, R.; Uphoff, M.; Paintner, T.; Björk, J.; Ruben, M.; Klappenberger, F.; Barth, J. V. Ho-Mediated alkyne reactions at low temperatures on Ag(111). *Chem. - Eur. J.* **2018**, DOI: 10.1002/chem.201803102.

(12) Écija, D.; Urgel, J. I.; Papageorgiou, A. C.; Joshi, S.; Auwärter, W.; Seitsonen, A. P.; Klyatskaya, S.; Ruben, M.; Fischer, S.; Vijayaraghavan, S.; Reichert, J.; Barth, J. V. Five-Vertex Archimedean Surface Tessellation by Lanthanide-Directed Molecular Self-Assembly. *Proc. Natl. Acad. Sci. U. S. A.* **2013**, *110*, 6678−6681.

(13) Urgel, J. I.; Ecija, D.; Auwärter, W.; Barth, J. V. Controlled Manipulation of Gadolinium-Coordinated Supramolecules by Low-Temperature Scanning Tunneling Microscopy. *Nano Lett.* **2014**, *14*, 1369−1373.

(14) Urgel, J. I.; Ecija, D.; Auwärter, W.; Papageorgiou, A. C.; Seitsonen, A. P.; Vijayaraghavan, S.; Joshi, S.; Fischer, S.; Reichert, J.; Barth, J. V. Five-Vertex Lanthanide Coordination on Surfaces: A Route to Sophisticated Nanoarchitectures and Tessellations. *J. Phys. Chem. C* **2014**, *118*, 12908−12915.

(15) Urgel, J. I.; Cirera, B.; Wang, Y.; Auwärter, W.; Otero, R.; Gallego, J. M.; Alcamí, M.; Klyatskaya, S.; Ruben, M.; Martín, F.; Miranda, R.; Ecija, D.; Barth, J. V. Surface-Supported Robust 2d Lanthanide-Carboxylate Coordination Networks. *Small* **2015**, *11*, 6358−6364.

(16) Écija, D.; Urgel, J. I.; Seitsonen, A. P.; Auwärter, W.; Barth, J. V. Lanthanide-Directed Assembly of Interfacial Coordination Architectures−from Complex Networks to Functional Nanosystems. *Acc. Chem. Res.* **2018**, *51*, 365−375.

(17) Ishikawa, N.; Sugita, M.; Ishikawa, T.; Koshihara, S.-Y.; Kaizu, Y. Lanthanide Double-Decker Complexes Functioning As Magnets at the Single-Molecular Level. *J. Am. Chem. Soc.* **2003**, *125*, 8694−8695.

(18) Gatteschi, D.; Sessoli, R.; Villain, J. *Molecular Nanomagnets*; Oxford University, 2006.

(19) Kyatskaya, S.; Galán Mascarós, J. R.; Bogani, L.; Hennrich, F.; Kappes, M.; Wernsdorfer, W.; Ruben, M. Anchoring of Rare-Earth-Based Single-Molecule Magnets on Single-Walled Carbon Nanotubes. *J. Am. Chem. Soc.* **2009**, *131*, 15143−15151.

(20) Rinehart, J. D.; Long, J. R. Exploiting Single-Ion Anisotropy in the Design of f-Element Single-Molecule Magnets. *Chem. Sci.* **2011**, *2*, 2078−2085.

(21) Westerström, R.; Dreiser, J.; Piamonteze, C.; Muntwiler, M.; Weyeneth, S.; Brune, H.; Rusponi, S.; Nolting, F.; Popov, A.; Yang, S.; Dunsch, L.; Greber, T. An Endohedral Single-Molecule Magnet with Long Relaxation Times: Dysc2n@c80. *J. Am. Chem. Soc.* **2012**, *134*, 9840−9843.

(22) Layfield, R. A. Organometallic Single-Molecule Magnets. *Organometallics* **2014**, *33*, 1084−1099.

(23) Liddle, S. T.; van Slageren, J. Improving F-Element Single Molecule Magnets. *Chem. Soc. Rev.* **2015**, *44*, 6655−6669.

(24) Donati, F.; Rusponi, S.; Stepanow, S.; Wäckerlin, C.; Singha, A.; Persichetti, L.; Baltic, R.; Diller, K.; Patthey, F.; Fernandes, E.; Dreiser, J.; Šljivančanin, Ž.; Kummer, K.; Nistor, C.; Gambardella, P.; Brune, H. Magnetic Remanence in Single Atoms. *Science* **2016**, *352*, 318−321.

(25) Natterer, F. D.; Yang, K.; Paul, W.; Willke, P.; Choi, T.; Greber, T.; Heinrich, A. J.; Lutz, C. P. Reading and Writing Single-Atom Magnets. *Nature* **2017**, *543*, 226−228.

(26) Natterer, F. D.; Donati, F.; Patthey, F.; Brune, H. Thermal and Magnetic-Field Stability of Holmium Single-Atom Magnets. *Phys. Rev. Lett.* **2018**, *121*, DOI: 10.1103/PhysRevLett.121.027201.

(27) Franke, K. J.; Schulze, G.; Pascual, J. I. Competition of Superconducting Phenomena and Kondo Screening at the Nanoscale. *Science* **2011**, *332*, 940−944.

(28) Gambardella, P.; Stepanow, S.; Dmitriev, A.; Honolka, J.; de Groot, F. M. F.; Lingenfelder, M.; Gupta, S. S.; Sarma, D. D.; Bencok, P.; Stanescu, S.; Clair, S.; Pons, S.; Lin, N.; Seitsonen, A. P.; Brune, H.; Barth, J. V.; Kern, K. Supramolecular Control of the Magnetic Anisotropy in Two-Dimensional High-Spin Fe Arrays at a Metal Interface. *Nat. Mater.* **2009**, *8*, 189−193.

(29) Barth, J. V. Molecular Architectonic on Metal Surfaces. *Annu. Rev. Phys. Chem.* **2007**, *58*, 375−407.

(30) Barth, J. V. Fresh Perspectives for Surface Coordination Chemistry. *Surf. Sci.* **2009**, *603*, 1533−1541.

(31) Suzuki, T.; Lutz, T.; Payer, D.; Lin, N.; Tait, S. L.; Costantini, G.; Kern, K. Substrate Effect on Supramolecular Self-Assembly: From Semiconductors to Metals. *Phys. Chem. Chem. Phys.* **2009**, *11*, 6498−6504.

(32) Cirera, B.; Đorđević, L.; Otero, R.; Gallego, J. M.; Bonifazi, D.; Miranda, R.; Ecija, D. Dysprosium-Carboxylate Nanomeshes with Tunable Cavity Size and Assembly Motif through Ionic Interactions. *Chem. Commun.* **2016**, *52*, 11227−11230.

(33) Stepanow, S.; Strunskus, T.; Lingenfelder, M.; Dmitriev, A.; Spillmann, H.; Lin, N.; Barth, J. V.; Wöll, C.; Kern, K. Deprotonation-Driven Phase Transformations in Terephthalic Acid Self-Assembly on Cu(100). *J. Phys. Chem. B* **2004**, *108*, 19392−19397.

(34) Wäckerlin, C.; Donati, F.; Singha, A.; Baltic, R.; Rusponi, S.; Diller, K.; Patthey, F.; Pivetta, M.; Lan, Y.; Klyatskaya, S.; Ruben, M.; Brune, H.; Dreiser, J. Giant Hysteresis of Single-Molecule Magnets Adsorbed on a Nonmagnetic Insulator. *Adv. Mater.* **2016**, *28*, 5195−5199.

(35) Dmitriev, A.; Spillmann, H.; Lin, N.; Barth, J. V.; Kern, K. Modular Assembly of Two-Dimensional Metal−organic Coordination Networks at a Metal Surface. *Angew. Chem.* **2003**, *115*, 2774−2777.

(36) Lingenfelder, M. A.; Spillmann, H.; Dmitriev, A.; Stepanow, S.; Lin, N.; Barth, J. V.; Kern, K. Towards Surface-Supported Supramolecular Architectures: Tailored Coordination Assembly of 1,4-Benzenedicarboxylate and Fe on Cu(100). *Chem. - Eur. J.* **2004**, *10*, 1913−1919.

(37) Barth, J. V.; Costantini, G.; Kern, K. Engineering Atomic and Molecular Nanostructures at Surfaces. *Nature* **2005**, *437*, 671.

(38) Payer, D.; Comisso, A.; Dmitriev, A.; Strunskus, T.; Lin, N.; Wöll, C.; DeVita, A.; Barth, J.; Kern, K. Ionic Hydrogen Bonds Controlling Two-dimensional Supramolecular Systems at a Metal Surface. *Chem. - Eur. J.* **2007**, *13*, 3900−3906.

(39) Klappenberger, F.; Arras, E.; Seitsonen, A. P.; Barth, J. V. Nature of the Attractive Interaction between Proton Acceptors and Organic Ring Systems. *Phys. Chem. Chem. Phys.* **2012**, *14*, 15995−16001.

(40) Jeffrey, G. A. *An Introduction to Hydrogen Bonding*; Oxford University Press, 1997.

(41) Cañas-Ventura, M. E.; Klappenberger, F.; Clair, S.; Pons, S.; Kern, K.; Brune, H.; Strunskus, T.; Wöll, C.; Fasel, R.; Barth, J. V. Coexistence of One- and Two-Dimensional Supramolecular Assemblies of Terephthalic Acid on Pd(111) Due to Self-Limiting Deprotonation. *J. Chem. Phys.* **2006**, *125*, 184710.

(42) Clair, S.; Pons, S.; Seitsonen, A. P.; Brune, H.; Kern, K.; Barth, J. V. Stm Study of Terephthalic Acid Self-Assembly on Au(111): Hydrogen-Bonded Sheets on an Inhomogeneous Substrate. *J. Phys. Chem. B* **2004**, *108*, 14585−14590.

(43) Lin, N.; Dmitriev, A.; Weckesser, J.; Barth, J. V.; Kern, K. Real-Time Single-Molecule Imaging of the Formation and Dynamics of Coordination Compounds. *Angew. Chem., Int. Ed.* **2002**, *41*, 4779−4783.

(44) Messina, P.; Dmitriev, A.; Lin, N.; Spillmann, H.; Abel, M.; Barth, J. V.; Kern, K. Direct Observation of Chiral Metal-Organic Complexes Assembled on a Cu(100) Surface. *J. Am. Chem. Soc.* **2002**, *124*, 14000−14001.

(45) Mugarza, A.; Lorente, N.; Ordejón, P.; Krull, C.; Stepanow, S.; Bocquet, M.-L.; Fraxedas, J.; Ceballos, G.; Gambardella, P. Orbital Specific Chirality and Homochiral Self-Assembly of Achiral Molecules Induced by Charge Transfer and Spontaneous Symmetry Breaking. *Phys. Rev. Lett.* **2010**, *105*, DOI: 10.1103/PhysRevLett.105.115702.

(46) Liu, C.; Cohen, J.; Adams, J.; Voter, A. EAM Study of Surface Self-Diffusion of Single Adatoms of Fcc Metals Ni, Cu, Al, Ag, Au, Pd, and Pt. *Surf. Sci.* **1991**, *253*, 334−344.

(47) Clair, S.; Pons, S.; Fabris, S.; Baroni, S.; Brune, H.; Kern, K.; Barth, J. V. Monitoring Two-Dimensional Coordination Reactions:

Directed Assembly of Co−terephthalate Nanosystems on Au(111). *J. Phys. Chem. B* **2006**, *110*, 5627−5632.

(48) Stepanow, S.; Lin, N.; Payer, D.; Schlickum, U.; Klappenberger, F.; Zoppellaro, G.; Ruben, M.; Brune, H.; Barth, J. V.; Kern, K. Surface-Assisted Assembly of 2d Metal−organic Networks That Exhibit Unusual Threefold Coordination Symmetry. *Angew. Chem., Int. Ed.* **2007**, *46*, 710−713.

(49) Hallmark, V. M.; Chiang, S.; Meinhardt, K.-P.; Hafner, K. Observation and Calculation of Internal Structure in Scanning Tunneling Microscopy Images of Related Molecules. *Phys. Rev. Lett.* **1993**, *70*, 3740−3743.

(50) Chiang, S. Scanning Tunneling Microscopy Imaging of Small Adsorbed Molecules on Metal Surfaces in an Ultrahigh Vacuum Environment. *Chem. Rev.* **1997**, *97*, 1083−1096.

(51) Lee, A. F.; Lambert, R. M.; Goldoni, A.; Baraldi, A.; Paolucci, G. On the Coverage-Dependent Adsorption Geometry of Benzene Adsorbed on Pd111: A Study by Fast XPS and NEXAFS. *J. Phys. Chem. B* **2000**, *104*, 11729−11733.

(52) Robledo, M.; Pacchioni, G.; Martín, F.; Alcamí, M.; Díaz-Tendero, S. Adsorption of Benzene on Cu(100) and on Cu(100) Covered with an Ultrathin Nacl Film: Molecule−substrate Interaction and Decoupling. *J. Phys. Chem. C* **2015**, *119*, 4062−4071.

(53) Cotton, S. *Lanthanide and Actinide Chemistry*; John Wiley and Sons, Ldt., 2006.

(54) Seitsonen, A. P.; Lingenfelder, M.; Spillmann, H.; Dmitriev, A.; Stepanow, S.; Lin, N.; Kern, K.; Barth, J. V. Density Functional Theory Analysis of Carboxylate-Bridged Diiron Units in Two-Dimensional Metal−Organic Grids. *J. Am. Chem. Soc.* **2006**, *128*, 5634−5635.

(55) Perdew, J. P.; Burke, K.; Ernzerhof, M. Generalized Gradient Approximation Made Simple. *Phys. Rev. Lett.* **1996**, *77*, 3865−3868.

(56) Blum, V.; Gehrke, R.; Hanke, F.; Havu, P.; Havu, V.; Ren, X.; Reuter, K.; Scheffler, M. Ab Initio Molecular Simulations with Numeric Atom-Centered Orbitals. *Comput. Phys. Commun.* **2009**, *180*, 2175−2196.

(57) Ruiz, V. G.; Liu, W.; Zojer, E.; Scheffler, M.; Tkatchenko, A. Density-Functional Theory with Screened Van Der Waals Interactions for the Modeling of Hybrid Inorganic-Organic Systems. *Phys. Rev. Lett.* **2012**, *108*, 146103.

(58) Krukau, A. V.; Vydrov, O. A.; Izmaylov, A. F.; Scuseria, G. E. Influence of the Exchange Screening Parameter on the Performance of Screened Hybrid Functionals. *J. Chem. Phys.* **2006**, *125*, 224106.

(59) Tersoff, J.; Hamann, D. R. Theory of the Scanning Tunneling Microscope. *Phys. Rev. B: Condens. Matter Mater. Phys.* **1985**, *31*, 805−813.

(60) Shrake, A.; Rupley, J. Environment and Exposure to Solvent of Protein Atoms. Lysozyme and Insulin. *J. Mol. Biol.* **1973**, *79*, 351−371.

Supporting Information: Assembly of Robust Holmium-Directed 2D Metal-Organic Coordination Complexes and Networks on the Ag(100) Surface

Martin Uphoff,†,§ Georg S. Michelitsch,‡,§ Raphael Hellwig,† Karsten Reuter,‡
Harald Brune,¶ Florian Klappenberger,*,† and Johannes V. Barth*,†

†*Department of Physics (E20), Technische Universität München, James-Franck-Str. 1, 85748 Garching, Germany*

‡*Department of Chemistry, Chair of Theoretical Chemistry, Technische Universität München, Lichtenbergstr. 4, 85748 Garching, Germany*

¶*Institute of Physics, Ecole Polytechnique Fédérale de Lausanne (EPFL), Station 3, 1015 Lausanne, Switzerland*

§*Contributed equally to this work*

E-mail: florian.klappenberger@tum.de; jvb@tum.de

Organic transition phase

Figure S1(a). shows the organic transition phase, that is formed by deprotonated TPA for low coverages. The phase exhibits a nearly quadratic unit cell of 8.4(1) Å×8.2(2) Å, measured along the slow and fast scanning axis, respectively. The error is calculated from the standard deviation. The islands have no fixed angle in orientation with respect to the lattice and the distances measured do not show any obvious connection to the lattice vectors. Whilst the difference in the two directions could be drift, it it also likely that the unit cell is indeed not perfectly quadratic. One reason for this is the orientation of the carboxylates, whereby depressions on the edges indicate the deprotonated carboxyl groups (Figure S1(b)). Hence, the molecules are all aligned in the same direction as integral TPA does on metal surfaces[S1]. Since the deprotonated molecule is shorter compared to pristine TPA, it is more difficult to determine if the unit cell is quadratic or rhombohedral. Secondly, the distances between the molecules differ from case to case (even when measured in the same frame). Thirdly, the phase is growing in chains with a width of two to three molecules rather than extended islands. They also can have slight bends. A strictly defined unit cell would not allow this behavior. The fact, that the phase only occurs in these small islands and smoothly connects to the precursor phase (c.f. Figure 1 in the manuscript) indicates it as being a transition phase between single molecules on the surface and extended islands of the precursor phase. Compared to inter-molecular interactions, the molecule-substrate interaction plays a more significant role for the formation of the full monolayer precursor phase, where in every other row the molecules turn by roughly 90° forming the T-facing structure of the precursor phase. Hence, the term transition phase is used.

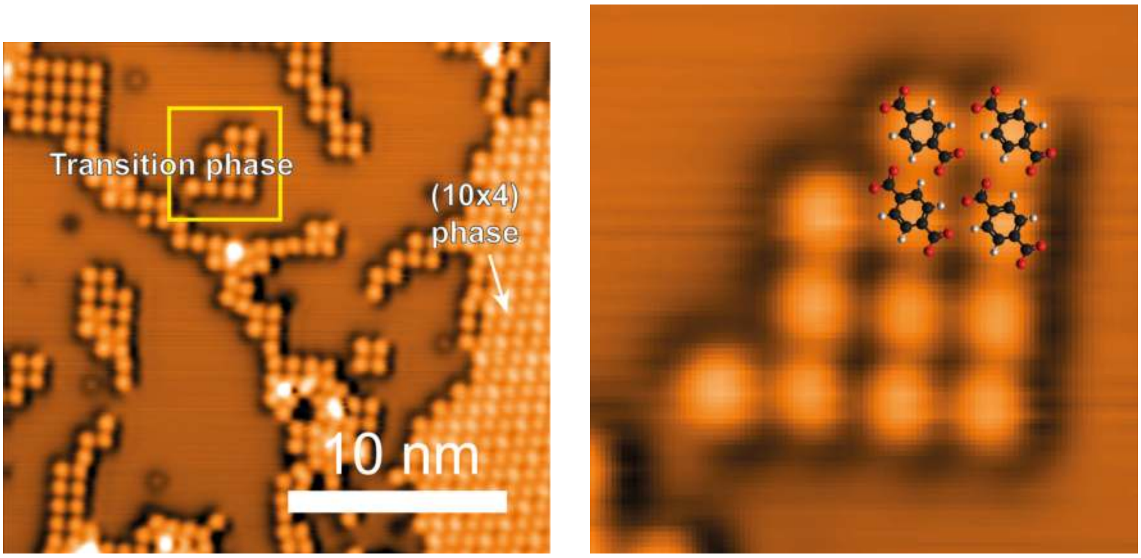

(a) **(b)**

Figure S1: (a) STM image ($I_T = 100\,\text{pA}, V_B = 1\,\text{V}$) of the transition phase (left) next to (10×4) precursor phase (right). The yellow square shows the area enlarged in (b). (b) Enlargement of (a). The depressions on the molecules indicate the position of the carboyxyl groups, revealing a parallel orientation of the molecules.

Chirality of Ho-TPA$_4$ complexes

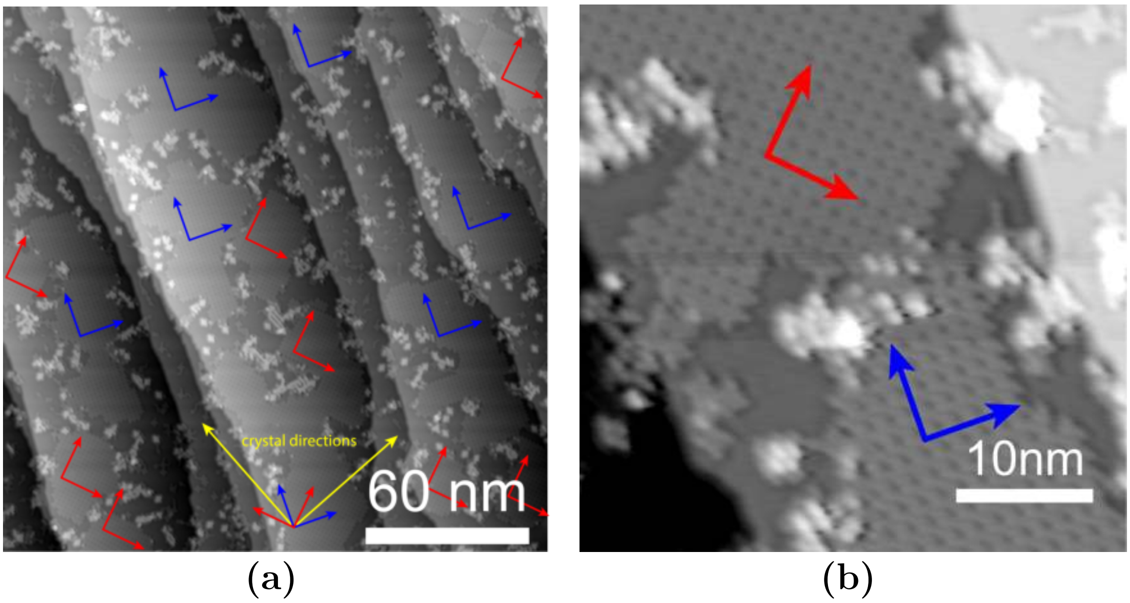

(a) (b)

Figure S2: Constant current STM images showing islands of the cloverleaf phase. There are two directions of growth, indicated by the rectangle arrow pairs in blue or red.

Ho-evaporator

The Ho used in the experiments was evaporated via a foil evaporator. A thin Ho foil (purity= 99.9 %, *Merck*) is heated up by applying a high current, high frequency RF voltage. Due to water cooling of the evaporator, only the foil heats up and emits Ho atoms and clusters of high purity.

Holmium coverage definition

Since Ho is significantly bigger than silver, a full ML of Ho will contain less atoms than a full ML of silver. Additionally, the Ag(100) surface has a quadratic unit cell whilst Ho crystallizes in the hexagonal closed packed structure. This gives a density of 0.652 Ho atoms per silver atom, assuming a full ML. All Ho coverages in this work refer to a full ML of

Ho in the (0001) surface covering the same silver area with a (100) surface. The deposition parameters were calibrated via deposition of Ho on a Ag(111) surface fully covered with Hexakis((trimethylsilyl)ethynyl)benzene (HEB), where Ho adsorbs as single atoms on the phenyl rings of the molecule and are easily countable.

Drift correction

Since STM data has a slow and a fast scan direction, piezo drift will cause a distortion of the images with different magnitudes to each direction. It is essential to overcome this obstacle especially when measuring unit cell sizes of superstructures without having atomic resolution at the same time. A precise calibration of the piezos is obviously essential for corrected length scales of STM data, but the drift effect will nevertheless remain present at all times. A simple and reliable method is to rotate the scan directions by 90° and compare the distorsions. While the calculation of the correction parameters is quite complicated manually, we used the MATLAB script from C. Ophus et al. to calculate the corrected images[S2].

Determination of the U-value

The U-value was determined by optimizing the geometry of $Ho[OAc]_3$ and determining the energetic difference between the occupied and unoccupied *4f* states. Then, the same system was simulated using DFT+U for different values of U and the optimal value determined via a linear fit as shown on the right in Figure S3.

Structural relaxation details

As mentioned in the main manuscript, the checkerboard structure exhibits a large strain as the metal support enforces a cell geometry upon the adsorbate. This is supported by the

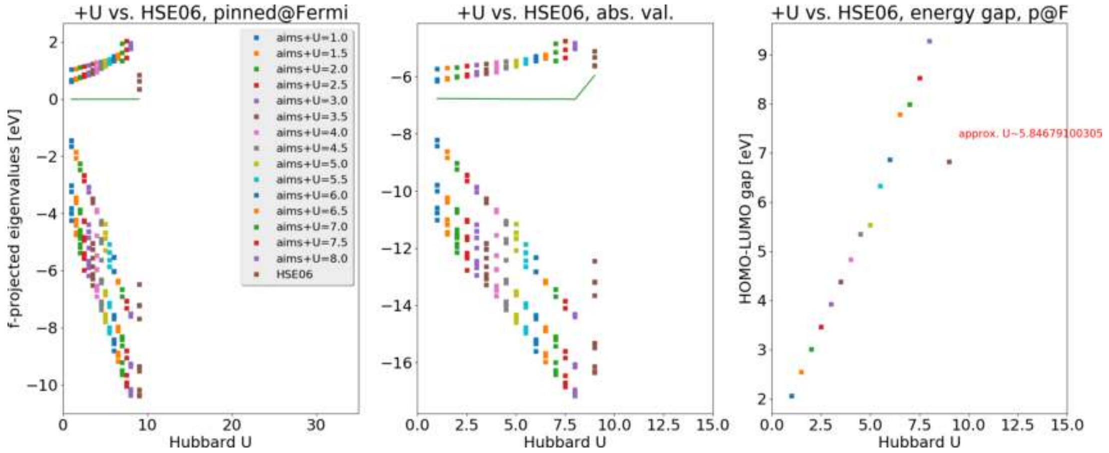

Figure S3: DFT+U screening for a suitable value to reproduce the energetic splitting between the occupied and unoccupied *4f* orbitals in the system. (fltr.: normalized to Fermi-level, absolute values, and the linear fit)

experimental observation of only small islands and stripes of this particular bonding environment. The theoretical modeling of the geometry focused on two different arrangements, where the Ho-atom is located at the hollow (**H1**,**H2**) and bridge (**B**) site, respectively. Relaxation of the first layer of Ag-atoms was permitted. The main features of the experimental STM signature are reproduced by structural models **H2** and **B**. However, the structural model **H2** does not describe a strain-free structure as the largest forces observed exceed 60 meV/Å. Furthermore, although only very small differences are present, the formation energy of structural model **B** is higher than the other two, hinting towards increased thermodynamic stability. The difficulty in assigning a structural model to the *checkerboard* structure supports the experimental observation of the preferred formation of the *cloverleaf* structure instead.

Node bonding environment

The bonding of the carboxylate linkers to the Ho node follows the same motive as already reported for similar Gd-complexes.[S3] Our DFT simulations predict in both observed surface-networks an eight-fold coordination with the carboxylate linker tilted by 52.4 - 53.9° (clover-

STM-simulation & overlay	**structure**	**comments**
H1 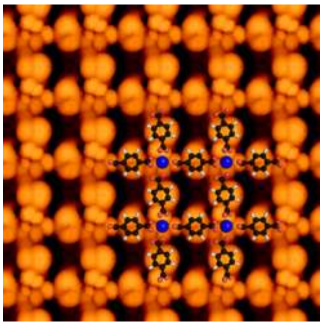	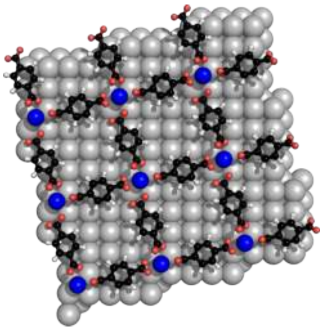	• Ho on hollow-site • $f_{max} < 0.025$ eV/Å • $\Delta E = 147.7$ meV • one TPA is only linked via one O atom to the Ho-atom, which leads to a non-checkerboard pattern observed in the corresponding Tersoff-Haman signatures
H2 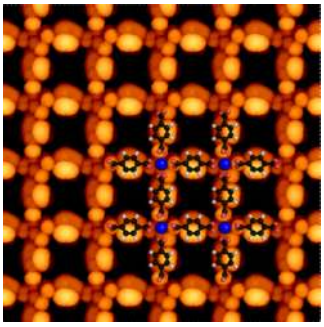	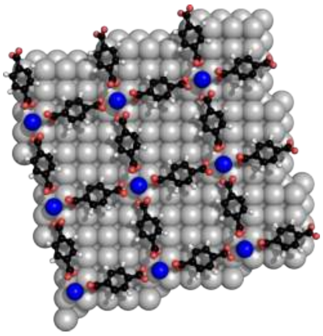	• Ho on hollow-site • $f_{max} <$ **0.060** eV/Å • $\Delta E = 144.3$ meV • In an unstable structure, both TPA molecules would link in a C_4 symmetric fashion to the Ho linker atom. The system shown experiences forces of **60 meV/Å**.
B 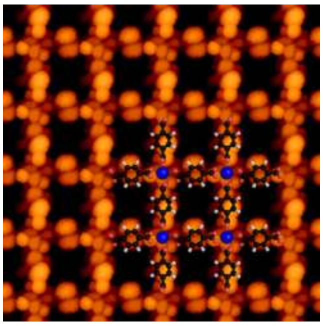	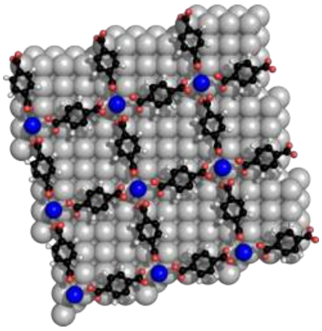	• Ho on bridge-site • $f_{max} < 0.025$ eV/Å • $\Delta E = 147.8$ meV • both TPA molecules are linked in a C_2 symmetric fashion to the Ho linker atom. The system experiences remaining forces up to 25 meV/Å and the STM signatures correspond to the experimental observation.

Figure S4: The different models for the checkerboard structure considered in the DFT simulations.

leaf) and 40.8 - 105° (checkerboard) out-of-plane with respect to the linker backbone. The average bond distance of Ho and O is 2.4Å (cloverleaf) and 2.6Å (checkerboard). A side-view of the bonding environment is given in Figure 5. Also shown in Figure 5 are the forces acting on the individual atoms in the non-equilibrium checkerboard-structure **H2** from Figure S4. The arrows point away from the Ho node, suggesting that an equilibrium would only be reached by detachment from the metal center.

References

(S1) Clair, S.; Pons, S.; Seitsonen, A. P.; Brune, H.; Kern, K.; ; Barth, J. V. Stm Study of Terephthalic Acid Self-Assembly on Au(111): Hydrogen-Bonded Sheets on an Inhomogeneous Substrate. *J. Phys. Chem. B* **2004**, *108*, 14585–14590.

(S2) Ophus, C.; Ciston, J.; Nelson, C. T. Correcting Nonlinear Drift Distortion of Scanning Probe and Scanning Transmission Electron Microscopies from Image Pairs with Orthogonal Scan Directions. *Ultramicroscopy* **2016**, *162*, 1 – 9.

(S3) Urgel, J. I.; Cirera, B.; Wang, Y.; Auwärter, W.; Otero, R.; Gallego, J. M.; Alcamí, M.; Klyatskaya, S.; Ruben, M.; Martín, F.; Miranda, R.; Ecija, D.; Barth, J. V. Surface-Supported Robust 2d Lanthanide-Carboxylate Coordination Networks. *Small* **2015**, *11*, 6358–6364.

.2 Paper #2

Remote functionalization in surface-assisted dehalogenation by conformational mechanics: organometallic self-assembly of 3,3',5,5'-tetrabromo-2,2',4,4',6,6'-hexafluorobiphenyl on Ag(111)

M. Lischka, G. S. Michelitsch, N. Martsinovich, J. Eichhorn, A. Rastgoo-Lahrood, T. Strunskus,
R. Breuer, K. Reuter, M. Schmittel, and M. Lackinger

Nanoscale **10**, 12035-12044 (2018)
DOI: 10.1039/C8NR01987H

Reprinted under the terms of the RSC Copyright Agreement.
©2018 The Royal Society of Chemistry

Published on 06 June 2018. Downloaded by Technical University of Munich on 11/19/2018 4:05:46 PM.

Nanoscale

PAPER

View Article Online
View Journal | View Issue

Cite this: *Nanoscale*, 2018, **10**, 12035

Remote functionalization in surface-assisted dehalogenation by conformational mechanics: organometallic self-assembly of 3,3′,5,5′-tetrabromo-2,2′,4,4′,6,6′-hexafluorobiphenyl on Ag(111)†

Matthias Lischka,[a,b] Georg S. Michelitsch,[c] Natalia Martsinovich,[d] Johanna Eichhorn,[a,b] Atena Rastgoo-Lahrood,[a,b] Thomas Strunskus,[e] Rochus Breuer,[f] Karsten Reuter,[c] Michael Schmittel[f] and Markus Lackinger *[a,b,g]

Even though the surface-assisted dehalogenative coupling constitutes the most abundant protocol in on-surface synthesis, its full potential will only become visible if selectivity issues with polybrominated precursors are comprehensively understood, opening new venues for both organometallic self-assembly and on-surface polymerization. Using the 3,3′,5,5′-tetrabromo-2,2′,4,4′,6,6′-hexafluorobiphenyl (Br_4F_6BP) at Ag(111), we demonstrate a remote site-selective functionalization at room temperature and a marked temperature difference in double- *vs.* quadruple activation, both phenomena caused by conformational mechanical effects of the precursor-surface ensemble. The submolecularly resolved structural characterization was achieved by Scanning Tunneling Microscopy, the chemical state was quantitatively assessed by X-ray Photoelectron Spectroscopy, and the analysis of the experimental signatures was supported through first-principles Density-Functional Theory calculations. The non-planarity of the various structures at the surface was specifically probed by additional Near Edge X-ray Absorption Fine Structure experiments. Upon progressive heating, Br_4F_6BP on Ag(111) shows the following unprecedented phenomena: (1) formation of regular organometallic 1D chains *via* remote site-selective 3,5′-didebromination; (2) a marked temperature difference in double- *vs.* quadruple activation; (3) an organometallic self-assembly based on reversibility of C–Ag–C linkages with a thus far unknown polymorphism affording both hexagonal and rectangular 2D networks; (4) extraordinary thermal stability of the organometallic networks. Controlled covalent coupling at the previously Br-functionalized sites was not achieved for the Br_4F_6BP precursor, in contrast to the comparatively studied non-fluorinated analogue.

Received 9th March 2018,
Accepted 6th June 2018

DOI: 10.1039/c8nr01987h

rsc.li/nanoscale

Introduction

Over the last decade, the bottom-up fabrication of metal–organic and covalent nanostructures on solid surfaces has gained significant interest and momentum.[1–4] The main idea and benefit of such on-surface synthesis are to combine the stability gained by strong interlinks with the versatility of molecular systems. This approach afforded an intriguing variety of atom-precise structures, comprising covalent 1D wires, chains, and ribbons, as well as 2D networks including first steps towards electronic conjugation.[5,6] For metal–organic networks the chemical structure of the ligands and choice of coordination centers both facilitate tuning and tailoring of network topologies and properties. In this respect, the introduction of iron or cobalt as the coordination center promises

---

[a] *Department of Physics, Technische Universität München, James-Franck-Str. 1, 85748 Garching, Germany. E-mail: markus@lackinger.org*
[b] *Center for NanoScience (CENS) & Nanosystems-Initiative-Munich, Schellingstr. 4, 80799 München, Germany*
[c] *Chair for Theoretical Chemistry and Catalysis Research Center, Technische Universität München, Lichtenbergstraße 4, 85747 Garching, Germany*
[d] *Department of Chemistry, University of Sheffield, Sheffield S3 7HF, UK*
[e] *Institute of Materials Science – Multicomponent Materials, Christian-Albrecht-Universität zu Kiel, Kaiserstr. 2, 24143 Kiel, Germany*
[f] *Center of Micro- and Nanochemistry and Engineering, Organische Chemie I, Universität Siegen, Adolf-Reichwein-Str. 2, 57068 Siegen, Germany*
[g] *Deutsches Museum, Museumsinsel 1, 80538 Munich, Germany*

† Electronic supplementary information (ESI) available: Additional STM & XPS data; additional DFT simulations; synthesis details. See DOI: 10.1039/c8nr01987h

This journal is © The Royal Society of Chemistry 2018

Published on 06 June 2018. Downloaded by Technical University of Munich on 11/19/2018 4:05:46 PM.

unsurpassed catalytic or magnetic properties.[7,8] Moreover, recently unique 5-fold coordination motifs were realized in a 2D environment using rare-earth metals, even resulting in networks with quasicrystalline characteristics.[9] An intriguing variant are the organometallic structures based on carbon–metal–carbon linkages that are routinely observed as metastable intermediates on silver and copper surfaces upon dissociation of halogen substituents that act as leaving groups. Both metal-coordination and organometallic linkages can become reversible, as important premise for self-assembly of highly ordered networks.[10] Moreover, structural equilibration in organometallic networks represents a viable route to improve the structural quality of the corresponding covalent networks that are obtained through a thermally activated isostructural conversion.[11–14] Yet, inducing reversibility in organometallic bonds typically requires higher temperatures as compared to their metal–organic counterparts. In general, the surface-templated bottom-up synthesis of 2D materials with unprecedented chemical, structural, and electronic properties is highly inspiring for nanotechnological applications in a broad variety of fields such as electronics, sensors, separation, and catalysis.[15,16]

In principle, on-surface synthesis facilitates reticular design of novel 2D materials, predetermining arbitrary ordered structures through the judicious choice of the assembling molecular units. However, limited regioselectivity, side reactions, surface influence, and the absence of error correction due to the irreversibility of newly established covalent links render this conceptually straightforward approach challenging in practice. In this respect, well-behaved and controllable coupling reactions for fusing the molecular units are of crucial importance. To date, surface-assisted Ullmann coupling is the most reliable and predictable workhorse to achieve linking *via* C–C bonds,[17] which furthermore benefits from the abundant availability of the employed halogenated precursors. Ullmann coupling is based on aryl halides that can easily be dissociated on metal surfaces, in most cases Cu, Ag, or Au. The generated surface-stabilized radicals may subsequently recombine to form new C–C linkages, either directly or *via* metastable organometallic intermediates.[14,18] Consequently, research on organometallic self-assembly was initially fueled by the large interest in on-surface synthesis of covalent nanostructures, but has now become a topic of its own.

Despite this relevance and significant research efforts into the dehalogenation as the preceding step for both organometallic self-assembly and Ullmann coupling, many central issues of reactivity, chemo- and regioselectivity are still poorly understood. For instance, 1,3-bis(*p*-bromophenyl)-5-(*p*-iodophenyl)benzene showed full deiodination and ~38% debromination after room temperature deposition onto Ag(111), but debromination was only completed at ~260 °C.[14] In stark contrast, 1,3,5-tris(*p*-bromophenyl)benzene was not debrominated at all after room temperature deposition onto Ag(111), but already fully debrominated upon annealing to ~120 °C.[19] Such examples of differential reactivity highlight the current lack of understanding, which prevents a higher level of control in on-surface synthesis that is an absolute necessity for improving the notoriously low structural qualities, currently the most crucial hindrance for applications.

Here we address the reactivity as well as chemo- and regioselectivity of surface-assisted debromination in 3,3′,5,5′-tetrabromo-2,2′,4,4′,6,6′-hexafluorobiphenyl (Br_4F_6BP, *cf.* Fig. 1(a) for its structure) as a prototypical representative of a perfluorinated oligobromoarene. Fluorine substitution constitutes an important strategy to chemically alter relevant properties of neighbouring groups and is additionally expected to influence formation, reversibility, and stability of organometallic networks. In general, fluorination enhances the electron acceptor properties, and attractive electronic properties were predicted for edge-fluorinated graphene nanoribbons.[20,21]

We explore the thermally activated surface chemistry of Br_4F_6BP by a multi-technique approach, comprising a deep structural, chemical, and first-principles computational

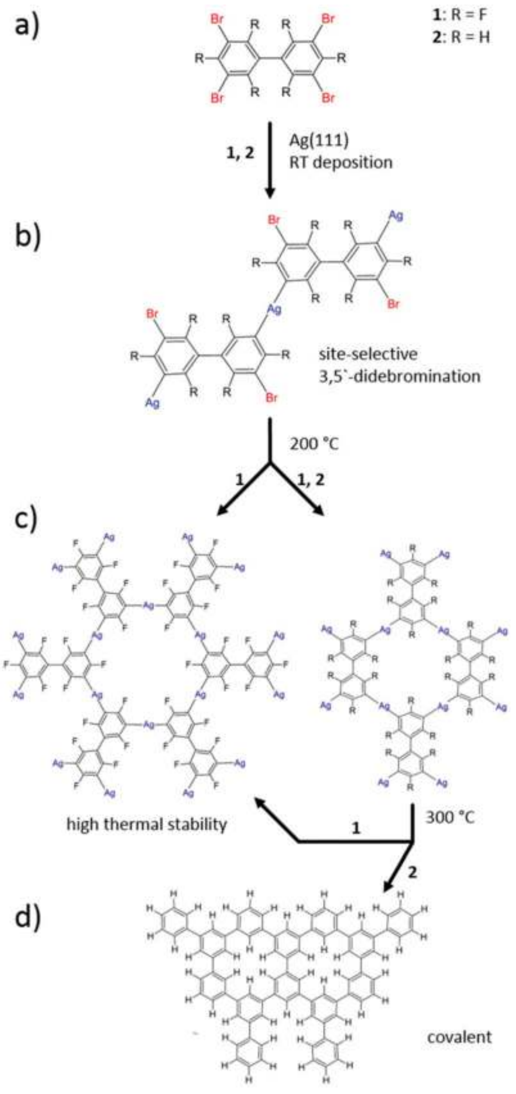

Fig. 1 Overview over the thermally induced structural and chemical changes of Br_4F_6BP and Br_4BP on Ag(111).

This journal is © The Royal Society of Chemistry 2018

Published on 06 June 2018. Downloaded by Technical University of Munich on 11/19/2018 4:05:46 PM.

characterization. The bond dissociation energy of F–C in the gas phase of 5.4 eV even exceeds the value of 5.1 eV for C–C bonds, suggesting that activation of the fluorinated sites is rather unlikely, even if the proximity of a surface can promote defluorination.[22,23] Given the high volatility of Br_4F_6BP, the more reactive Ag(111) surface was chosen, as thermally activated surface chemistry is not feasible on more noble Au(111) surfaces due to preferential desorption of the precursors upon heating (*cf.* ESI†). The key findings for Br_4F_6BP and its comparatively studied non-fluorinated analogue 3,3′,5,5′-tetrabromobiphenyl (Br_4BP) on Ag(111) are summarized in Fig. 1.

A priori, various effects of the perfluorination are conceivable: (1) the C–Br bond strength ought to be modified by inductive effects, resulting in altered debromination barriers/temperatures and reaction kinetics, respectively. By the same token, the strength of the C–Ag–C linkages in the organometallic intermediate could be altered. (2) The gas phase structure of Br_4F_6BP is highly non-planar with a large dihedral angle and rotational barrier at the biphenyl unit due to the *ortho*-fluorine substituents, which could have consequences for the surface chemistry and the regioselectivity of the second debromination step. (3) The *ortho*-fluorine atoms next to the reactive C–Br gives rise to an additional barrier for the covalent aryl–aryl coupling. (4) The high electronegativity of fluorine influences non-covalent intermolecular bonds that steer the organization of precursors as well as reaction intermediates and products. Direct effects are expected due to the negative partial charge, but fluorine substituents can also enhance the halogen bond strength of neighbouring bromine or iodine substituents,[24] or even directly form halogen bonds.[25]

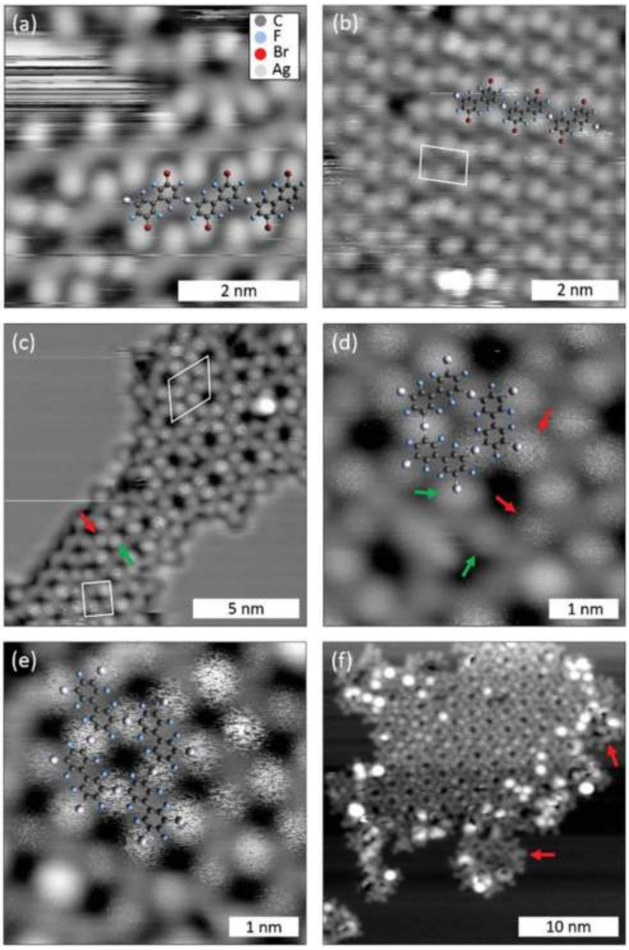

Fig. 2 STM images acquired (a)/(b) after RT deposition of Br_4F_6BP on Ag(111), and subsequent annealing to (c)–(e) 200 °C and (f) 300 °C. After RT deposition (a) more loosely and (b) densely packed ordered arrangements of organometallic chains were observed. Annealing to 200 °C resulted in coexisting organometallic flower ((c) overview, (d) close-up) and (e) checkerboard structures; (f) the flower structure persisted even after annealing to 300 °C. Unit cells are indicated by white lines ((a), (c)). Tunneling parameters: (a) 44 pA, −0.69 V; (b) 22 pA, 1.26 V; (c) 45 pA, 0.58 V; (d) 45 pA, 0.58 V; (e) 42 pA, 0.60 V; (f) 92 pA, 0.53 V. Voltage polarities refer to the tip.

Results

After room-temperature deposition (RT) of Br_4F_6BP onto Ag(111) two different structures were observed by Scanning Tunneling Microscopy (STM), representative images are depicted in Fig. 2(a) and (b) (*cf.* ESI† for overview images). Evidently, the structure shown in Fig. 2(a) consists of interdigitated 1D chains. A perfect geometrical match is achieved with organometallic chains based on C–Ag–C linkages that result from exclusive didebromination of the precursors across the diagonal, *i.e.* at the 3- and 5′-positions. The bright protrusions on alternating sides of the chains are attributed to remaining bromine substituents at the 5- and 3′-positions. The experimentally determined repeat distance of (1.06 ± 0.10) nm is consistent with the DFT-derived value of 1.02 nm found for a periodic planar chain, excluding direct covalent bond formation that would result in a ~0.25 nm smaller value.[14]

Chain interdigitation is likely driven by weak halogen bonding between the remaining Br- and the F-substituents. The more regular and densely packed structure in Fig. 2(b) features an oblique unit cell with $a = (1.06 \pm 0.06)$ nm, $b = (0.78 \pm 0.08)$ nm, $\gamma = 85°$. Also this structure matches perfectly with organometallic chains, yet with a higher packing density. This assignment is corroborated by the equal repeat distance in chain direction (corresponding to lattice parameter a) and the pronounced STM contrast at the positions of the remaining bromine substituents. The average chain length in the less densely packed structure corresponds to (12.7 ± 11) nm and increases only slightly to (14.7 ± 13.6) nm for the more densely packed structure. These lengths were evaluated for domains with packed chains, ignoring the relatively short chain segments in more defective areas (*cf.* ESI†).

The observed formation of organometallic structures agrees with previous studies of various brominated precursors on Ag, consistently reporting organometallic intermediates upon partial debromination at room temperature.[14,18,26,27] Yet, an intriguing aspect here is the remote site-selective didebromination exclusively at the 3- and 5′-positions, as required for chain formation. To unveil structural details of the chains and also

Published on 06 June 2018. Downloaded by Technical University of Munich on 11/19/2018 4:05:46 PM.

to explain the STM contrast, isolated chains were simulated either with enforced planar geometry or alternatively by constraining all Ag atoms to similar height. The latter conditions result in significant tilting of the phenyl rings in the biphenyl unit with a dihedral angle of ~49° and a slightly reduced repeat distance of 0.986 nm. Based on a comparison of the experimental STM images with the relatively pronounced contrast at the remaining bromine substituents and respective STM image simulations, better agreement with the STM images in Fig. 2(a) and (b) is achieved for tilted than for planar chains (*cf.* ESI†). Yet, the structure of adsorbed chains might become decisively modified through interactions with the surface. Therefore, additional DFT simulations were carried out including the Ag(111) surface (*cf.* ESI†). Among the stable structures two perfectly matching candidates were identified. Both structures feature a repeat distance of 1.05 nm along the chain, and interchain spacings of 0.77 nm and 1.05 nm, in accord with the experimental values of (0.78 ± 0.08) nm and (1.03 ± 0.10) nm for the more loosely and densely packed structures, respectively. Even in the presence of the surface, the biphenyl units remain significantly tilted, with large dihedral angles of ~58° and ~43° for the more densely and loosely packed structures. Consequently, the remaining bromine substituents also appear with a pronounced contrast in the corresponding STM image simulations (*cf.* ESI†).

The proposed 3,5′-didebromination after room temperature deposition is also corroborated by the corresponding Br 3d X-ray Photoelectron (XP) spectrum in Fig. 3(b) showing two chemically shifted Br species, each appearing as a spin–orbit doublet. The species with a higher Br $3d_{5/2}$ binding energy (BE) of 70.2 eV corresponds to carbon-bound Br on the molecule,[26] whereas the species at a lower BE of 68.1 eV indicates surface-bound, *i.e.* dissociated bromine.[14,18] Fitting the spectra results in a peak area ratio of ~65% molecule-bound and ~35% dissociated bromine. For perfect infinite chains, a debromination ratio of 50% is expected. Hence, the lower experimental value may indicate relatively short chains or other type of defects.

The strong evidence for organometallic linkages from STM is further corroborated by the C 1s XP spectrum in Fig. 3(a). As a guideline for the fitting of this rather complex C 1s spectrum with contributions from carbon atoms in various different chemical environments, core-level shifts were calculated for isolated species by DFT. The simulations were carried out on each symmetry-inequivalent carbon atom one at a time. All structures considered are depicted in Fig. 4, and the calculated core-level shifts are summarized in Table 1, where intact precursors are also included for comparison. Irrespective of the exact configuration, the following common features of the core-level shifts are identified: as anticipated, the fluorine-substituted carbons (C–F) exhibit the highest C 1s BEs in accord with literature.[28,29] Additional small relative shifts can occur at the non-equivalent positions. In contrast, the organometallic carbon atoms directly bound to Ag (C–Ag) always appear at the lowest BE. Interestingly, the relative order of C 1s BEs of the 1/1′ carbons (C–C) at the linkage of the two phenyl units and bromine-substituted (C–Br) carbons depends on the degree of debromination and the geometric structure.

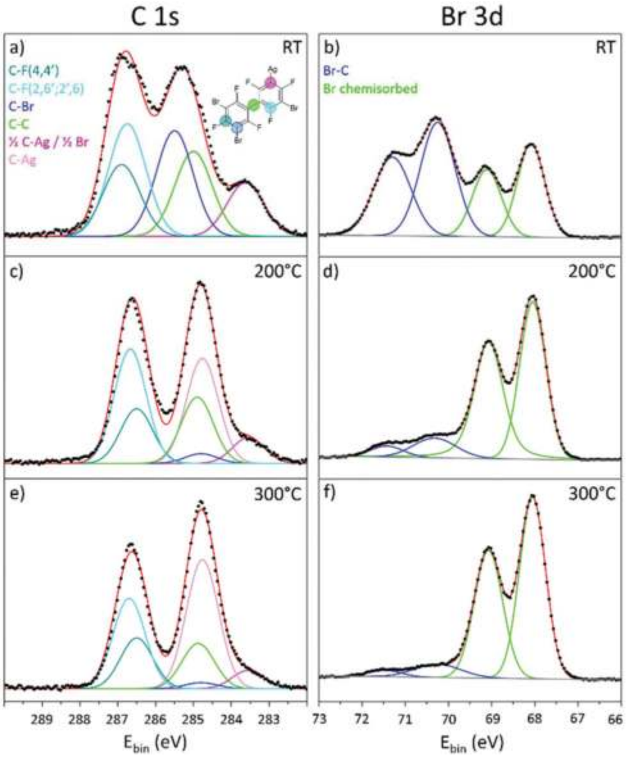

Fig. 3 XP spectra of C 1s (left column) and Br 3d (right column) acquired after RT deposition of Br_4F_6BP (upper row) and subsequent annealing at 200 °C (middle row) and 300 °C (lower row). Raw data are represented by dots; solid lines show fits with Gaussian line shape and linear background. C 1s fits are assigned to following colour scheme: C–F(4,4′), dark cyan; C–F(2,6′;2′,6), light blue; C–Br, blue; C–C, green; C–Ag in half brominated and half organometallic phenyl rings, magenta; C–Ag in fully organometallic phenyl rings, light pink; Br 3d fits are presented for Br–C in blue and chemisorbed Br in green; red lines correspond to the sum of all components.

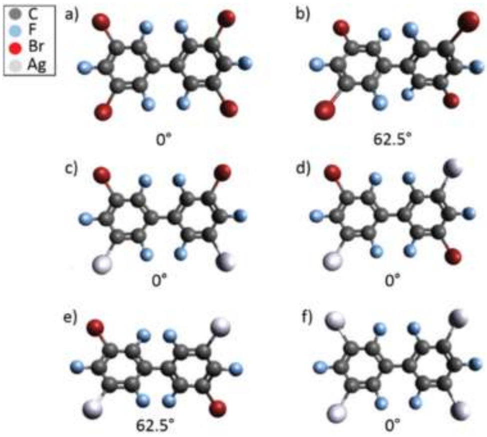

Fig. 4 Chemically distinct structures considered in the C 1s core-level shift simulations (the dihedral angles are indicated below): (a) fully brominated, planar; (b) fully brominated, non-planar with a dihedral angle of 62.5°; (c) 50% debrominated, 50% organometallic, *cis*, planar; (d) 50% debrominated, 50% organometallic, trans, planar; (e) 50% debrominated, 50% organometallic, trans, non-planar with a dihedral angle of 62.5°; (f) fully debrominated and organometallic, planar.

This journal is © The Royal Society of Chemistry 2018

Published on 06 June 2018. Downloaded by Technical University of Munich on 11/19/2018 4:05:46 PM.

Table 1 Calculated relative core-level shifts of C 1s in eV for the structures shown in Fig. 4. The carbon atom with the highest binding energy was used as reference. Core-level shifts are only given for one phenyl ring, the core-level shifts in the other phenyl ring are symmetry related

	(a)	(b)	(c)	(d)	(e)	(f)
C–F (4,4′)	−0.07	0.00	−0.29	−0.30	−0.08	−0.26
C–F (2,2′)	0.00[a]	−0.14[a]	−0.23	−0.24	−0.25	0.00[a]
C–F (6,6′)	0.00[a]	−0.14[a]	0.00	0.00	0.00	0.00[a]
C–Br	−1.25	−1.22	−1.31	−1.31	−1.15	—
C–C	−1.18	−1.91	−1.29	−1.30	−1.90	−1.15
C–Ag	—	—	−2.77	−2.79	−2.59	−2.54

[a] Symmetrically equivalent

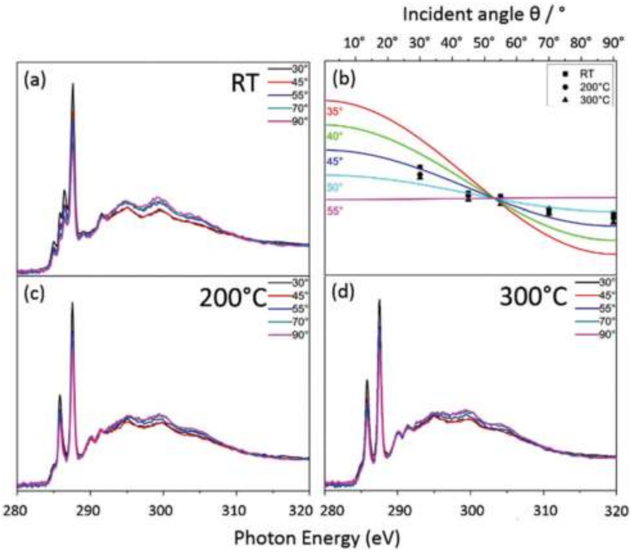

Fig. 5 Carbon K-edge NEXAFS spectra of Br_4F_6BP on Ag(111) acquired for five different incidence angles after (a) RT deposition and subsequent annealing to (c) 200 °C and (d) 300 °C. All spectra were energy- and flux-corrected, background-subtracted, and normalized. Incidence angles θ refer to the surface, *i.e.* 90° corresponds to normal incidence. (b) Shows intensity *vs.* incidence angle θ plots for the resonance corresponding to a photon energy at 285.9 eV; the coloured solid lines are theoretical curves for the stated tilt of the transition dipole moment with respect to the surface normal, evaluated for the known X-ray polarization of $P = 0.92$.

For a fully brominated and planar Br_4F_6BP monomer the C–Br BE is slightly higher than that of C–C as intuitively expected, whereas for a non-planar geometry the order is reversed with a significantly enhanced BE for C–C. In the half brominated and half organometallic compound, the BEs of C–C and C–Br are essentially similar for both planar structures, whereas for the non-planar structure C–C features a lower BE.

These simulation results in combination with additional information from Br 3d aided in fitting the C 1s peak: 35% debromination implies on average 2.4 remaining bromine substituents per molecule. Accordingly, the C–Br (with 2.4 such carbons per molecule) intensity is higher than that for the C–C species (with two such carbons per molecule). For the computationally somewhat undecided BE order of the not separately resolved C–C and C–Br species, Near-Edge X-ray Absorption Fine Structure (NEXAFS) provided additional information: the chemically distinct carbon species are also reflected as fine structure in the π*-resonance, normally even with higher sensitivity for the chemical environment of an atom than in XP Spectroscopy (XPS).[30] The strongest resonance at the highest photon energy is related to C–F with the highest C 1s BE, whereas the adjacent resonance at lower photon energies has the second strongest intensity. Hence, the C–Br BE is higher than that of C–C in agreement with the DFT results, in particular for the non-planar structure in Fig. 4(e). For fitting the XP spectra, two C–F species with slightly different BEs were considered as also suggested by the simulations. This additional information results in a good fit for C 1s as shown in Fig. 3(a) with relative amounts of 43% (50%) C–F, 25% (21.5%) C–Br, 20% (16.7%) C–C, 12.5% (12.5%) C–Ag. The values in parenthesis correspond to the percentages expected for 65% brominated sites and full conversion of 35% into organometallic sites after debromination.

To acquire quantitative information on the phenyl tilt angles, carbon K-edge NEXAFS experiments were performed. The spectra acquired after room temperature deposition of Br_4F_6BP onto Ag(111) for five different incidence angles are depicted in Fig. 5(a). All spectra show strong C 1s → π*-resonances for photon energies below 290 eV as expected for aromatic compounds.[31–34] The fine structure consists of four resolved peaks, nicely reflecting the chemical shifts of carbon. The strongest peak at the highest photon energy of 287.7 eV corresponds to C–F with the highest C 1s BE. These results are in accord with NEXAFS spectra of a perfluorinated oligo(*p*-phenylene).[35] The π*-resonances exhibit a pronounced dichroism, indicating a highly uniform orientation of all molecules on the surface. A detailed analysis of the dependence of the intensity of the resonance corresponding to the phenyl–phenyl carbons on the incidence angle results in an average orientation of the transition dipole moment of (45° ± 5°) with respect to the surface (*cf.* Fig. 5(b)). Direct interpretation as phenyl tilt angle is not indicated, as this value appears unrealistically high. DFT simulations of the organometallic chains adsorbed on Ag(111) suggest notably smaller tilt angles, *i.e.* half of the dihedral angle in the biphenyl unit for a symmetric adsorption geometry, of 29° (densely packed) and 22° (loosely packed) with respect to the surface. This discrepancy could be related to more subtle effects that result in apparent tilt angles, for instance hybridization of molecular with surface electronic states or upward bending of the fluorine substituents.[36] Additionally, complications for the direct interpretation of NEXAFS data can arise from core-hole localization and π* delocalization effects in the biphenyl.[37] Perspectively, it is important to explore whether higher level NEXAFS simulations with explicit evaluation of transition dipole moments and consideration of the underlying surface result in quantitative agreement.

After sample annealing to 200 °C subsequent STM imaging revealed the coexistence of two different regular 2D networks:

Published on 06 June 2018. Downloaded by Technical University of Munich on 11/19/2018 4:05:46 PM.

a flower (Fig. 2(d)) and a checkerboard structure (Fig. 2(e)) with hexagonal ($a = b = (1.84 \pm 0.18)$ nm) and centered rectangular unit cell ($a = (1.57 \pm 0.08)$ nm, $b = (1.30 \pm 0.10)$ nm), respectively. In particular the flower structure exhibits a high defect density and more disordered areas or vacancies were also discerned, mainly at phase boundaries. Both ordered structures are identified as organometallic networks with C–Ag–C interlinks between fully debrominated molecules. Accordingly, the checkerboard structure features two molecules per unit cell, whereas in the flower structure each unit cell accommodates three 120° rotated molecules resulting in a structure with *p6mm* symmetry. Scaled overlays with DFT-optimized geometries perfectly match with the STM data. Accordingly, the experimental lattice parameters are consistent with optimized unit cell parameters from periodic DFT simulations with enforced planar geometry, yielding $a = b = 1.86$ nm for the flower, and $a = 1.61$ nm, $b = 1.22$ nm for the checkerboard structure, respectively. Moreover, the pronounced STM contrast of the Ag atoms in the organometallic linkages as similarly observed in comparable networks on Ag(111),[14,18] is well reproduced in STM image simulations based on the corresponding structures (*cf.* ESI†). Complementary experiments with 4-fold decreased heating and cooling rates (1.5 °C min^{-1} instead of 5.8 °C min^{-1}) yielded similar results (*cf.* ESI†). Interestingly, comparable long-range ordered organometallic structures were not observed for the topologically similar 3,5,3″,5″-tetrabromo-*para*-terphenyl precursor on Cu(111).[38] A conceivable reason could be a diminished bond reversibility of the C–Cu–C linkages due to the higher organometallic bond strength.

Formation of fully cross-linked organometallic networks is triggered by progressive debromination, as also corroborated by Br 3d XP spectra indicating 86% debromination after annealing to 200 °C. Although the chemical state of the adsorbed molecules did not change markedly, the corresponding C 1s XP spectrum in Fig. 3(c) shows drastic alterations. It consists of two clearly separated main peaks, where the lowest BE peak features an additional low BE shoulder. Based on the STM results, the following assignment is proposed: the highest BE peak still corresponds to C–F. The small shoulder at the lowest BE could still be assigned to C–Ag, however, this leaves the question about the origin of the second main peak at a BE of 284.8 eV (Fig. 3(c)). STM unambiguously shows the formation of organometallic networks, which should also be reflected in XPS as increasing C–Ag intensity. To resolve this discrepancy, we propose that the second main component in C 1s can be assigned to C–Ag in fully debrominated phenyl rings within the organometallic networks (Fig. 3(c), ~284.8 eV, light pink). This implies that the chemical shift of C–Ag in the networks is ~1.24 eV smaller than that in the organometallic chains observed after room temperature deposition. This hypothesis is corroborated in the core-level shift simulations: in the half-brominated half-organometallic phenyl rings that mimic the chains, C–Ag is shifted by −2.79 eV with respect to the highest BE C–F, whereas the C–Ag shift decreases to −2.54 eV in the fully organometallic phenyl rings as in the 2D networks. Accordingly, we propose that the C–Ag shift depends on the number of organometallic bonds in the phenyl rings, with a significantly smaller BE for phenyl rings with two organometallic bonds (chains) than with four organometallic bonds (flower and checkerboard). Even though absolute values cannot be accurately reproduced by the model calculations, the trend is fully confirmed. Nevertheless, the strongest justification of our interpretation originates from the STM data, unambiguously showing organometallic networks. This interpretation is further supported by Br 3d XPS: 14% Br remained molecule-bound even after annealing to 200 °C. Assuming that all remaining Br are situated at the slightly tilted phenyl rings in the chains with one organometallic bond, this should result in 3% of the corresponding C 1s intensity, in reasonable agreement with a value of 7% from the fit. We note that this interpretation of the XPS data would not have been possible without STM data and C 1s core level shift simulations: the chemical shift of the C–Ag species observed after annealing to 200 °C in the fully organometallically linked phenyl rings towards typical values for carbon-bound carbon could easily have been misinterpreted as formation of fully covalent networks.

Further annealing to 300 °C resulted in disappearance of the checkerboard and prevalence of the flower structure as shown by the STM image in Fig. 2(f). This suggests that the flower structure is thermodynamically more stable, whereas the polymorphism observed for lower annealing temperatures of 200 °C can be attributed to kinetic effects. Even though the domain sizes increased considerably, the flower structure still exhibits a relatively high defect density. In addition, STM showed the emergence of more disordered not further resolved structures, mostly at the boundary of the remaining flower structure (Fig. 2(f) examples marked by red arrow). In XPS C 1s (Fig. 3(e)) appeared largely similar to the spectrum seen after annealing to 200 °C, only with a slight change of the intensity ratio at the expense of the C–F component. Moreover, the degree of debromination increases slightly to 91%, *i.e.* a safely detectable proportion of Br still remained molecule-bound (Fig. 3(f)), whereas the total amount of Br on the surface did not change.

Further NEXAFS experiments were also carried out after annealing to 200 °C and 300 °C, respectively. The spectra depicted in Fig. 5(c) and (d) appear largely similar for both annealing temperatures. In contrast to the room temperature spectra, the shape of the π*-resonances changed from one main peak with fine structure to two peaks with comparable intensity, mirroring the changes also observed in C 1s XPS. Again an unrealistically large apparent phenyl tilt angle of (50° ± 5°) is deduced from the intensity dependence. This is at odds with the STM results, since in the 2D networks, the biphenyl units are constrained to a planar geometry by the four intermolecular organometallic bonds. As already discussed above, a straightforward interpretation of NEXAFS data assuming the transition dipole moment perpendicular to the phenyl ring is not indicated here.

This journal is © The Royal Society of Chemistry 2018

Published on 06 June 2018. Downloaded by Technical University of Munich on 11/19/2018 4:05:46 PM.

Ordered organometallic networks could not be observed anymore after annealing at 400 °C. STM showed only disordered structures, where molecular units could not be discerned anymore (*cf.* ESI†). In XPS the C 1s intensity remained constant, whereas F 1s decreased to about 75%, indicating the onset of defluorination (*cf.* ESI†). A possible X-ray radiation damage of the fluorine functional groups appears unlikely, as an additional experiment with a 60% reduced dose showed similar results. Moreover, the total intensity of Br 3d on the surface decreased to 34% of the initial amount due to thermal desorption. The constant amount of carbon on the surface excludes sizable desorption of monomers. For such a relatively small molecule, stabilization on the surface at these high temperatures can only be achieved by forming larger aggregates, suggesting formation of covalent intermolecular bonds. However, the lack of molecular resolution in STM may indicate more disordered structures without defined interlinks.

Discussion

Partial debromination followed by the formation of organometallic bonds is commonly observed for comparable brominated precursors on Ag(111) around room temperature.[14,18] In this respect, the perfluorination as in Br_4F_6BP does not lead to significant changes. This is fully consistent with the expectations from our DFT-derived homolytic bond dissociation energies of C–Br bonds in the gas phase, resulting in a similar value of 4.4 eV for both Br_4F_6BP and its non-fluorinated analogue. A spectacular observation is the formation of regular 1D chains through remote site-selective didebromination at the 3- and 5′-positions. Yet, this unprecedented phenomenon can be rationalized by the interplay of bond formation between radicals and adatoms and electrostatically mediated intramolecular conformational mechanics: the first debromination occurs at a random site (referred to as 3), directly followed by formation of an organometallic bond with an Ag adatom. The relatively large difference of adsorption heights between Ag adatoms (0.236 nm in three-fold hollow sites according to the (111) lattice plane spacing or 0.244 nm according to our DFT simulations of organometallic chains) and aromatic backbones (0.316 nm for perfluoropentacene on Ag(111)[39] or 0.323 nm according to our DFT simulations of organometallic chains) tilts the first phenyl ring toward this organometallic bond. Accordingly, the adsorption height and consequently the debromination barrier of the Br at the 5-position increase, resulting in kinetic stabilization. The remote site-selective debromination at the second phenyl ring in 5′-position is mediated by the steric repulsion through the *ortho*-fluorine atoms, leading to a large dihedral angle between the two phenyl rings. This conformational tilt of the second phenyl ring in the opposite direction gives rise to a low adsorption height and debromination barrier at the 5′-position and kinetic stabilization of the Br at the 3′-position. In essence, the steric repulsion conveys the remote site-selective debromination across two phenyl rings. However, substantial differences in efficiency of this process were observed between different experimental runs: for the results shown in Fig. 2(b) overview images indicate a very high yield with almost no defects; this high regularity also enables the more dense packing of the chains; in contrast, for the results shown in Fig. 2(a) a markedly reduced selectivity of ∼60% was deduced from statistical analysis of STM data (*cf.* ESI†). Accordingly, a more subtle influence from additional preparation parameters such as deposition rate and surface temperature during deposition appears likely. To shed more light on the conformational mechanics, comparative STM experiments were carried out with the non-fluorinated analogue Br_4BP. In analogy to Br_4F_6BP, room temperature deposition of Br_4BP onto Ag(111) likewise results in the formation of 1D organometallic chains (*cf.* ESI†). These results unambiguously demonstrate that even the weaker steric repulsion of the *ortho*-hydrogens is sufficient to mediate a site-selective 3,5′-didebromination through conformational mechanics. Interestingly, deposition of Br_4BP onto Ag(111) held at 50 °C induces high defect densities, also related to progressive dissociation of the remaining bromine substituents (*cf.* ESI†). These additional experiments demonstrate that for Br_4BP the conformational mechanics is not very robust against higher thermal energy, hence only works in a relatively small temperature window.

The formation of organometallic networks from multiply brominated precursors on Ag(111) driven by the thermally activated progression of debromination is well documented.[14,18,40] In this sense, Br_4F_6BP-derived networks are a further example for "organometallic self-assembly", confirming the mandatory bond reversibility of C–Ag–C linkages. Yet, the observed polymorphism is quite uncommon for organometallic self-assembly. For Br_4F_6BP as precursor, the two experimentally observed regular structures correspond to the two least complex structures conceivable for these two-fold symmetric tectons and straight C–Ag–C linkages. Interestingly, all Ag atoms in the organometallic networks exhibit comparable apparent heights in STM, prohibiting any tilt within the biphenyl backbone. Given the large steric repulsion due to the *ortho*-fluorine atoms, co-planar adsorption appears surprising. On the other hand, DFT indicates a relatively modest energy cost of 1.32 eV for planarization of the Br_4F_6BP in the gas phase in accord with literature values.[41] The planarization is accompanied by a lengthening of the phenyl–phenyl bond from 0.1481 nm to 0.1544 nm to alleviate the electrostatic repulsion.

Even though STM indicates a largely similar adsorption height of all organometallic Ag atoms, closer inspection reveals more subtle differences: some Ag atoms appear rather noisy, whereas others could be stably imaged (examples are marked by red and green arrows, respectively, in Fig. 2(c)/(d)), ruling out tip instabilities. The distribution is not random: stable Ag atoms appear predominantly at domain boundaries and defects, whereas within the domains the majority of Ag atoms appear noisy (*cf.* ESI†). This peculiar difference is attributed to a weakening of the surface contacts for noisy Ag atoms as a consequence of constraining the intrinsically twisted biphenyl molecules to planarity by their integration within the

Published on 06 June 2018. Downloaded by Technical University of Munich on 11/19/2018 4:05:46 PM.

networks. Again, it is instructive to compare the 2D organometallic self-assembly of Br_4F_6BP and Br_4BP triggered by full debromination. In contrast to the fluorinated precursor, the non-fluorinated precursor exclusively forms the checkerboard pattern without any indications of polymorphism or the flower structure that was even the thermodynamically more stable polymorph for Br_4F_6BP (*cf.* ESI†). Moreover, the corresponding domain sizes remain comparatively small for Br_4BP. Even though apparently related to the perfluorination, the origin of these differences is not yet clear. A possible explanation is offered by differences in surface mobility, where the inherently non-planar structure of the Br_4F_6BP precursor should give rise to a higher diffusivity. In addition, for Br_4BP large areas of the surface were covered with densely packed domains of dissociated Br (*cf.* ESI†), imposing serious constraints on the formation of organic networks.[42] Yet, it remains unclear as to why this halogen poisoning is more pronounced for the non-fluorinated precursor.

A further very remarkable feature of the organometallic networks derived from Br_4F_6BP is their exceptional and unprecedented thermal stability up to 300 °C. In contrast, the Br_4BP derived organometallic intermediates are converted into covalent networks upon annealing to ~200 °C (*cf.* ESI†), in accord with hexagonal polyphenylene networks.[14] The extraordinary thermal stability of the Br_4F_6BP derived organometallic flower structure indicates high binding energies that could in principle arise either from strong molecule–molecule or strong molecule–surface interactions. However, a comparative X-ray standing wave study finds a significant enlargement of the adsorption height for perfluorinated pentacene on Ag(111), indicating a weakening of the molecule–surface interactions.[43] This suggests that the high stability of the organometallic networks here originates from strong molecule–molecule interactions as indeed rationalized by gas phase DFT simulations: planar organometallic dimers with one linear C–Ag–C linkage and three remaining Br substituents per biphenyl result in bond dissociation energies of 1.93 eV for the perfluorinated *vs.* 1.34 eV for the hydrogen-terminated dimer. Even though actual values may differ for the adsorbed system, perfluorination accounts for the extraordinary stability of the organometallic networks by increasing the C–Ag–C bond strength. By the same token, the higher bond strength restricts the reversibility, hence increases the temperatures required for structural equilibration. This may also account for both the relatively high defect densities in the organometallic networks and the relatively high temperatures required for conversion of the metastable checkerboard into the more stable flower structure.

In contrast to other organometallic networks,[14,18,44] and in particular to the comparable 3,5,3″,5″-tetrabromo-*para*-terphenyl precursor[45] and the non-fluorinated Br_4BP analogue, a thermally activated conversion into defined covalent networks was not observed here, not even for the highest annealing temperature of 300 °C. This is tentatively attributed to the combination of extraordinary stability of the organometallic networks, an additional barrier for covalent coupling due to the *ortho*-fluorine atoms, but also the onset of molecule degradation by defluorination at higher annealing temperatures (*cf.* ESI†).

Conclusions

In summary, Br_4F_6BP showed a rich combination of known and unprecedented surface chemistry on Ag(111) as summarized in Fig. 1: while formation and equilibration of organometallic structures is meanwhile well established, the formation of defined 1D organometallic chains for both the fourfold brominated perfluorinated Br_4F_6BP and non-fluorinated Br_4BP precursor is unique. This chain formation involves the regioselective activation of only two out of the precursor's four active sites. This is explained by a remote site-selective 3,5′-didebromination, mediated across the biphenyl unit by its conformational non-planarity due to the intramolecular repulsion of either the *ortho*-fluorine or *ortho*-hydrogen substituents. This constitutes an instructive and highly useful example of conformational mechanics in on-surface synthesis: formation of chemical bonds with the surface upon activation of specific sites of a molecular entity is accompanied by an increase of adsorption height, and hence deactivation at the opposing sites. The proposed symmetry breaking mechanism has broader implications for on-surface synthesis as it provides a rationale for the observed stepwise or uncommonly gradual and selective activation in apparently symmetric monomers.[14,18] In this respect, it is intriguing that already the significantly weaker steric hindrance in the non-fluorinated Br_4BP precursor is sufficient to drive this conformational mechanics.

In contrast, both the polymorphism and the exceptional stability of organometallic networks are unique observations for the Br_4F_6BP precursor. As indicated by our DFT simulations, the perfluorination can be held responsible for the high stability of the organometallic networks. Even though it decreases the adsorption energy of aromatic molecules on metals, by the same token the strength of intermolecular C–Ag–C linkages is markedly enhanced. The exceptional strength of the intermolecular organometallic bonds is even sufficient to overcome the large electrostatic repulsion within the molecules and incorporate them in into extended 2D networks. Yet, the role of the perfluorination for the polymorphism remains unclear. Tentatively, either the enhanced surface mobility of Br_4F_6BP due to the non-planar structure or the large amounts of adsorbed bromine for Br_4BP could be held responsible and would also be consistent with the larger domain sizes observed for Br_4F_6BP as compared to Br_4BP.

Interestingly, as already indicated by DFT-derived C–Br bond dissociation energies, there is no pronounced effect of the perfluorination on the debromination barrier, as debromination temperatures are within the typical range reported for non-fluorinated precursors.[14,18] Accordingly, in terms of activation, perfluorinated monomers are equally suitable for debrominative coupling on surfaces. Yet, covalent coupling into

This journal is © The Royal Society of Chemistry 2018

Published on 06 June 2018. Downloaded by Technical University of Munich on 11/19/2018 4:05:46 PM.

defined structures as templated by the organometallic flower structure remains elusive for Br_4F_6BP on Ag(111). This is an important finding as it provides valuable guidelines for the design of fluorinated monomers suitable for covalent aryl–aryl coupling, for instance by combining *ortho*-fluorine with *ortho*-hydrogen substitution. Alternatively, the substantially increased intermolecular bond strength in the organometallic networks derived from perfluorinated precursors provides a perspective for directly using the highly stable organometallic 2D polymers for improved structural quality.

Materials and methods

All STM, NEXAFS, and XPS experiments were carried out under ultrahigh vacuum (UHV) conditions with base pressures below 3×10^{-10} mbar (STM) and 8×10^{-10} mbar (XPS, NEXAFS). Ag(111) single crystals surfaces were prepared by cycles of 0.5 keV-Ar^+ sputtering and annealing at 500 °C. 3,3′,5,5′-tetrabromo-2,2′,4,4′,6,6′-hexafluorobiphenyl (Br_4F_6BP) was synthesized according to literature procedures[46,47] (*cf.* ESI†) and deposited by sublimation from a home-built Knudsen-cell with crucible temperatures between 55 °C and 80 °C at a pressure of 3×10^{-9} mbar.[48] The non-fluorinated analogue 3,3′,5,5′-tetrabromo-1,1′-biphenyl (Br_4BP) was purchased from Sigma Aldrich (≤100% purity). Its vapour pressure at room temperature is high enough to facilitate deposition from a Knudsen-cell without additionally heating the crucible. STM data were recorded at room temperature with a home-built microscope controlled by an SPM100 controller (RHK Technology Inc.). NEXAFS and XPS measurements were carried out in a Prevac endstation at the HE-SGM beamline at Helmholtz-Zentrum Berlin. NEXAFS carbon K-edge spectra were acquired in the analysis chamber using a home-built double channel plate detector in partial electron yield mode (U = −150 V). XP spectra of C 1s, Br 3d, and F 1s were measured with a Scienta R3000 electron analyzer at normal electron emission with a pass energy of 50 eV. Photon energies of 450 eV for C 1s and Br 3d and 750 eV for F 1s were used, respectively. For energy calibration a Ag $3d_{5/2}$ binding energy of 368.2 eV was used as internal standard.[49]

Dispersion-corrected DFT simulations were performed either with periodic boundary conditions (organometallic chains, flower and checkerboard structure) or for isolated molecules (C 1s core-level shifts) with the FHI-aims computing package.[50] Geometry optimizations for the unit cells containing one (organometallic chains and checkerboard structure) or three (flower structure) molecules with two (organometallic chains) and four (checkerboard and flower structure) Br atoms exchanged for Ag were performed with FHI-aims at "tight" computational settings, 4 × 4 × 1 k-point sampling, and using a 30 Å vacuum region. In these calculations electronic exchange and correlation (xc) was treated on the generalized-gradient approximation level with the PBE functional,[51] augmented by dispersive interactions through the Tkatchenko–Scheffler TSsurf method.[52] All structures were fully relaxed until residual forces were below 10 meV $Å^{-1}$. The adsorbed organometallic chains were optimized on Ag(111) slabs with 11 and 15 atoms per layer. A lattice parameter of $a_{Ag} = 4.152$ Å was used and the first of two layers was allowed to relax. The influence of the weakly interacting Ag(111) surface was neglected in the simulations of the 2D flower and checkerboard structures, but the unit cell size was optimized together with the geometry. STM image simulations were performed based on the DFT-optimized structures according to the Tersoff–Hamann approach.[53] Therefore, all electronic states in an energy window defined by the bias voltage and the Fermi energy were summed to produce the final image. C 1s core-level energies were calculated with a 1s core-hole on each symmetry-inequivalent carbon atom one at a time. The maximum overlap method was used to prevent variational collapse to the ground state.[54,55]

Conflicts of interest

There are no conflicts to declare.

Acknowledgements

The Nanosystems-Initiative-Munich (NIM) cluster of excellence is thankfully acknowledged for financial support. We thank Helmholtz-Zentrum Berlin for the allocation of synchrotron beamtime and J. E. and M. L. thankfully acknowledge traveling support. We are grateful to Dr Alexei Nefedov and Prof. Christoph Wöll (Karlsruhe Institute of Technology) for making their UHV system available for XPS and NEXAFS experiments. N. M. acknowledges the use of Iceberg and Sol computing clusters at the University of Sheffield.

Notes and references

1 J. V. Barth, G. Costantini and K. Kern, *Nature*, 2005, **437**, 671–679.

2 J. V. Barth, *Annu. Rev. Phys. Chem.*, 2007, **58**, 375–407.

3 D. F. Perepichka and F. Rosei, *Science*, 2009, **323**, 216–217.

4 L. Dong, Z. A. Gao and N. Lin, *Prog. Surf. Sci.*, 2016, **91**, 101–135.

5 J. Eichhorn, D. Nieckarz, O. Ochs, D. Samanta, M. Schmittel, P. J. Szabelski and M. Lackinger, *ACS Nano*, 2014, **8**, 7880–7889.

6 W. Z. Yuan, X. Y. Shen, H. Zhao, J. W. Y. Lam, L. Tang, P. Lu, C. Wang, Y. Liu, Z. Wang, Q. Zheng, J. Z. Sun, Y. Ma and B. Z. Tang, *J. Phys. Chem. C*, 2010, **114**, 6090–6099.

7 B. Wurster, D. Grumelli, D. Hötger, R. Gutzler and K. Kern, *J. Am. Chem. Soc.*, 2016, **138**, 3623–3626.

8 R. Gutzler, S. Stepanow, D. Grumelli, M. Lingenfelder and K. Kern, *Acc. Chem. Res.*, 2015, **48**, 2132–2139.

9 J. I. Urgel, D. Écija, G. Lyu, R. Zhang, C.-A. Palma, W. Auwärter, N. Lin and J. V. Barth, *Nat. Chem.*, 2016, **8**, 657–662.

Published on 06 June 2018. Downloaded by Technical University of Munich on 11/19/2018 4:05:46 PM.

10 M. D. Giovannantonio and G. Contini, *J. Phys.: Condens. Matter*, 2018, **30**, 093001.

11 C. J. Judd, S. L. Haddow, N. R. Champness and A. Saywell, *Sci. Rep.*, 2017, **7**, 14541.

12 M. Ammon, T. Sander and S. Maier, *J. Am. Chem. Soc.*, 2017, **139**, 12976–12984.

13 Q. Sun, L. Cai, H. Ma, C. Yuan and W. Xu, *ACS Nano*, 2016, **10**, 7023–7030.

14 J. Eichhorn, T. Strunskus, A. Rastgoo-Lahrood, D. Samanta, M. Schmittel and M. Lackinger, *Chem. Commun.*, 2014, **50**, 7680–7862.

15 Z. Chen, C. Molina-Jirón, S. Klyatskaya, F. Klappenberger and M. Ruben, *Ann. Phys.*, 2017, **529**, 1700056.

16 Q. Shen, H.-Y. Gao and H. Fuchs, *Nano Today*, 2017, **13**, 77–96.

17 M. Lackinger, *Chem. Commun.*, 2017, **53**, 7872–7885.

18 R. Gutzler, L. Cardenas, J. Lipton-Duffin, M. E. Garah, L. E. Dinca, C. E. Szakacs, C. Fu, M. Gallagher, M. Vondráček, M. Rybachuk, D. F. Perepichka and F. Rosei, *Nanoscale*, 2014, **6**, 2660–2668.

19 G. Kuang, S. Z. Chen, L. Yan, K. Q. Chen, X. Shang, P. N. Liu and N. Lin, *J. Am. Chem. Soc.*, 2018, **140**, 570–573.

20 P. Wagner, C. P. Ewels, J.-J. Adjizian, L. Magaud, P. Pochet, S. Roche, A. Lopez-Bezanilla, V. V. Ivanovskaya, A. Yaya, M. Rayson, P. Briddon and B. Humbert, *J. Phys. Chem. C*, 2013, **117**, 26790–26796.

21 D. Gunlycke, J. Li, J. W. Mintmire and C. T. White, *Nano Lett.*, 2010, **10**, 3638–3642.

22 H. Hayashi, J. Yamaguchi, H. Jippo, R. Hayashi, N. Aratani, M. Ohfuchi, S. Sato and H. Yamada, *ACS Nano*, 2017, **11**, 6204–6210.

23 C. Schmidt, T. Breuer, S. Wippermann, W. G. Schmidt and G. Witte, *J. Phys. Chem. C*, 2012, **116**, 24098–24106.

24 K. E. Riley, J. S. Murray, J. Fanfrlík, J. Řezáč, R. J. Solá, M. C. Concha, F. M. Ramos and P. Politzer, *J. Mol. Model.*, 2011, **17**, 3309–3318.

25 S. Kawai, A. Sadeghi, F. Xu, L. Peng, A. Orita, J. Otera, S. Goedecker and E. Meyer, *ACS Nano*, 2015, **9**, 2574–2583.

26 M. Smerieri, I. Píš, L. Ferrighi, S. Nappini, A. Lusuan, C. D. Valentin, L. Vaghi, A. Papagni, M. Cattelan, S. Agnoli, E. Magnano, F. Bondino and L. Savio, *Nanoscale*, 2016, **8**, 17843–17853.

27 I. Píš, L. Ferrighi, T. H. Nguyen, S. Nappini, L. Vaghi, A. Basagni, E. Magnano, A. Papagni, F. Sedona, C. D. Valentin, S. Agnoli and F. Bondino, *J. Phys. Chem. C*, 2016, **120**, 4909–4918.

28 D. T. Clark, D. Kilcast and W. K. R. Musgrave, *J. Chem. Soc. D*, 1971, 516b–5518.

29 D. T. Clark, D. Kilcast, D. B. Adams and W. K. R. Musgrave, *J. Electron Spectrosc. Relat. Phenom.*, 1972, **1**, 227–250.

30 G. Hähner, *Chem. Soc. Rev.*, 2006, **35**, 1244–1255.

31 K. H. Frank, P. Yannoulis, R. Dudde and E. E. Koch, *J. Chem. Phys.*, 1988, **89**, 7569–7576.

32 H. Oji, R. Mitsumoto, E. Ito, H. Ishii, Y. Ouchi, K. Seki, T. Yokoyama, T. Ohta and N. Kosugi, *J. Chem. Phys.*, 1998, **109**, 10409–10418.

33 K. Hänel, S. Söhnchen, S. Lukas, G. Beernik, A. Birkner, T. Strunskus, G. Witte and C. Wöll, *J. Mater. Res.*, 2004, **19**, 2049–2056.

34 S. Söhnchen, S. Lukas and G. Witte, *J. Chem. Phys.*, 2004, **121**, 525–534.

35 K. K. Okudaira, K. Ohara, H. Setoyama, T. Suzuki, Y. Sakamoto, M. Imamura, S. Hasegawa, K. Mase and N. Ueno, *Nucl. Instrum. Methods Phys. Res.*, 2003, **199**, 265–269.

36 C. Mainka, P. S. Bagus, A. Schertel, T. Strunskus, M. Grunze and C. Wöll, *Surf. Sci.*, 1995, **341**, L1055–L1060.

37 M. G. Ramsey, F. P. Netzer, D. Steinmüller, D. Steinmüller-Nethl and D. R. Lloyd, *J. Chem. Phys.*, 1992, **97**, 4489–4495.

38 Q. Fan, C. Wang, L. Liu, Y. Han, J. Zhao, J. Zhu, J. Kuttner, G. Hilt and J. M. Gottfried, *J. Phys. Chem. C*, 2014, **118**, 13018–13025.

39 S. Duhm, S. Hosoumi, I. Salzmann, A. Gerlach, M. Oehzelt, B. Wedl, T.-L. Lee, F. Schreiber, N. Koch, N. Ueno and S. Kera, *Phys. Rev. B: Condens. Matter Mater. Phys.*, 2010, **81**, 045418.

40 M. Bieri, S. Blankenburg, M. Kivala, C. A. Pignedoli, P. Ruffieux, K. Müllen and R. Fasel, *Chem. Commun.*, 2011, **47**, 10239.

41 F. Grein, *J. Phys. Chem. A*, 2002, **106**, 3823–3827.

42 S. Schlögl, W. M. Heckl and M. Lackinger, *Surf. Sci.*, 2012, **606**, 999–1104.

43 N. Koch, A. Gerlach, S. Duhm, H. Glowatzki, G. Heimel, A. Vollmer, Y. Sakamoto, T. Suzuki, J. Zegenhagen, J. P. Rabe and F. Schreiber, *J. Am. Chem. Soc.*, 2008, **130**, 7300–7304.

44 J. P. Beggan, N. M. Boyle, M. T. Pryce and A. A. Cafolla, *Nanotechnology*, 2015, **26**, 365602.

45 J. Dai, Q. Fan, T. Wang, J. Kuttner, G. Hilt, J. M. Gottfried and J. Zhu, *Phys. Chem. Chem. Phys.*, 2016, **18**, 20627–20634.

46 Y. Sakamoto, T. Suzuki, A. Miura, H. Fujikawa, S. Tokito and Y. Taga, *J. Am. Chem. Soc.*, 2000, **122**, 1832–1833.

47 F. Leroux, R. Simon and N. Nicod, *Lett. Org. Chem.*, 2006, **3**, 948–954.

48 R. Gutzler, W. M. Heckl and M. Lackinger, *Rev. Sci. Instrum.*, 2010, **81**, 015108.

49 G. Johansson, J. Hedman, A. Berndtsson, M. Klasson and R. Nilsson, *J. Electron Spectrosc. Relat. Phenom.*, 1973, **2**, 295–317.

50 V. Blum, R. Gehrke, F. Hanke, P. Havu, V. Havu, X. Ren, K. Reuter and M. Scheffler, *Comput. Phys. Commun.*, 2009, **180**, 2175–2196.

51 J. P. Perdew, K. Burke and M. Ernzerhof, *Phys. Rev. Lett.*, 1996, **77**, 3865–3868.

52 V. G. Ruiz, W. Liu, E. Zojer, M. Scheffler and A. Tkatchenko, *Phys. Rev. Lett.*, 2012, **108**, 146103.

53 J. Tersoff and D. R. Hamann, *Phys. Rev. B: Condens. Matter Mater. Phys.*, 1985, **31**, 805–813.

54 N. A. Besley, A. T. B. Gilbert and P. M. W. Gill, *J. Chem. Phys.*, 2009, **130**, 124308.

55 A. T. B. Gilbert, N. A. Besley and P. M. W. Gill, *J. Phys. Chem. A*, 2008, **112**, 13164–13171.

This journal is © The Royal Society of Chemistry 2018

Electronic Supplementary Material (ESI) for Nanoscale.
This journal is © The Royal Society of Chemistry 2018

Electronic Supplementary Information

Remote functionalization in surface-assisted dehalogenation by conformational mechanics: organometallic self-assembly of 3,3',5,5'-tetrabromo-2,2',4,4',6,6'-hexafluorobiphenyl on Ag(111)

Matthias Lischka,[a,b] Georg S. Michelitsch,[c] Natalia Martsinovich,[d] Johanna Eichhorn,[a,b] Atena Rastgoo-Lahrood,[a,b] Thomas Strunskus,[e] Rochus Breuer,[f] Karsten Reuter,[c] Michael Schmittel,[f] and Markus Lackinger [a,b,g]

[a.] *Department of Physics, Technische Universität München, James-Frank-Str. 1, 85748 Garching, Germany. E-mail: markus@lackinger.org*

[b.] *Center for NanoScience (CENS) & Nanosystems-Initiative-Munich, Schellingstr. 4, 80799 München, Germany*

[c.] *Chair for Theoretical Chemistry and Catalysis Research Center, Technische Universität München, Lichtenbergstraße 4, 85747 Garching, Germany*

[d.] *Department of Chemistry, University of Sheffield, Sheffield S3 7HF, U.K.*

[e.] *Institute of Materials Science – Multicomponent Materials, Christian-Albrecht-Universität zu Kiel, Kaiserstr. 2, 24143 Kiel, Germany*

[f.] *Center of Micro- and Nanochemistry and Engineering, Organische Chemie I, Universität Siegen, Adolf-Reichwein-Str. 2, 57068 Siegen, Germany*

[g.] *Deutsches Museum, Museumsinsel 1, 80538 Munich, Germany*

1. Additional STM and XPS data: Br_4F_6BP on Ag(111)

Overview STM images after room-temperature deposition

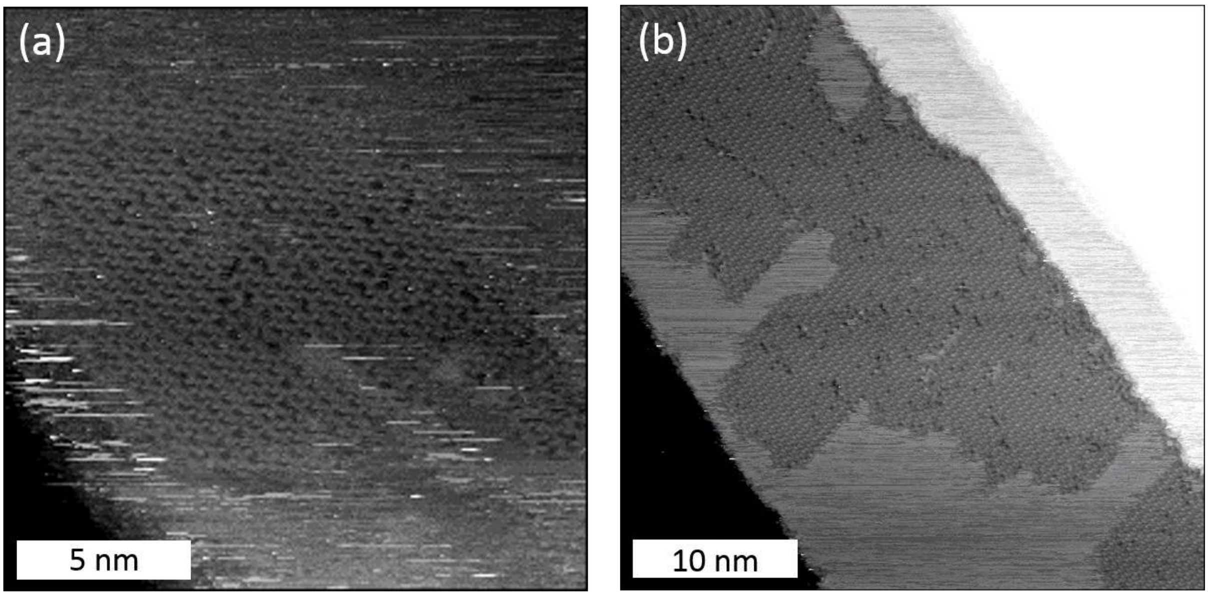

Figure S1. Overview STM images acquired after RT deposition of Br_4F_6BP onto Ag(111), showing (a) more loosely (corresponding to Fig. 2(a) of the main text) and (b) more densely (corresponding to Fig. 2(b) of the main text) packed arrangements of 1D organometallic chains; Interestingly, the average chain lengths as derived from these images are relatively similar, corresponding to (a) (12.7 ± 11) nm and (b) (14.7 ± 13.6) nm (b). (tunneling parameters: (a) 0.09 V, 115 pA; (b) 0.91 V, 91 pA)

Overview STM images after annealing

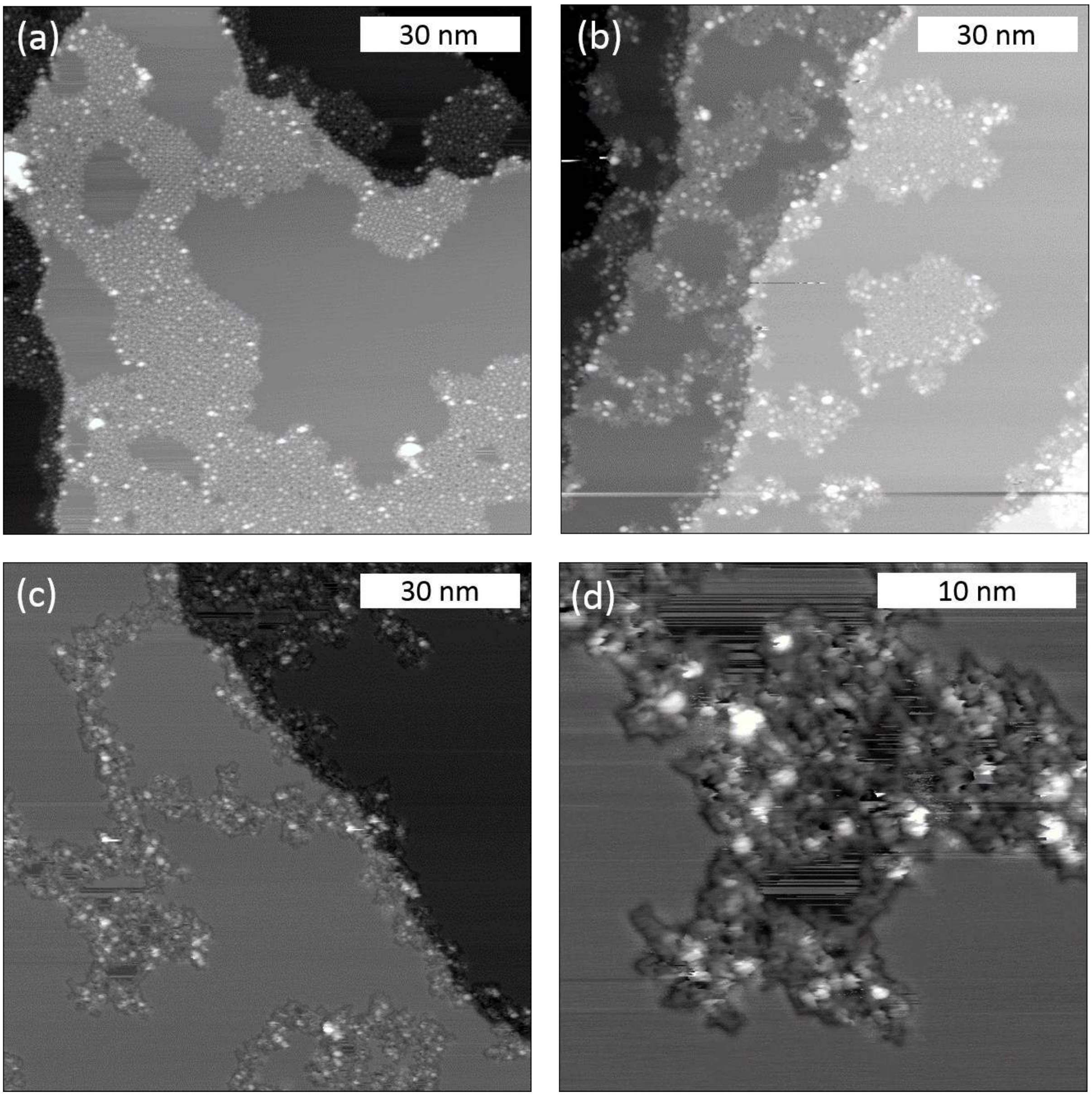

Figure S2. Overview STM images acquired after RT deposition of Br_4F_6BP onto Ag(111) and subsequent annealing to (a) 200 °C, (b) 300 °C, and (c) / (d) 400°C; ordered molecular structures were not resolved anymore after annealing to 400 °C, even though the disordered aggregates appear with relatively uniform height; formation of covalent aggregates is highly plausible, but cannot unambiguously confirmed by these data. (tunneling parameters: all overview images (100 × 100) nm² (a) 0.93 V, 63 pA; (b) 0.88 V, 93 pA; (c) 0.88 V, 90 pA; (d) 0.88 V, 110 pA)

Annealing to 200 °C with reduced heating and cooling rates

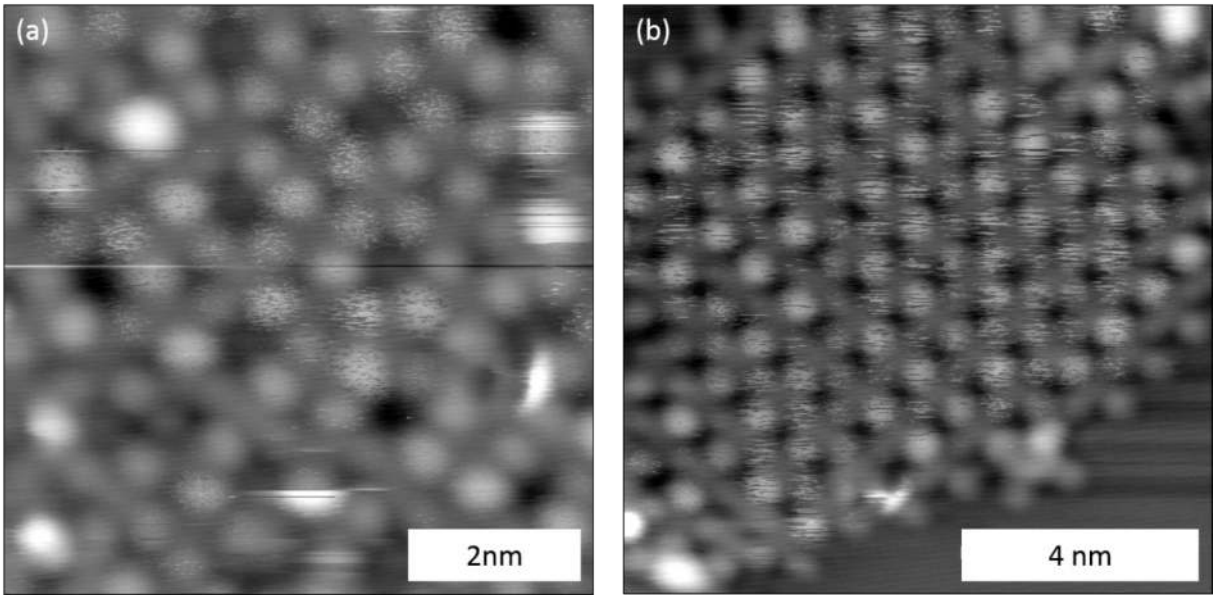

Figure S3. STM images acquired after RT deposition of Br_4F_6BP onto Ag(111) and subsequent annealing to 200 °C with a reduced heating and cooling rate of 1.5 °C min^{-1}. Yet, no differences to heating treatments for the (a) flower and (b) checkerboard structure with the normally applied heating and cooling rate of 5.8 °C min^{-1} could be discerned. (tunneling parameters: (a) 0.71 V, 39 pA; (b) 0.93 V, 45 pA)

Statistical analysis of the 3,5’ site-selectivity

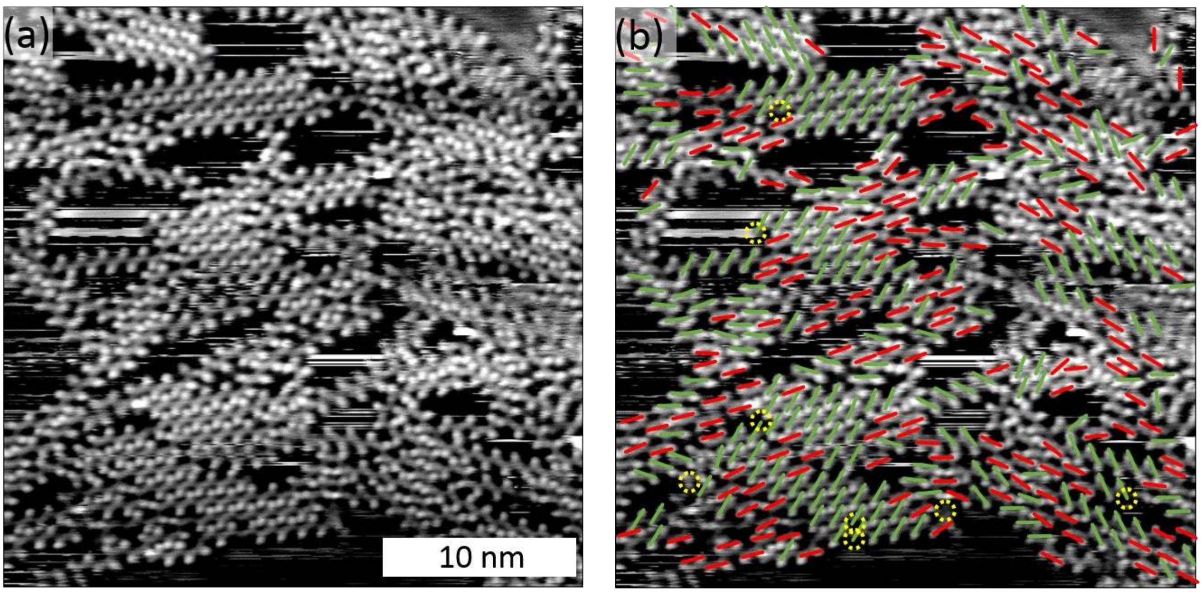

Figure S4. Statistical analysis of a STM image with predmoninatley organometallic chains acquired after room-temperature deposition of Br_4F_6BP onto Ag(111) (corresponding to Fig. 2(a) of the main text); (a) original image; (b) same image with color coding for the site-slectivity: green corresponds to the targeted site-selective 3,5’-didebromaintion (255 counts), whereas red indicates defects with 3,3’-didebromaintion (180 counts); yellow circles show molecules with one remaing bromine substituent. (tunneling parameters: 1.26 V, 22 pA)

Spatial distribution of noisy appearing vs. stably imaged Ag atoms

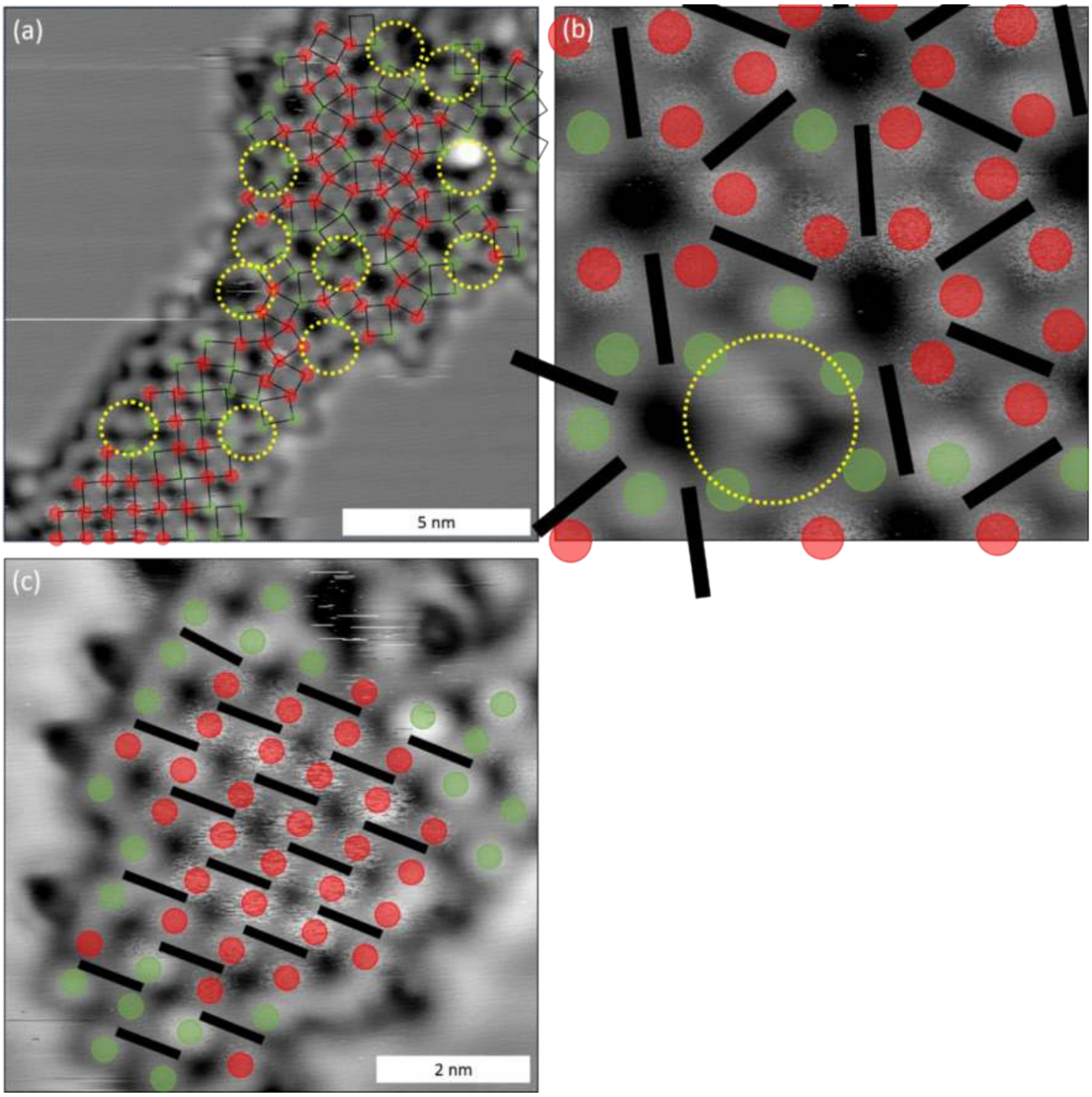

Figure S5. STM images of Br_4F_6BP on Ag(111) acquired after annealing to 200 °C; (a) overview, (b) flower, (c) checkerboard structure; two different types of STM contrast could be distinguished for Ag atoms in the organometallic linkages: **(1)** noisy appearing Ag atoms (red) and **(2)** stable appearing Ag atoms. The color code aids in illustratating the spatial distribution of both contrast types, black bars symbolize biphenyl units. Nosiy Ag atoms are the dominant species within well ordered organometallic domains, whereas stable Ag atoms (green) are mostly located at domain boundaries and around vacancies (marked by yellow circles). (tunneling parameters: (a) 0.58 V, 45 pA; (b) 0.58 V, 45 pA; (c) 0.60 V, 47 pA)

F 1s XP spectra of Br_4F_6BP on Ag(111)

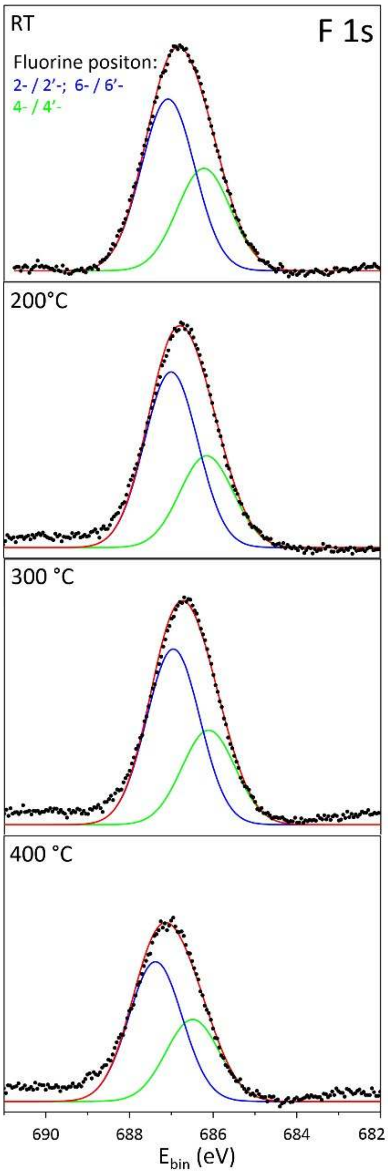

Figure S6. F1s XP spectra acquired after RT deposition of Br_4F_6BP onto Ag(111) and successive annealing to the indicated temperatures up to 400 °C. Raw data are represented by dots; solid lines show fits with Gaussian line-shape and linear background. F 1s spectra were fitted with two components corresponding to the inequivalent fluorine substituents: F at 4- / 4'-position: green; F at 2- / 2'-position and 6- / 6'-position: blue; according to the molecular structure a fixed 1:2 ratio was applied; Annealing at 400 °C already results in a loss of fluorine due to degradation of the molecules by defluorination.

XPS fitting parameters for Br_4F_6BP on Ag(111)

Carbon 1s @RT Fig. 2a						Bromine 3d @RT Fig. 2b				
Peak	Peak type	FWHM	E_B (eV)	rel. Area (%)	Assigned to	Peak type	FWHM	E_B (eV)	rel. Area (%)	Assigned to
1	Gaussian	1.2	283.6	12	C-Ag (½ Br / ½ C-Ag	Gaussian	0.7	68.1	22	Chemisorbed Br (Br $d_{5/2}$)
2	Gaussian	1.2	285.0	20	C-C	Gaussian	0.8	69.1	17	Chemisorbed Br (Br $d_{3/2}$)
3	Gaussian	1.1	285.5	24	C-Br	Gaussian	0.9	70.2	35	Br-C (Br $d_{5/2}$)
4	Gaussian	1.2	286.8	27	C-F (4,4’)	Gaussian	1.0	71.3	26	Br-C Br $d_{3/2}$)
5	Gaussian	1.2	286.9	17	C-F (2,6’;2’,6)					

Carbon 1s @200°C Fig. 2c						Bromine 3d @200°C Fig. 2d				
Peak	Peak type	FWHM	E_B (eV)	rel. Area (%)	Assigned to	Peak type	FWHM	E_B (eV)	rel. Area (%)	Assigned to
1	Gaussian	1.0	283.6	7	C-Ag (½ Br / ½ C-Ag	Gaussian	0.7	68.0	45	Chemisorbed Br (Br $d_{5/2}$)
2	Gaussian	1.0	284.8	28	C-Ag	Gaussian	0.8	69.1	42	Chemisorbed Br (Br $d_{3/2}$)
3	Gaussian	1.0	284.8	3	C-Br	Gaussian	1.2	70.3	9	Br-C (Br $d_{5/2}$)
4	Gaussian	1.0	284.9	18	C-C	Gaussian	0.9	71.4	4	Br-C Br $d_{3/2}$)
5	Gaussian	1.0	286.5	15	C-F (2,6’;2’,6)					
6	Gaussian	1.0	286.7	30	C-F (4,4’)					

Carbon 1s @300°C Fig. 2e						Bromine 3d @300°C Fig. 2f				
Peak	Peak type	FWHM	E_B (eV)	rel. Area (%)	Assigned to	Peak type	FWHM	E_B (eV)	rel. Area (%)	Assigned to
1	Gaussian	1.0	283.6	5	C-Ag (½ Br / ½ C-Ag	Gaussian	0.7	68.1	51	Chemisorbed Br (Br $d_{5/2}$)

2	Gaussian	1.0	284.8	38	C-Ag	Gaussian	0.8	69.1	39	Chemisorbed Br (Br $d_{3/2}$)
3	Gaussian	1.0	284.8	2	C-Br	Gaussian	1.3	70.2	7	Br-C (Br $d_{5/2}$)
4	Gaussian	1.0	284.9	13	C-C	Gaussian	0.9	71.5	2	Br-C Br $d_{3/2}$)
5	Gaussian	1.0	286.5	15	C-F (2,6’;2’,6)					
6	Gaussian	1.0	286.7	27	C-F (4,4’)					

Fluorine 1s RT					
Peak	Peak type	FWHM	E_B (eV)	rel. Area (%)	Fluorine position assigned to
1	Gaussian	1.5	686.2	37	4- / 4’-
2	Gaussian	1.5	687.1	63	2- / 2’-; 6- / 6’-
Fluorine 1s 200°C					
Peak	Peak type	FWHM	E_B (eV)	rel. Area (%)	Fluorine position assigned to
1	Gaussian	1.5	686.1	34	4- / 4’-
2	Gaussian	1.5	687.0	66	2- / 2’-; 6- / 6’-
Fluorine 1s 300°C					
Peak	Peak type	FWHM	E_B (eV)	rel. Area (%)	Fluorine position assigned to
1	Gaussian	1.5	686.1	35	4- / 4’-
2	Gaussian	1.5	687.0	65	2- / 2’-; 6- / 6’-
Fluorine 1s 400°C					
Peak	Peak type	FWHM	E_B (eV)	rel. Area (%)	Fluorine position assigned to
1	Gaussian	1.5	686.5	37	4- / 4’-
2	Gaussian	1.5	687.4	63	2- / 2’-; 6- / 6’-

2. Additional STM data: Br_4BP on Ag(111)

Chain formation *via* site-selective 3,5'-didebromination and influence of surface temperature

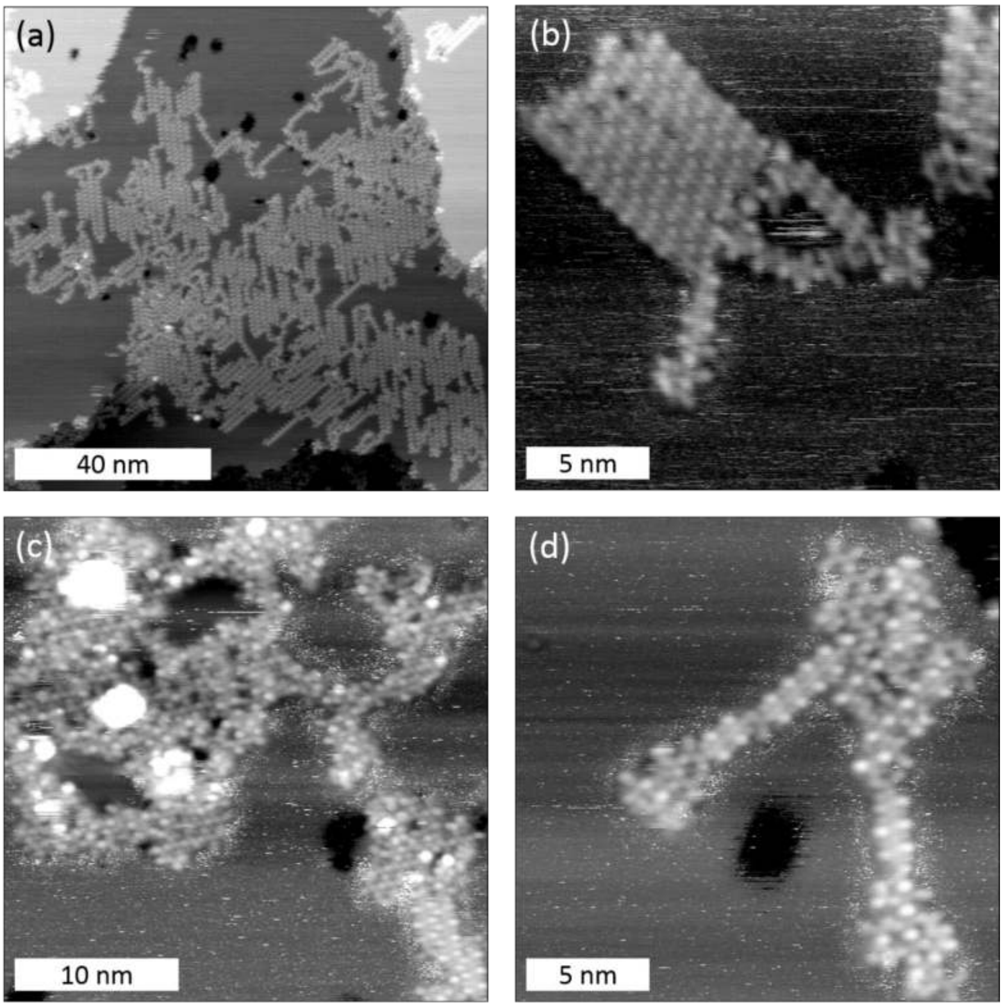

Figure S7. STM images acquired after deposition of non-fluorinated Br_4BP onto Ag(111) with (a) / (b) the surface held at RT and (c) / (d) the surface preheated to 50°C; (a) overview image showing the formation of linear structures, more clearly resolved as organometallic chains in the close-up in (b); the repeat distance of (1.06 ± 0.04) nm perfectly matches the Br_4F_6BP derived organometallic chains; Yet, the chain formation by site-selective 3,5'-didebromination is highly sensitive on the surface temperature as shown in (c) and (d): deposition onto Ag(111) preheated to 50 °C induces a higher density of defects and also leads to the first expression of 2D patterns by progressive debromination; only short segments of organometallic chains are still observed; (tunneling parameters: (a) 0.86 V, 94 pA; (b) 0.48 V, 93 pA; (c) 1.49 V, 95 pA; (d) 1.49 V, 96 pA).

STM images of Br_4BP on Ag(111) after annealing

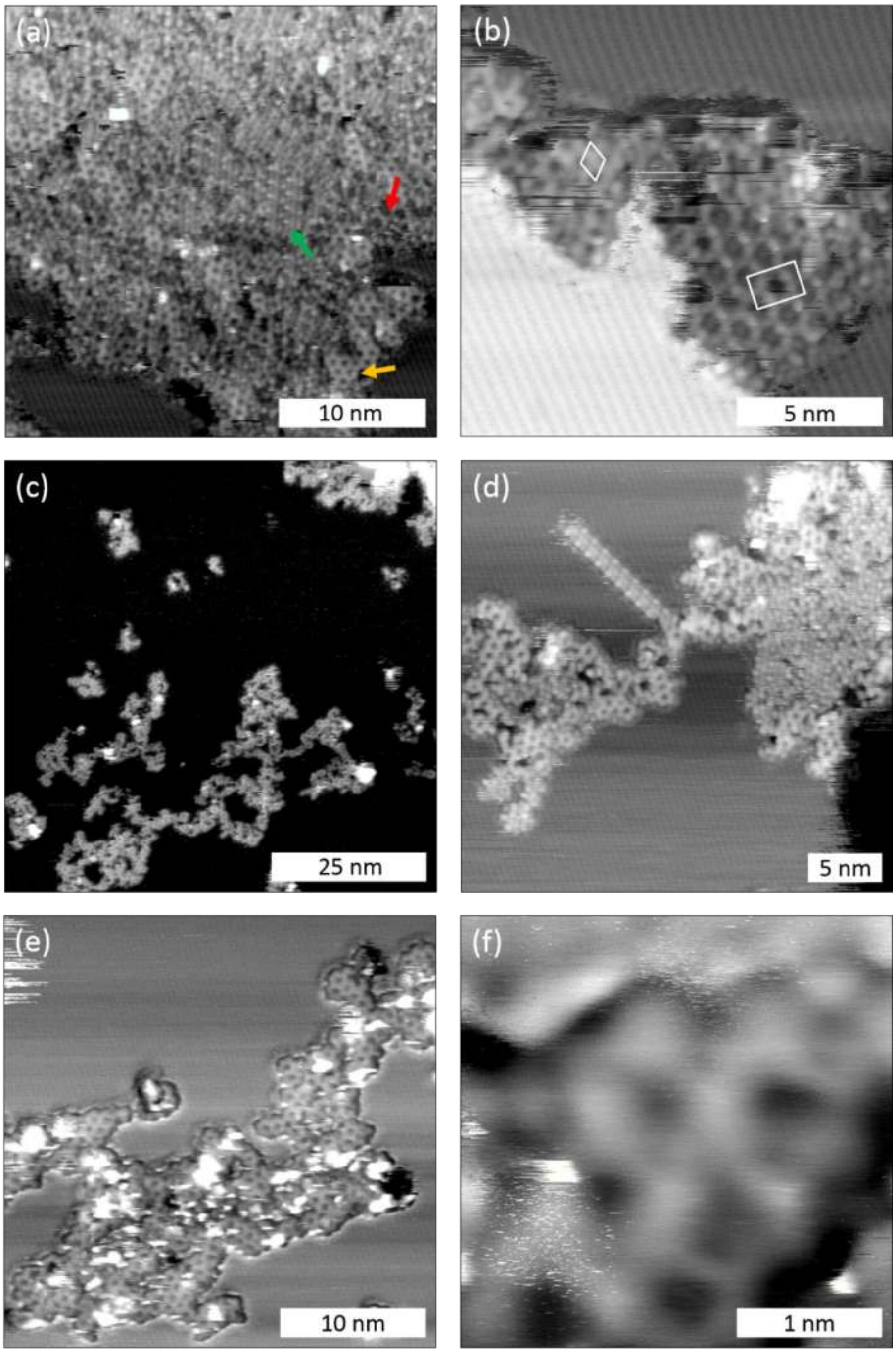

Figure S8. STM images of Br_4BP on Ag(111) acquired after subsequent annealing to (a) / (b) 200 °C; (c) / (d) 300 °C; (e) / (f) 400 °C, with a heating and cooling rate of 3.33 °C min^{-1}. After annealing at 200°C three different structures can be observed by STM: (1) 1D organometallic chains (green arrow), (2) small patches of the centered rectangular

organometallic checkerboard structure (red arrow in (a), white rectangle in (b)) with lattice parameters of a = (1.75 ± 0.10) nm, b = (1.20 ± 0.07) nm that are within the experimental error identical to the Br_4F_6BP derived checkerboard structure; (3) a porous hexagonal structure with a = b = (0.83 ± 0.06) nm (yellow arrow in (a), white diamond in (b)) whose lattice parameters could not be match with any of the Br_4F_6BP derived structures, but corresponds to a covalent checkerboard structure that is identical to the "porous graphene" previously reported by Fasel and coworkers;[1] upon further annealing the 1D chains are progressively replaced by the organometallic checkerboard pattern, yet with relatively small domain sizes and a high amount of more disordered areas; subsequently, the organometallic structures are converted into covalent structures, as deduced from the change of lattice parameters; In contrast to Br_4F_6BP, for Br_4BP large areas of the surface are covered by closed layers of dissociated Br (see striped structures in (b)); the origin of this interesting difference is not clear, but might account for the high disorder and small domain sizes in the organometallic self-assembly of Br_4BP; (tunneling parameters: (a) 0.89 V, 85 pA; (b) 0.89 V, 84 pA; (c) 1.10 V, 94 pA; (d) 1.52 V, 95 pA; (e) 1.27 V, 91 pA; (f) 1.27 V, 91 pA)

3. Additional DFT simulations

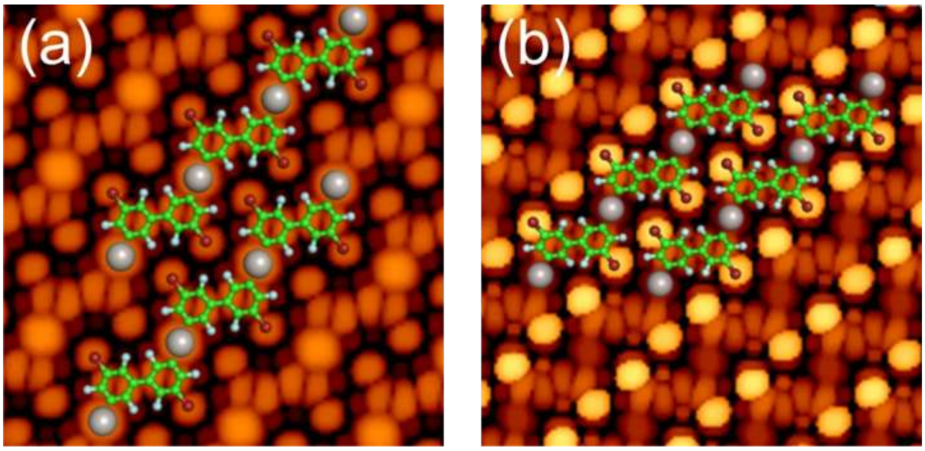

Figure S9. STM image simulations of free-standing organometallic chains, i.e. without Ag(111) substrate. (a) geometry constrained to planar; (b) only Ag atoms constrained to similar height, resulting in a tilting of the phenyl rings in the biphenyl unit with a dihedral angle of ~49°. In the adsorbed state for a symmetric geometry, the phenyl tilt angle with respect to the surface is given by half of the dihedral angle. The underlying DFT-optimized structures are shown as overlays.

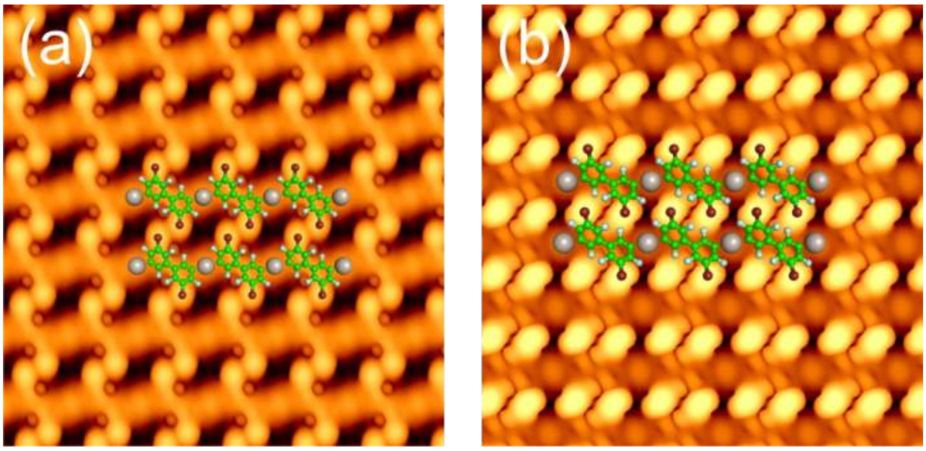

Figure S10. STM image simulations of adsorbed organometallic chains including the Ag(111) substrate; the underlying DFT-optimized structures are shown as overlays: (a) less densely packed structure with a repeat distance along the chain of 1.05 nm and a similar chain separation of 1.05 nm (b) more densely packed structure with a repeat distance along the chain of 1.05 nm and a chain separation of 0.78 nm; in both structures the phenyl rings remain tilted with respect to the surface; the simulated STM images match well with the experiment;

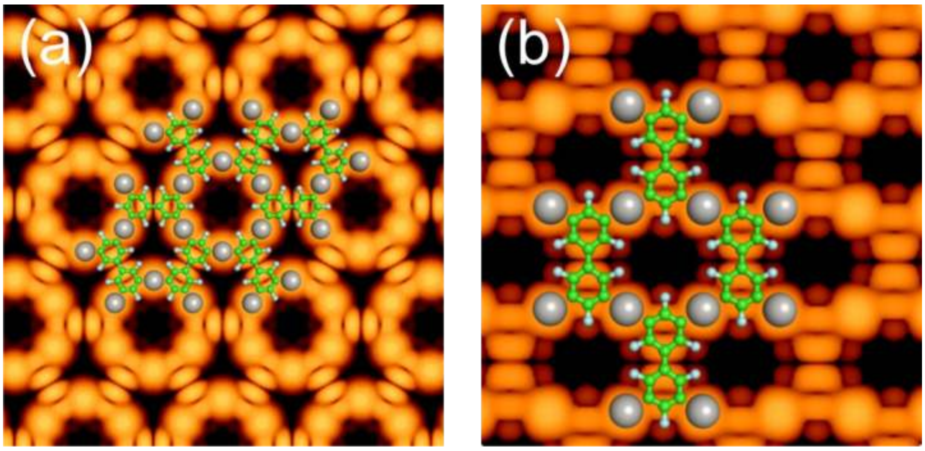

Figure S11. STM image simulations of both organometallic (a) flower and (b) checkerboard structure. The underlying DFT-optimized structures with enforced planar geometry are shown as overlays. In both cases, the Ag atoms in the C-Ag-C linkages appear with a pronounced contrast in accordance with the experiment.

4. Additional STM and XPS data of Br_4F_6BP on Au(111)

STM images of Br_4F_6BP on Au(111)

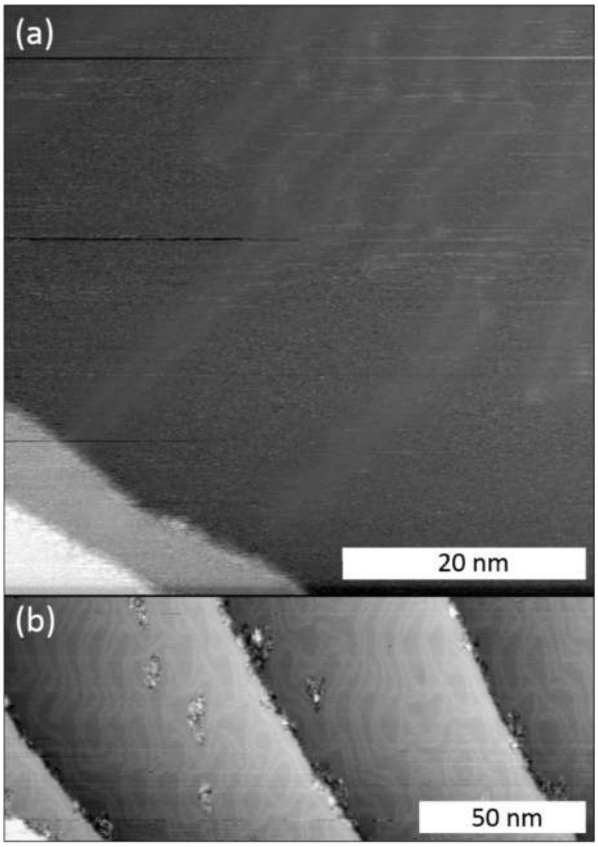

Figure S12. STM data acquired after deposition of Br_4F_6BP on Au(111) at (a) RT and (b) after annealing to 200 °C. At RT, the intact monomers are too mobile to be imaged with STM and the surface appears empty, even though the herringbone reconstruction is locally perturbed. Upon annealing, the majority of molecules was desorbed (cf. XPS in Fig. S13), yet not further resolved aggregates were found scattered across the surface. (tunneling parameters: (a) 1.54 V, 48 pA; (b) 0.98 V, 82 pA).

C 1s and Br 3d XP spectra of Br_4F_6BP on Au(111)

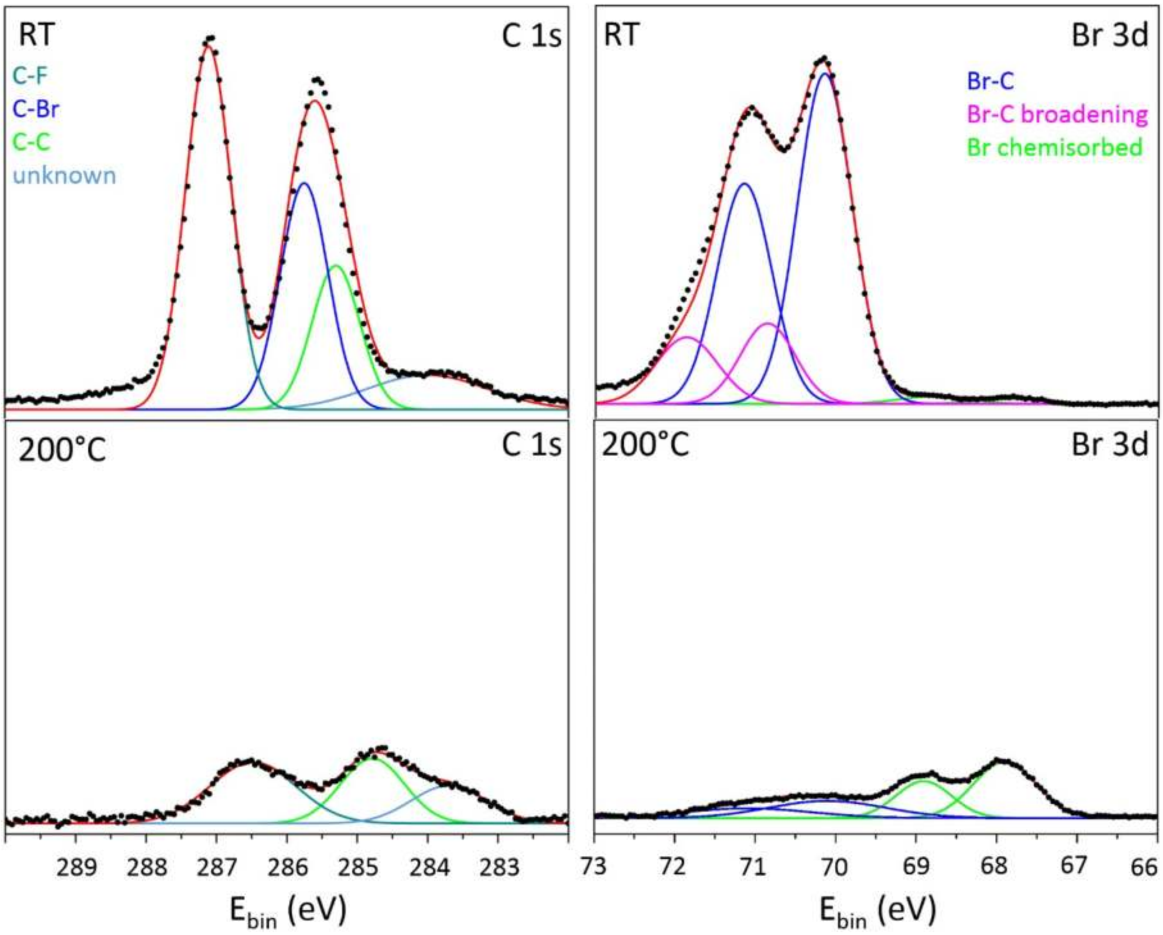

Figure S13. C 1s and Br 3d XP spectra acquired after deposition of Br_4F_6BP onto Au(111) at (a) RT and (b) after annealing to 200 °C. At RT almost no Br substituents were dissociated, hence mostly intact monomers are present on the surface. Obtaining a reasonable fit required an additional Br 3d doublet with a higher binding energy, accounting for 21% of the total intensity. This additional Br species is tentatively assigned to either molecules in special adsorption sites (e.g. step-edges) or second layer coverage, but the exact origin remains unclear at the moment. After annealing, most molecules and Br desorbed, with small remainders of a carbonaceous species and split off Br still present. Raw data are represented by dots; solid lines show fits (fitted with a Gaussian line shape and linear background), where red lines corresponds to the sum of all components.

XPS fitting parameters for Br_4F_6BP on Au(111)

Carbon 1s @RT						Bromine 3d @RT				
Peak	Peak type	FWHM	E_B (eV)	rel. Area (%)	Assigned to	Peak type	FWHM	E_B (eV)	rel. Area (%)	Assigned to
1	Gaussian	2	284	11	-	Gaussian	1	67.8	1	Chemisorbed Br (Br $d_{5/2}$)
2	Gaussian	0.8	285.3	18	C-C	Gaussian	1	68.8	1	Chemisorbed Br (Br $d_{3/2}$)
3	Gaussian	0.8	285.8	28	C-Br	Gaussian	0.8	70.2	46	Br-C (Br $d_{5/2}$)
4	Gaussian	0.8	287.1	43	C-F	Gaussian	0.8	70.9	11	Br-C (Br $d_{5/2}$) broadening
5						Gaussian	0.8	71.2	31	Br-C Br $d_{3/2}$)
6						Gaussian	0.9	71.9	10	Br-C Br $d_{3/2}$) broadening

Carbon 1s @200°C						Bromine 3d @200°C				
Peak	Peak type	FWHM	E_B (eV)	rel. Area (%)	Assigned to	Peak type	FWHM	E_B (eV)	rel. Area (%)	Assigned to
1	Gaussian	1.3	283.7	23	-	Gaussian	0.9	67.8	40	Chemisorbed Br (Br $d_{5/2}$)
2	Gaussian	1.1	284.8	33	C-C	Gaussian	0.8	68.9	29	Chemisorbed Br (Br $d_{3/2}$)
3	Gaussian	1.4	286.5	43	C-F	Gaussian	1.7	70.1	23	Br-C (Br $d_{5/2}$)
4						Gaussian	1.9	71.1	14	Br-C (Br $d_{3/2}$)

5. Synthesis details

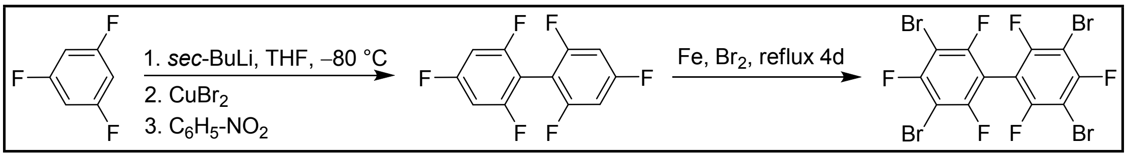

(1) Synthesis of Br_4F_6BP was accomplished after Leroux *et al.*:[2] At –80 °C *sec*-butyllithium (38.6 mmol) in cyclohexane (30.0 mL) was added dropwise to a solution of 1,3,5-trifluorobenzene (5.10 g, 3.90 mL, 38.6 mmol) in tetrahydrofuran (90.0 mL). After completion of the addition, stirring was continued for 3 h under nitrogen atmosphere. Still at –80 °C copper-(II)-bromide (8.60 g, 38.6 mmol) was added in one portion under vigorous stirring and 45 minutes later nitrobenzene (4.75 g, 4.00 mL, 38.6 mmol) was added dropwise. The reaction mixture was brought to room temperature overnight and filtered through a column of basic alumina (100 g). The filter cake was eluted with n-hexane. After evaporation of all volatiles the residue was purified by column chromatography on flash-silica with *n*-hexane. Further purification by vacuum-sublimation (80 °C .. 90 °C at 0.01 mbar) afforded a colorless powder. Yield: 7.10 g (70%). ^{1}H NMR (400 MHz, CDCl3): δ 6.80 (m, 4H).

(2) Synthesis of Br_4F_6BP was prepared after Sakamoto *et al.*:[3] At 0 °C bromine (7.00 mL, 21.8 g, 136 mmol) was added to a mixture of 2,2',4,4',6,6'-hexafluorobiphenyl (2.00 g, 7.63 mmol) and iron powder (1.50 g, 26.9 mmol). After removal of the ice bath the reaction mixture was refluxed for 4 days. At room temperature the reaction mixture was poured into aqueous sodium thiosulfate solution and was extracted with dichloromethane. The organic phase was washed with brine and dried over sodium sulphate. After evaporation of the volatiles the residual solid was recrystallized from ethanol. Subsequent vacuum sublimation (90 °C .. 110 °C at 0.01 mbar) afforded a colorless powder. Yield: 2.42 g (55%). Mp: 162 °C. IR (KBr, cm^{-1}): 1599 (s), 1427 (s), 1056 (s), 765 (s), 706 (s), 639 (w), 589 (s), 568 (s). ^{19}F NMR (564 MHz, $CDCl_3$): δ 70.4 (m, 4F), 60.3 (m, 2F). ^{13}C NMR (100 MHz, $CDCl_3$): δ 158.0 (d, 1J = 250 Hz), 156.4 (d, 1J = 250 Hz), 102.8, 95.0. Anal. Calcd for $C_{12}Br_4F_6$: C, 24.95. Found: C, 25.20

^{13}C-NMR: (100 MHz, CDCl$_3$): Br$_4$F$_6$BP

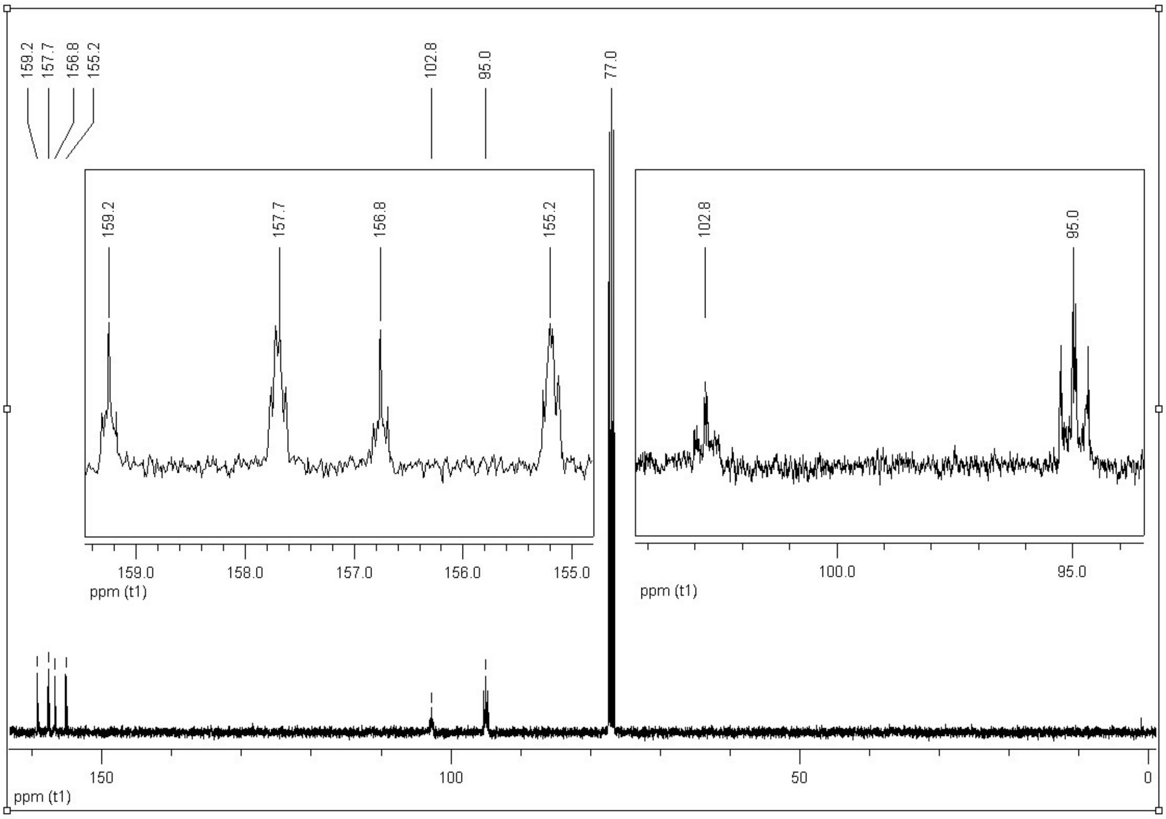

^{19}F-NMR (564 MHz, CDCl$_3$): Br$_4$F$_6$BP

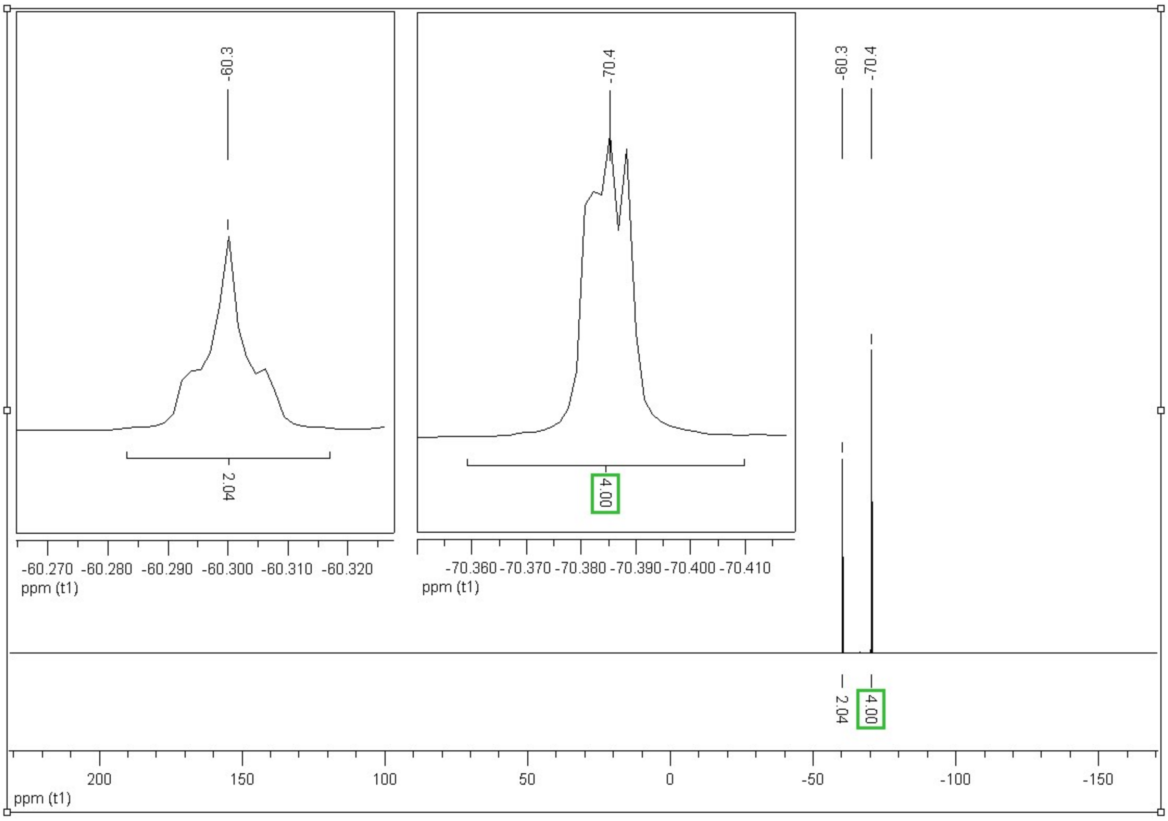

References

1. M. Bieri, M. Treier, J. Cai, K. Aït-Mansour, P. Ruffieux, O. Gröning, P. Gröning, M. Kastler, R. Rieger, X. Feng, K. Müllen and R. Fasel, *Chem. Commun.*, 2009, **0**, 6919-6921.
2. F. Leroux, R. Simon and N. Nicod, *Lett. Org. Chem.*, 2006, **3**, 948-954.
3. Y. Sakamoto, T. Suzuki, A. Miura, H. Fujikawa, S. Tokito and Y. Taga, *J. Am. Chem. Soc.*, 2000, **122**, 1832-1833.

.3 Paper #3

Efficient Simulation of Near-Edge X-ray Absorption Fine Structure (NEXAFS) in Density-Functional Theory: Comparison of Core-Level Constraining Approaches
G. S. Michelitsch and K. Reuter
J. Chem. Phys., accepted (2019)

Reprinted under the terms of the AIP Copyright Agreement.
©2018 AIP Publishing LLC

Efficient Simulation of Near-Edge X-ray Absorption Fine Structure (NEXAFS) in Density-Functional Theory: Comparison of Core-Level Constraining Approaches

Georg S. Michelitsch[1] and Karsten Reuter[1]
Chair for Theoretical Chemistry and Catalysis Research Center, Technische Universität München, Lichtenbergstr. 4, D-85748 Garching, Germany[a)]

(Dated: 29 January 2019)

Widely employed Near-Edge X-Ray Absorption Fine Structure (NEXAFS) spectroscopy probes a system by excitation of core electrons to unoccupied states. A variety of different methodologies are available to simulate corresponding spectra from first-principles. Core-level occupation constraints within ground-state Density-Functional Theory (DFT) represent a numerically most efficient means to this end that provides access to large systems, examples being surface adsorption, proteins, polymers, liquids, and buried, condensed phase interfaces (e.q. solid-liquid and solid-solid). Here, we systematically investigate the performance of different realizations of this approximate approach through the simulation of K-edge NEXAFS-spectra of a set of carbon and nitrogen-containing organic molecules. Variational collapse to the ground state and oscillatory convergence are the major complications of these approximate computational protocols. We present a modified version of the maximum-overlap method to achieve a self-consistent inclusion of electrons in virtual states for systems where convergence is hampered due to degeneracies. Our results demonstrate that reliable spectra allowing for a semi-quantitative analysis of experimental data are already obtained at the semi-local level of density functionals and with standard numeric atomic orbital basis sets.

Keywords: NEXAFS, core-hole constraining approaches, DFT, spectroscopy

I. INTRODUCTION

Core-level spectroscopies are among the most established characterization techniques in modern materials science, providing both chemical and structural information. In modern nanosciences, not only X-Ray Photoelectron Spectroscopy (XPS), but also advanced techniques such as Near-Edge X-Ray Absorption Fine Structure (NEXAFS) are important tools to study molecules in the gas phase as well as molecules or thin layers of molecules immobilized on a support.[1–8] Furthermore, dynamical systems such as liquids[9–15] and soft matter such as molecular crystals[16], polymers[17,18], and proteins[19] are objects of intense study, followed by the dynamics of material growth as for example graphene on copper[20] and oxidation processes of bulk condensed matter[21]. Always exciting a (core) electron in an energetically low-lying state through X-ray radiation, it is the energy and type of radiation that distinguishes different such spectroscopies. In XPS, the electron is entirely ejected, whereas in NEXAFS and related techniques the electron is excited to an unoccupied state. More information about the system can be obtained by multiple measurements with different polarity of the light (revealing magnetic properties) or at varying incidence angles (revealing orientational differences).

Notwithstanding this versatility, in surface-adsorption, supramolecular or dynamically changing systems, the multiplicity of chemical environments for the same species renders a straightforward interpretation of experimental spectra increasingly complex. Many overlapping peaks in the same energetic region combine to a single unresolved and broadened peak, while orbital hybridization diminishes the usefulness of reference spectra obtained for gas-phase molecules. In this situation, simulated spectra from independent first-principles calculations become invaluable for a reliable assignment.[18,22–30] However, especially for large systems such as frequently encountered in supramolecular or surface-adsorption contexts exceeding computational costs largely restrict the types of methodology that can be employed. While in principle highly accurate techniques such as time-dependent density-functional theory (DFT)[31–36], the Bethe-Salpeter approximation[37,38], coupled-cluster approaches[39–41], or multi-reference calculations[42–44] are available for an often quantitative simulation of NEXAFS spectra, in practice it is presently often only effective core-level occupation constraining approaches in ground-state DFT that are numerically feasible. This is especially true in cases of dynamically changing systems, where the experimental signature is a combination of many different molecular arrangements (e.g. liquids[9–15]) or a large number of possible (yet chemically different) excitation centers (e.g. proteins[19]). In these aforementioned effective constraining approaches, specific occupations of single-particle Kohn-Sham (KS) levels are enforced to mimic the core-excited state, and then the lowest-energy electronic configuration under this constraint is self-consistently determined.[45–50] On the positive side, this captures a dominant contribution to the important core-hole relaxation energy at numerical costs that are at the level of a regular ground-state DFT calcu-

---

[a)] georg.michelitsch@ch.tum.de

lation. On the negative side, different ways of changing the occupation of the targeted core and virtual states give rise to a range of differing computational protocols in this class of techniques. Most importantly, there are variants that explicitly consider the occupation of the formerly unoccupied KS state, requiring multiple calculations for different final states to assemble the total NEXAFS spectrum.[51,52] Other so-called implicit variants such as the Transition Potential (TP)[53] and eXcited electron and Core Hole (XCH)[54] method either neglect the excited final-state electron or only include it in an averaged way, and would, therefore, allow to compute a full spectrum with only one single calculation. As such the computational effort to simulate the spectroscopic signature can vary largely between different variants, while the advantage in terms of accuracy is often not clear. Although by explicitly considering the excited electron in the simulation better results are expected, the realization of such simulations is often impossible in practice due to problems associated with variational collapse and convergence of the electronic structure. Here, we partially address this problem with the introduction of a variant of the maximum overlap method[55], optimized for the usage in highly symmetric systems plagued by degeneracies. As has also been noted earlier[56], local basis set based approaches typically have problems to converge resonances above the ionization threshold. We acknowledge this problem (and further details on the performance of the MOM approach in our case can be seen in the supporting information) and also recognize it as probably one of the major arguments why we are interested in implicit variants, which by construction, eliminate the need for the inclusion of an excited electron. As for the variety of these implicit variants, we wish to elaborate on the different motivations as of why they were introduced and classify them according to similarities. This should help in the understanding as to which variant should be chosen based on the system under study and as of how the accuracy can be systematically improved. While establishing this hierarchy, we noticed the presence of gaps in terms of implicit approximations. We filled this gaps with the introduction of the Generalized Transition Potential (GTP) and eXcited transition potential (XTP), as well as eXcited Generalized Transition Potential (XGTP) approaches. In the current manuscript, we do not include mixed approaches which either correct selected excitation energies of an implicit spectrum by the explicit calculation via a ΔSCF ansatz[3] or via explicit modeling of the chemical shift of each atom via an additional explicit consideration of the lowest possible transition[57].

As particularly the class of explicit variants requires an adequate description of the (typically more diffuse) unoccupied KS states, a number of studies have assessed the numerical convergence of correspondingly simulated spectra for more common localized (Gaussian) basis sets.[47,55,58–63] In contrast, much less is known on the basis set requirements of the latter class of implicit variants (intuitively deemed less demanding) and generally for numeric atomic orbital (NAO) type basis sets.[64] Aiming to establish a numerically most efficient, yet robust protocol for large-scale NEXAFS simulations with NAO basis sets as for instance implemented in the full-potential DFT code FHI-aims[64,65], we, therefore, present a systematic investigation using a test set of nitrogen- and carbon-containing compounds. With an eye to maximally support the experimental assignment, we evaluate the influence of different basis sets and DFT functionals on both the correct peak positions and the peak intensities. We include variants explicitly treating the final state, like Δ Self-Consistent-Field (ΔSCF)[51] or the Transition State (TS)[52] model, and more approximate implicit variants like TP[53] or XCH[54,66–68]. The major and encouraging result is that a semi-quantitative spectral assignment is already possible for numerically most efficient implicit variants, standard basis set sizes and semi-local DFT functionals.

II. THEORY

A. Core-hole constraining approaches

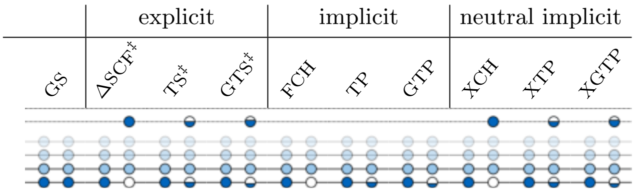

		explicit			implicit			neutral implicit		
	GS	ΔSCF‡	TS‡	GTS‡	FCH	TP	GTP	XCH	XTP	XGTP
	$\Delta\epsilon$	ΔE	$\Delta\epsilon$	$\Delta\epsilon$	$\Delta\epsilon$	$\Delta\epsilon$	$\Delta\epsilon$	$\Delta\epsilon$	$\Delta\epsilon$	$\Delta\epsilon$
q_c	1	0	½	⅓	0	½	⅓	0	½	⅓
q_v	0	1	½	⅔	0	0	0	1	½	⅔

FIG. 1. Schematic illustration of the occupational constraints used in various core-hole constraining approaches. The table shows the corresponding fractional occupations of the core, q_c, and virtual, q_v, Kohn-Sham eigenstate, whether the evaluation is based on total energy differences (ΔE) or KS eigenvalue differences ($\Delta\epsilon$), and whether the scheme explicitly considers the final-state excited electron (‡) or not. Explicit consideration requires that one separate calculation needs to be performed for each excited state configuration on each atom (many q_v for a single q_c), whereas the implicit neutral approaches typically explore only the lowest energy core-excited state (a single q_c constraint per atom).

Core-level occupation constraining approaches generally rely on time-dependent perturbation theory to compute the NEXAFS spectrum using Fermi's golden rule

$$P_{\mathrm{i}\to\mathrm{f}}(\omega) \;=\; \frac{2\pi}{\hbar}\mu_{\mathrm{if}}^2\Delta(E_{\mathrm{f}}-E_{\mathrm{i}}-\hbar\omega) \quad . \qquad (1)$$

An incident X-ray with frequency ω induces an electronic transition from an initial state i to a final state f with matching energy difference $\Delta E = E_{\mathrm{f}} - E_{\mathrm{i}}$ with a probability proportional to the transition dipole moment μ_{if}^2.

In order to determine this probability within ground-state DFT the excited-state energy E_f is then approximately computed by modifying the occupation of the single-particle KS states and achieving self-consistency under this occupational constraint. Various variants differ in the way how these occupations are modified, and whether they explicitly optimize every transition i $\rightarrow$ f separately or do this only implicitly in an average way. They are graphically summarized in Figure 1 and will be shortly introduced in the following.

In ΔSCF[51] the excited-state energy is computed as a total energy difference by explicitly removing one electron from the corresponding core level c and adding it to the virtual level v, resulting in a transition energy

$$\begin{aligned}\Delta E_{\Delta\mathrm{SCF}} = E_\mathrm{f} - E_\mathrm{i} = E(q_\mathrm{c} = 0, q_\mathrm{v} = 1) -\\ E(q_\mathrm{c} = 1, q_\mathrm{v} = 0) \quad . \end{aligned} \tag{2}$$

Here, q_c is the occupation of the core-state KS orbital and q_v is the occupation of the virtual KS state above the Fermi level. Throughout the work, we thereby stay within the realm of collinear spin-resolved DFT, where the maximum occupancy of a KS orbital is 1, and we follow the convention to denote total energies with negative numbers; the more negative, the more stable.

Other core-hole constraining approaches use this basic equation of ΔSCF as the starting point, rewrite it as an integral over the varying occupations during the electronic transition and employ the Slater-Janak theorem[69] $\frac{\partial E}{\partial q_\mathrm{i}} = \epsilon_\mathrm{i}$ to arrive at eq. (2) in terms of KS eigenvalues ϵ_i:

$$\begin{aligned}\Delta E_{\Delta\mathrm{SCF}} &=\\ &= \int_{x=1}^{0} \frac{dE(q_\mathrm{c} = x, q_\mathrm{v} = 1-x)}{dx} dx\\ &= \int_{x=1}^{0} \left\{ \frac{\partial E(q_\mathrm{c} = x, q_\mathrm{v} = 1-x)}{\partial q_\mathrm{v}} \right.\\ &\qquad \left. - \frac{\partial E(q_\mathrm{c} = x, q_\mathrm{v} = 1-x)}{\partial q_\mathrm{v}} \right\} dx\\ &= \int_{x=1}^{0} \{\epsilon_\mathrm{c}(q_\mathrm{c} = x, q_\mathrm{v} = 1-x)\\ &\qquad - \epsilon_\mathrm{v}(q_\mathrm{c} = x, q_\mathrm{v} = 1-x)\}\, dx \quad . \end{aligned} \tag{3}$$

Here, we performed a substitution and split the integral in two parts, because $\frac{\partial q_c}{\partial x} = 1$ and $\frac{\partial q_v}{\partial x} = -1$. In Slater's Transition State (TS) approach[52], the integral in eq. (3) is approximated via the midpoint rule $\int_a^b f(x)dx \simeq (b-a)f((a+b)/2)$. This results in

$$\begin{aligned}\Delta E_\mathrm{TS} = \epsilon_\mathrm{v}(q_\mathrm{c} = 0.5, q_\mathrm{v} = 0.5) -\\ \epsilon_\mathrm{c}(q_\mathrm{c} = 0.5, q_\mathrm{v} = 0.5) \quad . \end{aligned} \tag{4}$$

and bears the advantage that the transition energy can be obtained from two KS levels of one constrained-occupation DFT calculation. The Generalized Transition State (GTS) variant instead approximates the integral of eq. (3) by a two-point Gaussian quadrature including the ground state ($x = 0$) as the first point and $x = 1/3$ as the second, thereby lowering the integration error to fourth order[70,71]

$$\begin{aligned}\Delta E_\mathrm{GTS} &=\\ \left[\frac{1}{4}\epsilon_\mathrm{v}(q_\mathrm{c} = 1, q_\mathrm{v} = 0) + \frac{3}{4}\epsilon_\mathrm{v}(q_\mathrm{c} = {}^1\!/\!_3, q_\mathrm{v} = {}^2\!/\!_3)\right] &-\\ \left[\frac{1}{4}\epsilon_\mathrm{c}(q_\mathrm{c} = 1, q_\mathrm{v} = 0) + \frac{3}{4}\epsilon_\mathrm{c}(q_\mathrm{c} = {}^1\!/\!_3, q_\mathrm{v} = {}^2\!/\!_3)\right] &\quad . \end{aligned} \tag{5}$$

ΔSCF, TS and GTS all consider explicitly into which virtual state v the core electron is excited to. These explicit core-hole constraining variants therefore require a separate calculation for every transition i$\rightarrow$f to assemble the full NEXAFS spectrum. Implicit variants instead deem the actual impact of the excited electron on the KS level positions less important. Several of these variants therefore modify the occupation of the core level c, but leave the virtual level v indeed unoccupied also in the approximate calculation of the final-state energy E_f. These variants include the Transition Potential (TP)[53,72,73] and the Generalized Transition Potential (GTP) variant, representing the direct implicit analogs to TS and GTS:

$$\begin{aligned}\Delta E_\mathrm{TP} =& \epsilon_\mathrm{v}(q_\mathrm{c} = 0.5, q_\mathrm{v} = 0) -\\ & \epsilon_\mathrm{c}(q_\mathrm{c} = 0.5, q_\mathrm{v} = 0) \quad . \end{aligned} \tag{6}$$

$$\begin{aligned}\Delta E_\mathrm{GTP} &=\\ \left[\frac{1}{4}\epsilon_\mathrm{v}(q_\mathrm{c} = 1, q_\mathrm{v} = 0) + \frac{3}{4}\epsilon_\mathrm{v}(q_\mathrm{c} = {}^1\!/\!_3, q_\mathrm{v} = 0)\right] &-\\ \left[\frac{1}{4}\epsilon_\mathrm{c}(q_\mathrm{c} = 1, q_\mathrm{v} = 0) + \frac{3}{4}\epsilon_\mathrm{c}(q_\mathrm{c} = {}^1\!/\!_3, q_\mathrm{v} = 0)\right] &\quad . \end{aligned} \tag{7}$$

The Full Core Hole (FCH)[13,74,75] approach, in turn, excites a full core electron as in ΔSCF

$$\begin{aligned}\Delta E_\mathrm{FCH} =& \epsilon_\mathrm{v}(q_\mathrm{c} = 0, q_\mathrm{v} = 0) -\\ & \epsilon_\mathrm{c}(q_\mathrm{c} = 0, q_\mathrm{v} = 0) \quad . \end{aligned} \tag{8}$$

The FCH approach was successfully applied to the simulation of X-ray absorption spectra of water and ice[13], and fullerenes[57,76], while the TP approximation was found to perform well for organic molecules[53,77,78]. Interestingly, the obvious GTP analog to the GTS variant has not been considered before, and we include it in this study for completeness.

The big numerical advantage of these implicit approaches is that a full NEXAFS spectrum can be obtained from a single (core-level constrained) DFT calculation, simply evaluating the transition energies to the different virtual KS states. A certain disadvantage, especially with respect to an envisioned application to surface-adsorption systems typically calculated in periodic boundary condition supercells, is that an effectively charged system is created by removing (parts of) a core electron without compensating for it through the occupation of a virtual state. As such, the XCH approach[54] is finally of particular interest. This approach creates a charge neutral final state by following the ΔSCF philosophy to excite a full core electron to a virtual KS state. Simultaneously, however, it maintains the advantages of implicit variants by simply choosing the lowest unoccupied molecular orbital (LUMO) as this virtual KS state throughout. In other words, one occupation-constrained calculation is performed with the excited electron in the LUMO (designated by variable q_{l}), and the entire spectrum is determined from it by reading off all virtual KS level positions

$$\begin{aligned}\Delta E_{\mathrm{XCH}} =&\epsilon_{\mathrm{v}}(q_{\mathrm{c}}=0, q_{\mathrm{l}}=1) - \\ &\epsilon_{\mathrm{c}}(q_{\mathrm{c}}=0, q_{\mathrm{l}}=1) \quad . \end{aligned} \tag{9}$$

Interestingly, the obvious transfer of this idea to the half core-hole TP and GTP approaches has also not yet been tried. To arrive at a systematic assessment, we therefore also consider corresponding XTP and XGTP occupation constraints in this study and will refer to this class of variants (XTP, XGTP, XCH) as charge-neutral implicit approaches, in contrast to the prior class of ionized implicit variants (TP, GTP, FCH)

$$\begin{aligned}\Delta E_{\mathrm{XTP}} = &\epsilon_{\mathrm{v}}(q_{\mathrm{c}}=0.5, q_{\mathrm{l}}=0.5) - \\ &\epsilon_{\mathrm{c}}(q_{\mathrm{c}}=0.5, q_{\mathrm{l}}=0.5) \quad . \end{aligned} \tag{10}$$

$$\begin{aligned}&\Delta E_{\mathrm{XGTP}} = \\ &\left[\frac{1}{4}\epsilon_{\mathrm{v}}(q_{\mathrm{c}}=1, q_{\mathrm{l}}=0) + \frac{3}{4}\epsilon_{\mathrm{v}}(q_{\mathrm{c}}={}^{1}\!/_{3}, q_{\mathrm{l}}={}^{2}\!/_{3})\right] - \\ &\left[\frac{1}{4}\epsilon_{\mathrm{c}}(q_{\mathrm{c}}=1, q_{\mathrm{l}}=0) + \frac{3}{4}\epsilon_{\mathrm{c}}(q_{\mathrm{c}}={}^{1}\!/_{3}, q_{\mathrm{l}}={}^{2}\!/_{3})\right] \quad . \end{aligned} \tag{11}$$

B. Preventing variational collapse

The targeted non-ground-state KS occupation is the key conceptual aspect that distinguishes the various core-hole constraining variants. The major practical concern common to all variants is to achieve this occupation in the ensuing SCF cycle and prevent the variational collapse to the ground state. The objective is thus to identify in every SCF step of the constrained-occupation calculation which core orbital has the largest overlap with the targeted core orbital of the ground-state calculation so as to be able to enforce its occupation according to the recipe of the particular variant, cf. Table I. For the explicit approaches, the same holds for the identification of the virtual orbital that is to be filled, while for the charge-neutral implicit approaches, this holds for the identification of the LUMO. Recent approaches to this problem include local SCF (LSCF)[79,80], linear expansion (leΔSCF)[81,82], constricted variational (CV-ΔSCF)[83–87], orthogonality constrained (OC-ΔSCF)[88,89] and σ-SCF[90]. For the small molecular systems considered in this work, we instead maintain an originally specified occupational constraint during the SCF cycle by employing the maximum overlap method (MOM)[55,91]. At every SCF step, this method evaluates which KS state has the largest overlap with the occupation-constraint KS state in the previous SCF step and then modifies its occupation accordingly. To this end, it forms the orbital overlap matrix $\mathbf{O}$

$$\mathbf{O} = (\mathbf{C}^{\mathrm{old}})^{\dagger}\mathbf{S}\mathbf{C}^{\mathrm{new}} \quad , \tag{12}$$

where $\mathbf{C}^{\mathrm{old}}$ and $\mathbf{C}^{\mathrm{new}}$ are the molecular-orbital coefficient matrices of the previous and current SCF iteration, respectively, and $\mathbf{S}$ is the overlap matrix. The projection of a state in the new KS eigenspace on the old eigenspace can then be written as

$$p_s = \sum_{r}^{n} O_{rs} = \sum_{\nu}^{N}\left[\sum_{\mu}^{N}\left(\sum_{r}^{n} C^{\mathrm{old}}_{r\mu}\right) S_{\mu\nu}\right] C^{\mathrm{new}}_{\nu s} \quad . \tag{13}$$

Here, p_s is the projection of state s in the subspace of the new KS eigenvector projected on the KS eigenvector in the previous iteration. n spans all occupied states of the old KS eigenvector, and μ and ν are iterators over all basis functions of total number N. In our study of core-hole excitations, we want to propagate a single state through the SCF cycle. Therefore, we project the previously constrained KS state on to a subspace of the new eigenvector to identify the new state with a modified occupation, essentially inverting the typical MOM-procedure. To this extent we calculate the projection $\tilde{p}_s$ of the constrained state on a subspace spanning from n_{i} to n_{f}. The occupational constraint is then propagated on the KS state of largest $\tilde{p}_s$

$$\tilde{p}_s = \sum_{\nu}^{N}\left[\sum_{\mu}^{N}\left(\sum_{r=n_{\mathrm{i}}}^{n_{\mathrm{f}}} C^{\mathrm{new}}_{r\mu}\right) S_{\mu\nu}\right] C^{\mathrm{old}}_{s\nu} \quad . \tag{14}$$

In the original MOM approach the subspace to be projected on was split into all occupied and all virtual KS states of the ground state calculation, and then constraints to enforce the hole and to enforce the occupation of a virtual state were separately projected on each manifold. In this work, we found this most general procedure to lead to massive convergence problems (SCF oscillations). We therefore developed a more restricted approach as follows: For K-edge NEXAFS, we are specifically interested in the lowest-energy 1s states of carbon (or nitrogen). We therefore restrict the occupied subspace to the m degenerate lowest-energy KS states of the ground-state calculations for a molecule containing m C (or N) species. For those variants that additionally require an enforced occupation of an virtual state LUMO+k, we initially define the unoccupied MOM subspace to only consist of the ground-state orbitals [LUMO, LUMO+k]. This considers that the occupation of a virtual orbital typically lowers its energy. We found that only in a few cases, state reordering shifts the targeted KS state above this range. In those cases, reflected by MOM overlaps ($\tilde{p}_s$) below 10% we then gradually expanded the MOM subspace to [LUMO, LUMO+$k+x$],

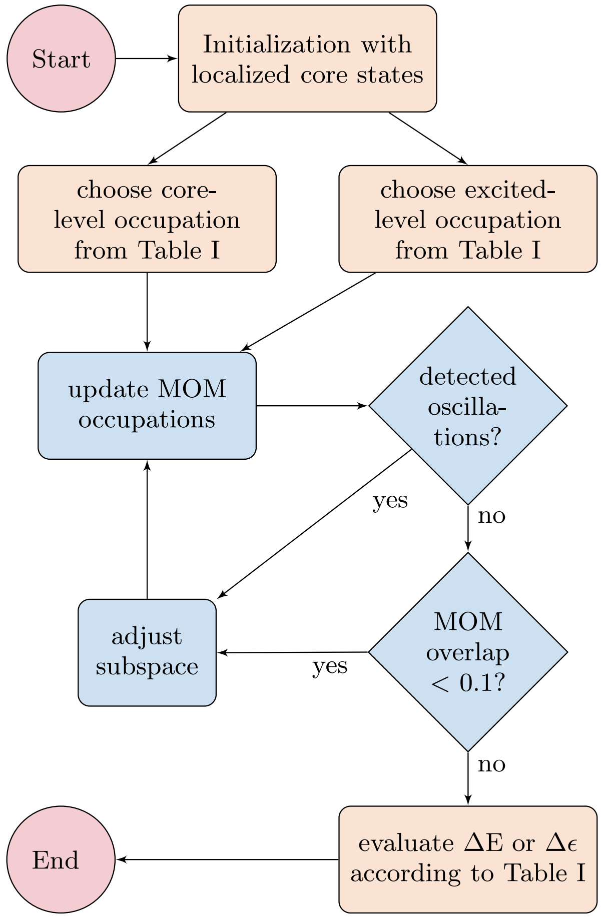
Start
Initialization with localized core states
choose core-level occupation from Table I
choose excited-level occupation from Table I
update MOM occupations
detected oscillations?
yes
no
adjust subspace
MOM overlap < 0.1?
yes
no
evaluate ΔE or Δϵ according to Table I
End

FIG. 2. Employed workflow to achieve robust NEXAFS simulations using the maximum-overlap method (MOM). The part highlighted in blue is executed at each SCF step until SCF convergence is achieved.

$x > 1$ until higher overlaps where found. In those cases, where oscillations between degenerate orbitals still prevail in the restricted [LUMO, LUMO+k] subspace, we instead gradually shrank the subspace further to [LUMO, LUMO+$k-x$], $x > 1$. A schematic workflow of our approach is shown in Fig. 2. We validated that this workflow led to the correct occupations by comparing the initial and final eigenvector belonging to the state with a modified occupation in terms of their major constituent basis functions. We find that the principal character of the KS state does not change if we apply our modified MOM-procedure. A comparison of our modified MOM procedure in comparison with the original approach including occupational smearing is provided in the supporting information. While the modified MOM-procedure thus enabled the systematic benchmark performed in this work, we nevertheless emphasize that reaching convergence and correct occupations in case of the explicit variants is a strenuous endeavor that requires a lot of human interference and control, as is also highlighted in the supporting information where our modified method, although prevailing over the original approach, can not resolve the entirety of explicitly occupied virtual states. This is another aspect that strongly favors the implicit variants, for which achieving correct occupations of the modified core state was generally found to be straightforward with our modified MOM-procedure. We note in this respect, that a popular alternative to the MOM method in plane-wave implementations of DFT is the usage of pseudopotentials, where either the atom carrying the core-hole is described by a pseudopotential created with a core-ionization[18,22,54,92] or through the reverse strategy of self-consistently determining the core-hole state (described in an all-electron form) and replacing all other atoms of the same species by an effective pseudo-potential (ECP)[3,53,93]. Either way, the requirement for a mechanism to keep the core-hole localized is lifted.

C. Computational Details

The collinear spin-resolved DFT calculations were performed using the FHI-aims package[64,65]. Electronic exchange and correlation (xc) were treated on the generalized-gradient approximation (GGA) level with the PBE[94] functional and at the hybrid functional level with the PBE0[95] functional. The ground-state geometry of all molecules was fully relaxed until residual forces were below 10^{-3}eV/Å. The occupational-constraint excited state calculations were then conducted on these optimized ground-state geometries.

FHI-aims uses numeric-atomic orbital (NAO) localized basis sets. The standard basis sets for semi-local functionals are categorized into tier levels of increasing basis set size and accuracy. Basis set convergence was evaluated by running tier1, tier2, and tier3 calculations. As further detailed in the original FHI-aims publication,[64] the tier1 set consists of the minimal basis (chosen as the solution of the free atom) and, additionally, ionic and hydrogenic basis functions, determined in an automated procedure and ordered by their magnitude of improvement of interatomic binding energies. The tiers naturally arise as groups of different angular momenta *spd* (tier1), *spd(f,g)* (tier2), etc. similar to the intuitive construction in Gaussian basis sets[96–98] and are hierarchically organized, with a higher tier always including all functions of the lower tier. The tier basis sets were constructed and optimized for total energy differences and the usage at the local-density (LDA) and generalized-gradient approximation (GGA) functional level.[64] They may be used for higher-rung functionals, too. However, a valence-correlation-consistent NAO-VCC basis set family[99] has been specifically constructed for such calculations, following the same principle as also used for Dunning-type Gaussian basis sets[100] at the cc-pV2Z, cc-pV3Z, and cc-pV4Z level. In terms of available basis functions, these basis sets are comparable to the tier1, tier2, and tier3 basis sets, respectively. For all basis sets, integration on the numerical grids was carried out at the "tight" level implemented in FHI-aims.[64]

For the occupation-constraint calculations, the core-state orbitals were first maximally localized at the end of the ground-state calculation by following the procedure outlined by Foster and Boys[101,102]. This was then used as an initial guess with the modified occupations as shown in Figure 1 and preventing variational collapse during the ensuing SCF cycle following the MOM scheme described in Fig. 2. To determine intensities belonging to each transition energy, we evaluated the transition dipole moment between the core state i and each unoccupied state f entering eq. (1) as

$$\mu_{\mathrm{if}} = \langle \phi_{\mathrm{i}} | \hat{x} | \phi_{\mathrm{f}} \rangle \quad , \tag{15}$$

where ϕ_{i} and ϕ_{f} are the KS eigenvectors of states i and f, respectively. For the explicit models, each transition dipole moment was determined from the corresponding calculation with a modified final state occupation of state f.

III. RESULTS

A. Benchmark approach

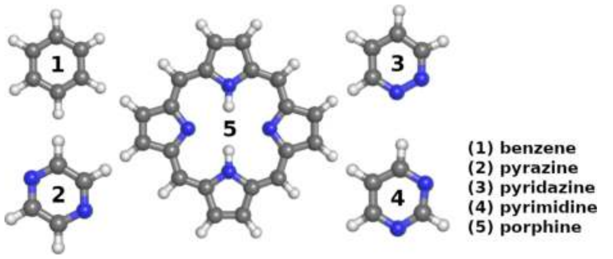

FIG. 3. C and N containing molecules forming the considered benchmark set (C = gray spheres, N = blue spheres, H = white spheres).

For our benchmark study we consider the five molecules shown in Fig. 3: benzene (C_6H_6) and the four heterocyclic molecules pyrazine ($C_4N_2H_4$), pyridazine ($C_4N_2H_4$), pyrimidine ($C_4N_2H_4$), and porphine ($C_{20}N_4H_{14}$). The small size of the molecules and the C_2 rotational axis present in their gas-phase structure would in principle readily allow for highly accurate computational spectroscopy approaches. However, when adsorbed at a transition metal surface, the likely break of symmetry[103] and the necessity to explicitly treat the extended surface in a periodic boundary supercell[22] approach rapidly increases the computational cost to render effective core-hole constraining approaches an appealing option. We compare the calculated NEXAFS spectra to experimental data either from gas-phase measurements (benzene[77], pyridazine[104], pyrimidine[104], pyrazine[104]) or from multilayer magic-angle measurements, where no angle-dependency is present and the molecule-surface interaction can be neglected (porphine[105]). In our comparison we specifically focus on the near-edge region and therefore consider the three lowest-energy excitations/peaks. This corresponds to an interval of approximately 3 eV above the carbon 1s edge and approximately 6.5 eV above the nitrogen 1s edge. To quantify the deviation from the experimental signatures, we measure the error in the simulated peak position relative to the first edge peak

$$\mathrm{error}_{\mathrm{eng}}[\%] = 100 - \frac{(\text{peak energy - edge peak energy})_{\mathrm{comp}}}{(\text{peak energy - edge peak energy})_{\mathrm{exp}}} \quad . \tag{16}$$

This measure of the error in energy is taken relative to the correct (experimental) value and both over- and underestimation of the excitation energy is captured in the following analysis, where a positive value corresponds to an underestimation and a negative value to an overestimation of the transition energy. An equivalent approach is pursued for the simulated intensities, here normalizing to the edge peak intensity

$$\mathrm{error}_{\mathrm{int}}[\%] = \frac{(\text{peak intensity/edge peak intensity})_{\mathrm{comp}}}{(\text{peak intensity/edge peak intensity})_{\mathrm{exp}}} \quad . \tag{17}$$

For the considered molecules, the experimental near-edge spectrum corresponds primarily of well-separated high-intensity peaks. This allows for a facile identification and assignment of the peaks. Only in a few cases, particularly for the C-edge spectra of the larger compound porphine, some experimentally observed peaks are made up from two (or more) overlapping resonances. In this case, we used the higher intensity resonance for the benchmarking and are well aware of the possible (small) systematic error thus included in our analysis.

B. Method comparison: Transition Energies

Figure 4 compiles the box-plots of the error in the calculated transition energies for the different core-hole occupation constraining approaches. Here we first focus on the PBE functional and tier2 basis sets, as this would currently correspond to the affordable state-of-the-art to describe metal-adsorption systems (or possibly including a +U correction for semiconductor-adsorption systems). We return to a discussion of the xc functional and the basis set size dependence below. The median error of all approaches is rather low and lies generally around and below 10%. A notable exception are the transition potential based approaches (TP, GTP and XGTP), which seem to have a particular problem with reproducing the carbon peak positions. Among the computationally most demanding explicit variants, the TS approach performs best (median error: -2.9%). However, the best performing charge-neutral implicit approaches, XTP (median error: +1.6%) and XCH (median error: +4.8%) are comparably good. Within the considered near-edge region,

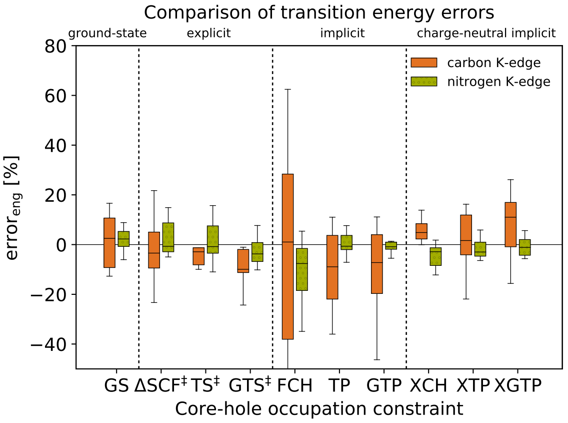

FIG. 4. Box plot of the error in the transition energies as defined in eq. (16) for the considered range of core-hole occupation constraining approaches (using DFT-PBE and a tier2 basis set). The upper and lower limits of the rectangles (interquartile range, IQR) mark the 75% and 25% percentiles, the internal horizontal line marks the median, and the "error bars" mark the 99% and 1% percentiles (defining the maximum absolute errors, MAEs).

peak position deviations around 10% correspond to absolute errors below a few tenths of eV, in line with 1s→ π^* excitation energy accuracies of previous reports in the GTS approximation[46,73,106]. This would generally be sufficient for an assignment of experimental spectra as exemplified below. The superficial look at the median error would therefore suggest essentially all of the tested variants as viable.

A more differentiated view is instead obtained from the more detailed analysis of the interquartile range (IQR) and maximum absolute errors (MAEs) also contained in the box plot in Fig. 4. Here, clear performance differences arise between the different variants, revealing partly exceedingly large errors. In particular, for the FCH variant, the low median error seems to arise from a favorable cancellation of partly unacceptably large errors. Reports, which prefer this FCH variant over other approximations do this on account of a better description of the intensities[13,57], which, as discussed in a moment, is indeed the case. Other authors also report exceedingly large energetic deviations of the FCH variant, with much better results obtained from a TP[53], or even a GS calculation[107]. Interestingly, also with respect to the IQR, which contains 50% of the data and thus spans from the lower to the upper quartile, and the MAEs, there is a significant element-specific performance, with all variants better able to reproduce the nitrogen spectra.

Henceforth considering the IQR as a good performance indicator, we also arrive at partly unexpected insights regarding the approximation of the excited-state energy itself. The consideration of the core-hole relaxation energy contribution through the explicit change of level occupations in the ΔSCF method does intriguingly not lead to a dramatic performance improvement as compared to a straightforward ground-state calculation. In fact, in case of the nitrogen 1s peaks, it even worsens the IQR. Even more surprisingly, the TS and GTS approaches, which are in principle nothing but a reformulation of the ΔSCF approach plus an integral approximation, lead to somewhat improved IQRs as compared to ΔSCF itself. This suggests a favorable cancellation of errors either within these effective approaches or in the interplay with the approximate DFT functional. Such cancellation effects would also help to understand why the complete neglect of the excited electron in the implicit TP and GTP variants apparently lowers the N 1s IQR compared to the physically more accurate explicit approaches, whereas the C 1s IQRs show the expected trend with explicit variants exhibiting the lowest IQR, implicit variants (FCH, TP, GTP) the highest IQR – and the implicit charge-neutral variants (XCH, XTP, XGTP) with their average consideration of the excited electron somewhat performing intermediate between these two.

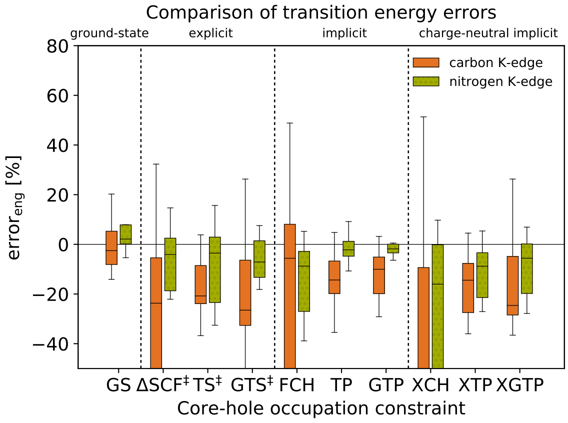

FIG. 5. Same as Fig. 4, but now using the hybrid functional PBE0 and a NAO-VCC-3Z basis set.

In order to assess the role of the DFT functional in such error cancellation we, therefore, repeated all calculations with the hybrid functional PBE0. For the pure gas-phase molecules, this functional will definitely yield a significantly improved ground-state electronic structure. The results obtained with the FHI-aims NAO-VCC-3Z basis set are summarized in Fig. 5. While no experience with this recommended basis set class for levels of theory including exact exchange exists for NEXAFS calculations, triple-zeta type Gaussian bases are frequently recommended for the calculation of core ionization or core excitation[47,59,60,63]. Intriguingly, we obtain a rather mixed result. For a few variants (GS, TP, GTP) we obtain the anticipated improvement with this higher-rung functional, in particular with respect to the C1s IQRs that were found to be particularly problematic at the DFT-GGA level. For all others, errors, in fact, increase at least by 10-20%. A closer look reveals that these are unanimously those variants that include the occupation of virtual states, i.e., the explicit variants (ΔSCF, TS, GTS) and the charge-neutral implicit variants (XCH, XTP, XGTP). The FCH approach remains in its IQR performance as abysmal as it was before.

We should note that the performance of a hybrid functional for the virtual KS states of the electronic ground state was for instance already analyzed previously by van Meer *et al.* (there as basis for a time-dependent DFT-treatment)[108]. The conclusion was that the eigenstates were too diffuse, in some instances even unphysical. Other authors also reported large error bars in ΔSCF calculations of 0.5 eV for first-row elements and 1.5 eV for second-row elements when using a hybrid functional[55]. This could suggest that the partly good performance obtained for these variants at the PBE level results indeed (largely) from an effective error cancellation between approximate semi-local DFT functional and effective treatment of the core-excitation. To this end, we also have to note the construction concept of the FHI-aims NAO basis sets though. While the correlation-consistent Dunning Gaussian basis sets were validated based on single and double excitations[100], the basis functions in both classes of FHI-aims basis sets (tier and NAO-VCC-nZ bases) targeted the total ground-state energy. In NAO-VCC-nZ this relates to spherically symmetric atoms in the frozen-core random-phase approximation[99], and for the tier basis sets, the total energy of atomic dimers in the LDA-approximation[64]. They were hitherto only validated to perform well for covalent bonds and isomerization energies. In particular, the lack of additional diffuse functions (present in the aug-type Dunning basis sets) and the optimization of valence-correlation consistency only in the NAO-VCC-nZ bases, could yield a particularly bad description of the energy differences between occupation-constrained core and valence states entering the NEXAFS transition energies. The really slow basis set convergence described below for the NAO-VCC-nZ bases could indeed hint at the inadequacy of these basis sets in describing these important KS energy differences.

While a full identification of the reason behind the poor performance of explicit and implicit charge-neutral variants at hybrid level has to await the construction of new tailored basis sets (which is beyond the scope of the present study), we note that it is predominantly GGA functionals that are currently of interest/affordable for surface-adsorption calculations. In fact, already the PBE0/NAO-VCC-3Z calculations behind the gas-phase molecule benchmark of the explicit variants in Fig. 5 involved a computational cost that fully defeats the purpose of these effective NEXAFS simulation approaches.

C. Method comparison: Transition Intensities

For computational spectroscopic support, a reliable description of the peak intensities is almost as important as the correct description of the peak energies. In Fig. 6 we, therefore, compile the determined errors in the intensities as evaluated according to eq. (17), and again explicitly summarizing mean errors, IQRs, and MAEs in the shown box plot. Here, a simple ground-state calculation is clearly inadequate, with exceeding errors in all three performance indicators. All other variants perform significantly better, in fact with not too much variation between them. Their median is consistently below 100%, which means that the intensity of the edge peak is consistently overestimated with respect to the other higher transitions. We suspect additional contributions to the experimental intensity of the edge peak as a possible reason for this consistent overestimation. One contribution could come from forbidden transitions, which receive finite intensity in experiment through thermally induced motion/symmetry breaking and thus reduce the actual intensity of the edge peak. There are currently two major ways as of how these broadening of the peaks and the associated decrease in main peak intensity can be included in the simulation, either by resolving the vibronic structure (coupling of vibrational and electronic states via the linear coupling model[3,7,109,110]) or by following the Herzberg-Teller effect[111] and including temperature broadening by either doing classical or ab-initio MD sampling of the system and then averaging over different snapshots of the trajectory[9–13,15,16,112–114]. Another methodology calculates the spectroscopic signatures for geometries at the turning point of each vibrational mode[17].

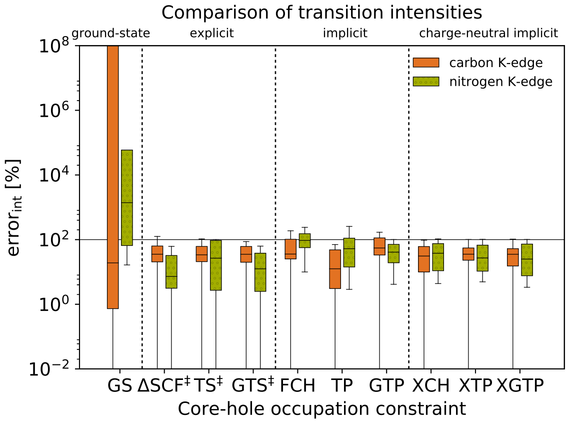

FIG. 6. Same as Fig. 4 (using DFT-PBE and a tier2 basis set), but now for the error in the transition intensities.

While such vibrational simulations would certainly be desirable, we note that apart from this overestimation of the edge peak all IQRs are consistently small. This demonstrates that even without such vibrational corrections, essentially all variants will be able to reliably determine the remaining spectral profile. Noteworthy, the FCH approach has the smallest IQR and is the only variant with an IQR partially above 100%, as had also been noticed for GGA-type calculations of water[54]. This holds as well for our benchmarks at the hybrid functional PBE0

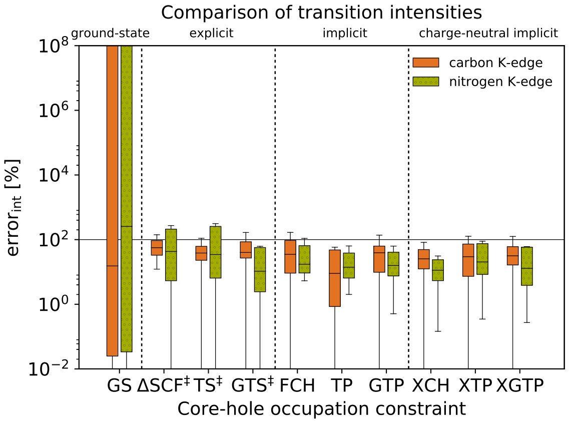

FIG. 7. Same as Fig. 6, but now for the error in the transition intensities using PBE0 and a NAO-VCC-3Z basis set.

level, which we compile for completeness in Fig. 7, even though as discussed above there are presently clear issues with calculations at this level of theory in FHI-aims. Correspondingly, we also exemplify the reliable determination of the spectral profile for the GGA-level aspired for the surface-adsorption context, and in particular in Fig. 8 we show a comparison of experimental data for the porphine molecule[105] and the constituent resonances as determined by the simulation using the charge-neutral implicit XTP variant.

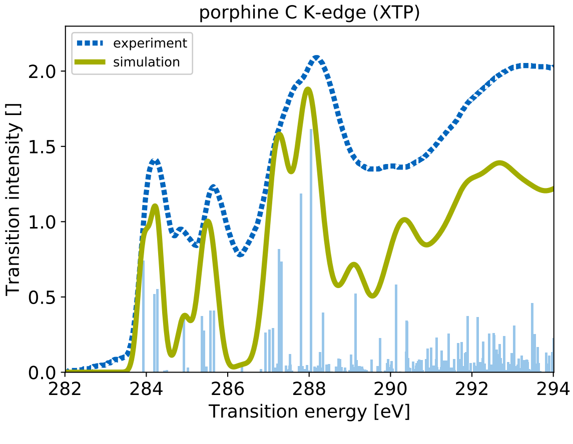

FIG. 8. Experimental[105] and simulated NEXAFS carbon K-edge spectrum of the porphine molecule. Simulation at the PBE/tier-2 level of theory using the XTP approximation. Shown are the calculated transition energies (light blue) and a spectrum generated by the superposition of the Gaussian-broadened delta peaks with linearly increasing broadening between 0.32 and 1.6 eV toward higher transition energies, which is common practice in the computational analysis of NEXAFS spectra[3,115] (green curve).

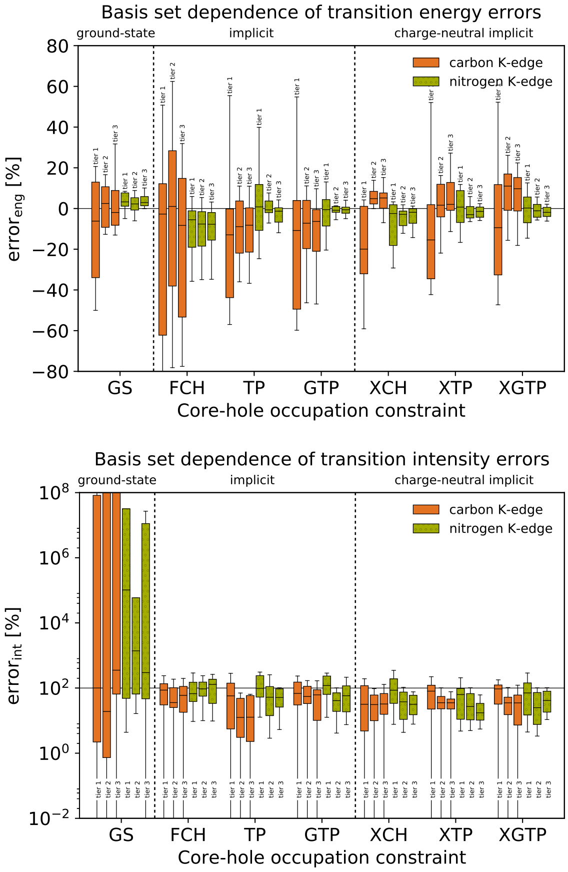

FIG. 9. Convergence of the excitation energy (upper panel) and excitation intensities (lower panel) with respect to the hierarchical tier basis sets for PBE calculations. See Fig. 4 for an explanation of the shown box plots.

D. Basis set dependence

NEXAFS probes the unoccupied, more delocalized states of the given system. One would therefore generally expect a slower convergence with basis set size for localized bases[116], even if only the energetically lowest-lying unoccupied states are targeted in simulations of the near-edge region. This has been confirmed in the spectroscopic context in simulations of excitations to outer-shell valence states using the ΔSCF method[62]. As shown in Fig. 9 for PBE and in Fig. 10 for PBE0 we indeed observe consistent improvements in the transition energies notably for the IQRs when increasing the hierarchic tier and NAO-VCC-nZ basis sets in FHI-aims. Nevertheless, at the tier2 and NAO-VCC-3Z basis sets employed as default in the previous sections a convergence is reached that justifies the conclusions made. We expect a similar convergence also for the explicit variants for which we could not afford a systematic convergence test at the largest (tier3, NAO-VCC-3Z) basis set, partly due to insuperable convergence problems.

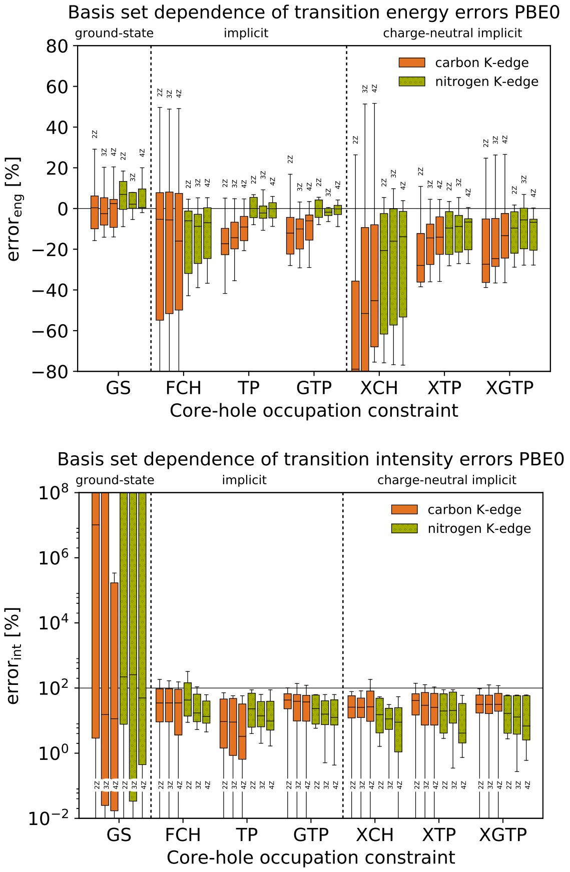

FIG. 10. Same as Fig. 9, but for the hierarchical NAO-VCC-nZ basis sets for PBE0 calculations.

At the PBE level, the smallest tier1 basis set is clearly not apt to describe the transitions, and we observe partly abrupt changes to the next larger tier2 basis set, in particular in the more sensitive performance indicators IQR and MAE. Here, we ascribe the especially pronounced improvements in the carbon spectra for instance to the additionally available p-type basis functions in the tier2 set. Further available functions in the tier3 set do not seem to lead to any systematic improvement, but this might also simply be masked by error cancellation with the approximate DFT functional as discussed above. Literature is also not clear at this point, with diffuse functions once found to be required in GGA calculations of K-edge absorption spectra of small molecules using ΔSCF[62]. In contrast and also at the GGA level, van Meer *et al.* report that a large basis set introduced a clustering of many spurious states with low oscillator strengths in the virtual space at an energy of -ϵ_{HOMO}, above which the states do not correspond well to excitation energies anymore[108]. Similarly, when using hybrid DFT functionals in another study[58], the authors also experienced that including too many diffuse basis functions can lead to a decrease in accuracy – a behavior we also observe for many variants in the nitrogen transition energies.

Generally, however, we emphasize particularly the different convergence behavior of the different variants and of the MAEs at the two functional levels. In our view, the prior clearly indicates again quite a degree of unsystematic error cancellation between finite basis set and effective treatment of the excited state energy. In turn, the latter seems to support our assessment that there is a general problem with the presently available NAO-VCC-nZ basis sets for such kind of simulations. In fact, we obtain even worse performance and comparably bad convergence behavior when using the tier basis sets designed for the semi-local functionals in the PBE0 calculations. As already seen when comparing the different variants in Section III.C the transition intensities are much less demanding in this respect. Satisfactory relative intensities will already be obtained with moderate basis sets and quite consistently over all variants.

IV. CONCLUSION AND OUTLOOK

We have systematically assessed a wide range of variants within the core-level occupation constraining approach to simulating NEXAFS spectra. Its comparably high numerical efficiency makes this approach particularly appealing for (very) large systems as typically encountered in the context of supra-molecular assembly or surface adsorption. At the same time, its highly approximate treatment of the excited state energies calls for systematic tests concerning its reliability. Using a dedicated set of C- and N-containing molecules, our benchmark indeed points at quite some degree of error cancellation between the effective treatment of the excited state energy, the approximate exchange-correlation functional and the finite localized basis set used in the underlying DFT calculations. Focusing not only on the average reproduction of transition energies and intensities, but also considering more sensitive performance indicators like the interquartile range and maximum absolute error, our study identified in particular the presently available hierarchical numeric-atomic orbital basis sets (tier and NAO-VCC-nZ) in the general program package FHI-aims as not suitable for NEXAFS simulations on the basis of higher-rung functionals including exact exchange.

For the representative semi-local DFT functional PBE, we instead find all tested variants to overall yield reliable spectra already at a moderate basis set size. Reliable here refers to an accuracy that affords a semi-quantitative analysis of experimental data. Particularly appealing for surface adsorption calculations are the so-called charge-neutral implicit variants, as they conform easily with periodic boundary condition supercells. Within this class of variants, we find in particular the XCH and XTP variants to perform most robustly in our benchmark, with the latter variant in our view having a somewhat better motivated mathematical basis (and thus potentially exhibiting a better transferability). The implicit nature of these variants, i.e. allowing to obtain a full NEXAFS spectrum out of one constrained-occupation DFT calculation, renders them numerically much more feasible than earlier explicit variants, for many of which in fact already the compilation of the NEXAFS spectra for the present set of gas-phase molecules becomes real cumbersome. Simultaneously, the here established protocol of preventing variational collapse of the exciton through the maximum overlap method ensured a swift self-consistency for these charge-neutral implicit variants as known from the alternative class of ionized implicit variants that completely neglect the excited electron in the unoccupied subspace.

SUPPLEMENTARY MATERIAL

Supplementary material including more details on our modified maximum overlap method (MOM) as well as the convergence behavior of explicit methods for small molecules is available online.

ACKNOWLEDGMENTS

The authors gratefully acknowledge support by the TUM Institute for Advanced Studies and the compute and data resources provided by the Leibniz Supercomputing Centre (www.lrz.de). We are also thankful for fruitful discussions with Katharina Diller, Reinhard Maurer, and Volker Blum.

[1] J. Stöhr, *NEXAFS Spectroscopy*, Springer Series in Surface Sciences, Vol. 25 (Springer Berlin Heidelberg, Berlin, Heidelberg, 1992).

[2] J. G. Chen, Surf. Sci. Rep. **30**, 1 (1997).

[3] C. Kolczewski, R. Püttner, O. Plashkevych, H. Ågren, V. Staemmler, M. Martins, G. Snell, A. S. Schlachter, M. Sant'Anna, G. Kaindl, and L. G. M. Pettersson, J. Chem. Phys. **115**, 6426 (2001).

[4] H. Wende, Rep. Prog. Phys. **67**, 2105 (2004).

[5] J. J. Rehr and A. L. Ankudinov, Coord. Chem. Rev. **249**, 131 (2005).

[6] H. Öström, H. Ogasawara, L.-A. Näslund, K. Andersson, L. G. M. Pettersson, and A. Nilsson, J. Chem. Phys. **127**, 144702 (2007).

[7] G. Fronzoni, O. Baseggio, M. Stener, W. Hua, G. Tian, Y. Luo, B. Apicella, M. Alfé, M. de Simone, A. Kivimäki, and M. Coreno, J. Chem. Phys. **141**, 044313 (2014).

[8] C. Gattinoni, P. Tsaousis, C. Euaruksakul, R. Price, D. A. Duncan, T. Pascal, D. Prendergast, G. Held, and A. Michaelides, Langmuir (2019), 10.1021/acs.langmuir.8b03528.

[9] L. Kong, X. Wu, and R. Car, Phys. Rev. B **86**, 1 (2012), arXiv:1204.0268.

[10] P. Wernet, Science **304**, 995 (2004).

[11] M. Iannuzzi, J. Chem. Phys. **128**, 204506 (2008).

[12] W. Chen, X. Wu, and R. Car, Phys. Rev. Lett. **105**, 1 (2010), arXiv:0909.3752.

[13] B. Hetényi, F. De Angelis, P. Giannozzi, and R. Car, J. Chem. Phys. **120**, 8632 (2004).

[14] J. W. Smith and R. J. Saykally, Chem. Rev. **117**, 13909 (2017).

[15] Y. Matsui and T. Mizoguchi, Chem. Phys. Lett. **649**, 92 (2016).

[16] C. P. Schwartz, R. J. Saykally, and D. Prendergast, J. Chem. Phys. **133**, 044507 (2010).

[17] S. D. Perera, S. Shokatian, J. Wang, and S. G. Urquhart, J. Phys. Chem. A **122**, 9512 (2018).

[18] G. M. Su, S. N. Patel, C. D. Pemmaraju, D. Prendergast, and M. L. Chabinyc, J. Phys. Chem. C **121**, 9142 (2017).

[19] J. Stewart-Ornstein, A. P. Hitchcock, D. Hernández Cruz, P. Henklein, J. Overhage, K. Hilpert, J. D. Hale, and R. E. W. Hancock, J. Phys. Chem. B **111**, 7691 (2007).

[20] W. Y. Rojas, A. D. Winter, J. Grote, S. S. Kim, R. R. Naik, A. D. Williams, C. Weiland, E. Principe, D. A. Fischer, S. Banerjee, D. Prendergast, and E. M. Campo, Langmuir **34**, 1783 (2018).

[21] R. Poloni, A. L. Mariano, D. Prendergast, and J. Garcia-Barriocanal, J. Chem. Phys. **149**, 234706 (2018), arXiv:1810.08500.

[22] K. Diller, R. J. Maurer, M. Müller, and K. Reuter, J. Chem. Phys. **146**, 214701 (2017).

[23] C. Kolczewski, K. Hermann, S. Guimond, H. Kuhlenbeck, and H. J. Freund, Surf. Sci. **601**, 5394 (2007).

[24] R. Püttner, P. Schmidt-Weber, T. Kampen, C. Kolczewski, K. Hermann, and K. Horn, J. Electron. Spectrosc. Relat. Phenom. **215**, 16 (2017).

[25] M. Cavalleri, K. Hermann, A. Knop-Gericke, M. Hävecker, R. Herbert, C. Hess, A. Oestereich, J. Döbler, and R. Schlögl, J. Catal. **262**, 215 (2009).

[26] I. Zhovtobriukh, N. A. Besley, T. Fransson, A. Nilsson, and L. G. Pettersson, J. Chem. Phys. **148**, 144507 (2018).

[27] T. Fransson, Y. Harada, N. Kosugi, N. A. Besley, B. Winter, J. J. Rehr, L. G. Pettersson, and A. Nilsson, Chem. Rev. **116**, 7551 (2016).

[28] W. S. Drisdell, L. Leppert, C. M. Sutter-Fella, Y. Liang, Y. Li, Q. P. Ngo, L. F. Wan, S. Gul, T. Kroll, D. Sokaras, A. Javey, J. Yano, J. B. Neaton, F. M. Toma, D. Prendergast, and I. D. Sharp, ACS Energy Lett. **2**, 1183 (2017).

[29] N. Hellgren, J. Guo, C. Såthe, A. Agui, J. Nordgren, Y. Luo, H. Ågren, and J. E. Sundgren, Appl. Phys. Lett. **79**, 4348 (2001).

[30] B. Gao, Z. Wu, H. Ågren, and Y. Luo, J. Chem. Phys. **131**, 034704 (2009).

[31] M. Stener, G. Fronzoni, and M. de Simone, Chem. Phys. Lett. **373**, 115 (2003).

[32] N. A. Besley and F. A. Asmuruf, Phys. Chem. Chem. Phys. **12**, 12024 (2010).

[33] P. Verma and R. J. Bartlett, J. Chem. Phys. **145**, 034108 (2016).

[34] A. Nakata, Y. Imamura, and H. Nakai, J. Chem. Theory Comput. **3**, 1295 (2007).

[35] N. A. Besley, M. J. Peach, and D. J. Tozer, Phys. Chem. Chem. Phys. **11**, 10350 (2009).

[36] A. Nakata, Y. Imamura, and H. Nakai, J. Chem. Phys. **125**, 064109 (2006).

[37] J. Vinson and J. J. Rehr, Phys. Rev. B Condens. Matter **86**, 1 (2012).

[38] J. Vinson, J. J. Rehr, J. J. Kas, and E. L. Shirley, Phys. Rev. B Condens. Matter **83**, 115106 (2011).

[39] M. Nooijen and R. J. Bartlett, J. Chem. Phys. **102**, 6735 (1995).

[40] S. Coriani, O. Christiansen, T. Fransson, and P. Norman, Phys. Rev. A **85**, 1 (2012).

[41] B. Peng, P. J. Lestrange, J. J. Goings, M. Caricato, and X. Li, J. Chem. Theor. Comput. **11**, 4146 (2015).

[42] J. P. Coe and M. J. Paterson, Theor. Chem. Acc. **134**, 3 (2015).

[43] S. I. Bokarev, M. Dantz, E. Suljoti, O. Kühn, and E. F. Aziz, Phys. Rev. Lett. **111**, 1 (2013).

[44] G. Grell, S. I. Bokarev, B. Winter, R. Seidel, E. F. Aziz, S. G. Aziz, and O. Kühn, J. Chem. Phys. **143**, 074104 (2015).

[45] W. Egelhoff, Surf. Sci. Rep. **6**, 253 (1987).

[46] L. Triguero, O. Plashkevych, L. Pettersson, and H. Ågren, J. Electron. Spectrosc. Relat. Phenom. **104**, 195 (1999).

[47] Y. Takahata and D. P. Chong, J. Electron. Spectrosc. Relat. Phenom. **133**, 69 (2003).

[48] C. Matteo, M. Odelius, D. Nordlund, A. Nilsson, and L. G. M. Pettersson, Phys. Chem. Chem. Phys. **15**, 2854 (2005).

[49] Z. H. Zeng, X. F. Ma, W. C. Ding, and W. X. Li, Sci. China Chem. **53**, 402 (2010).

[50] S. García-Gil, A. García, and P. Ordejón, Eur. Phys. J. B **85**, 239 (2012).

[51] P. S. Bagus, Phys. Rev. **139**, A619 (1965).

[52] J. C. Slater, Adv. Quant. Chem. **6**, 1 (1972).

[53] L. Triguero, L. Pettersson, and H. Ågren, Phys. Rev. B **58**, 8097 (1998).

[54] D. Prendergast and G. Galli, Phys. Rev. Lett. (2006).

[55] N. A. Besley, A. T. B. Gilbert, and P. M. W. Gill, J. Chem. Phys. **130**, 124308 (2009).

[56] J. S. Uejio, C. P. Schwartz, R. J. Saykally, and D. Prendergast, Chem. Phys. Lett. **467**, 195 (2008).

[57] M. Nyberg, Y. Luo, L. Triguero, L. Pettersson, and H. Ågren, Phys. Rev. B **60**, 7956 (1999).

[58] A. E. Fouda and N. A. Besley, Theor. Chem. Acc. **137**, 1 (2018).

[59] I. Tolbatov and D. M. Chipman, Theor. Chem. Acc. **133**, 1 (2014).

[60] Y. Takahata and D. P. Chong, Bull. Chem. Soc. Jap. **73**, 2453 (2000).

[61] S. Carniato and P. Millié, J. Chem. Phys. **116**, 3521 (2002).

[62] D. P. Chong and Y. Takahata, Chem. Phys. Lett. **418**, 286 (2006).

[63] D. P. Chong, P. Aplincourt, and C. Bureau, J. Phys. Chem. A **106**, 356 (2002).

[64] V. Blum, R. Gehrke, F. Hanke, P. Havu, V. Havu, X. Ren, K. Reuter, and M. Scheffler, Comput. Phys. Commun. **180**, 2175 (2009).

[65] X. Ren, P. Rinke, V. Blum, J. Wieferink, A. Tkatchenko, A. Sanfilippo, K. Reuter, and M. Scheffler, New J. Phys. **14**, 053020 (2012).

[66] K. Lie, R. Høier, and R. Brydson, Phys. Rev. B Condens. Matter **61**, 1786 (2000).

[67] R. Buczko, G. Duscher, S. J. Pennycook, and S. T. Pantelides, Phys. Rev. Lett. **85**, 2168 (2000).

[68] R. Ahuja, P. Brühwiler, B. Johansson, N. Mårtensson, O. Eriksson, and J. Wills, Phys. Rev. B Condens. Matter **54**, 14396 (1996).

[69] J. Janak, Phys. Rev. B **18**, 7165 (1978).

[70] A. R. Williams, R. A. DeGroot, and C. B. Sommers, J. Chem. Phys. **63**, 628 (1975).

[71] D. P. Chong, Chem. Phys. Lett. **232**, 486 (1995).

[72] M. Stener, A. Lisini, and P. Decleva, Chem. Phys. **191**, 141 (1995).

[73] C.-h. Hu and D. P. Chong, Chem. Phys. Lett. **262**, 729 (1996).

[74] I. Tanaka, H. Araki, M. Yoshiya, T. Mizoguchi, K. Ogasawara, and H. Adachi, Phys. Rev. B Condens. Matter **60**, 4944 (1999).

[75] C. Elsasser and S. Kostlmeier, Ultramicroscopy **86**, 325 (2001).

[76] Y. Deng, B. Gao, M. Deng, and Y. Luo, J. Chem. Phys. **140**, 0 (2014).

[77] R. Püttner, C. Kolczewski, M. Martins, a. S. Schlachter, G. Snell, M. Sant'Anna, J. Viefhaus, K. Hermann, and G. Kaindl, Chem. Phys. Lett. **393**, 361 (2004).

[78] K. Diller, F. Klappenberger, M. Marschall, K. Hermann, a. Nefedov, C. Wöll, and J. V. Barth, J. Chem. Phys. **136**, 014705 (2012).

[79] N. Ferré and X. Assfeld, J. Chem. Phys. **117**, 4119 (2002).

[80] P.-F. Loos and X. Assfeld, Int. J. Quantum Chem. **107**, 2243 (2007).

[81] J. Gavnholt, T. Olsen, M. Engelund, and J. Schiøtz, Phys. Rev. B **78**, 075441 (2008).

[82] R. J. Maurer and K. Reuter, J. Chem. Phys. **139**, 014708 (2013).

[83] T. Ziegler, M. Seth, M. Krykunov, J. Autschbach, and F. Wang, J. Chem. Phys. **130**, 154102 (2009).

[84] Y. C. Park, M. Krykunov, and T. Ziegler, Mol. Phys. **113**, 1636 (2015).

[85] Y. C. Park, F. Senn, M. Krykunov, and T. Ziegler, J. Chem. Theory Comput. **12**, 5438 (2016).

[86] J. Cullen, M. Krykunov, and T. Ziegler, Chem. Phys. **391**, 11 (2011).

[87] M. Krykunov and T. Ziegler, J. Chem. Theory Comput. **9**, 2761 (2013).

[88] F. A. Evangelista, P. Shushkov, and J. C. Tully, J. Phys. Chem. A **117**, 7378 (2013).

[89] W. D. Derricotte and F. a. Evangelista, Phys. Chem. Chem. Phys. **17**, 14360 (2015).

[90] H.-Z. Ye, M. Welborn, N. D. Ricke, and T. Van Voorhis, J. Chem. Phys. **147**, 214104 (2017).

[91] A. T. B. Gilbert, N. A. Besley, and P. M. W. Gill, J. Phys. Chem. A **112**, 13164 (2008).

[92] S.-P. Gao, C. J. Pickard, A. Perlov, and V. Milman, J. Phys. Condens. Matter **21**, 104203 (2009).

[93] I. Minkov, F. Gel'mukhanov, R. Friedlein, W. Osikowicz, C. Suess, G. Öhrwall, S. L. Sorensen, S. Braun, R. Murdey, W. R. Salaneck, and H. Ågren, J. Chem. Phys. **121**, 5733 (2004).

[94] J. Perdew, K. Burke, and M. Ernzerhof, Phys. Rev. Lett. **77**, 3865 (1996).

[95] C. Adamo and V. Barone, J. Chem. Phys. **110**, 6158 (1999).

[96] A. K. Wilson, T. van Mourik, and T. H. Dunning, J. Mol. Struct. THEOCHEM **388**, 339 (1996).

[97] M. J. Frisch, J. A. Pople, and J. S. Binkley, J. Chem. Phys. **80**, 3265 (1984).

[98] F. Weigend and R. Ahlrichs, Phys. Chem. Chem. Phys. **7**, 3297 (2005).

[99] I. Y. Zhang, X. Ren, P. Rinke, V. Blum, and M. Scheffler, New J. Phys. **15**, 123033 (2013).

[100] T. H. Dunning, J. Chem. Phys. **90**, 1007 (1989).

[101] J. Foster and S. F. Boys, Rev. Mod. Phys. **32**, 300 (1960).

[102] M. Rossi, M. Ceriotti, and D. E. Manolopoulos, J. Phys. Chem. Lett. **7**, 3001 (2016).

[103] G. Fronzoni, G. Balducci, R. De Francesco, M. Romeo, and M. Stener, J. Phys. Chem. C **116**, 18910 (2012).

[104] G. Vall-Llosera, B. Gao, a. Kivimäki, M. Coreno, J. Álvarez Ruiz, M. De Simone, H. Ågren, and E. Rachlew, J. Chem. Phys. **128**, 044316 (2008).

[105] F. Bischoff, K. Seufert, W. Auwärter, S. Joshi, S. Vijayaraghavan, D. Écija, K. Diller, A. C. Papageorgiou, S. Fischer, F. Allegretti, D. A. Duncan, F. Klappenberger, F. Blobner, R. Han, and J. V. Barth, ACS Nano **7**, 3139 (2013).

[106] D. P. Chong, C. H. Hu, and P. Duffy, Chem. Phys. Lett. **249**, 491 (1996).

[107] R. Laskowski, T. Gallauner, P. Blaha, and K. Schwarz, J. Phys. Condens. Matter **21**, 104210 (2009).

[108] R. Van Meer, O. V. Gritsenko, and E. J. Baerends, J. Chem. Theory Comput. **10**, 4432 (2014).

[109] W. Domcke and L. Cederbaum, Chem. Phys. **25**, 189 (1977).

[110] O. Plashkevych, T. Privalov, H. Ågren, V. Carravetta, and K. Ruud, Chem. Phys. **260**, 11 (2000).

[111] G. Herzberg and E. Teller, Z. Phys. Chem. **21B**, 410 (1933).

[112] S. Jahn and P. M. Kowalski, Rev. Mineral. Geochem. **78**, 691 (2014).

[113] C. P. Schwartz, J. S. Uejio, R. J. Saykally, and D. Prendergast, J. Chem. Phys. **130**, 184109 (2009).

[114] C. P. Schwartz, J. S. Uejio, R. J. Saykally, and D. Prendergast, J. Chem. Phys. **130**, 184109 (2009).

[115] C. Kolczewski and K. Hermann, J. Chem. Phys. **118**, 7599 (2003).

[116] N. M. Boffi, M. Jain, and A. Natan, J. Chem. Phys. **144**, 084104 (2016).

Supporting information for: Efficient Simulation of Near-Edge X-ray Absorption Fine Structure (NEXAFS) in Density-Functional Theory: Comparison of Core-Level Constraining Approaches

Georg S. Michelitsch and Karsten Reuter

January 24, 2019

1 Comparison of our MOM procedure with previous approaches

In the Tables 1 and 2 pictorial representations of the Kohn-Sham eigenstates of the ground state as well as after a self-consistent optimization using our modified maximum overlap method (MOM) as well as the original MOM are given. The last column is original MOM with the modification of additional smearing present on the excited electron, which thus delocalizes on energetically close eigenstates, another (less successful) approach to overcome oscillations during the SCF cycle. The problem of oscillations arises for these particular systems of high symmetry due to degeneracies in the virtual states. Although our method does not recover all virtual states from the original ground state calculation, it manages to converge many lower-lying excited states.

KS state#	ground state	our MOM	regular MOM	smearing MOM	KS#	ground state	our MOM	regular MOM	smearing MOM
22	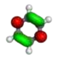	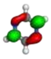	oscillations	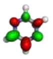	34	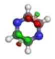	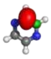	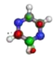	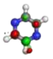
23	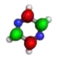	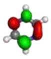	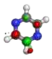	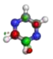	35	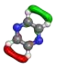	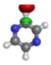	oscillations	oscillations
24	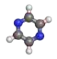	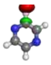	oscillations	oscillations	36	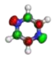	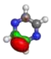	oscillations	oscillations
25	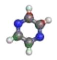	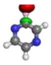	oscillations	oscillations	37		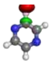	oscillations	oscillations
26	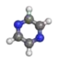	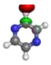	oscillations	oscillations	38		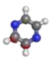	oscillations	oscillations
27	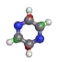	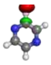	oscillations	oscillations	39	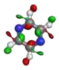	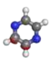	oscillations	oscillations
28			oscillations	oscillations	40	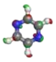	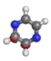	oscillations	oscillations
29	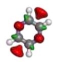	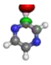	oscillations	oscillations	41	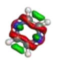	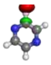	oscillations	oscillations
30			oscillations	oscillations	42	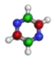	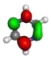	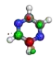	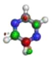
31	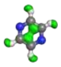	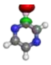	oscillations	oscillations	43	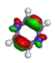	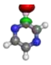	oscillations	oscillations
32	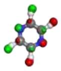	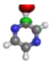	oscillations	oscillations	44	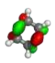	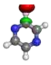	oscillations	oscillations
33	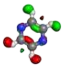	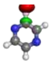	oscillations	oscillations	45	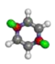	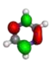	oscillations	oscillations

Table 1: Final states of an excited electron resulting from occupation of the given virtual states of the ground state calculation following different MOM-approaches. Our approach is prone to variational collapse in some cases but always converges. The regular MOM leads to oscillations between degenerate states owed to high symmetry in the system and thus does not converge most of the states. Introducing smearing leads to a similar result as the regular MOM but leaks charge to neighboring KS states (here: 0.2 e$^-$) A carbon core hole is present.

KS state #	ground state	our MOM	regular MOM	smearing MOM	KS state #	ground state	our MOM	regular MOM	smearing MOM
22	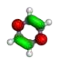	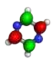	oscillations	oscillations	34	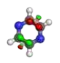	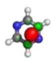	oscillations	oscillations
23	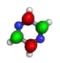	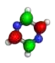	oscillations	oscillations	35	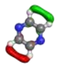	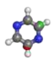	oscillations	oscillations
24	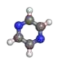	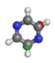	oscillations	oscillations	36	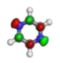	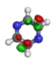	oscillations	oscillations
25	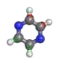	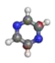	oscillations	oscillations	37		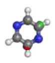	oscillations	oscillations
26	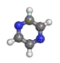	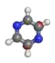	oscillations	oscillations	38		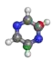	oscillations	oscillations
27	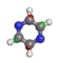	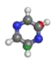	oscillations	oscillations	39	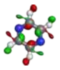	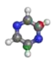	oscillations	oscillations
28	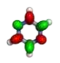		oscillations	oscillations	40	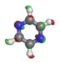	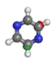	oscillations	oscillations
29	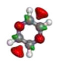	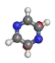	oscillations	oscillations	41	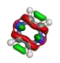	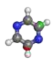	oscillations	oscillations
30	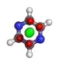	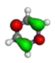	oscillations	oscillations	42	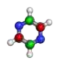	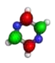	oscillations	oscillations
31	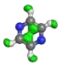	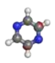	oscillations	oscillations	43	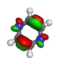	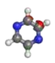	oscillations	oscillations
32	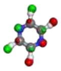	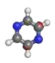	oscillations	oscillations	44	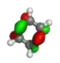	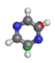	oscillations	oscillations
33	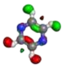	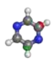	oscillations	oscillations	45	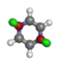	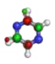	oscillations	oscillations

Table 2: Final states of an excited electron resulting from occupation of the given virtual states of the ground state calculation following different MOM-approaches. Our approach is prone to variational collapse in some cases but always converges. The regular MOM leads to oscillations between degenerate states owed to high symmetry in the system and thus does not converge most of the states. Introducing smearing leads to a similar result as the regular MOM but leaks charge to neighboring KS states (here: 0.2 e^-) A nitrogen core hole is present.

2 Convergence of the excitation energy for explicit approaches

Figure 1 shows the convergence behaviour of the explicit approaches for small molecules. Small molecules are harder to converge using the MOM procedure because only few atoms and thus also a smaller amount of basis functions is present. Following the maximum overlap criterion as outlined in the main manuscript and evaluating the magnitude of the elements of the overlap matrix between two consecutive Kohn-Sham eigenvectors thus becomes more difficult, since the virtual states are mostly delocalized among all atoms and have contributions from many basis functions in similar percentage, which in turn lead to similar values of the overlap followed by a stepwise collapse into few low-lying solutions. As can be seen from the figures below the lowest excitation energies are found in all basis sets. The tendency to discover other excited states increases with the size of the basis.

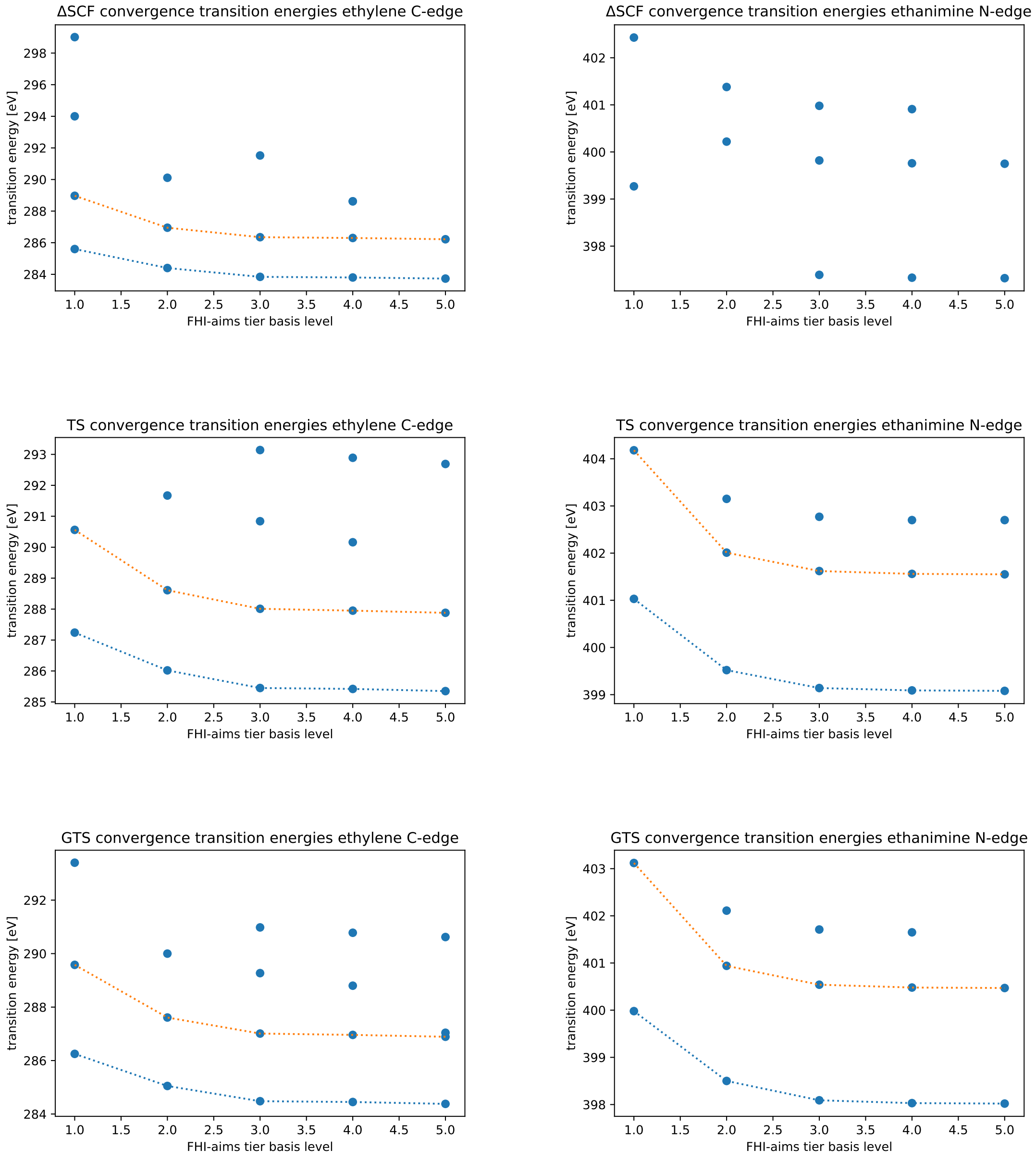
ΔSCF convergence transition energies ethylene C-edge

ΔSCF convergence transition energies ethanimine N-edge

TS convergence transition energies ethylene C-edge

TS convergence transition energies ethanimine N-edge

GTS convergence transition energies ethylene C-edge

GTS convergence transition energies ethanimine N-edge

Figure 1: The convergence behaviour of the lowest lying states in the ethylene and ethanimine molecules suggests that the states close to the edge are already converged at tier 2, and definitely converged at tier 3 of the FHI-aims numerical atomic orbital basis. Furthermore the much better agreement of the GTS method with the results from the ΔSCF is apparent as compared to the TS approach.